Performances of the SVOM/ECLAIRs instrument in the low-energy band and consequences for the detection of X-ray-rich gamma-ray bursts

Wenjin Xie

Université Paris Cité

École doctorale Astronomie et Astrophysique d'Ile-de-France (127)
CEA Paris-Saclay

Performances of the SVOM/ECLAIRs instrument in the low-energy band and consequences for the detection of X-ray-rich gamma-ray bursts

---

Par Wenjin XIE

Thèse de doctorat en Astronomie et astrophysique

Dirigée par Bertrand CORDIER

Présentée et soutenue publiquement le 29/04/2024

Devant un jury composé de :

Etienne PARIZOT Professeur des universités, *Université Paris Cité*	Président
Maria-Grazia BERNARDINI Associate Professor, *INAF, Observatorio Astronomico di Brera*	Rapportrice
Jérome CHENEVEZ Associate Professor, *Technical University of Denmark*	Rapporteur
Sarah ANTIER Astronome adjoint, *Observatoire de la Côte d'Azur*	Examinatrice
Jean-Luc ATTEIA Astronome, *Institut de Recherche en Astrophysique et Planétologie*	Examinateur
Bertrand CORDIER Ingénieur-Chercheur, *CEA Paris-Saclay, IRFU*	Directeur de thèse
Nicolas DAGONEAU Ingénieur-Chercheur, *CEA Paris-Saclay, IRFU*	Co-encadrant Membre invité

Abstract

Résumé court

Mots-clés: Astrophysique des hautes énergies ; Sursauts gamma ; Imagerie à masque codé ; Ciel transitoire ; SVOM ; ECLAIRs

SVOM (Space-based multi-band astronomical Variable Objects Monitor) est une mission franco-chinoise dédiée à l'étude du ciel des phénomènes transitoires. Sa mise en service est prévue pour 2024. ECLAIRs est un télescope à masque codé doté d'un grand champ de vue. Il est conçu pour détecter et localiser les sursauts gamma (GRB) dans une gamme d'énergie allant de 4 keV à 120 keV. En 2021, le télescope ECLAIRs a fait l'objet de plusieurs campagnes d'étalonnage dans des chambres d'essai sous vide afin d'évaluer ses performances.

Entre 4 et 8 keV, la réponse en coups du plan de détection présente des inhomogénéités entre les pixels de différents lots de production. L'inhomogénéité de l'efficacité est causée par des pixels à faible efficacité (LEP) provenant de l'un des deux lots, ainsi que par des pixels à seuil élevé (HTP) dont le seuil a été relevé pour éviter les effets de diaphonie. En outre, des bruits inattendus ont été détectés dans les régions du plan de détection proches des caloducs.

J'ai étudié l'impact de ces inhomogénéités et du bruit des caloducs à basse énergie sur le trigger embarqué d'ECLAIRs. Je propose différentes stratégies afin d'atténuer ces impacts et d'améliorer les performances du trigger.

J'ai analysé les données des campagnes d'étalonnage et effectué des simulations avec le modèle sol du logiciel du trigger afin de concevoir et d'évaluer les différentes stratégies. La majeure partie de l'impact des HTP peut être corrigée en les excluant du traitement. Pour corriger l'impact des LEP, une correction d'efficacité dans l'image du plan du détecteur semble être une bonne solution. Une solution efficace pour le bruit des caloducs consiste à sélectionner les pixels bruyants et à les ignorer dans la bande 4–8 keV.

A partir de données d'étalonnage, j'ai aussi calculé la valeur de l'efficacité dans la gamme 4–8 keV. J'ai obtenu une surface effective de 142 cm^2 à 4.5 keV et de 310 cm^2 à 8 keV. Ces chiffres tiennent compte de l'influence des LEP et des HTP.

Après avoir étudié et corrigé les effets instrumentaux dans la bande 4–8 keV, je me suis intéressé à l'apport de cette bande basse énergie dans la performance de détection par le trigger d'ECLAIRs pour différents types de GRBs. J'ai effectue cette étude en utilisant le logiciel ECLGRM développé par différentes institutions (CNRS, CEA, CNES), et le banc de test du logiciel embarqué d'ECLAIRs (UGTS).

Grâce à ces simulations, j'ai calculé les sensibilités de déclenchement d'ECLAIRs pour différents GRBs à différentes positions dans le champ de vue. J'ai ainsi constaté que la sensibilité d'ECLAIRs pour la détection des GRB mous augmentait de manière significative après l'ajout de la bande d'énergie 4–8 keV. Pour les GRB dont l'énergie du pic est égale à

5 keV, le SNR de la détection augmente d'environ 60%.

Pour simuler un scénario plus réaliste, j'ai effectué des simulations sur 57 échantillons de GRBs HETE-2 en utilisant le banc d'essai UGTS (même matériel que le logiciel embarqué d'ECLAIRs) avec la configuration des bandes sélectionnée pour la phase de recette en vol. J'ai comparé les performances de détection des algorithmes du trigger "taux de comptage" (CRT) et "image" (IMT) dans l'UGTS et j'ai constaté que CRT pouvait détecter 55 des 57 GRBs de l'échantillon et que IMT pouvait en détecter 52. Ce résultat suggère que le trigger taux de comptage est plus sensible que le trigger image pour les GRBs moyennement longs (< 40 s).

Short abstract

Keywords: High energy astrophysics; Gamma-ray burst; Coded mask imaging; Transient sky; SVOM; ECLAIRs

The Space-based multi-band astronomical Variable Objects Monitor (SVOM) is a Chinese-French mission dedicated to the study of the transient sky. It is scheduled to start operations in 2024. ECLAIRs is a coded-mask telescope with a large field-of-view. It is designed to detect and localize Gamma-Ray Bursts (GRBs) in the energy range from 4 keV up to 120 keV. In 2021, the ECLAIRs telescope underwent various calibration campaigns in vacuum test-chambers to evaluate its performances.

Between 4 and 8 keV, the counting response of the detection plane shows inhomogeneities between pixels from different production batches. The efficiency inhomogeneity is caused by Low-Efficiency Pixels (LEPs) from one of the two batches, together with High-Threshold Pixels (HTPs) whose threshold was raised to avoid cross-talk effects. In addition, some unexpected noise was found in the detection plane regions close to the heat pipes.

I studied the impact of these inhomogeneities and of the heat-pipe noise at low energies on the ECLAIRs onboard triggers. I also suggest different strategies in order to mitigate these impacts and to improve the onboard trigger performances.

I analyzed the data from the calibration campaigns and performed simulations with the ground model of the ECLAIRs trigger software in order to design and evaluate the different strategies. Most of the impact of HTPs can be corrected by excluding them from processing. To correct the impact of LEPs, an efficiency correction in the detector plane image seems to be a good solution. An effective solution for heat-pipe noise is to select noisy pixels and ignore them in the 4–8 keV band.

From calibration data, I also calculated the efficiency value in the 4–8 keV range. I obtained an effective area of 142 cm^2 at 4.5 keV and 310 cm^2 at 8 keV. These values take into account the influence of LEP and HTP.

After studying and correcting instrumental effects in the 4–8 keV band, I investigated the contribution of this low-energy band to ECLAIRs trigger performance for different types of GRBs. I carried out this study using ECLGRM software developed by various institutions (CNRS, CEA, CNES), and the ECLAIRs trigger test bench (UGTS).

Through simulations, I obtain the ECLAIRs trigger sensitivities for different GRBs at different locations.

I found that the sensitivity of ECLAIRs for soft GRB detection increased significantly after adding the 4–8 keV energy bands. For GRBs with peak energies equal to 5 keV, the SNR of the detection is increased by about 60%.

To simulate a realistic scenario, I performed trigger simulations on 57 HETE-2 GRB samples using the UGTS (same hardware as the ECLAIRs onboard trigger) test bench with the selected trigger band configuration to begin the commissioning phase. I compared the triggering performance of count-rate trigger (CRT) and image trigger algorithms (IMT) in UGTS and found that CRT could trigger 55 out of 57 GRB of the sample and IMT could trigger 52. This result suggests that count-rate triggering is more sensitive than image trigger for weakly medium-long GRBs (< 40 s).

简短摘要

关键词：高能天体物理学；伽马射线暴；编码孔径成像；瞬变天空；SVOM 卫星；ECLAIRs

空间多波段天文变源监测器（SVOM）是一个中法合作的任务，致力于研究瞬变天空。预计将于 2024 年开始运行。ECLAIRs 是一个大视场的编码孔径望远镜，设计用于在 4 keV 至 120 keV 的能量范围内探测和定位伽马射线暴（GRB）。2021 年，ECLAIRs 望远镜在真空测试舱内进行了各种标定活动，以评估其性能。

在 4–8 keV 之间，探测平面的计数响应在来自不同生产批次的像素之间表现出不均匀性。效率不均匀性是由来自两个批次之一的低效率像素（LEP）以及为避免串扰效应而提高阈值的高阈值像素（HTP）引起的。此外，在探测平面靠近热管的区域发现了一些意外的噪声。

我研究了这些不均匀性和低能热管噪声对 ECLAIRs 在轨触发器的影响。我还提出了不同的策略来减轻这些影响并提高在轨触发器性能。

我分析了标定活动的数据，并使用 ECLAIRs 触发器软件的地面模型进行了模拟，以设计和评估不同的策略。通过在触发算法中排除 HTP 影响，可以纠正大部分 HTP 的影响。为了纠正 LEP 的影响，在探测器计数图像中进行效率校正是一个很好的解决方案。对于热管噪声，一个有效的解决方案是筛选出噪声像素并在触发算法中的 4–8 keV 波段忽略它们的计数。

从标定数据中，我还计算了 4–8 keV 范围内的像素的效率值。并且计算了 ECLAIRs 的有效探测面积，在 4.5 keV 时 ECLAIRs 望远镜的的有效面积为 142 cm^2，在 8 keV 时为 310 cm^2。这些值考虑了 LEP 和 HTP 的影响。

在研究和校正了 4–8 keV 波段的仪器效应后，我研究了这个低能量波段对不同类型 GRB 的 ECLAIRs 触发器性能的贡献。我使用由不同机构（CNRS、CEA、CNES）共同开发的 ECLGRM 软件以及 ECLAIRs 触发器测试平台（UGTS）进行了这项研究。通过模拟，我得到了 ECLAIRs 触发器对不同位置不同 GRB 的灵敏度。我发现，在添加了 4–8 keV 能量波段后，ECLAIRs 对软 GRB 探测的灵敏度显著提高。对于峰值能量等于 5 keV 的 GRB，ECLAIRs 探测的信噪比提高了约 60%。

为了模拟真实情况，我使用 UGTS（与 ECLAIRs 在轨触发器使用相同的硬件）测试平台对 57 个 HETE-2 GRB 样本进行了触发器模拟，使用选定的触发器波段配置开始调试阶段。我比较了 UGTS 中计数率触发器（CRT）和图像触发器算法（IMT）的触发性能，发现 CRT 可以触发样本中的 55 个 GRB，而 IMT 可以触发 52 个。这一结果表明，对于较弱的中长 GRB（< 40 s），计数率触发比图像触发更灵敏。

Résumé long

Contexte

Les sursauts gamma (GRB) sont les phénomènes explosifs les plus cataclysmiques de l'Univers. On pense généralement que les GRBs proviennent de l'effondrement d'une étoile massive ou de la fusion d'étoiles compactes dans un système binaire. Dans les deux cas un trou noir super-accrétant ou un magnétar en rotation rapide se forme, ce qui produit un jet via différents mécanismes, le faisant éjecter vers l'extérieur à des vitesses relativistes.

Malgré des décennies d'observations et d'études théoriques, de nombreuses questions sur la physique des GRBs restent ouvertes concernant le moteur central, la géométrie du jet, l'accélération des particules, le mécanisme de rayonnement et la nature des GRBs moux tels que les flashs de rayons X, etc. L'extension de la bande d'énergie de détection jusqu'aux rayons X mous est importante pour détecter les GRBs mous et améliorer notre compréhension de la physique des GRBs.

La mission SVOM est le fruit d'une collaboration entre la Chine et la France et vise à étudier le phénomène des GRBs et le ciel transitoire dans plusieurs longueurs d'onde. Le lancement de la mission est prévu pour juin 2024. Le satellite SVOM est équipé de quatre instruments scientifiques : un télescope à rayons gamma mous appelé ECLAIRs, un spectromètre à rayons gamma appelé Gamma-Ray Monitor, et deux télescopes de suivi à champ étroit dans les bandes des rayons X (MXT) et du visible (VT).

ECLAIRs est un télescope à masque codé doté d'un grand champ de vue, qui est principalement utilisé pour la détection et la localisation des GRBs sur le satellite SVOM. Le plan de détection d'ECLAIRs est équipé de 6400 pixels de détection en tellurure de cadmium (CdTe) à faible courant de fuite, qui ont une zone de détection d'environ 1000 cm^2. La gamme d'énergie de détection s'étend de 4 keV à 120 keV. La plage d'énergie de détection à partir de 4 keV pour les GRBs est un avantage unique d'ECLAIRs par rapport à d'autres instruments.

Avant la mission SVOM, il existait différentes caméras à rayons X à grand champ dans le cadre de la mission BeppoSAX (Beppo Satellite italiano per Astronomia X, 1996-2002) et de la mission HETE-2 (High-Energy Transient Explorer 2, 2000-2008). Cependant, les caméras à grand champ de BeppoSAX (WFC, 2–30 keV) n'avaient pas de trigger embarqué, et le moniteur de rayons X à grand champ de HETE-2 (WXM) avait un trigger embarqué, mais sa gamme d'énergie était limitée à 2–25 keV. Pour les instruments encore en activité, comme Swift/BAT et Fermi/GBM, les seuils d'énergie de détection relativement élevés (respectivement de 15 keV et 8 keV), ont limité la capacité des deux missions à observer efficacement les GRB mous. En revanche, SVOM est conçu pour être déclenché à partir de 4 keV.

Inhomogénéité de l'efficacité

En 2021, ECLAIRs a fait l'objet de sérieux tests d'étalonnage au CNES (Toulouse, France), et j'ai extrait les données brutes pour les analyser en détail. Au cours du processus d'analyse des données, j'ai constaté que l'efficacité des pixels du détecteur présentait un caractère inhomogène dans la bande 4–8 keV.

Il existe trois populations de pixels que nous avons appelées pixels à seuil élevé (HTP, 400 pixels), pixels à haute efficacité (HEP, 4000 pixels) et pixels à faible efficacité (LEP, 2000

pixels). Les HTP ont un seuil de départ à 7 keV. Les HEP ont une efficacité supérieure à celle des LEP. J'ai constaté que la différence d'efficacité entre les LEP et les HEP diminue avec l'énergie entre 4 et 8 keV, la différence peut être décrite par une fonction linéaire : $\Delta_{\text{eff}} = -0.052 \times E_{\text{keV}} + 0.417$. Au-dessus de 8 keV, ces trois populations de pixels sont homogènes.

En ce qui concerne la raison de la différence d'efficacité entre LEP et HEP, j'ai proposé qu'elle soit due à la différence d'épaisseur du matériau de surface (Pt ou TeO_2) entre les différentes populations. J'ai calculé la différence d'épaisseur pour différents modèles possibles : si un seul composant est concerné, on trouve une différence d'épaisseur pour le Pt $\sim$123 nm , ou pour le $TeO_2 \sim$ 460 nm. Une possibilité plus réaliste pourrait être due à un effet combiné des deux matériaux.

Pour obtenir l'efficacité absolue des pixels, j'ai analysé l'ensemble des données obtenues avec une source de rayons X (Fe^{55}). Pour la population HEP, l'efficacité est de 0.777 ± 0.022 et pour la population LEP, l'efficacité est de 0.694 ± 0.023.

J'ai ensuite essayé de calculer la surface effective globale dans la bande 4–8 keV. Par surface effective globale, nous entendons le nombre de centimètres carrés effectifs qui restent après que tous les effets ont été pris en compte : l'efficacité des pixels, la transparence globale des couches multi-isolantes (MLI) au-dessus du plan du détecteur et la transparence globale du masque.

La fraction d'ouverture du masque est de 0.4. J'ai calculé la transparence de la MLI en utilisant le jeu de données obtenu avec la source de Fe^{55}. J'ai obtenu une valeur de 0.665, alors que la valeur théorique est de 0.887. Nous avons donc décidé d'effectuer un test MLI spécifique au CEA. Finalement, nous avons obtenu une transparence MLI de 0.845 ± 0.003 et avons décidé d'appliquer cette valeur dans le calcul de l'efficacité globale d'ECLAIRs.

Sur la base de l'efficacité du plan de détection à 5.9 keV et de la distribution relative des coups dans la bande 4–8 keV, j'ai calculé la valeur de l'efficacité du plan de détection dans la gamme 4–8 keV. Finalement, j'ai obtenu une surface effective de 142 cm^2 à 4.5 keV et de 310 cm^2 à 8 keV. Ces chiffres tiennent compte de l'influence du LEP et du HTP.

Pour évaluer l'impact de l'inhomogénéité de l'efficacité (LEP et HTP) sur les performances de déclenchement à bord d'ECLAIRs, j'ai effectué une simulation impliquant ces pixels HTP et LEP. L'idée principale était d'ajouter les pixels LEP et HTP dans le plan de détection en modifiant l'efficacité du pixel. J'ai ensuite simulé le fond diffus de rayons X et traité les données pour obtenir la distribution du SNR du ciel, et enfin pour calculer le SNR maximum dans le ciel et le seuil de déclenchement. Le seuil dynamique prédéfini a été fixé à 6.5 $\times \sigma_{SNR}$ afin d'éviter les faux déclenchements causés par les résidus de bruit de fond.

Idéalement, après le processus de déconvolution d'ECLAIRs, le SNR des cartes du ciel est normalement distribué avec $\sigma_{SNR} \sim 1$ sur une échelle de temps d'observation de 20 minutes. La valeur de σ_{SNR} détermine le seuil de déclenchement dynamique. Après avoir introduit l'effet de l'inhomogénéité de l'efficacité, la valeur de σ_{SNR} dans la bande 4–8 keV a augmenté pour atteindre 5.75 pour les HTP et 1.43 pour les LEP.

J'ai développé des approches pour atténuer l'impact de l'inhomogénéité de l'efficacité pour le trigger d'ECLAIRs. Pour les HTP, la majeure partie de leur impact peut être corrigée en fixant leurs poids à 0 dans la table configurant l'ajustement du bruit de fond et dans celle configurant la déconvolution, ce qui signifie l'exclusion de ces pixels pendant le traitement des données par le logiciel embarqué. Pour corriger l'impact des LEP, la correction de l'efficacité dans l'image du plan de détection avant la déconvolution semble être

une bonne solution.

Bruit des caloducs

Lors de l'analyse de l'ensemble des données du test en vide thermique (TVAC), j'ai remarqué des comptages inhabituels dans la bande 4–8 keV de part et d'autre du plan de détection en l'absence d'une source de rayons X. Bien que la cause de ces bruits soit inconnue, nous avons observé ce bruit dans une région proche des caloducs et l'avons baptisé "bruit des caloducs". Par la suite, j'ai étudié les caractéristiques de ce bruit, son effet sur les performances de détection d'ECLAIRs, et j'ai cherché des moyens d'atténuer son impact.

J'ai constaté que les pixels affectés par le bruit des caloducs affichent un taux de comptage relativement élevé dans la gamme 4–8 keV. Dans un intervalle de temps de 10 ms, les comptages sont toujours compris entre 0 et 2 dans la bande 4–8 keV pour les pixels normaux. Cependant, pour les pixels affectés par ce bruit, les comptages dans la bande 4–8 keV dépassent souvent 2 et atteignent 5–25 comptages (intervalle de 10 ms). Cela signifie que nous pourrions être en mesure de séparer le bruit des caloducs et le bruit de fond du ciel dans les comptages sur 10 ms.

Afin d'évaluer l'impact potentiel du bruit des caloducs sur la détection d'ECLAIRs, j'ai effectué des simulations à l'aide d'un logiciel de simulation du trigger et des données issues du TVAC. Cela consiste à sommer les données des pixels affectés par le bruit des caloducs avec le bruit de fond en rayons X simulé, puis à traiter les données afin d'obtenir la distribution du SNR du le ciel, et enfin à calculer le SNR maximal pdu le ciel et le seuil de déclenchement, qui est 6.5 fois l'écart-type du SNR ($6.5 \times \sigma_{\mathrm{SNR}}$).

J'ai constaté que l'introduction de comptages du bruit des caloducs dans une simulation d'une observation de 20 minutes entraîne une augmentation du seuil de déclenchement d'environ 100%, par rapport aux observations sans bruit de caloducs. Même si nous avons augmenté le seuil de déclenchement, il reste un taux de fausses alertes de 99,26% dans la gamme 4–8 keV et de 4,44% dans la gamme 4–120 keV sur des échelles de temps de 20 minutes.

Afin d'atténuer les effets du bruit des caloducs sur le trigger d'ECLAIRs, j'ai développé une stratégie pour résoudre ce problème, dont l'idée principale est de supprimer les pixels affectés du traitement embarqué. J'ai identifié deux méthodes pour sélectionner les pixels affectés dans les données du TVAC : une méthode de sélection en distribution pour des échelles de temps d'observation de <0.5 s et une méthode de sélection en fréquence pour des échelles de temps d'observation de $\geq$0.5 s.

En sélectionnant et en ignorant 5% des pixels bruyants à l'aide de ces deux méthodes, il est possible d'éviter les fausses alertes causées par le bruit des caloducs. Cette méthode permet également de réduire l'augmentation du seuil de déclenchement du trigger image sur 20 minutes à environ 20% dans la bande 4–8 keV (sans la méthode d'atténuation, cette valeur serait d'environ 100%).

En fait, en fonctionnement, le bruit des caloducs sera accompagné du CXB, ce qui peut fausser la sélection des pixels bruyants. Pour résoudre ce problème, je suggère d'utiliser des données lorsque le champ de vue est complètement obscurci par la Terre pour sélectionner les pixels bruyants dans les futures phases de la mission (mise en service et exploitation). Le nombre de photons du CXB étant inférieur d'un facteur 10 dans ce cas, la sélection des pixels bruyants devrait être plus efficace et plus fiable.

Lorsque ECLAIRs sera opérationnel, je suggère d'utiliser une seule table de poids pour configurer l'ajustement du CXB et les déconvolutions d'images, et ce pour toutes les échelles de temps allant de 10 ms à 20 min. Notre objectif est de minimiser l'effet du bruit des caloducs en ne sacrifiant pas plus de 5% des pixels dans la bande 4–8 keV. Nous avons choisi la méthode de sélection en fréquence. Nous l'avons fait pour plusieurs raisons.

1. Le bruit des caloducs affecte principalement les observations à long terme, et nos simulations montrent que la méthode de sélection en fréquence est plus performante dans ce cas, en particulier pour les observations sur 20 minutes.

2. Le logiciel embarqué supprime automatiquement les données des pixels dont le nombre de coups augmentent de manière significative sur une courte période de temps (10 ms), ce qui équivaut à ignorer les pixels bruyants avec la méthode de sélection en distribution.

En 2023, le satellite SVOM entièrement intégré a subi un test en vide thermique à Shanghai. Nous avons analysé méticuleusement l'ensemble des données du test initial du 28 septembre 2023 (premier cycle d'état froid) et du test de bout en bout effectué le 6 octobre 2023.

Nous avons effectué les mêmes simulations de bruit de caloducs que précédemment, mais nous avons remplacé l'ensemble de données issues du test TVAC de Toulouse par celui de Shanghai. Grâce à des simulations dans lesquelles nous avons ajouté les comptages du TVAC au CXB simulé dans le processus de déclenchement, nous avons observé que ces bruits affectaient marginalement le seuil de déclenchement, entraînant généralement une augmentation de 1% à 12%. Il est important de noter que ces bruits n'ont pas entraîné de fausses alertes.

Entre ces deux campagnes, le télescope ECLAIRs n'était pas dans la même configuration. A Toulouse, les caloducs du télescope étaient en configuration verticale, alors qu'à Shanghai les caloducs étaient en configuration horizontale. Par conséquent, l'absence de bruit observée à Shanghai pourrait suggérer que le problème est lié à l'impact de la gravité sur le fluide circulant dans les caloducs.

Détection de GRBs riches en rayons X

Mes autres travaux ont porté les performances de déclenchement d'ECLAIRs pour différents types de GRBs en utilisant le logiciel ECLGRM et le banc de test de l'UGTS. J'ai évalué l'amélioration du SNR pour la détection des GRBs grâce à la bande 4–8 keV.

ECLGRM est un outil de simulation pour les instruments ECLAIRs et GRM. Il peut générer le fichier d'événement GRB requis par le logiciel de déclenchement avec les fichiers GRB d'entrée (fichiers de courbes de lumière et de spectre), et peut appliquer un algorithme représentatif du trigger taux de comptage. Ma contribution à ECLGRM a été le développement d'un outil personnalisé de génération de GRBs. Cet outil est capable de générer des courbes de lumière compatibles et des fichiers de spectre d'énergie basés sur les paramètres clés du GRB d'entrée. Grâce à cet outil, nous pouvons facilement générer n'importe quel GRB.

J'ai d'abord effectué une simulation pour les GRBs longs classiques (LGRBs), en me concentrant sur la manière dont les positions des GRBs dans le champ de vue affectent les

capacités de détection par ECLAIRs. Sans surprise, les simulations ont montré que la valeur du SNR diminue progressivement du centre vers les bors du champ de vue.

J'ai ensuite essayé d'évaluer la sensibilité de déclenchement d'ECLAIRs pour des GRBs longs avec des énergies de pic variées (E_p) à différentes positions dans le champ de vue. On constate que la sensibilité est d'environ 10^{-8}–10^{-7} erg/cm^2/s dans la bande 4–150 kev. Fait remarquable, pour un LGRB classique de 30 s avec E_p = 200 keV, la sensibilité dans l'axe d'ECLAIRs est de 4.5 $\times$ 10^{-8} erg/cm^2/s dans la bande 4–150 keV, alors que pour un flash de rayons X avec E_p = 20 keV avec la même durée de 30 s, la sensibilité dans l'axe dans la bande 4–150 keV est de 1.5 $\times$ 10^{-8} erg/cm^2/s, soit trois fois mieux. Cette performance est due à la contribution de la bande de basse énergie et au spectre du GRB.

J'ai décidé d'explorer plus précisément la contribution de la bande 4–8 keV à l'amélioration de la sensibilité de déclenchement à différentes énergies de pic. L'idée est de simuler le déclenchement d'ECLAIRs dans la bande 8–120 keV et dans la bande 4–120 keV. J'ai ensuite comparé le SNR maximal détecté dans ces deux bandes d'énergie.

J'ai constaté que l'amélioration de la sensibilité est significative pour la détection des GRB mous grâce à l'apport de la bande 4–8 keV. L'amélioration du SNR détecté est d'environ 60% pour les GRBs dont le pic d'énergie est égal à 5 keV et de 20% pour les GRBs dont le pic d'énergie est égal à 20 keV. Pour les GRBs de plus de 100 keV, la contribution de la bande 4–8 keV devient négligeable.

Pour simuler une détection plus réaliste des GRBs, j'ai effectué les mêmes simulations en utilisant l'échantillon de GRBs HETE-2 (au lieu de GRBs synthétiques simulés). Dans ce processus, les 57 GRBs avec du bruit de fond ont été simulés par le logiciel ECLGRM. Nous avons constaté que 56 de ces GRBs pouvaient être détectés avec succès, chacun avec un SNR > 10 dans la bande 4–120 keV. Le bonus de la bande 4–8 keV dans l'amélioration de la détection semble augmenter inversement avec le E_p du GRB. Il est de 50% pour les GRBs dont le E_p est d'environ 5 keV, et de 20% pour le E_p d'environ 30 keV, par rapport aux GRBs dont le E_p est > 30 keV, pour lesquels l'amélioration du SNR est généralement comprise entre 0% et 20%.

Enfin, pour se rapprocher de la réalité encore plus, j'ai effectué des simulations de déclenchement sur les 57 échantillons de GRBs HETE-2 en utilisant le banc de test de l'UGTS. J'ai défini les configurations des bandes en énergie avec les valeurs qui seront utilisées pour la phase de mise en service en vol (5–8, 8–50, 8–120, 20–120 keV). J'ai également utilisé le seuil dynamique qui change automatiquement en fonction de l'écart-type de l'image du ciel en SNR.

Le banc de test de l'UGTS est la copie exacte du logiciel embarqué à bord d'ECLAIRs. L'algorithme de déclenchement de l'UGTS comprend le trigger taux de comptage (CRT) et le trigger image (IMT).

J'ai comparé les performances de déclenchement de CRT et de IMT et j'ai constaté que CRT peut détecter 55 GRBs sur 57 et que IMT peut en détecter 52. Ce résultat suggère que pour les GRBs moyennement longs (< 40 secondes), le trigger taux de comptage est plus sensible que le trigger image. Cela peut être dû au fait que la sommation des images du ciel par IMT, bien qu'utile pour intégrer les coups des GRBs, ne compense pas l'augmentation du seuil dynamique utilisé pour éviter les fausses alertes induites par les résidus du bruit de fond.

Prospective

Le projet SVOM a été retardé pour diverses raisons, mais surtout à cause de l'épidémie de Covid-19, qui a pénalisé les développements en France et en Chine. Initialement, j'aurais dû traiter et analyser des données d'ECLAIRS réelles collectées depuis le ciel. Avec mon directeur de thèse, nous avons réorienté mon travail, qui s'est finalement basé sur l'analyse des calibrations au sol et des simulations numériques associées. Les résultats obtenus me donnent encore plus envie de traiter les données réelles et de participer à l'aventure scientifique de SVOM.

A l'avenir, grâce à l'avantage de sensibilité d'ECLAIRs dans la bande 4–15 keV (par rapport à Fermi et Swift) et à la combinaison d'observations simultanées multi-longueurs d'onde avec des télescopes embarqués et des télescopes au sol, il sera possible de faire des percées dans l'étude des GRBs mous. Par exemple, le moteur central des XRF, la structure du jet et l'environnement de l'explosion.

Sur une note personnelle, si je peux rester dans la collaboration SVOM après ma thèse, j'aimerais aller dans la direction étudiée dans cette thèse et mettre en place un projet de recherche centré sur l'étude des sursauts riches en rayons X.

Long abstract

Background

Gamma-ray bursts (GRBs) are the most cataclysmic explosive phenomena in the Universe. They are widely believed to originate from the collapse of a massive star or the merger of a compact binary stars, which results in the formation of a super-accreting black hole or a rapidly rotating magnetar, which then drives a jet through different mechanisms, causing it to break outward at relativistic velocities.

Despite decades of observations and theoretical studies, many questions about GRB physics remain open concerning the central engine, the jet geometry, particle acceleration, the radiation mechanism, and about the nature of soft GRBs such as X-ray flashes and so on. Extending the detection energy band of the telescope down to soft X-rays is important for detecting soft GRB events and enhancing our understanding of GRB physics.

The SVOM mission is a collaboration between China and France that aims to study the GRB phenomenon and the transient sky in multi-wavelength. The mission is scheduled to be launched in June 2024. The SVOM satellite is equipped with four scientific instruments: a soft gamma-ray telescope called ECLAIRs, a gamma-ray spectrometer named Gamma-Ray Monitor, and two narrow-field follow-up telescopes in the X-ray and visible bands. These are the Microchannel X-ray Telescope and the Visible Telescope.

ECLAIRs is a coded masked telescope with a large field of view, which is mainly used for detection and localization of GRBs on the SVOM satellite. The detection plane of the ECLAIRs is equipped with 6400 low leakage current cadmium telluride (CdTe) detector pixels, which have a detection area of about 1000 cm^2. The detection energy range is from 4 keV to 120 keV. The detection energy range down to 4 keV for GRBs is a unique advantage of ECLAIRs compare to other GRB telescopes.

Prior to the SVOM mission, there were different wide-field X-ray cameras in the Beppo Satellite italiano per Astronomia X (BeppoSAX, 1996-2002) and High-Energy Transient Ex-

plorer 2 (HETE-2, 2000-2008) mission. But the Wide Field Cameras (WFC, 2–30 keV) on BeppoSAX had no onboard trigger, and the HETE-2 Wide-Field X-Ray Monitor (WXM) had an onboard trigger, but its energy range was restricted to 2–25 keV. For the still operating GRB missions, the relatively high detection energy thresholds of Swift/BAT (2004-) and Fermi/GBM (2008-) triggers, starting at 15 keV and 8 keV, respectively, limited the ability of both missions to effectively observe soft GRB events.

Efficiency inhomogeneity

In 2021, ECLAIRs was under serious calibrated test in CNES (Toulouse, France), I took the raw data out and performed the detailed analysis. During the data analysis process, I found that the efficiency of the detector pixels shows an inhomogeneity character in the 4–8 keV band. There are three population pixels we named High Threshold Pixels (HTP, 400 pixels), High Efficiency Pixels (HEP, $\sim$ 4000 pixels) and Low Efficiency Pixels (LEP, $\sim$ 2000 pixels). HTPs have a threshold start at 7 keV. HEPs have a higher efficiency compare to LEPs. I found that the efficiency difference between LEP and HEP decreases with the energy in 4–8 keV, the difference could be described with a linear function: $\Delta_{\text{eff}} = -0.052 \times E_{\text{keV}} + 0.417$. Above 8 keV, those three pixel populations show the homogeneity properties.

For the reason of the efficiency difference between LEP and HEP, I proposed it may be due to the thickness difference of the surface material (Pt or TeO_2) between different population CdTe pixels. I calculated the thickness difference value for possible models: if only one material component is concerned, we found a thickness difference for Pt $\sim$123 nm , or for TeO_2 $\sim$ 460 nm. A more realistic possibility could be due to a combined effect of the thickness difference of both materials.

To obtained the absolute efficiency of CdTe pixels, I analyzed the dataset obtained with an Fe^{55} X-ray source. For the HEP population, the efficiency is 0.777 $\pm$ 0.022, and for LEP population the efficiency is 0.694 $\pm$ 0.023.

Then I attempted to calculate the global effective area in the 4–8 keV band. By global effective area we mean the number of effective square centimeter that remain after all the effects have been taken into account: the efficiency of the pixels, the overall transparency of the multi-insulation layers (MLI) above the detector plane and the overall transparency of the mask.

The open fraction of the mask is 0.4. I calculated the transparency of the MLI layer using the Fe^{55} dataset. I obtained a value of 0.665, whereas the theoretical value is 0.887. So we decided to conduct a dedicated MLI test in CEA. Finally, we got an MLI transparency of 0.845 $\pm$ 0.003 and decided to apply this value in the ECLAIRs global efficiency calculation.

Based on the detection plane efficiency at 5.9 keV and the relative count distribution in the 4–8 keV band, I computed the efficiency value of the detection plane in the 4–8 keV range. Finally I got an effective area of 142 cm^2 at 4.5 keV and 310 cm^2 at 8 keV. This takes into account the influence of LEP and HTP.

To evaluate the impact of efficiency inhomogeneity (LEP and HTP) on the onboard trigger performances of ECLAIRs, I performed a dedicated trigger simulation which involved those HTP and LEP pixels. The main idea of the simulations was to add LEP and HTP pixels into the detection plane by changing the pixel's efficiency. Then I simulated the onboard X-ray background, and processed the data to obtain the sky's SNR distribution, and finally to calculate the maximum SNR in the sky and the trigger threshold. The preset dynamic

threshold was set to 6.5 x σ_{SNR} in order to avoid the false trigger caused by the background fluctuations.

Ideally, after the deconvolution process of ECLAIRs, the SNR of sky maps is normally distributed with $\sigma_{SNR} \sim 1$ in a 20 min observation timescale. The σ_{SNR} determine the dynamic trigger threshold. After introducing the effect of efficiency inhomogeneity, the σ_{SNR} in the 4–8 keV band increased to 5.75 and 1.43 for HTP and LEP, respectively.

I developed the approaches to mitigate the impact of efficiency inhomogeneity for the ECLAIRs onboard trigger. For the HTP, most of their impact can be corrected by setting their weights to 0 in the background fitting table and in the deconvolution table of the trigger algorithm, which means excluding those pixels during the data processing in the trigger. To correct the impact of LEP, the efficiency correction in the detector plane image before the deconvolution seems to be a good solution.

Heat-pipe noise

While analyzing the TVAC dataset, I noticed some unusual counts in the 4–8 keV band on either side of the detector plane in the absence of an X-ray source. Although the cause of these noises is unknown, we observed this noise in a region close to the heat pipe and named it "heat-pipe noise". Subsequently, I studied the characteristics of heat-pipe noise, its effect on ECLAIRs trigger performances, and investigated ways to mitigate its impact.

I found that pixels affected by heat-pipe noise display a relatively high count-rate in the 4–8 keV range. In the 10 ms time-bin, counts are always between 0 and 2 in the 4–8 keV band for the normal pixels. However, for the heat-pipe noise pixels, counts in the 4–8 keV band often exceed 2 and reach 5-–25 counts in the 10 ms time-bin. This means that we may be able to separate the heat-pipe noise from the normal background in the 10 ms time-bin counts based on this characteristic.

In order to assess the potential impact of heat-pipe noise on the detection of ECLAIRs, I performed simulations using trigger simulation software and TVAC data. The simulation works by adding the heat-pipe noise data to the detector plane while simulating the onboard X-ray background, then processing the data to obtain a SNR distribution for the sky, and finally calculating the maximum SNR for the sky and the trigger threshold, which is 6.5 times the standard deviation of the SNR (6.5 $\times\sigma_{\mathrm{SNR}}$).

I found that introducing heat-pipe noise counts from the TVAC data in a simulation of a 20 min observation results in an increase in the trigger threshold (6.5 $\times$ σ_{SNR}) of approximately 100%, compared to observations without heat-pipe noise. Even though we increased the trigger threshold, it still cause a false trigger rate of 99.26% in the 4–8 keV band and 4.44% in the 4–120 keV band in 20 min timescales.

In order to mitigate the effects of heat-pipe noise on the ECLAIRs on-orbit triggers, I developed a strategy to address this problem, the main idea of which is to remove affected pixels from the triggering algorithm. I identified two methods for selecting pixels affected by heat-pipe noise in TVAC data: a distribution selection method for observation time scales of <0.5 s and a frequency selection method for observation time scales of $\geq$0.5 s.

By selecting and ignoring 5 % of the noisy pixels with these two methods, the false triggers caused by heat-pipe noise can be avoided. And it could reduces the threshold increment for 20-minutes image trigger to around 20% in 4–8 keV (without the mitigation method, this value would be about 100%).

In fact, in operation, the heat-pipe noise will be accompanied by CXB, which can bias the selection of noisy pixels. To address this issue, I suggest to use data when the field of view is completely obscured by the Earth to select noisy pixels in the future commissioning and operational phases. Since the number of CXB photons is more than a factor of 10 less in this case, it should be more efficient and reliable for selecting noisy pixels.

When ECLAIRs is in operation, I suggest to use only one weight table to configure CXB fitting and image deconvolutions, and this for all timescales from 10 ms to 20 min. Our goal is to minimize the effect of heat-pipe noise by sacrificing no more than 5% of the pixels in the 4–8 keV band. We chose the frequency selection method. We did this for several reasons.

1. The heat-pipe noise mainly affects long-term observations, and our simulations show that the frequency selection method performs better in this case, especially for 20-minute observations.

2. The onboard software automatically removes pixel data with significantly increase in counts within a short period of time (10 ms), which is equivalent to ignoring noisy pixels with the distribution selection method.

In 2023, the fully integrated SVOM satellite underwent a TVAC test in Shanghai. We meticulously analyzed the dataset from the initial test on September 28th, 2023 (first cold-state cycle), and the end-to-end test conducted on October 6th, 2023.

We performed the same heat-pipe noise simulations as before, but replaced the Toulouse TVAC dataset with the Shanghai TVAC dataset. Through simulations where we added the TVAC noise counts with the simulated CXB in the trigger process, it was observed that these noises marginally affected the trigger threshold, typically resulting in an increment of 1% to 12%. Importantly, these noises did not result in any false triggers.

Between these two campaigns, the ECLAIRs telescope was not in the same configuration. In Toulouse, the telescope's heat pipes were in a vertical configuration, whereas in Shanghai the heat pipes were in a horizontal configuration. As a result, the absence of noise observed in Shanghai could suggest that the problem is linked to the impact of gravity on the fluid circulating in the heat pipes.

Simulation of ECLAIRs for the detection of X-Ray Rich GRBs

My other work has investigated the triggering performance of ECLAIRs for different types of GRBs using the ECLGRM software and the UGTS test bench, and attempted to assess the SNR improvement in detecting GRBs in the 4–8 keV band.

ECLGRM is a simulation tool for the instruments ECLAIRs and GRM. It could generate the GRB event file required by the triggering software with the input GRB files (lightcurve and spectrum files), and can perform the count-rate trigger to obtained the detected result of simulated GRBs. My contribution to ECLGRM was the development of a customized GRB generation tool. This tool is able to generate compatible light curve and energy spectrum files based on the key parameters of the input GRB. With this tool, we can easily generate any GRB we wanted.

I first conducted a simulation for the classical long GRB (LGRBs), focusing on how the GRB positions affect the detection capabilities of ECLAIRs. Not surprisingly, in the

simulations we found that the SNR value decreases gradually from the center to the sides of the field of view.

Then we tried to assess the ECLAIRs trigger sensitivity in different positions for long GRBs with varied peak energies (E_p). It is found that the sensitivity is around 10^{-8}–10^{-7} erg/cm^2/s in the 4–150 keV band for bursts with different peak energy and different positions of GRBs. Remarkably, for a classical 30 s LGRB with E_p = 200 keV, the on-axis sensitivity of ECLAIRs is 4.5 $\times$ 10^{-8} erg/cm^2/s in the 4–150 keV band, while for an X-ray Flash with E_p = 20 keV with the same 30 s duration, the on-axis sensitivity in the 4–150 keV band is 1.5 $\times$ 10^{-8} erg/cm^2/s, three times better. This performance is due to the contribution of the low-energy band and to the change of the GRB spectrum.

I decided to explored more accurately the contribution of the 4–8 keV band to improving trigger sensitivity at different peak energies. The idea is to simulate the ECLAIRs trigger in the 8–120 keV band and in the 4–120 keV band, respectively. Then I compared the maximum SNR detected in these two energy bands.

I found that the sensitivity improvement is significant for soft GRB detection after involving the 4–8 keV band. The improvement of detected SNR is approximately 60% for GRB with peak energy equal to 5 keV and 20% for GRB with peak energy equal to 20 keV. For the GRB above 100 keV, the contribution of the 4–8 keV band becomes negligible.

To simulate a more realistic detection of GRBs, I conducted the same simulations by using the HETE-2 GRB sample (instead of simulated synthetic GRBs). In this process, the 57 GRBs with background were simulated by ECLGRM software. We found that 56 of these GRBs could successfully trigger ECLAIRs, each with a SNR > 10 in the 4–120 keV band. The bonus of the 4–8 keV band in improving the detection appears to increase inversely with the E_p of the GRB. It is $\sim$50% for GRB with $E_p \approx$ 5 keV, and $\sim$20% for $E_p \approx$ 30 keV, compared to GRBs with E_p > 30 keV, where SNR improvement is generally between 0%–20%.

Finally, to simulate an even more realistic simulation, I performed trigger simulations on the 57 HETE-2 GRB samples using the UGTS test bench. I set the trigger band configurations with the values that will be used for the commissioning phase (5–8, 8–50, 8–120, 20–120 keV). I also used the dynamic threshold that changes automatically with the standard deviation of the sky SNR image.

The UGTS test bench is the exact copy of the onboard trigger system of ECLAIRs. The UGTS trigger algorithm include the count-rate trigger (CRT) and the image trigger (IMT).

I compared the trigger performances of CRT and IMT and found that CRT can trigger 55 out of 57 GRBs and IMT can trigger 52. This result suggests that for weakly medium-long GRBs (< 40 seconds), count rate trigger is more sensitive than image trigger. This may be due to the fact that IMT' s image stacking processing, while helpful in integrating GRB events, does not compensate for the increase in dynamic threshold used to avoid false triggers induced by background residuals.

Prospect

The SVOM project was delayed for various reasons, but mainly because of the Covid-19 epidemic, which penalized developments in France and China. Initially I should have processed and analyzed real ECLAIRs data collected from the sky. With my thesis supervisor, we reoriented my work, which was finally based on the analysis of ground calibrations and associated numerical simulations. The results obtained make me even more enthusiastic

about processing the real data and taking part in the SVOM scientific adventure.

In the future, based on the sensitivity advantage of ECLAIRs in the 4–15 keV band (compared to Fermi and Swift) and the combination of simultaneous multi-wavelength observations with both on-board telescopes and ground-based telescopes, it will be possible to make breakthroughs in the study of the soft GRBs. For example, the center engine of the X-ray flash, the jet structure, and the outburst environment.

On a personal note, if I can remain in the SVOM collaboration after my thesis, I would like to go in the direction studied in this thesis and set up a research project focusing on the study of X-ray rich bursts.

摘要

研究背景

伽马射线暴（GRB）是宇宙中最剧烈的爆炸现象。普遍认为，GRB 起源于大质量恒星的坍塌或致密双星的合并，这导致形成一个超吸积黑洞或快速旋转的磁星，然后通过不同的机制驱动喷流，使其以相对论速度向外突破。

尽管经过几十年的观测和理论研究，但有关 GRB 物理的许多问题仍然悬而未决，这些问题涉及中央引擎的性质、喷流的几何结构、粒子加速机制、辐射产生机制以及软 GRB 的性质（如 X 射线闪等）。将望远镜的探测能带扩展到软 X 射线范围对于探测软 GRB 事件和加深我们对 GRB 物理的了解至关重要。

SVOM 是中法合作的一个天文卫星项目，旨在通过多能段的观测研究伽玛暴和高能暂现源现象。该卫星计划于 2024 年 6 月发射。SVOM 卫星配备了四台科学仪器：一个名为 ECLAIRs 的软伽马射线望远镜，一个名为伽马射线监视器（GRM）的光谱仪，以及两个窄场跟踪望远镜，它们是微通道 X 射线望远镜（MXT）和可见光望远镜（VT）。

ECLAIRs 是一台具有大视场的编码掩模望远镜，在 SVOM 卫星上主要用于探测和定位 GRB。ECLAIRs 的探测平面配备了 6400 个低漏电流的硒化镉（CdTe）探测器像素，探测面积约为 1000 cm^2。其探测能量范围从 4 keV 到 120 keV。与其他 GRB 望远镜相比，ECLAIRs 对 GRB 的探测能量范围低至 4 keV，这是 ECLAIRs 的独特优势。

在 SVOM 任务之前，BeppoSAX 卫星（1996-2002）和 HETE-2 卫星（2000-2008）任务中搭载了不同的大视场 X 射线相机。然而，BeppoSAX 上的广角相机中（WFC，2-30 keV）没有在轨触发功能，而 HETE-2 的广角 X 射线监视器（WXM）具有在轨触发功能，但其能量范围仅限于 2-25 keV。对于正在运行的 GRB 卫星任务，Swift/BAT（2004 年-) 和 Fermi/GBM（2008 年-) 的探测能量阈值相对较高，分别从 15 keV 和 8 keV 开始，这限制了这两个望远镜有效观测软 GRB 事件的能力。

像素的效率不均匀性

2021 年，ECLAIRs 在法国图卢兹国家空间研究中心（CNES）进行了严格的校准测试，我获取了原始数据并进行了详细分析。

在数据分析过程中，我发现探测器像素的效率在 4–8 keV 能段表现出不均匀性。有三个像素群，我们分别命名为高阈值像素（HTP，400 像素）、高效像素（HEP，4000 像素）和低效像素（LEP，2000 像素）。HTP 的起始阈值为 7 keV。4–8 keV 能段下，我发现 HEP 的效率比 LEP 更高。LEP 和 HEP 的效率差异随着能量的增加而减小，这个

差异可以用一个线性函数来描述：$\Delta_{\text{eff}} = -0.052 \times E_{\text{keV}} + 0.417$ 。在 8 keV 以上，这三类像素表现出均匀性。

对于 LEP 和 HEP 之间效率差异的原因, 我认为可能是由于不同类别 CdTe 像素表面材料 (Pt 或 TeO_2) 的厚度差异所致。我计算了可能模型的厚度差异值: 如果只考虑一种材料成分, 我们发现 Pt 的厚度差异约为 123 nm, 或者 TeO_2 的厚度差异约为 460 nm。更现实的可能性是两种材料厚度差异的综合效应。

为了获得碲化镉像素的绝对效率，我分析了以 Fe^{55} 为 X 射线源的数据集。对于 HEP 像素群，效率为 0.777 ± 0.022，而对于 LEP 像素群，效率为 0.694 ± 0.023。

然后，我尝试计算 ECLAIRs 在 4-8 keV 能段的整体有效面积。所谓整体有效面积，是指在考虑了像素效率、探测器平面上方多重绝缘层（MLI）的总体透明度和掩膜的总体透明度等所有影响之后，剩余的有效平方厘米数。

ECLAIRs 编码板的开口率为 0.4。我使用 Fe^{55} 数据集计算了多绝缘层的透明度。我得到的数值是 0.665，而理论值是 0.887。因此，我们决定在 CEA 中进行一次专门的 MLI 测试。最后，我们得到的 MLI 透明度为 0.845 ± 0.003，并决定在 ECLAIRs 有效面积的计算中应用该值。

根据在 5.9 keV 得到的探测平面的绝对效率和 4-8 keV 能段的相对计数分布，我计算出了 4–8 keV 范围内的探测平面的效率。最后我得到了考虑了 LEP 和 HTP 的影响下的 ECLAIRs 的有效面积：在 4.5 keV 时为 142 cm^2，在 8 keV 时为 310 cm^2。

为了评估效率不均匀性（LEP 和 HTP）对 ELCIAR 在轨触发性能的影响，我进行了一项专门的触发模拟，这个模拟考虑到了这些 HTP 和 LEP 像素。模拟的主要思路是通过改变像素的效率，在探测平面上添加 LEP 和 HTP 像素，然后模拟在轨 X 射线背景，并对数据进行处理，以获得天空的信噪比（SNR）分布，最后计算出天空的最大 SNR 和触发阈值。预设的动态阈值为 $6.5 \times \sigma_{SNR}$ ，以避免本底波动引起的误触发。

理想情况下，ECLAIRs 经过反卷积处理后，在 20 分钟的观测时间尺度内，获取的天空图像的 SNR 为正态分布，$\sigma_{SNR} \sim 1$。σ_{SNR} 的值决定了 ECLAIRs 的动态触发阈值。在引入效率不均匀性的影响后，4–8 keV 能段中，σ_{SNR} 值为分别增加到 5.75 和 1.43。

我开发了一些方法来减轻 ECLAIRs 在轨触发器中效率不均匀性的影响。对于 HTP, 它们的大部分影响可以通过在触发算法的背景拟合表和反卷积表中将它们的权重设置为 0 来校正, 这意味着在触发器的数据处理过程中排除这些像素。为了校正 LEP 的影响, 在反卷积之前对探测器平面图像进行效率校正似乎是一个很好的解决方案。

热管噪声及其对在轨触发的影响

在分析 TVAC 数据集时，我注意到在没有 X 射线源的情况下，探测器平面两侧的 4–8 keV 能段中出现了一些异常计数。虽然这些噪声的原因尚不清楚，但因为是在靠近热管的区域观察到了这种噪声，所以将其命名为" 热管噪声"。随后，我研究了热管噪声的特征，它对 ECLAIRs 触发性能的影响，并研究了减轻其影响的方法。

我发现，受热管噪声影响的像素在 4–8 keV 范围内显示出相对较高的计数率。在 10ms 的时间范围内，正常像素的 4–8 keV 能段的计数率始终在 0 和 2 之间。然而，对于热管噪声像素，在 10 ms 时间范围内，4–8 keV 能段下的计数率多次超过 2，有时候可达到 5-25 个计数。这意味着我们可以根据这一特征将热管噪声与正常背景区分开来。

为了评估热管噪声对 ECLAIRs 探测伽玛暴的潜在影响，我使用触发模拟软件和 TVAC 数据进行了模拟。模拟的方法是在探测器平面上添加热管噪声数据，同时模拟在轨 X 射线本底，然后处理数据以获得天空的 SNR 分布，最后取出天空图像的最大 SNR 和触发阈值，触发阈值是 SNR 统计的标准偏差的 6.5 倍（$6.5 \times \sigma_{SNR}$ ）。

我发现与没有热管噪声的观测结果相比，在 20 分钟观测模拟中，引入 TVAC 数据中的热管噪声计数会导致触发阈值增加约 100%。即使提高了仪器的触发阈值，在 20 分钟的时间尺度内，这些噪声仍然会在 4−8 keV 能段内引起 99.26% 的误触发率，在 4−120 keV 能段内引起 4.44% 的误触发率。

为了减轻热管噪声对 ECLAIRs 在轨触发的影响，我开发了一种策略来解决这一问题，其主要思想是将受热管噪声影响的像素从触发算法中剔除。我确定了两种方法来选择 TVAC 数据中受影响的像素：一种是适用于观测时间尺度为 <0.5 秒的分布选择方法，另一种是适用于观测时间尺度为 ≥0.5 秒的频率选择方法。

通过这两种方法选择并忽略 5% 的噪声像素，可以避免热管噪声引起的误触发。而且，在 4−8 keV 的情况下，可以将 20 分钟图像触发的阈值增量降低到约 20%(如果不采用缓解方法, 这个值约为 100%)。

事实上, 在实际运行中, 热管噪声会伴随着宇宙 X 射线背景 (CXB), 这可能会影响噪声像素的挑选。为了解决这个问题, 我建议在未来的调试和运行阶段, 使用视场完全被地球遮挡时的数据来选择噪声像素。由于这种情况下 CXB 光子数减少了 10 倍以上, 因此选择噪声像素应该更有效和可靠。

当 ECLAIRs 开始运行时，我建议仅使用一个权重表来配置像素在 CXB 拟合和图像反卷积的权重（忽略像素或者降低其影响权重）, 并将其应用于从 10 毫秒到 20 分钟的所有时间尺度。我们的目标是通过牺牲不超过 5% 的像素（在 4−8 keV 能段），将热管噪声的影响降到最低。对于噪声像素的挑选，我们选择了频率选择法。这样做主要有两个原因：1: 热管噪声主要影响长期观测，我们的模拟结果表明，在这种情况下，频率选择方法的性能表现更好，尤其是在长时间（如 20 分钟）的观测中。2: 在轨分析软件会在短时间内（10 毫秒）自动删除计数明显超标的像素数据，这种作用相当于用分布选择法挑选像素后后忽略其计数的功能。

在 2023 年，完全整装好的 SVOM 卫星在上海进行了 TVAC 测试。我们仔细分析了 2023 年 9 月 28 日首次测试（第一个冷态周期）和 2023 年 10 月 6 日端到端测试的数据集。

我们进行了与之前相同的热管噪声模拟，但将图卢兹 TVAC 数据集替换为上海 TVAC 数据集。我在触发过程中将 TVAC 噪声计数与模拟 CXB 相结合，通过模拟观察到这些噪声对触发阈值的影响很小，通常会导致 1% 到 12% 的增量。重要的是，这些噪声没有导致任何误触发。

在两次不同的真空测试的时候（图卢兹和上海），ECLAIRs 望远镜的配置并不相同。在图卢兹，望远镜的热管是垂直安装状态，而在上海，热管是水平安装状态。因此，在上海观察到的现象可能表明，热管噪声的问题可能与重力对热管中循环流体的影响有关。

ECLAIRs 对富 X 射线伽玛暴的探测模拟

我的另一个工作是利用 ECLGRM 软件和 UGTS 测试台研究 ECLAIRs 对不同类型的伽玛暴的触发性能，并试图评估 4-8 keV 能段对提高伽玛暴探测的信噪比的贡献。

ECLGRM 是 ECLAIRs 和 GRM 望远镜的模拟工具。它可以利用输入的伽玛射线暴信息（光曲线和频谱文件）生成触发软件所需的伽玛射线暴事件文件，并可以执行计数率触发算法，以获得模拟 GRB 的探测结果。我对 ECLGRM 的贡献是开发了一个定制的 GRB 生成工具。这个工具是根据输入 GRB 的关键参数生成兼容的光变曲线和能谱谱文件。有了这个工具，我们就可以很容易地在软件中模拟任何我们想要的 GRB。

首先, 我对经典的长伽马暴 (LGRBs) 进行了模拟, 重点研究了伽马暴位置如何影响 ECLAIRs 的探测能力。不出所料, 在模拟中我们发现, 对于同一个伽玛暴，ECLAIRs 探

测到的信噪比 (SNR) 值从视场中心到外围逐渐降低。

然后, 我尝试评估 ECLAIRs 对具有不同峰值能量 (E_p) 的长伽马暴在不同位置的触发灵敏度。研究发现, 对于具有不同峰值能量和不同视场位置的伽马暴, 在 4–150 keV 能段内, 灵敏度约为 10^{-8}–10^{-7} erg/cm^2/s。值得注意的是, 对于一个 E_p = 200 keV 的经典 30 秒长伽马暴,ECLAIRs 在 4–150 keV 能段的轴向灵敏度为 4.5×10^{-8} erg/cm^2/s, 而对于一个具有相同 30 秒持续时间的 E_p = 20 keV 的 X 射线闪, 在 4–150 keV 能段的轴向灵敏度为 1.5×10^{-8} erg/cm^2/s, 提高了三倍。这种性能归因于 ECLAIRs 低能段的贡献和 GRB 能谱形状的改变。

我决定更详细地研究 4–8 keV 能段对提高不同峰值能量下触发灵敏度的贡献。我的想法是分别在 8-120 keV 能段和 4-120 keV 能段模拟 ECLAIRs 对不同 GRB 的触发。然后，比较在这两个能量能段检测到的最大 SNR。

我发现，在涉及 4–8 keV 能段后，软 GRB 探测的灵敏度有了显著提高。对于峰值能量等于 5keV 的 GRB，探测到的 SNR 值大约提高了 60%；对于峰值能量等于 20keV 的 GRB，探测到的 SNR 大约提高了 20%。对于 100keV 以上的 GRB，4–8keV 能段的贡献变得可以忽略不计。

为了模拟更真实的 GRBs 探测，我使用 HETE-2 GRBs 样本（而不是模拟合成 GRBs）进行了同样的模拟。在这个过程中，ECLGRM 软件模拟了 57 个带背景的 GRB。我们发现其中 56 个 GRB 可以成功触发 ECLAIRs，每个 GRB 在 4-120 keV 能段的信噪比都大于 10。ECLAIRs 的 4–8keV 能段对 GRB 的探测提高效果与其 E_p 成反比。对于 E_p 约为 5keV 的 GRB 来说，加入 4-8keV 能段的贡献后，它的 SNR 提高 ∼50%。而当 $E_p \approx$ 30 keV 时，则为 ∼20%。对于 E_p>30keV 的 GRB，信噪比的提高一般在 0%-20% 之间。

最后，为了进行更加逼真的模拟，我使用 UGTS 测试台对 57 个 HETE-2 GRB 样本进行了触发模拟。我设定 ECLAIRs 的触发能段的参数为调试阶段将来所使用的值（5–8、8–50、8–120、20–120 keV）。我还使用了依据天空信噪比图像标准偏差而自动调节的动态阈值。UGTS 测试台是 ECLAIRs 星载触发系统的完全一样。UGTS 触发算法包括计数率触发（CRT）和图像触发（IMT）。

我比较了 CRT 和 IMT 的触发性能，发现 CRT 可以触发 57 个 GRB 中的 55 个，IMT 可以触发 52 个。这一结果表明，对于微弱的中长 GRB（< 40 秒），计数率触发比图像触发更灵敏。这可能是由于 IMT 的图像叠加处理虽然有助于叠加 GRB 的光子计数，但并不能补偿为避免背景残差引起误触发而增加的动态阈值。

总结展望

SVOM 项目由于种种原因被推迟，但主要是因为 Covid-19 疫情，法国和中国的项目推进受到了影响。最初，我本应处理和分析 ECLAIRs 望远镜在太空收集的真实的观测数据。在我的论文导师的帮助下，我们重新确定了我的工作方向，最终博士课题的主题变为 ECLAIRs 地面校准数据的分析和相关的数值模拟。这些工作获得的结果让我对处理真实数据和参与 SVOM 科学探险更加充满热情。

在未来，基于 ECLAIRs 在 4–15 keV 能段的灵敏度优势（与 Fermi 和 Swift 任务相比），并结合星载望远镜和地面望远镜同时进行多波长观测，将有可能在软 GRB 研究方面取得突破性进展。例如，X 射线闪光的中心引擎、喷流结构和爆发环境等。

就我个人而言，如果毕业论文完成后我能继续留在 SVOM 的合作项目中，我讲沿着本论文研究的方向发展，设立一个研究项目，重点研究富 X 射线伽玛暴。

Contents

Chapter 1

Gamma Ray Bursts (GRBs)

Contents

1.1 GRB observation history

The earliest detection of GRBs dates back to the Cold War era. The nuclear explosion monitoring satellite Vela accidentally discovered the first GRB from space in 1967. Soon after the

first GRB discovery, many countries sent gamma-ray detectors in space to observe these phenomena, and published the catalogs of GRB detections, spectra and positions. Thanks to these successful missions, the theoretical framework for GRBs was gradually constructed and consistently improved. In this context, a brief introduction to the history of GRB discovery is presented, following a timeline based on key dates and satellite projects.

1.1.1 BATSE (1991-2000)

The Burst and Transient Source Experiment (BATSE) was a GRB detection device installed on the Compton Gamma Ray Observatory (CGRO), consisting of eight Large Area Detectors (LAD) and eight Spectroscopy Detectors (SD).

The LADs had an effective detection energy range of 20 keV–1.9 MeV, primarily used for monitoring GRB outbreaks and measuring lightcurves. The SDs had a detection energy range of 10 keV–100 MeV and were mainly used for measuring the spectrum. BATSE's effective monitoring area covered the whole sky (except for the parts obscured by Earth), and its sensitivity to GRBs was $3{\times}10^{-8}$ erg s^{-1} cm^{-2}.

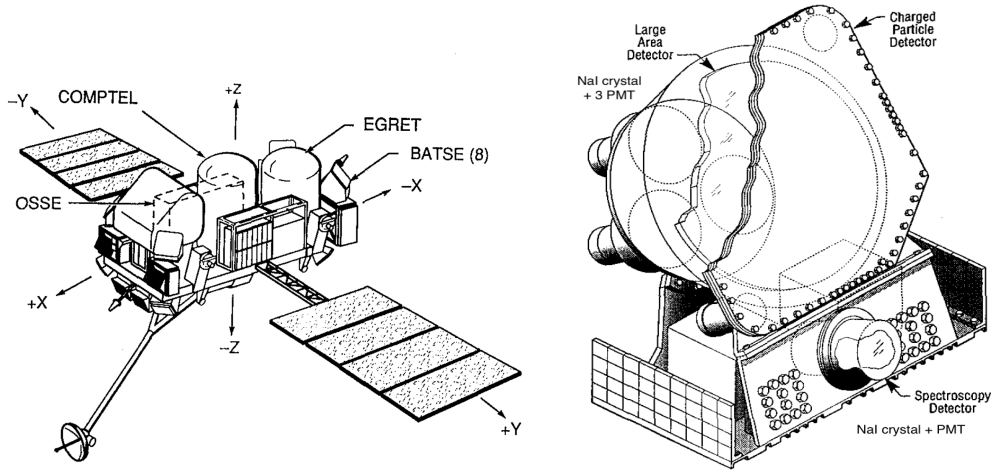

Figure 1.1: One of the eight identically configured BATSE detector modules. Each module contains a Large Area Detector (LAD) and a Spectroscopy Detector (SD). Each LAD is composed of a NaI scintillation crystal and three photo-multiplier tubes (PMTs), while each SD consists of a different-sized NaI crystal and a PMT (C. Meegan, 1993).

Owing to its advantage of full-sky field-of-view (FOV) combined with a high sensitivity to GRB gamma-ray signals, BATSE detected a total of 2704 GRBs from 1991 to 2000. Its main scientific contributions are summarized below.

- The discovery of the isotropic GRB distribution in the sky which suggests that GRBs are likely of cosmological origin.
- The categorization of GRBs into long and short bursts, with a rough dividing line in their typical gamma-ray duration (T_{90}) distribution, at about 2 seconds (Kouveliotou

Table 1.1: BATSE instrument Characteristics.

Detectors	
Number of detectors	8 Large Area Detectors (LAD)
	8 Spectroscopy Detectors (SD)
Field-of-view	Full Sky
Sensitive area	2,025 cm^2 per LAD
	127 cm^2 per SD
Energy range	20–1,900 keV for LAD
	10–100 MeV for SD
Experiment sensitivities	
Burst sensitivity	3×10^{-8} ergs/cm^2 (1 sec burst)
Time resolution	2 μs minimum
Burst location accuracy	3.0° (10^{-6} ergs/cm^2)

Source: https://heasarc.gsfc.nasa.gov/docs/cgro/batse/

et al., 1993), and finding that generally long bursts tend to be softer while short bursts are harder. These findings suggested different progenitor systems between long and short GRBs.

- The spectral analysis of the BATSE GRB samples showed that their gamma-ray spectra are non-thermal, and are well-fitted by a smoothly broken power law, also called the Band function (Band et al., 1993).

1.1.2 BeppoSAX (1996-2002)

BeppoSAX (1996-2002), an X-ray astronomy satellite, was a joint project of Italy and the Netherlands launched in 1996 (Boella et al., 1997). Onboard, it carried a suite of Wide Field Instruments (WFIs) and Narrow Field Instruments (NFIs). The Wide Field Instruments included a GRB Monitor (GRBM: 40–700 keV) and two Wide-Field Cameras (WFCs: 2–30 keV), as shown in Figure 1.2.

The WFCs are equipped with two identical wide-field cameras. Each camera is composed of a Multi-Wire Proportional Counter and a two-dimension coded-mask. The two cameras pointed in opposite directions, with both a FOV of 40 X 40 deg^2. Together they covered 7% of the sky. The angular resolution was 5 arcmin. The GRBM consists of four CsI(Na) scintillation detectors initially planned for anti-coincidence shielding.

Once the GRB Monitor or other GRB detectors (like BASTE) detect a burst, the WFCs could localize the GRB in the X-ray, thereby offering more precise location information for further observations of the GRB. The Narrow Field Instruments had high sensitivity and could detect the fading x-ray emission of the GRB afterglow.

The main contributions of BeppoSAX for GRB science are summarized below (Frontera, 2019).

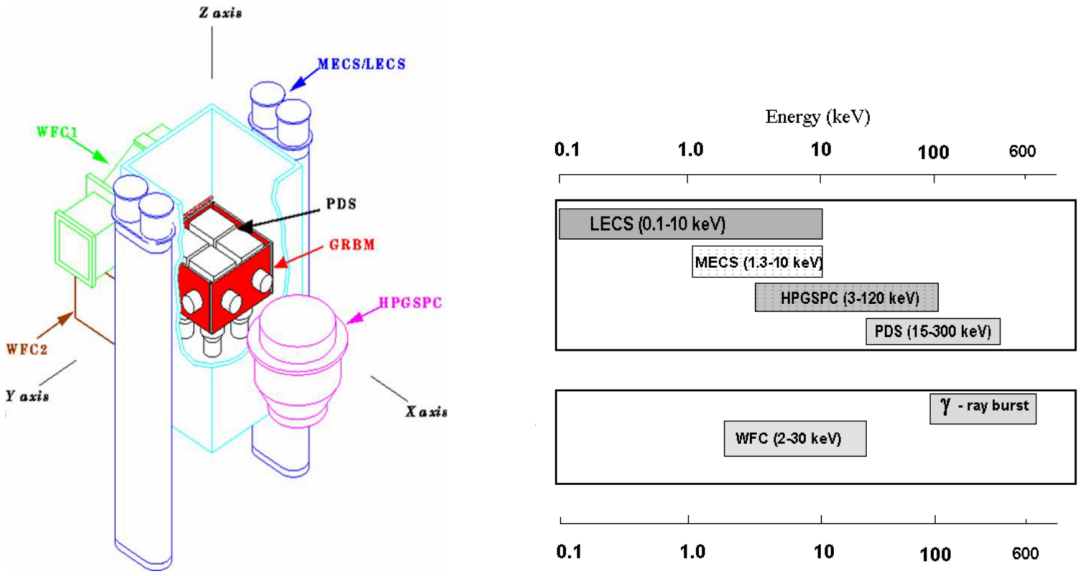

Figure 1.2: The onboard BeppoSAX science instruments (Frontera, 2019).

Table 1.2: BeppoSAX instruments (Boella et al., 1997)

Instrument	Energy range (keV)	FoV (degree @ FWHM)	Angular res. (arcmin)	Area (cm^2)	Energy res. (% @ FWHM)
1 LECS[1]	0.1–10	0.5	3.5@0.25 keV	22@0.25 keV	$8 \times (E/6)^{-0.5}$
3 MECS[1]	1.3–10	0.5	1.2@6 keV	150@6 keV	$8 \times (E/6)^{-0.5}$
1 HPGSPC[1]	4–120	1.1	collimated	240@30 keV	$4 \times (E/60)^{-0.5}$
1 PDS[1]	15–300	1.3	collimated	600@80 keV	$15 \times (E/60)^{-0.5}$
2 WFC[2]	2–30	20×20	5	140@10 keV	$18 \times (E/6)^{-0.5}$

Note: (1) narrow field instruments (NFI); (2) per unit through mask; (3) radius containing 50% of the power.

- The first X-ray afterglow was discovered with GRB 970228 (Costa et al., 1997). In this case, the temporal and spectral properties of the afterglow favor a non-thermal radiative process.

- Thanks to the precise BeppoSax localization of GRB 970508, several subsequent telescopes detected its X-ray, optical, and radio afterglow, and, for the first time, obtained a redshift measurement (Metzger et al., 1997), directly establishing the cosmological origin of GRBs.

- The discovery of the GRB/Supernova connection by the localization of GRB980425/SN1998bw (Kulkarni et al., 1998). Nowadays, it is clearly established that most of the long GRBs originate from the explosions of type Ic supernovae (also called hypernovae, Cano et al., 2017).

- The discovery of the "Amati relation", which connects the peak energy of the prompt gamma-ray spectra with the total gamma-ray energy isotropically released. The Amati relation remains the most robust GRB correlation, and it is now confirmed by almost all the long GRBs detected so far.

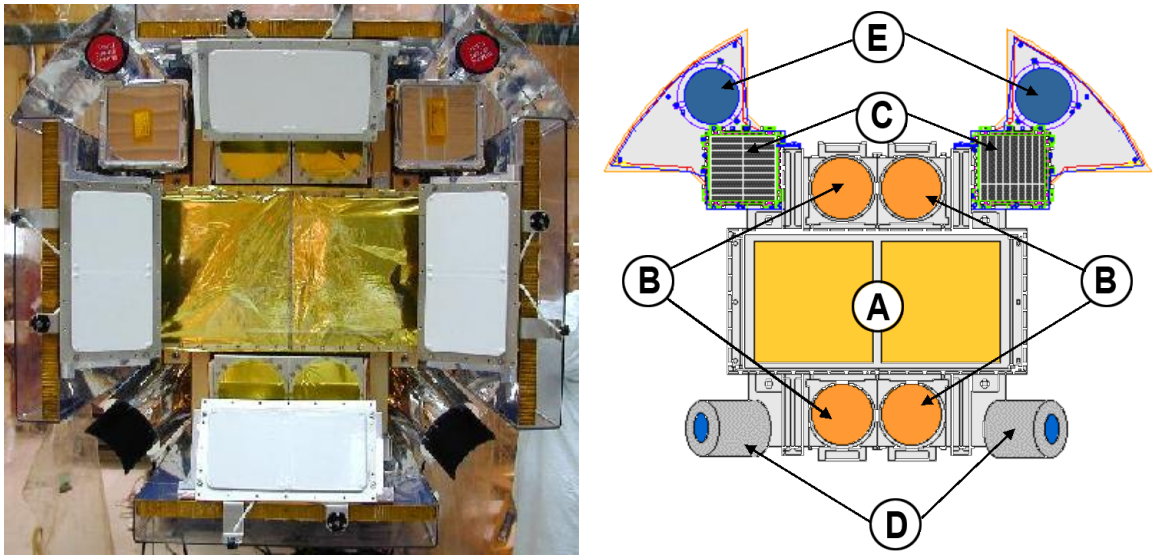

Figure 1.3: Left: a front view of HETE-2 space observatory (instrument side). Right: diagram of the front panel (instrument side). A: WXM (Wide-field X-ray Monitor), B: FREGATE (omnidirectional gamma spectrometer), C: SXC (soft X-ray Camera), D: optical cameras for the attitude control system, E: aiming cameras associated with the SXC detector.

- The discovery of the very soft GRB X-ray flashes. These events were detected in the 2–25 keV energy band with WFCs but were not detected by the GRBM instrument at higher energies.

1.1.3 HETE-2 (2000-2008)

HETE-2 (High Energy Transient Explorer, 2000-2008) was an astronomy satellite launched in 2000 through a collaboration between the United States, Japan, and France. Its payload comprised the French Gamma-Ray Telescope (FREGATE: 6–400 keV), a Wide Field X-ray Monitor (WXM: 2–30 keV), and a Soft X-ray Camera (SXC: 0.5–10 keV), as shown in Figure 1.3.

The prime objectives of FREGATE were the detection and spectroscopy of the GRBs, as well as the long-term monitoring of the bursting source. There was also a burst alert network, consisting of 14 VHF burst alert stations, that allows the satellite to distribute the burst data in near real-time. The WXM and SXC were designed to quickly localize GRBs at arcmin accuracy, for the first time directly onboard the satellite, allowing further observations of the afterglow and redshift measurements performed by the ground-based telescope.

HETE-2 provided precise localizations for more than one hundred GRBs. The contributions of the HETE-2 mission to GRB research are significant.

- The detection of GRB 030329 and its associated supernovae SN 2003dh confirmed the theory that long-duration bursts originate from the collapse of massive stars (Stanek

Table 1.3: Parameters of instruments in the HETE-2 mission

Parameter	FREGATE	WXM	SXC
Instrument type	Cleaved NaI(Tl)	1D-Coded Mask with gas detector	1D-Mask with CCID-20
Energy range	6–400 keV	2–25 keV	1–14 keV
Effective area	160 cm^2	$\sim$ 175 cm^2 per unit	7.4 cm^2 per SXC
Field-of-view	$\sim$4 sr	1.6 sr	1.88 sr
Spectral resolution	$\sim$13% @ 81 keV	$\sim$25% @ 20 keV	129 eV @ 5.9 keV
Localization resolution	Not specified	$19'$ @ 5σ	$40''$ (systematics limit)
Sensitivity	$\sim 1 \times 10^{-7}$ erg/cm^2/s	$\sim 8 \times 10^{-9}$ erg/cm^2/s (2-10 keV)	1.0 ph/cm^2/s (5.5σ)

et al., 2003).

- The extensive observation of GRBs: HETE-2 observed over 250 GRBs, 118 with accurate localization, and 25 with a redshift determined by ground-based follow-up telescopes.

- The wealth of afterglow observation data has allowed scientists to delve deeply into the physics of GRBs, such as the power-law decay behavior of multi-wavelength afterglows confirming the predictions of the GRB fireball model (Rees et al., 1992; Sari, Piran, and Narayan, 1998); the detection of early optical flashes verified the reverse shock model; and the discovery of breaks in late optical afterglows suggests the collimation of GRB jets (Rhoads, 1999).

- Different types of long bursts were discovered, such as X-ray rich GRBs (X-ray rich GRB) and X-ray flashes, as well as GRBs classified based on optical observations as optically bright or optically dark.

1.1.4 Swift (2004-)

Swift is a multi-wavelength satellite dedicated to the study of GRB. The mission is in collaboration with the United States, the United Kingdom and Italy, launched in 2004. The Swift satellite is composed of three science instruments: Burst Alert Telescope (BAT: 15–350 keV), X-Ray Telescope (XRT: 0.3–10 keV), and UV-Optical Telescope (UVOT: 170–650 nm). The main characteristics of those instruments are listed in Table 1.4.

BAT is a coded mask telescope with a large FOV (1.4 sr) and a high sensitivity to accurately localize keV–MeV photons within a few arcmin. The combination of the large BAT ' s FOV with a unique versatile platform, which could quickly slew the follow-up instruments (XRT and UVOT) towards the triggering sources, allows Swift to deeply explore the largely unknown early radiative processes of GRB afterglows. In addition, the high sensitivities of the XRT and UVOT instruments have contributed to the quick GRB localization and redshift measurements over the past two decades.

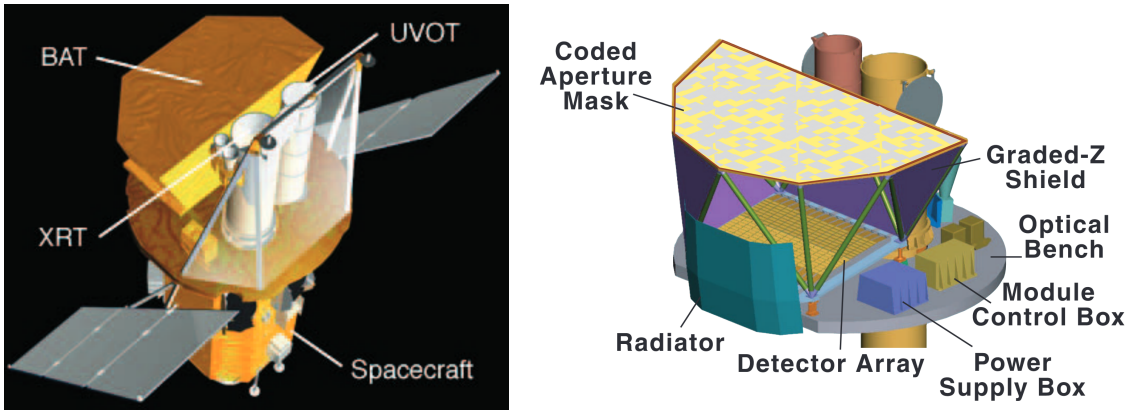

Figure 1.4: Left: schema of the Swift satellite. Right: three instruments onboard Swift.

Table 1.4: Swift mission instrument characteristics

Parameter	**BAT**	**XRT**	**UVOT**
Instrument type	Coded mask + CdZnTe	JET-X Wolter + CCD	Ritchey-Chrétien + CCD
Energy range	15–150 keV	0.2–10 keV	170–600 nm
Effective area	5240 cm² (detector)	110 cm² at 1.5 keV	Aperture = 30 cm
Field-of-view	1.4 sr	23.6' x 23.6'	17' x 17'
Spectral resolution	∼7 keV	∼190 eV at 10 keV	B ∼ 22.3%
Localization resolution	<1-4 arcmin	18 arcsec	0.9 arcsec
Sensitivity	$\sim 10^{-8}$ erg/cm²/s	2×10^{-14} erg/cm²/s	B = 24 in 1000 s

Swift has observed more than 1600 GRBs since 2004. Based on its fast slewing capability, it detected the majority of X-ray afterglow emissions from the early phase to the late decay phase. These observations have advanced the scientific study of GRBs in many ways. The main contribution of Swift for GRBs science is summarized below.

- Swift provided follow-up observations of short GRBs to determine their redshifts and the relative location of the host galaxy, those results strongly suggest that the short GRB form a different population with respect to the long GRB.

- The observations of Swift suggests that the separation of long GRBs and short GRBs is blurred. Some rest-frame short GRB properties were found to be very consistent with the soft long GRB population. As a result, additional information from the multi-wavelength afterglow emission and the host environment of GRBs are usually needed to probe their the nature of their progenitor systems (B. Zhang, B.-B. Zhang, et al., 2009).

- Swift provided a large number of very early X-ray afterglow observations, revealing the general behavior of the canonical X-ray afterglow lightcurves; Abundant early X-ray afterglow data have advanced the study of physical processes in the early afterglow of GRBs (B. Zhang, Y. Z. Fan, et al., 2006).

- Swift discovered X-ray flares and X-ray plateau which likely related to the late activity of the central engine of GRBs, which provided important observational data for the study of the central engine (B. Zhang, Y. Z. Fan, et al., 2006);

- Swift observations have greatly expanded the range of GRB redshift measurements up to z = 9.4 (Cucchiara et al., 2011), allowing to study the GRB population across the Universe and bring new clues to study evolution of the Universe from the dark ages to nowadays.

1.1.5 Fermi (2008 -)

The Fermi Gamma-Ray Space Telescope (Fermi, 2008-) was launched in 2008. Fermi is a wide-FOV, high-energy gamma-ray satellite with a broad energy band (covering seven orders of magnitude), providing unparalleled, wide-range, high-precision spectral observational data for researching GRB radiation mechanisms. It mainly comprises two payloads: the GRB Monitor (GBM: 8 keV–40 MeV, (Charles Meegan et al., 2009)), covering the entire sky except for the area occluded by Earth, and the Large Area Telescope (LAT: 20 MeV–300 GeV, Atwood et al., 2009).

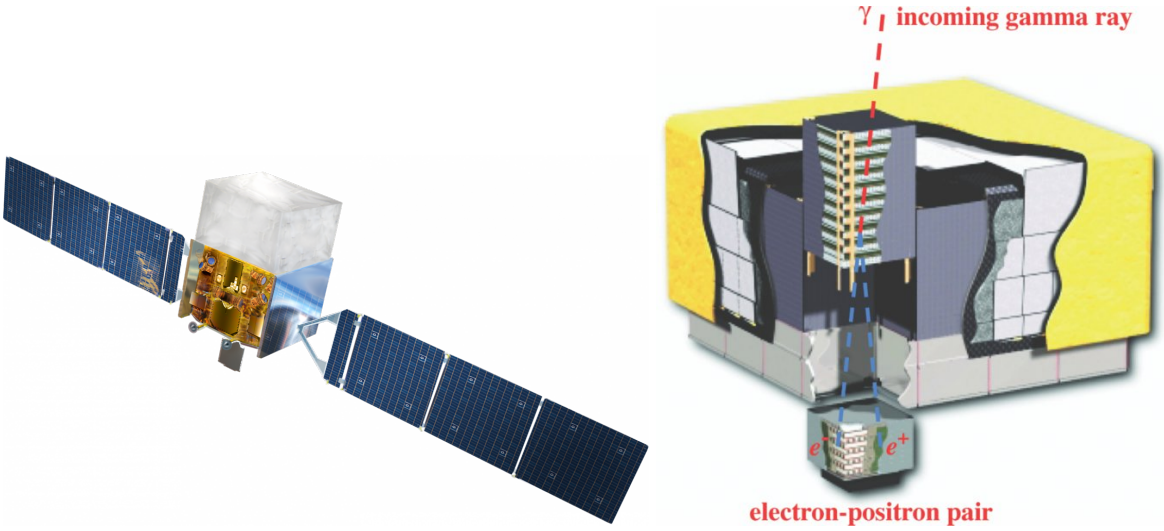

Figure 1.5: Left: Fermi Mission. Right: diagram of the LAT instrument.

The Fermi satellite’s unmatched high-precision spectral detection capacity has significantly improved our understanding of GRB radiation physics. The main contributions of Fermi for GRBs science is given below.

- The duration of radiation observed by Fermi’s LAT is longer than that observed by GBM, indicating that high-energy radiation (> 100 MeV) might be derived from external shocks (Kumar et al., 2010).

- Detailed GRB spectral data have advanced the study of the components and radiation mechanisms of GRB jets. For instance, the observed evolution of the spectrum con-

Table 1.5: Characteristics of Fermi mission instruments

Parameter	**GBM**	**LAT**
Instrument type	12 NaI + 2 BGO scintillators	pair-conversion telescope
Energy range	8 keV - 40 MeV	20 MeV –300 GeV
Effective area	∼100 cm² for each unit	9500 cm²
Field-of-view	full sky	2.4 sr
Spectral resolution	∼15% at 100 keV	8%–9% at 1–10 GeV
Localization resolution	<15 deg	GRB location < 10’
Sensitivity	0.7 ph/cm^2/s	3×10^{-9} ph/cm^2/s

tradicts predictions of the external shock model, and the complexity of the spectrum implies the complexity of the physical origins of GRBs (B.-B. Zhang et al., 2011).

- The detection of photons much greater than 10 GeV (Cenko et al., 2011) in some GRBs provides crucial constraints for the physical study of GRBs, such as the bulk Lorentz factor, the particle acceleration mechanism in relativistic shocks, and the radiation physics of relativistic particles (Vasileiou et al., 2013).

1.1.6 Multi-messenger, 2017 -

The Laser Interferometric Gravitational Wave Observatory (LIGO) consists of two detectors, each with a 4-kilometer-long L-shaped arm, that began operating in the 10–1000 Hz frequency range in 2015 (B. Abbott et al., 2009). Another gravitational wave (GW) observatory, Virgo, located in Italy, is also L-shaped with a 3-kilometer arm and operates at similar times to LIGO (F. Acernese et al., 2015). Both instruments will reach their design sensitivity in the next few years. LIGO will be able to detect GW events generated for binary mergers in the 150 Mpc range in O4 operation (2024–2025) and in the 250 Mpc range in O5 operation (2027–2030). Since 2015 when LIGO detected GW for the first time, more than 90 GWs have been successfully detected (mostly from BBH mergers). The detection of GWs has become a new messenger for humans to study the Universe, opening a new era of multi-messenger astronomy.

The most famous event is GW 170817, with a counterpart GRB 170817A and multi-wavelength afterglow detected (LIGO et al., 2017; B. P. Abbott et al., 2017).

GW/GRB 170817 is the first direct observational evidence for the merger of two neutron stars, organized in a compact binary system (BNS), to form a short GRB, associated with additional visible and infrared radiation from a neutron-rich ejecta called a kilonova (Villar et al., 2017).The discovery of GW/GRB 170817 confirmed that the short GRB could be generated from the merger of BNS.

Moreover, it also provided unprecedented detail information on the physics of short gamma-ray bursts. It showed that the important part of the energy radiated was in the form of gravitational waves. In addition, it made possible to:

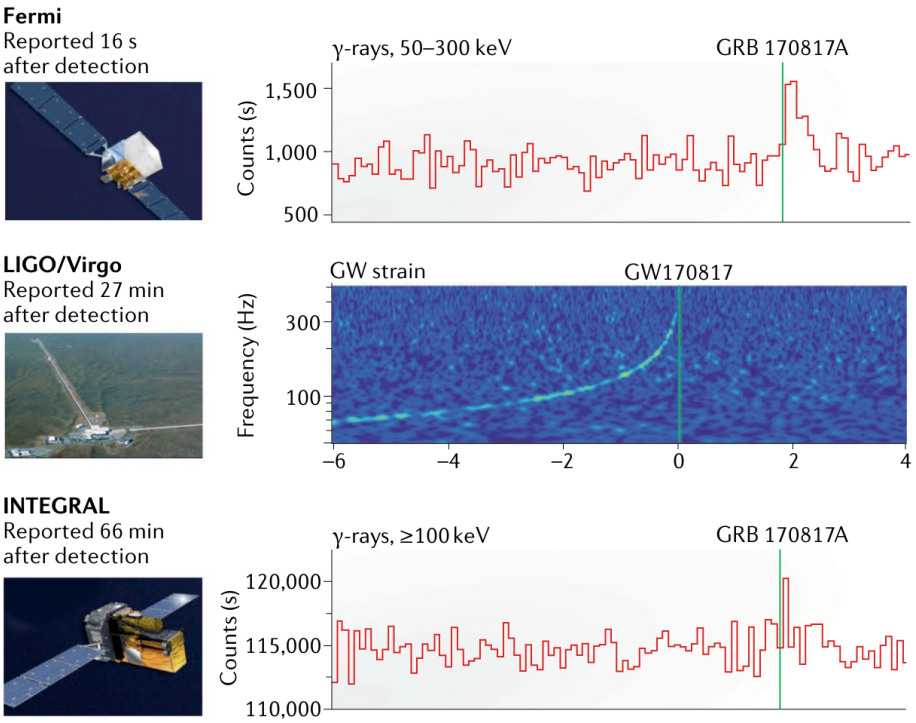

Figure 1.6: Combined multi-messenger detection results for GW 170817 and GRB 170817A (Abbott et al., 2017).

- Estimate the fraction of mass ejected during a neutron star merger.
- Test the kilonova emission models and their temporal and chromatic evolution resulting from the radioactivity and opacity induced by the heavy elements synthesised, by neutron capture (r-process) within the ejecta.
- Estimate the geometry of the ejecta and the radiation emitted, which are the subject of much debate.
- Estimate the fraction of heavy elements synthesised by these r-processes (lanthanide fraction) and identify some of them by spectroscopy. However, these major results were only possible thanks to unprecedented global coordination of electromagnetic observational resources with the gravitational wave detectors.

The GRB 170817 was detected by the Fermi and INTEGRAL satellite. Here we make a brief introduction of INTEGRAM mission (Winkler et al., 2003). INTEGRAL have three main instruments: a soft gamma-ray imager IBIS (15-10MeV) , an gamma-ray spectrometer SPI (20 keV-8 MeV) and X-ray telescope JEM-X (3-35 keV). Although the INTEGRAL mission was not initially designed for a GRB oriented mission, thanks to its excellent sensitivity and wide FoV, It has also been used as a real-GRB localization instrument. To date (April, 2024) , INTEGRAl has detected 148 GRBs. Those detection provides some significant contribution for GRB science:

(a) Detection of GRB170817A associated with GW 170817 (Savchenko et al., 2017). (b) Detection and observation of the GRB 031203 associated with SN 2003 lw (Malesani et al.,

2004); (c) Polarization measurement of GRBs, for example GRB 041209 and GRB 061122 (Diego Götz et al., 2009; D. Götz, Covino, et al., 2013). It shows that the GRBs are highly polarized and strengthens the contribution of the synchrotron radiation to the GRB emission; (d) Discovery (inferred) of a low-luminosity GRB population (Bošnjak et al., 2014).

1.2 Observation characteristics of GRBs

1.2.1 GRB prompt emission

Duration and lightcurve

Based on the observation of BATSE, the prompt emission phase of a GRB is defined as the time period in the sub-megaelectronvolt (sub-MeV) energy range that exceeds the background level of the instrument. The duration of a typical GRB is usually defined by the so-called "T_{90}", which is the time interval between the points where the detector collects 5% and 95% of the total energy or photon flux. This definition depends on the sensitivity of the instrument. Instruments that more sensitive will measure a longer T_{90}.

Based on the duration T_{90}, GRBs can be roughly classified into long GRBs (T_{90} > 2 s) and short GRBs (T_{90} < 2 s), as shown in the Figure 1.7. The duration of short GRBs is typically 0.2-0.3 s, while long GRBs are concentrated around 20-30 s. It has been found that in general the energy spectrum of short GRBs is hard and the spectrum of long GRBs is soft (not absolute).

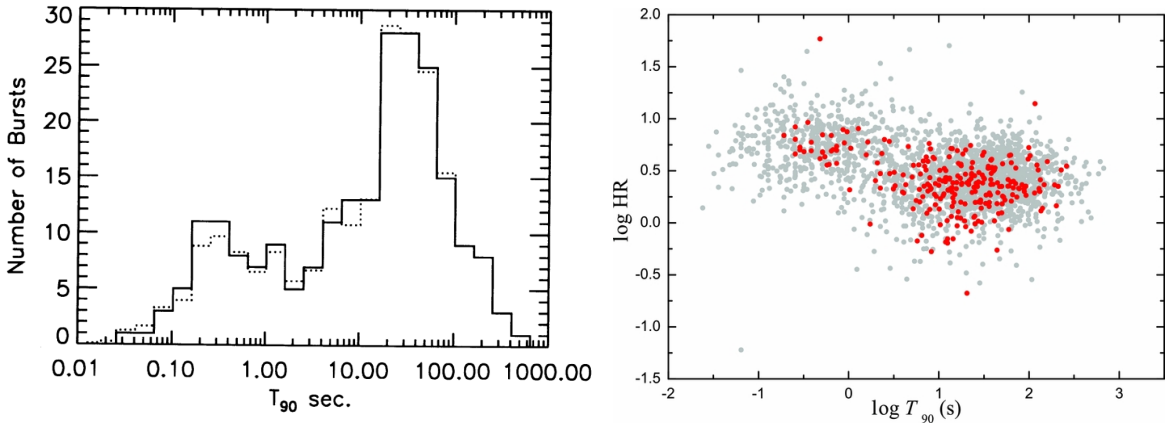

Figure 1.7: GRB duration and harnness ratio. Left: T_{90} distribution of 222 GRBs from first BASTE catalog (Kouveliotou et al., 1993). The solid line histogram is from the original data and the dashed line histogram is after convolution error. Right: hardness ratio (HR) versus T_{90}. The HR defined as the ratio of the flux in the 100–350 keV band to the flux in the 50–100 keV band. the dark and red point conresponding to the GRBs detected by GBM and BATSE, respectively(Qin et al., 2012).

The lightcurve of the prompt emission in GRBs is irregular, with different GRBs exhibiting different variability patterns. A typical instance of prompt emission is a single pulse

GRB characterized by rapid rise followed by an exponential decay. Additionally, some GRBs exhibit multiple pulses; others alternate between quiescent and active (single or multiple pulses) phases; some GRBs have faint precursor radiation; and there are some short GRBs followed by an extended emission. Overall, the lightcurve of prompt emission is diverse and changes dramatically. Figure 1.8 shows the BASTE detection of different types of GRB lightcurve curves.

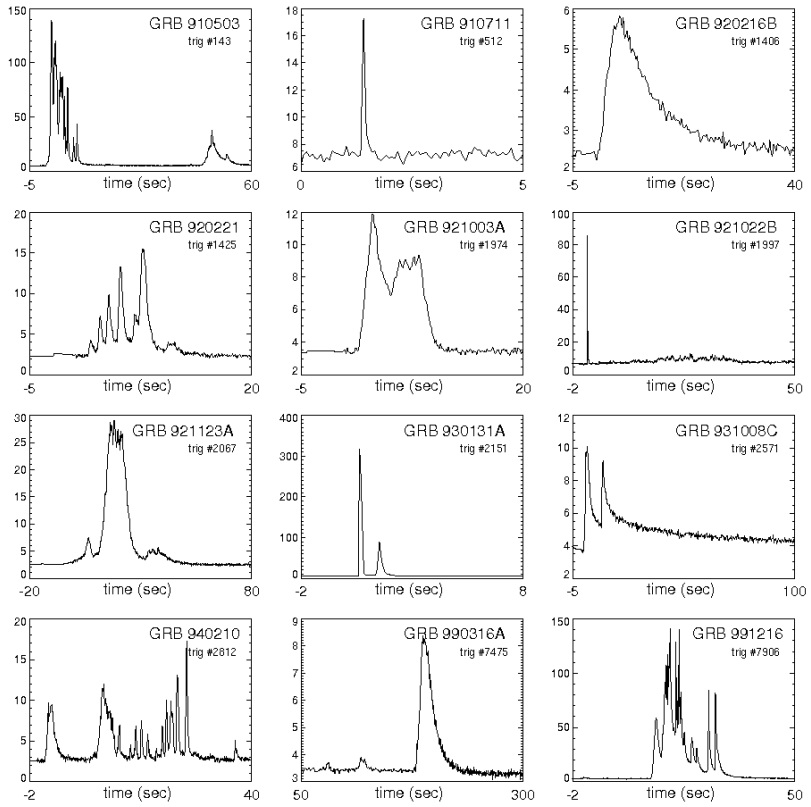

Figure 1.8: Different types of GRB prompt lightcurve detected by BASTE.

Spectrum

It seems from the first GRB observations (BATSE and BeppoSAX) that their emission is only non-thermal. With the increased sensitivity of observational instruments and the growth of observational samples, it has been found that the energy spectrum of prompt emission comprises three basic components (B.-B. Zhang et al., 2011), as shown in Figure 1.9: a non-thermal Band spectrum, a quasi-thermal spectrum, and a high-energy extended component could be described in Power-Law (PL).

The energy spectrum of the prompt emission in GRBs is generally a non-thermal spectrum. This non-thermal spectrum extends to high-energy ranges and exhibits a power-law distribution in flux. It is typically generated by the acceleration of electrons in non-equilibrium environments. Some of the non-thermal part could be explained by the black-body radiation from a fireball. But the number of samples of prompt radiation from GRBs detected in the low-energy band (few keV) is small, and their origin has been controversial.

When the sensitive detection energy interval of the instrument is wide enough (typi-

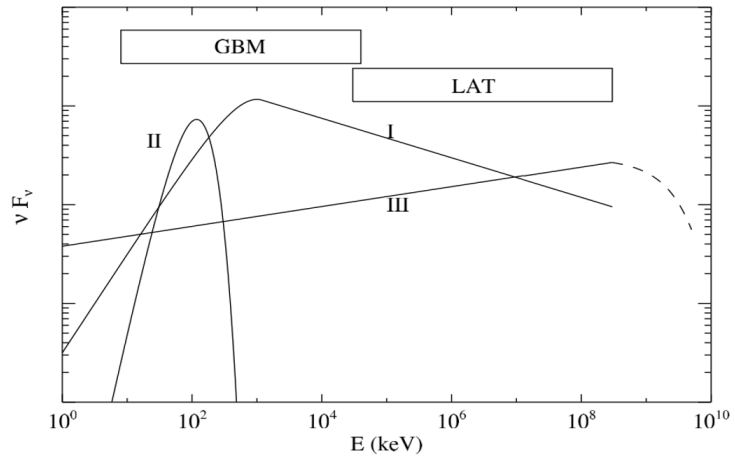

Figure 1.9: Components that may exist in the GRB energy spectrum: (I) Band spectrum; (II) thermal spectrum; (III) high-energy extensional components. Credit: B.-B. Zhang et al. (2011).

cally from 10 keV to 1 MeV), the detected GRB energy spectrum can generally be fitted with a Band function, which is a smoothly connected inflected power-law function (Band et al., 1993), and the mathematical expression of the Band spectrum is:

$$N\left(E\right)=A\begin{cases}\left(\frac{E}{E_{piv}}\right)^{\alpha}\exp\left(-\frac{E}{E_{0}}\right),E<\left(\alpha-\beta\right)E_{0}\\\left[\frac{\left(\alpha-\beta\right)E_{0}}{E_{piv}}\right]^{\alpha-\beta}\exp\left(\beta-\alpha\right)\left(\frac{E}{E_{piv}}\right)^{\beta},E\geqslant\left(\alpha-\beta\right)E_{0}\end{cases}\tag{1.1}$$

where α is the low-energy spectral index, β is the high-energy spectral index, E_0 is the break energy, and $E_{\rm p}$ is the peak energy, calculated as $E_p = (\alpha + 2)E_0$. A and E_{piv} are normalized parameters. In the statistical sample of BASTE, $\alpha \sim -1$, $\beta \sim -2.2$, and $E_{\rm p}$ are concentrated in the range of 200–300 keV (Band et al., 1993) . E_{piv} = 100 keV for the BASTE, Swift/BAT and Fermi/GRM.

The low-energy part of the Band spectrum is a power-law plus an exponential cutoff component, and the high-energy component is a steeply decreasing power-law function. If the energy range of the detector is not wide enough or a GRB is not bright enough, the spectrum of a GRB sometimes can be fitted by a cut-off power-law (CPL) or a power-law function as following form:

$$N(E)=A\left(\frac{E}{E_{piv}}\right)^{\alpha}\exp\left(-\frac{E}{E_{c}}\right)\tag{1.2}$$

$$E_p=(2+\alpha)E_c\tag{1.3}$$

This is essentially the first part of the Band function. In this case the break energy E_0 is replaced by the cutoff energy E_c when calculating the peak energy E_p. For narrow detector

bandpasses and weak GRBs, GRB spectra can sometimes only be fitted with simple power laws:

$$N(E) = A \left(\frac{E}{E_{piv}} \right)^{-\hat{\Gamma}} \tag{1.4}$$

where $\hat{\Gamma}$ is the photon index. In fact, if other instruments with wider spectral windows are simultaneously observing, the spectrum usually can be fitted with a Band or cutoff power law function with the measured E_p. Note that the high-energy power-law component found in the LAT/Fermi range (> 10 MeV) likely comes from the Inverse Compton diffusion of the keV-MeV photons at higher energies (or other mechanism) and is not due to the narrow bandpass of the detector.

Luminosity

The gamma-ray prompt luminosity of a GRB is usually expressed in erg/s, which represents the energy released by the astronomical source per unit time. Due to the rapid variability of GRBs, a specific time window needs to be determined to uniformly describe their luminosity. Typically, the average luminosity (i.e., the total isotropic energy divided by the the total duration of the GRB in the cosmological rest frame) and the peak luminosity (i.e. the luminosity during the peak of the burst) are used to characterize and study the the energy released in GRBs. The GRB Peak luminosity ranges from 10^{47} erg/s to 10^{54} erg/s (GRB 170817 and GRB 221009A).

For GRB detectors with a narrow sensitive detection energy range, only a part of the energy is detected. To compare GRBs detected by different instruments, the luminosity is typically corrected (k-correction or bolometric correction) based on spectral parameters to the energy range of 1-10^4 keV, which is referred to as bolometric luminosity. In practical observations, to obtain the bolometric luminosity of a GRB, it is necessary to detect the energy flux (P) and redshift (z). The formula for calculating the bolometric luminosity of a GRB is:

$$L = 4\pi D_L^2 F_\gamma \times k \tag{1.5}$$

In this formula, D_L is the luminosity distance, which can be calculated from the detected redshift by considering a cosmological model; F_γ is the flux of the GRB; k is the value of the bolometric correction, and the formula for calculating k is:

$$k = \frac{\int_{1/(1+z)}^{10^4/(1+z)} EN(E)dE}{\int_{e_1}^{e_2} EN(E)dE} \tag{1.6}$$

$N(E)$ represents the photon spectrum. The e_1 and e_2 are the lower and the upper limit of the telescope's energy band. The factor $1+z$ taking into account the red-shift correction for the photon's energy. What the instrument actually detects is photon counts. For a GRB with a photon count rate of P, its observed energy flux is calculated based on the photon

spectrum using the following formula:

$$F_\gamma = \frac{P \int_{e_1}^{e_2} EN(E)dE}{\int_{e_1}^{e_2} N(E)dE} \tag{1.7}$$

1.2.2 Afterglow observation

X-ray Afterglow observation

GRB afterglows had been predicted to exist before their discovery in the 1990s (Paczynski et al. (1993); P. Mészáros and Rees (1997)).The basic physical picture being that the central object suddenly releases a large amount of energy in a small region of space, potentially causing a fireball to move at relativistic speeds. As an ambient medium surrounds the GRB (even if it is of low density), it will slow down the relativistic jets creating a shock discontinuity, the so-called external shocks. In external shocks, electrons and protons would be accelerated, and magnetic field are amplified, generating multi-wavelength afterglows through processes such as synchrotron radiation and/or synchrotron self-Compton radiation (B. Zhang, 2018). Therefore, in theory, the afterglow is characterized by the multi-wavelength radiation resulting from the interaction of the fireball with the surrounding ambient medium of the GRB.

The first X-ray afterglow of a GRB was discovered in 1997 (GRB 970228) by the BeppoSAX astronomical satellite (Costa et al., 1997), and subsequently, BeppoSAX also detected late X-ray afterglows of some GRBs. After the launch of the Swift satellite, the discovery of GRB X-ray afterglows became routine. Thanks to the Swift satellite's rapid pointing ability (able to target sources within tens of seconds), it also detected early X-ray afterglows of most GRBs. To date, the Burst Alert Telescope (BAT) and X-Ray Telescope (XRT) on the Swift satellite have detected thousands of GRBs and observed most of the corresponding X-ray afterglow light curve features.

Typical X-ray afterglow lightcurves can be classified into five basic phases (Figure 1.10: the fast decay phase, the shallow decay phase (referred to as a plateau if the slope is near 0), the normal decay phase, the post-jet break decay phase, and X-ray flares (B. Zhang, Y. Z. Fan, et al., 2006).

The fast decay phase (I) smoothly connects with the end of the prompt emission and is considered the natural "tail" of the prompt emission, with the simplest explanation being the "curvature effect" produced at high latitudes (Charles D. Dermer, 2004). If the shallow decay phase or plateau (II) is followed by a normal decay phase, its origin can be explained by an external shock model with continuous energy injection, with the energy source being either a long-duration central engine (Z. G. Dai et al., 1998) or a multi-shell Lorentz factor fireball model. If a steep decline follows the X-ray plateau phase, it cannot be explained by the standard external shock model and requires the introduction of an internal energy dissipation process, commonly referred to as an "internal plateau" (Lyons et al., 2010). The normal decay phase (III) can be explained by the standard external shock model, and the final jet break phase (IV) can also be explained by the jet break effect of the external shock model. X-ray flares (V) may originate from the reactivation of the central engine in its later

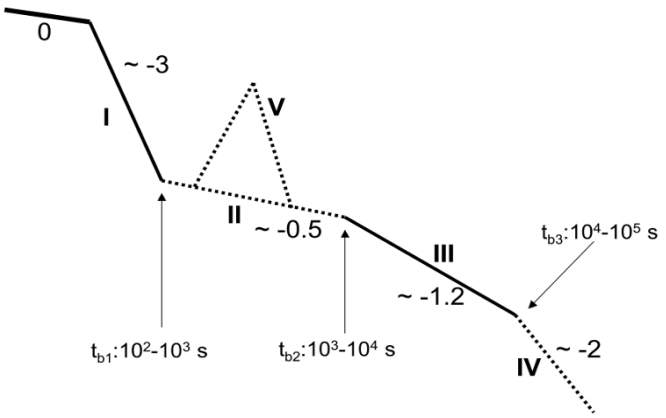

Figure 1.10: Typical X-ray afterglow components: I. fast decay phase, II. shallow decay phase (if the slope is close to 0, it is a plateau), III. normal decay phase, IV 'post' jet break phase; V. X-ray flares; 0 is the prompt emission phase. Credit: B. Zhang, Y. Z. Fan, et al. (2006).

stages.

Optical afterglow observation

The optical afterglow of GRBs is more complex than the behavior of X-rays and exhibits different characteristics depending on the different GRBs. The GRB optical afterglow can be decomposed into early-time (within the first few hours) and late-time (several hours later) components. The late-time optical afterglow is relatively "regular". If the late afterglow is sufficiently bright, the light curve may be fitted with two broken power laws : from a normal decay to a steeper decay, where the two power indices are typically $\alpha_1 \sim 1$ and $\alpha_2 \sim 2$ respectively.

Specifically, it can be categorized into several different components, as illustrated in Figure 1.11 (Li et al., 2012):

- Ia. prompt optical, which tracks the gamma-ray emission, may be correlated to the prompt emission.
- Ib. early optical flash (reverse shock flash), possibly caused by external reverse shock.
- II. early shallow-decay segment, which maybe related to the subsequent activity of the center engine.
- III. standard afterglow component with a starting hump followed by a normal decay segment, which could be explained with the external forward shockwave model.
- IV. post jet-break phase, which is consistent with the predictions of the standard external forward shock model.
- V. optical flares, which may have the same physical origin as the X-ray flares produced by the late activity of the Central Engine.

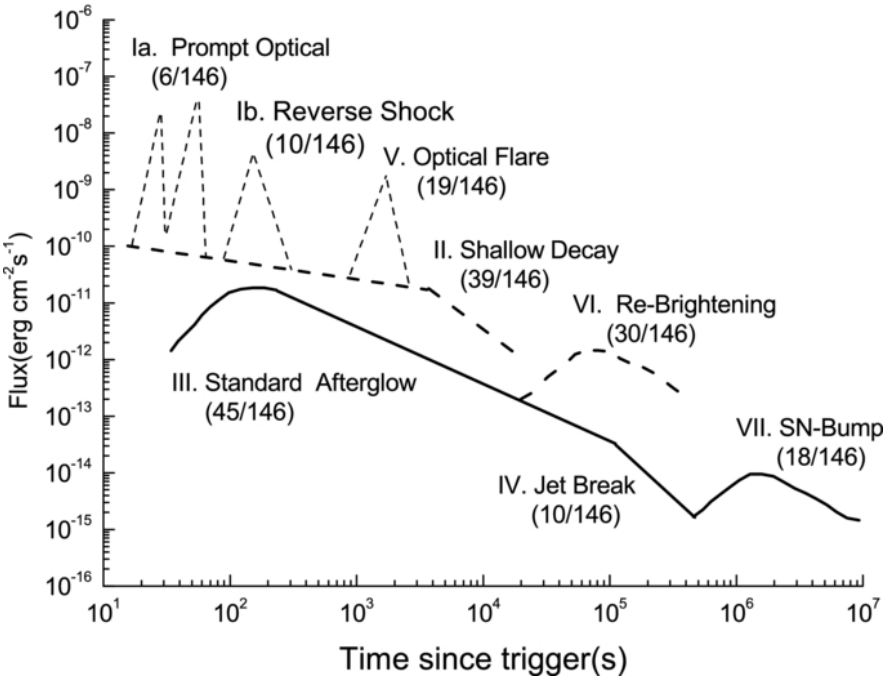

Figure 1.11: Schematic lightcurves of multiple optical components based on optical lightcurve analysis of 146 GRBs (Li et al., 2012).

- VI. re-brightening humps. The possible explanatory models include density bumps or voids in the medium, multiple injections of energy into the blast wave, energy angle fluctuations per unit solid angle, or the presence of multiple jet components.

- VII. supernova (SN) bumps for long GRBs are thought to have originated in supernova explosions.

1.3 GRB model and physics

1.3.1 A general picture

Current research suggests that long GRBs may be caused by the collapse of massive stars, while short GRBs caused by the merger of binary of compact objects. This collapse or merger results in a super-accreting black hole or a rapidly spinning magnetar, which then acts as the central engine, driving jets ejected nearly at the speed of light.

As illustrated in Figure 1.12, energy dissipation within the jet results in prompt emission, and the jet's interaction with the external medium produces an afterglow. Essentially, the difference between prompt emission and afterglow lies in the radiation mechanism of gamma photons and their emission locations.

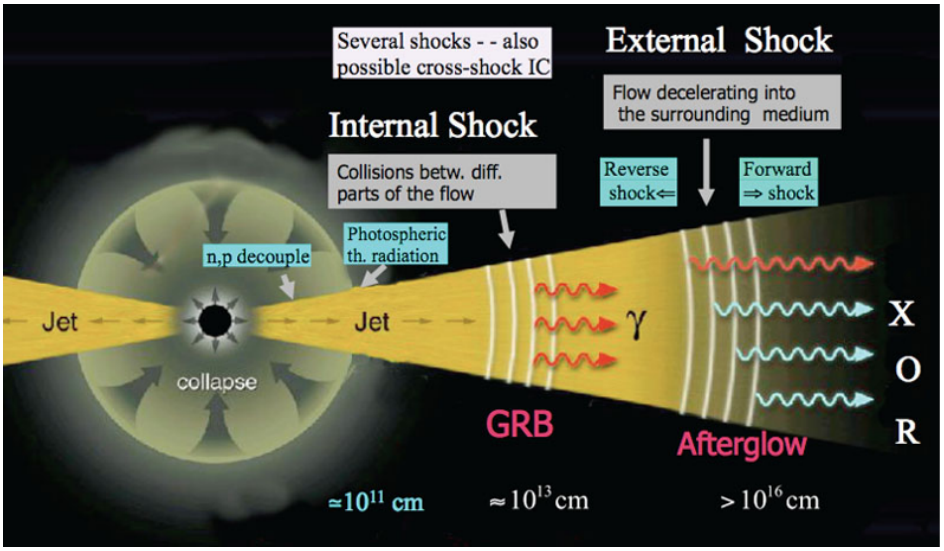

Figure 1.12: Model diagram of the GRB radiations: internal shock wave generates the GRB prompt emission, external shock wave generates multi-band afterglow emission. Credit: Meszaros et al. (2014).

1.3.2 Progenitor and central engine

Regarding the central engine of GRBs, there are currently two main candidate models widely studied: one involves a newly formed black hole (BH) with an accretion disk (Narayan, Paczynski, et al., 1992; Narayan, Piran, et al., 2001), and the other a newly formed, rapidly rotating magnetar (Usov, 1992, Z. G. Dai et al., 1998). In the case of a super-accreting black hole plus accretion disk, the relativistic GRB jets could be driven by the Blandford-Znajek (BZ) mechanism (Blandford et al., 1977) or by electron-positron neutrino pair annihilation (Mochkovitch et al., 1993;Popham et al., 1999; Liu et al., 2018). In the case of a magnetar, rotational energy can be extracted to produce relativistic stellar winds and release electromagnetic energy away through the magnetic dipole radiation mechanism (Z. G. Dai et al., 1998), or arise from differential rotation mechanism (Siegel et al., 2014).

In the scenario of a super-accreting black hole, when the accretion rate is high enough, the temperature of the accretion disk near the black hole's radius becomes so high that it can facilitate the capture process of electrons and positrons.

$$e^- + p \rightarrow n + \nu_e, \quad e^+ + n \rightarrow p + \bar{\nu}_e \tag{1.8}$$

This process generates a large number of neutrinos and antineutrinos, which carry away significant energy, lowering the temperature of the accretion disk. This region of the accretion flow is named the Neutrino Dominated Accretion Flow (NDAF). In the outer region, where the accretion rate and temperature are lower and insufficient to produce a large number of neutrinos, this area is referred to as Advection Dominated Accretion Flow (ADAF).

After the generation of neutrino-antineutrino pairs, annihilation occurs outside the accretion disk, producing photons and electron-positron pairs ($\bar{\nu}\nu \rightarrow e^+e^-$). Along the axis

of the black hole's rotation, this annihilation process results in a larger optical depth, and neutrinos can also strip away some baryons from the accretion disk, thereby facilitating the creation of relativistic jets in this direction.

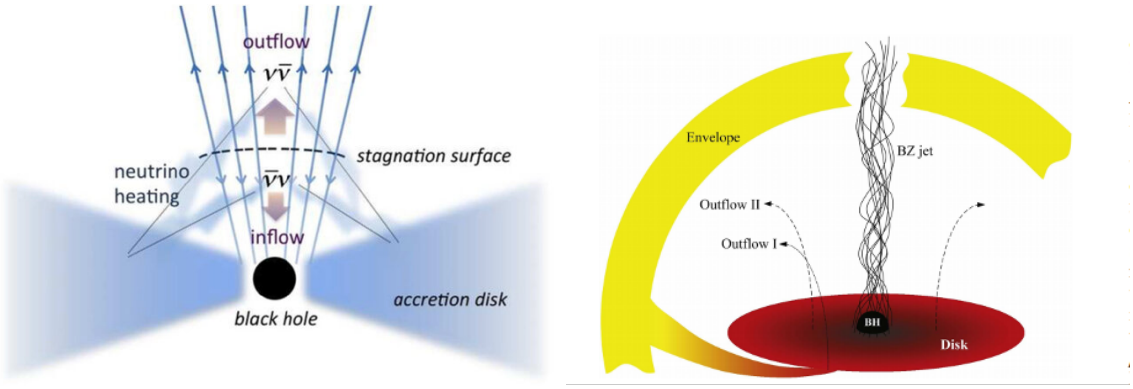

Figure 1.13: Two possible mechanisms of jet flow under the super accretion black hole: neutrino annihilation (left) and BZ mechanism to extract rotation energy (right). Source: Liu et al. (2018); Nagataki (2018).

A super-accreting black hole carries significant angular momentum, and the accretion process can accelerate the rotation of the black hole. If a strong magnetic field passes through the black hole and links to external physical loads (such as baryons), then the rotational energy of the black hole can be extracted through the Blandford-Znajek (BZ) mechanism, providing immense energy for the generation and propulsion of jets. At this point, due to the rapid rotation of the central engine, magnetic field lines converge in a collimated annular space, resulting in a focused, Poynting-flux-dominated relativistic jet (Thompson, 1994). In this case, the energy is primarily transported by electromagnetic fields rather than by kinetic energy of particles.

A new-born neutron star (magnetar) can also serve as the origin of GRBs under reasonable parameters. The energy of the GRB can be provided by the rotational energy of the magnetar. For a magnetar with a moment of inertia I of 10^{45} g cm^2 and a rotational speed Ω of 10^4 s^{-1}, the total rotational energy is:

$$E_k = \frac{1}{2} I \Omega^2 \approx 5 \times 10^{52} \text{ erg} \tag{1.9}$$

This energy is already sufficient to produce a typical GRB. Another possible source of energy for a newborn NS is the accretion of NDAF, which releases gravitational energy from the accreting material. However the total amount of accreted energy is finite, otherwise the NS would collapse and would be replaced by a BH-torus engine.

When the central engine is a newborn magnetar, its energy can be extracted in three ways: slowing down of rotation (spin-down), magnetic reconnection flares caused by differential rotation, and NDAF emission (same mechanism as for BH). The simplest way to extract rotational energy through spin-down is via magnetic dipole radiation and relativistic stellar wind radiation. An X-ray "internal plateau" is an important observational evidence of magnetar as a central engine (Chen et al., 2017), as shown in Figure 1.14. If we

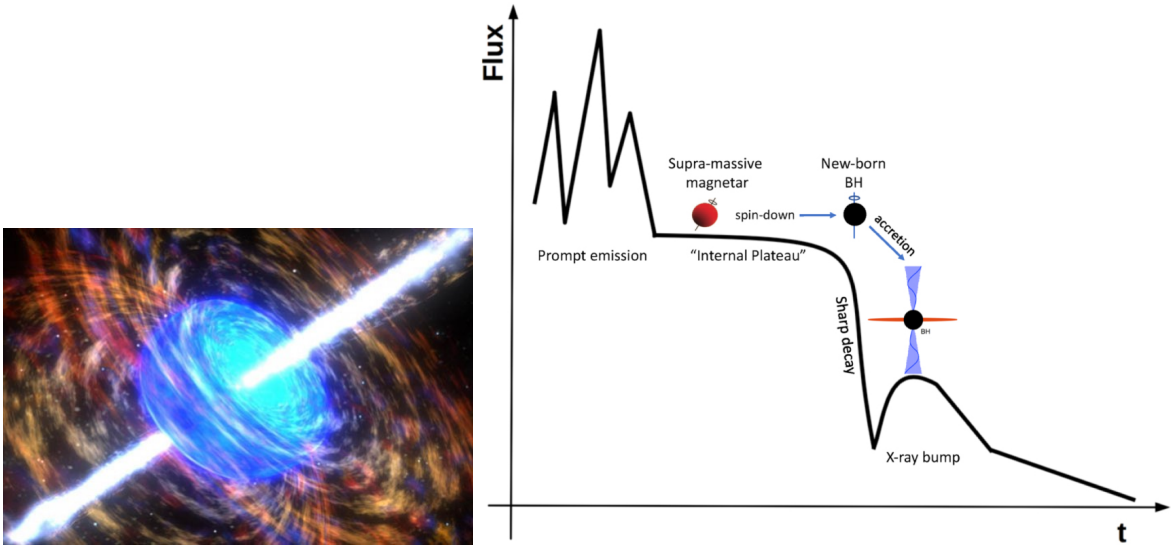

Figure 1.14: Imagery of a magnetar as the central engine of a GRB (left) and predicted X-ray lightcurves (right). Source: Chen et al. (2017)

simply consider a magnetar with rigid body rotation (no differential rotation). Assuming the extraction of rotational energy is dominated by magnetic dipole radiation, the evolution of its luminosity is as follows (Usov, 1992; B. Zhang and Peter Mészáros (2001)):

$$L(t) = \frac{L_0}{(1 + t/t_{0,\mathrm{em}})^2} \approx \begin{cases} L_0, & t \ll t_{0,\mathrm{em}} \\ \left(L_0 \left(t/t_{0,\mathrm{em}}\right)\right)^{-2}, & t \gg t_{0,\mathrm{em}} \end{cases} \tag{1.10}$$

Here, L_0 is the initial luminosity, and $t_{0,em}$ is the characteristic timescale, with their values approximately being:

$$t_{0,\mathrm{em}} = \frac{3cI}{B_p^2 R^6 \Omega_0^2} \approx 2.1 \times 10^3 \,\mathrm{s} \left(I_{45} B_{p,15}^{-2} P_{0,-3}^2 R_6^{-6}\right) \tag{1.11}$$

The formula employs a simplified notation, $Q_n = Q/10^n$. The characteristic luminosity is calculated using the characteristic timescale:

$$L_0 = \frac{I\Omega_0^2}{2t_{0,\mathrm{em}}} = \frac{B_p^2 R^6 \Omega_0^4}{6c^3} \approx 1.0 \times 10^{49} \,\mathrm{erg\ s^{-1}} \left(B_{p,15}^2 P_{0,-3}^{-4} R_6\right) \tag{1.12}$$

In the formula, B_p represents the surface magnetic field strength at the poles of the magnetar, P_0 is the initial period of rotation, and R is the radius of the magnetar.

1.3.3 Jet structure and prompt emission mechanism

Figure 1.15 summarizes the energy flow in a GRB jet, depicting how various forms of energy are converted from one to another and produce the observed GRB radiation (B. Zhang,

2018). Different conversion processes form different prompt emission models of GRB.

The ingredients of energy transfer process is as follows:

- A central engine forms after a catastrophic event in a massive star or binary system. This central engine continues to power the outflow for a certain period of time, during which gravitational energy (for accretion systems) or spin energy (for spin systems) is released in the form of thermal energy (Starling et al., 2012) or Poynting flux energy (Drenkhahn et al., 2002), respectively.

- The Poynting energy can convert to the thermal energy by Magnetic dissipation. A portion of the initial thermal energy is released as photons at the photospheric surface of the jet. The remaining kinetic and/or Poynting flux energy is "dissipated" inside the jet and converted into kinetic energy of the particles or magnetic dissipation sites (for Poynting flux energy) in the internal shocks.

- A fraction of the internal energy is given to electrons or other leptons, which are then radiated as electromagnetic radiation to contribute the prompt emission of non-thermal GRBs. The prompt emission may originate from one or more internal emission regions.

The energy conversion process of the traditional fireball model is: gravitational energy is converted to internal energy, thermal energy accelerates the ejecta close to the speed of light to be converted to kinetic energy. The kinetic energy in the ejecta is converted to photon radiation by internal shock dissipation, and part of the thermal energy is dissipated through the photosphere.

The radiation mechanism of prompt emission (internal shock dissipation) is an unsettled issue. The main candidates include synchrotron radiation from optically thin regions, and quasi-thermal, Compton emission near the photosphere. There is also the possibility of synchrotron self-Compton (SSC), external inverse Compton (EIC), and hadronic cascades to account for part of the high-energy transient emission spectrum.

GRB jets driven by the central engine are generally considered to be collimated, mainly because: (1) The total energy is enormous, with some GRBs having isotropic energies reaching 10^{55} erg/s (An et al., 2023), which is typically unachievable by the collapse and death of ordinary stars. (2) The luminosity of GRBs far exceeds the Eddington luminosity. (3) A significant portion of observed GRB afterglows exhibit steep decay in the later stages, indicating the presence of jet breaks.

Based on theoretical and observational studies, GRB jets are considered to be narrowly collimated relativistic jets with an opening angle of just a few degrees (Sari, Piran, and Halpern, 1999).

The energy distribution models of jets are typically categorized into uniform jets and structured jets, with structured jets primarily consisting of two models: power-law jets and Gaussian jets. For uniform jets, their angular energy distribution is uniform as follows:

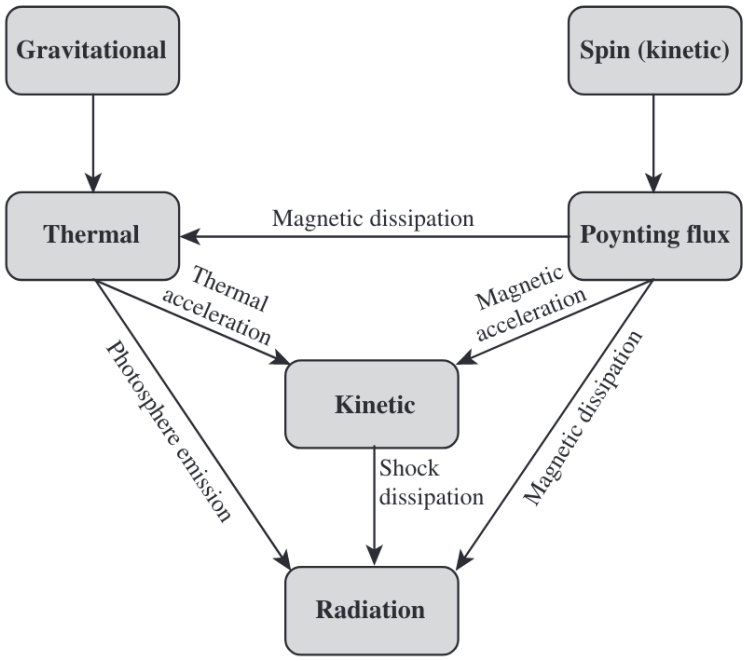

Figure 1.15: The energy flow chart for the GRB prompt emission. Credit: B. Zhang (2018)

$$\frac{dE}{d\Omega} = \begin{cases} \epsilon_0, & \theta \leq \theta_j \\ 0, & \theta > \theta_j \end{cases} \tag{1.13}$$

Where θ_j is the opening angle of the jet and ϵ_0 is the energy per unit angle. For power-law jets (Lloyd-Ronning et al., 2004), the expression is as follows:

$$\frac{dE}{d\Omega} = \begin{cases} \epsilon_0, & \theta \leq \theta_j \\ \epsilon_0 \left(\frac{\theta}{\theta_j}\right)^{-k_\theta}, & \theta > \theta_j \end{cases} \tag{1.14}$$

For Gaussian jets (B. Zhang, X. Dai, et al., 2004a, Salafia et al., 2015), the expression is as follows:

$$\frac{dE}{d\Omega} = \epsilon_0 \cdot \exp\left(-\frac{1}{2}\frac{\theta^2}{\theta_0^2}\right) \tag{1.15}$$

Most studies suggest that the specific opening angle distribution of jets ranges from 1 to 10 deg, and the exact parameters of structured jets are still under investigation. The constraints on these parameters are of significant importance for the study of the structure and physics of relativistic jets.

1.4 X-ray rich GRB and X-ray flash

In this section, we will give the detail for these burst since those are the interested burst for SVOM misson, particularly for ECLAIRs detection.

1.4.1 Classification

Bright GRBs usually have peak energy spectra in the sub-MeV to MeV range. However, it is now well established that, in addition to the shifting of the energy spectrum to lower energy bands caused by high redshift, the phenomenon of GRB itself consists of a broadly distributed peak energy.

Based on the peak energy of the observed energy spectrum, GRBs can be broadly categorized: classical GRB, X-ray rich GRB (XRR), X-ray flash (XRF). This categorization has no clear boundaries and is roughly divided into (Takanori Sakamoto et al., 2008):

- X-ray Flash : E_{peak} < 30 keV
- X-ray Rich GRB : 30 keV < E_{peak} < 100 keV
- Classical GRB: E_{peak} > 100 keV

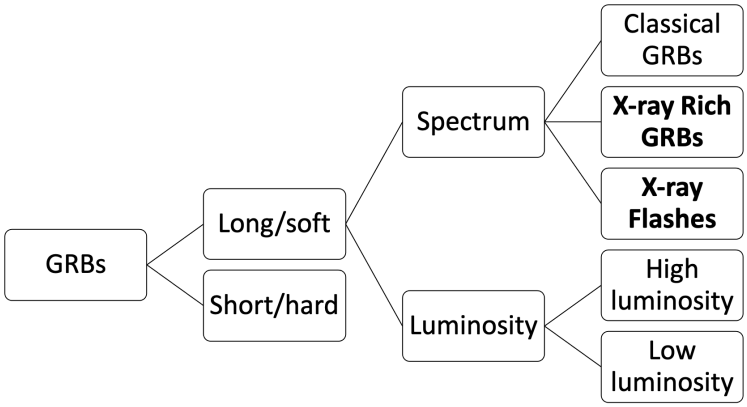

Figure 1.16: GRB classification chart based on peak energy of the spectrum and the GRB luminosity

In general, the higher the peak energy, the brighter the GRB, as shown in Figure 1.17 where we use $E_{p,z}$ to denote the redshift-corrected (rest-frame) peak energy, $E_{p,z}$ = (1+z) E_{peak} .

The empirical relationship between the peak energy and the isotropic energy (E_{iso}) can be expressed as follows (Amati, 2006):

$$\frac{E_{p,z}}{100\ \text{keV}} \approx 0.95 \times \left(\frac{E_{\text{iso}}}{10^{52}\ \text{erg}}\right)^{0.49} \tag{1.16}$$

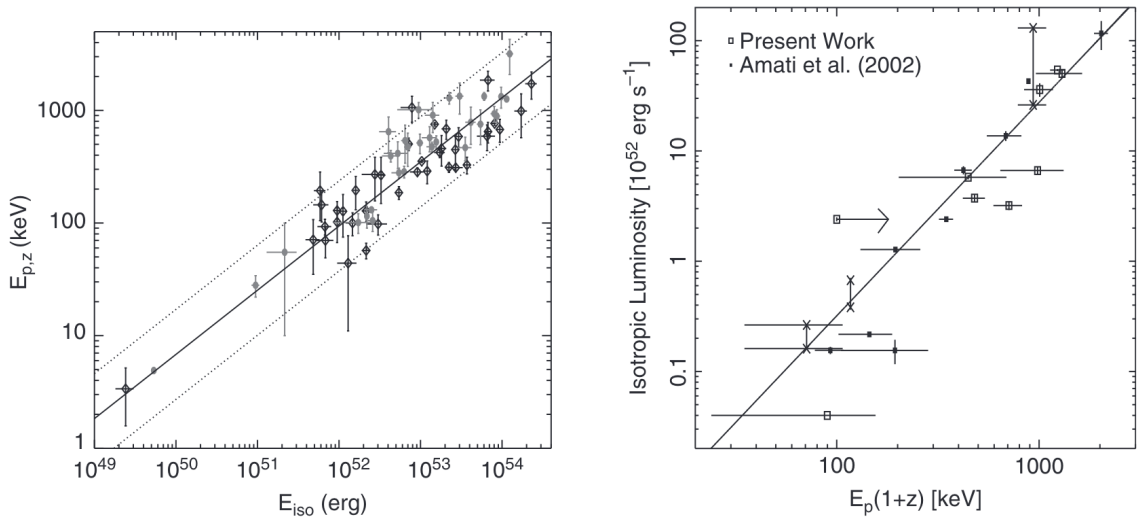

Figure 1.17: Left: empirical relationship between the peak energy and isotropic energy ($E_{p,z}$-E_{iso}, Amati, 2006). Right: empirical relationship between the peak energy and isotropic luminosity. ($E_{p,z}$-L_{iso}, Yonetoku et al., 2004)

This relationship is found in long GRBs with known redshifts, and it covers a wide range from high luminosity hard GRB to low luminosity X-ray flashes. Another related correlation between the peak energy and the peak isotropic luminosity ($L_{p,iso}$) could be written as (Yonetoku et al., 2004, B. Zhang, 2018):

$$\frac{E_{p,z}}{100\ \mathrm{keV}} \approx 1.8 \left(\frac{L_{p,\mathrm{iso}}}{10^{52}\ \mathrm{erg\ s^{-1}}} \right)^{0.52} \tag{1.17}$$

These correlations can in principle be cosmologically parameterized using LGRBs , but their physical interpretation is still unknown and there is still an open debate about their robustness.

1.4.2 Mystery of XRR/XRF physics origin

The physical origin of XRR and XRF is still unclear. The main explanations are divided into two basic points of view: intrinsic properties or off-axis viewing.

The jet off-axis observation effect has traditionally been used to explain the observed phenomena of XRF/XRR, and the main models include:

- P. Mészáros, Ramirez-Ruiz, et al. (2002) suggested that X-ray photons (20-100 keV) are actually produced by the thermal cocoon around the GRB jet as it bursts, and that the XRF and XRR events may result from off-axis observations of the jet.
- Ryo Yamazaki et al. (2002) suggested that the XRFs events are the result of off-axis observations of highly collimated GRB jets and that the low values of the peak and

isotropic energies are due to relativistic beam effects. It is however usually considered that the luminosity decreases much faster than the photon's energy, thus we can only see GRBs slightly off-axis.

- B. Zhang, X. Dai, et al. (2004b) suggested that these events may arise from off-axis observations of universal structured jets with luminosity decay similar to a power law or Gaussian function.

The intrinsic models mainly include:

- XRF and XRR may come from the "dirty fireball" model in which baryonic matter fills the jet, leading to a bulk Lorentz factor $<<$ 300 (Huang et al., 2002; C. D. Dermer et al., 2004).
- In internal shock models, these XRF/XRR events may also come from small-bulk Lorentz factor contrasts between high-bulk Lorentz factor shells and colliding relativistic shells (T. Sakamoto et al., 2005).
- Lamb et al., 2005 suggested that XRFs, XRRs and GRBs may arise from different opening angles of the jet, where the emissivity is a constant. In this model, XRFs are produced by jets with larger opening angles, while GRBs are produced by jets with smaller opening angles.

It has been shown that these events form a continuum in nature and are therefore likely to have similar physical origins (T. Sakamoto et al., 2005). Most low luminosity GRBs are X-ray flashes and may have somewhat different physical origins within the framework of the same progenitor model.

Bi et al. (2018) also compared the property of XRFs, XRRs and classical GRBs, and found that the properties of gamma ray emission, X-ray emission, light curve, association with supernovae, and the host galaxy of XRFs and XRRs are similar with the classical GRBs. But the physical origin of XRF and XRR is still unclear. It may be explained by the off-axis viewing or an thermal component of the burst (for some of the GRBs).

For example, GRB 090618 (identified as an XRR) was detected by the Swift X-ray telescope with thermal X-ray emission, and this XRR was associated with the SN explosion (Cenko et al., 2011). Starling et al. (2012) presented 11 Swift-detected GRBs associated with optical SN explosions, and explicitly identified the thermal X-ray signature.

1.4.3 SVOM/ECLAIRs advantage for detection the soft GRBs

Understanding the properties of XRFs and XRRs and clarifying the relationship between these two types of events and GRBs can deepen the understanding of the GRB transient emissions. For an in-depth study of this field, GRB detectors with a wide energy range and a low energy threshold are expected to be used in future XRF/XRR studies.

Prior to the SVOM mission, the relatively narrow spectral coverage of the Swift and Fermi GBM triggers, starting at 15 keV and 8 keV, respectively, limited the ability of both missions to effectively observe soft GRB events. Instead, SVOM is designed to be triggered from 4 keV. Due to the low energy threshold of 4 keV, SVOME/ECLAIRs will be sensitive to soft GRBs such as XRF, XRR, and high redshift GRBs. We expect that this advantage will increase the number of XRF and XRR samples and, in combination with observations from SVOM's other band telescopes, provide redshift and detailed spectral information for these soft GRBs.

During my thesis, I focus on the performance of the SVOM/ECLAIRs trigger for detecting GRBs, especially at 4–8 keV. In Chapters 2 and 3, I describe the SVOM mission and the ECLAIRs telescope in detail. In Chapter 4, I detail the inhomogeneity of the ECLAIRs detection plane in the 4–8 keV band and its potential impact on onboard triggering. In Chapter 5, I describe the heat pipe noise found in the 4-8 keV band, its potential impact on triggering, and suggested solutions to solve it. The simulated detection of different types of GRBs by ECLAIRs, in particular for soft GRBs, is presented in Chapter 6. Finally, the summary and prospects of the thesis can be found in Chapter 7.

Chapter 2

The SVOM mission

Contents

The Space-based multi-band astronomical Variable Objects Monitor mission (SVOM, J. Wei et al. 2016, B. Cordier et al. 2015) is a collaboration between China and France that aims to study the GRB phenomenon and the transient sky in general. The science instruments of this mission include both space-based telescopes and ground-based telescopes. The SVOM

satellite (Figure 2.1) is scheduled to be launched in June 2024 from Xichang, China. The mission consortium is composed mainly of Chinese and French research institutes and universities, and it is supervised by the China National Space Administration (CNSA), the Chinese Academy of Sciences (CAS), and the Centre National d'Etudes Spatiales (CNES).

In the following discussion, we will outline the overall framework of the SVOM mission and provide details on each science instrument. The ECLAIRs telescope will be detailed in the dedicated Chapter 3.

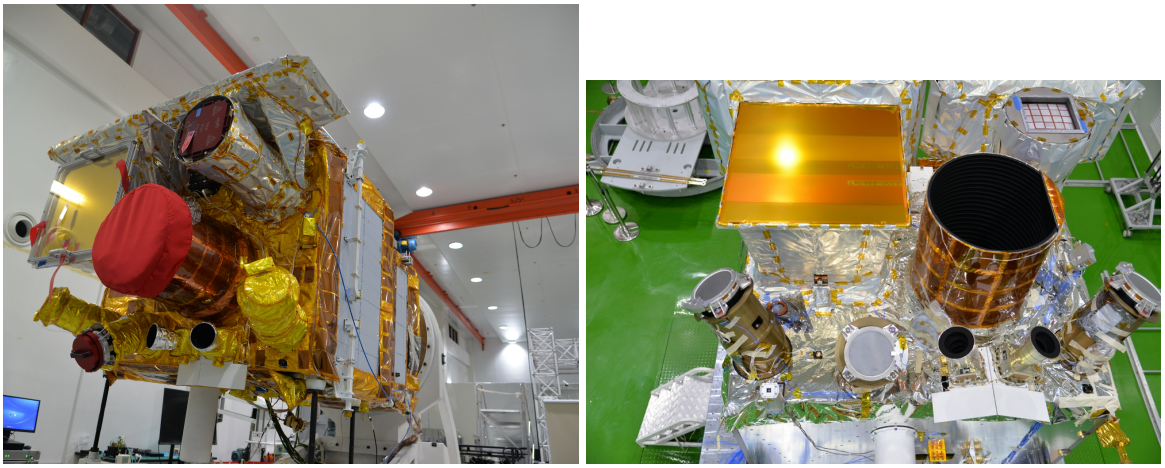

Figure 2.1: Physical view of the SVOM satellite and its 4 payload telescopes. These photos were taken in Shanghai in 2024. Credit: SVOM cooperation team.

2.1 SVOM satellite overview

SVOM is a mission designed to detect, localize and follow up GRBs as well as other high-energy transients from space and ground. SVOM could monitor the sky and observe sources in multi-wavelength.

The SVOM satellite is equipped with four main observation instruments designed to cover a broad band of wavelengths. These include the wide field-of-view (FOV) soft gamma-ray telescope ECLAIRs, the gamma-ray spectrometer Gamma-Ray Monitor (GRM), and telescopes for follow-up observations in X-ray and visible-band, namely the Microchannel X-ray Telescope (MXT) and the Visible Telescope (VT). In addition to these space-based instruments, there are several ground-based optical instruments for follow-up observations. These consist of a set of wide-field cameras called the Ground Wide Angle Cameras (GWAC), and two Ground Follow-up Telescopes (GFTs).

The sequence of observation of a GRB or high-energy transient is described below.

1. The wide field onboard telescopes ECLAIRs and GRM monitor the high-energy sky from hard X-ray to γ-ray.

2. When a bright enough new GRB occurs in the sky, ECLAIRs or GRM (or both) will

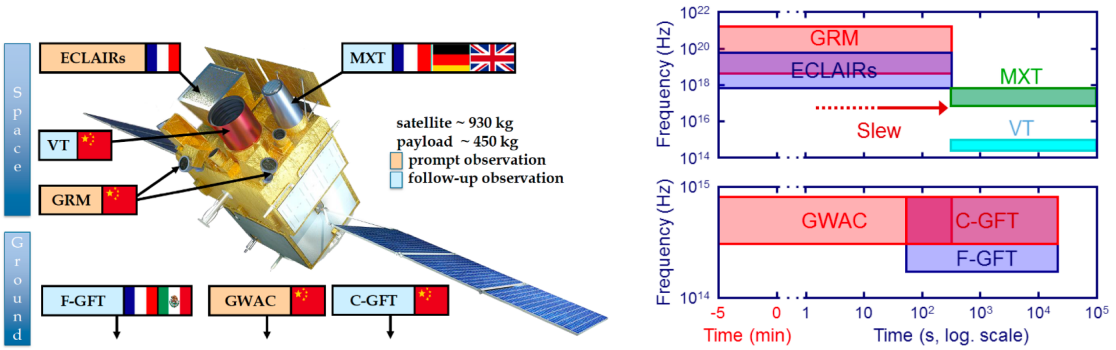

Figure 2.2: Left: overview of the SVOM mission, including the space and ground instruments. Right: spectrum coverage of SVOM onboard telescopes (top) and ground-based telescopes (bottom), corresponding to the GRB detection and follow-up sequence. The burst is detected at time $t = 0$ (J. Wei et al., 2016).

be triggered. If ECLAIRs detects a high signal-to-noise ratio (SNR) signal, it will send to the satellite an estimated GRB position and a slew request toward this position.

3. The satellite will transmit the trigger alert messages and preliminary results (e.g. lightcurves, positions) to the ground via the Very High Frequency (VHF) network (see Section 2.7.3).

4. At the same time, GWAC is often observing the same region of the sky monitored by ECLAIRs and may detect the optical photons of the prompt emission of the GRB if it exists.

5. The SVOM satellite performs a slew action in tens of seconds to minutes, to make the narrow instruments MXT and VT point to the estimated position of the GRB. A more precise position will be obtained and sent to the ground after the follow-up observation of MXT and VT.

6. The ground-based telescopes (C-GFT and F-GFT) perform the follow-up observation after receiving the first position signal from the satellite.

2.2 ECLAIRs

ECLAIRs is a coded mask hard X-ray telescope onboard SVOM. It is designed to monitor and locate the X-ray to γ-ray transients in the energy range of 4–150 keV. ECLAIRs mainly consists of a coded mask and a detector plane, which is connected to the electronics readout system and the onboard computer, as well as the structure, the shield (optical and X-ray), and the thermal system. We detail this instrument in Chapter 3.

2.3 Gamma-Ray Monitor

The Gamma-Ray Monitor (GRM) is one of the four main scientific instruments onboard the SVOM satellite, developed at the Institute of High Energy Physics (IHEP, China). GRM features a wide FOV for monitoring the gamma-ray sky.

GRM consists of three identical detector modules called the Gamma Ray Detectors (GRD), each pointing in different directions to enable the crude onboard localization of the GRBs. It also includes one electronics box (GEB) responsible for the scientific processing, management, and power supply, as well as one particle monitor (GPM) for monitoring the charged particle counts onboard.

The position and orientation of each GRD on the satellite platform are depicted in Figure 2.3. Each GRD provides an individual detection FOV of approximately 3.4 sr, each oriented at an angle of 30 deg to the satellite's optical axis (ECLAIRs, MXT and VT optical axis). These GRDs are distributed 120 deg apart in the plane perpendicular to the optical axis. Consequently, the cumulative FOV for the GRM system totals 5.6 sr. The overlap where at least two GRDs have a shared FOV is 2.8 sr, while the region covered by all three GRDs collectively amounts to 1.0 sr, at the center of ECLAIRs FoV. A comparison of the GRM's FOV with that of ECLAIRs is illustrated in the right panel of Figure 2.3. The GRM's detection energy band spans from 15 keV to 5 MeV. Key design specifications of the GRM are summarized in Table 2.1.

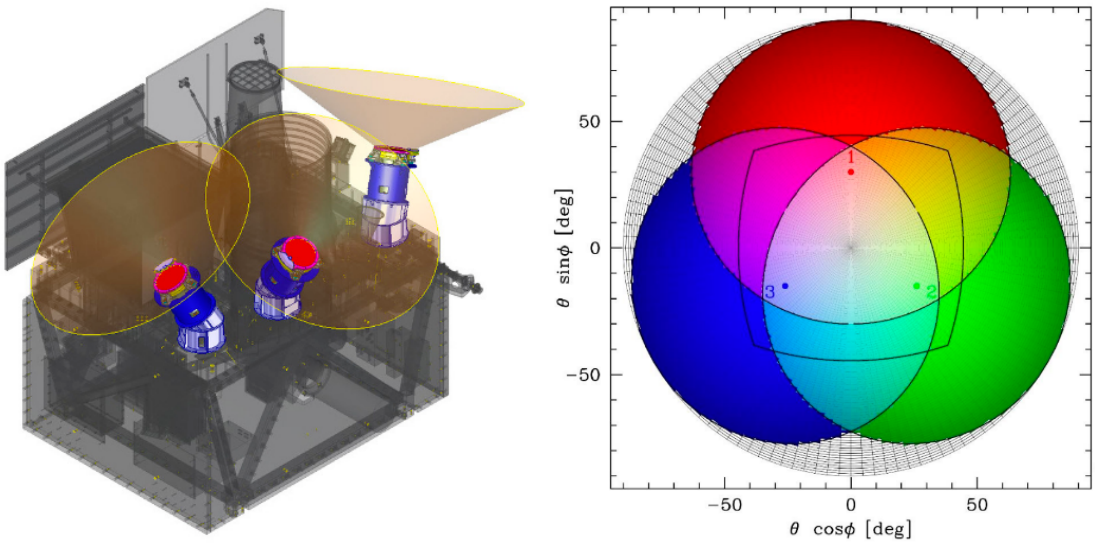

Figure 2.3: Overview of GRM. Left: schematic drawing of GRM, which shows the position and the orientation of the three GRD detection modules on the platform. Right: FOV of the three GRDs (blue, green and red) compared to the ECLAIRs FOV (solid line in the middle). Credit: IHEP.

Table 2.1: Main characteristics of GRM (Wen et al., 2021).

Parameter	Value
Energy band	15 keV ~ 5 MeV
Field-of-view	$\pm 60^\circ$ (single GRD)
Detection area	200 cm^2 (single GRD @ 100 keV)
Deadtime	<8 μs
Time accuracy	<20 μs
Energy resolution	$\leq$19% @ 59.5 keV
Expected detection rate of GRBs	$>$90 GRBs per year
GRB localization accuracy	$<5^\circ$ (Fluence $> 1\times10^{-6}$ erg cm^{-2} @1–1000 keV, 1 s)

2.3.1 Technical description of GRM

Each GRD is composed of a sodium iodide (NaI) crystal box, a photomultiplier (PMT), and its front-end electronics. Beneath the NaI crystal, there is a quartz glass, a magnetic shielding, a high-voltage distributor. Mechanical structures are positioned to support the detector's functionality. Additionally, an auxiliary calibration detector (GCD) is installed on the edge of the top surface of each GRD. This GCD aims to perform in-orbit relative energy calibration with an alpha source of ^{241}Am and to stabilize the detector' s gain by adjusting the high voltage.

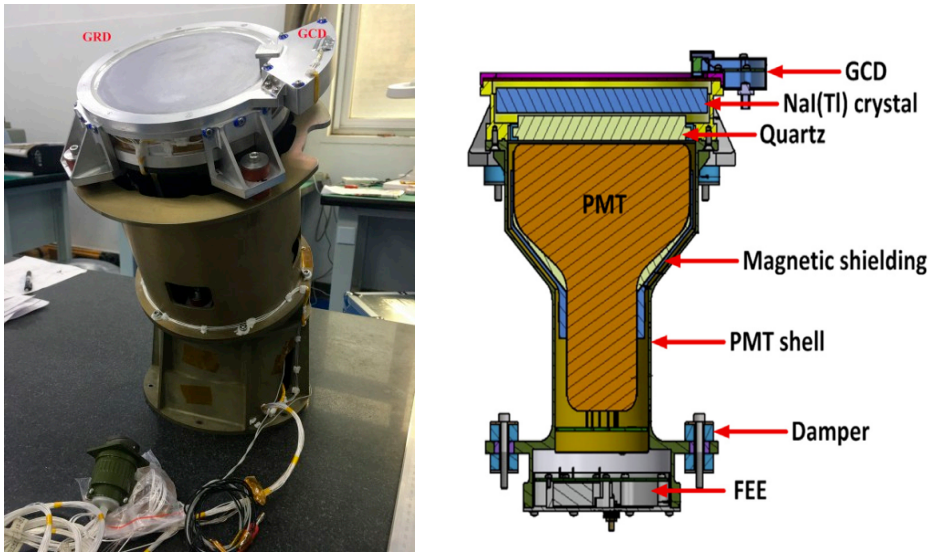

Figure 2.4: Mechanical figure and schematic diagram of a single GRD. Credit: IHEP, Wen et al. (2021).

When an incoming X-ray or γ-ray photon interacts with the NaI crystal, it interacts with an electron, which loses its energy in the crystal, leading to the emission of several scintillation fluorescence photons. These photons are then transmitted by the quartz glass to the surface of the PMT. Upon interacting with the PMT's surface material, initial photoelectrons are produced. With the application of a high voltage, these initial electrons strike the metal anodes inside the PMT, leading to an avalanche multiplication effect. This signif-

icantly amplifies the number of electrons, often by a few million times. These multiplied electrons make a short pulse, which is ultimately collected by the front-end electronics to produce the detection output signal, whose amplitude is roughly proportional to the energy deposited in the crystal.

The NaI crystal has a surface area of 200 cm^2 and a thickness of 15 mm. To enhance the transmittance of low-energy X-ray photons, the box's entrance window is made of a 1.5 mm thick beryllium layer. The effective area of a GRD varies as a function of the energy and also depends on the angle of incidence (Figure 2.5). The most sensitive energy band for the GRD is around 100 keV, with an effective area of 200 cm^2.

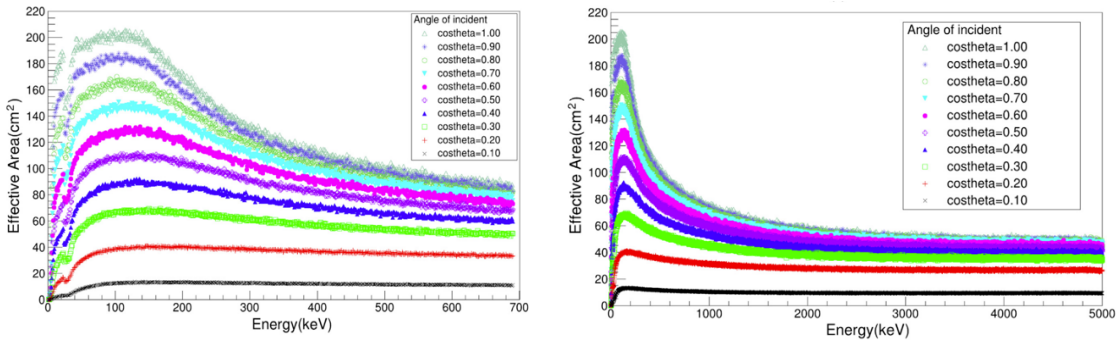

Figure 2.5: Simulated effective area of one GRD for various energies and angles of incidence. On the left, the effective area is presented for an energy band ranging from 15 keV to 700 keV. On the right, a broader energy band from 15 keV to 5 MeV is depicted (Wen et al., 2021).

The energy resolution, depicted as a function of energy, is shown in Figure 2.6. As the energy increases, the relative energy resolution of the detector improves. During the calibration tests of the qualification model of GRM, it was observed that the energy resolution aligns with the design requirements.

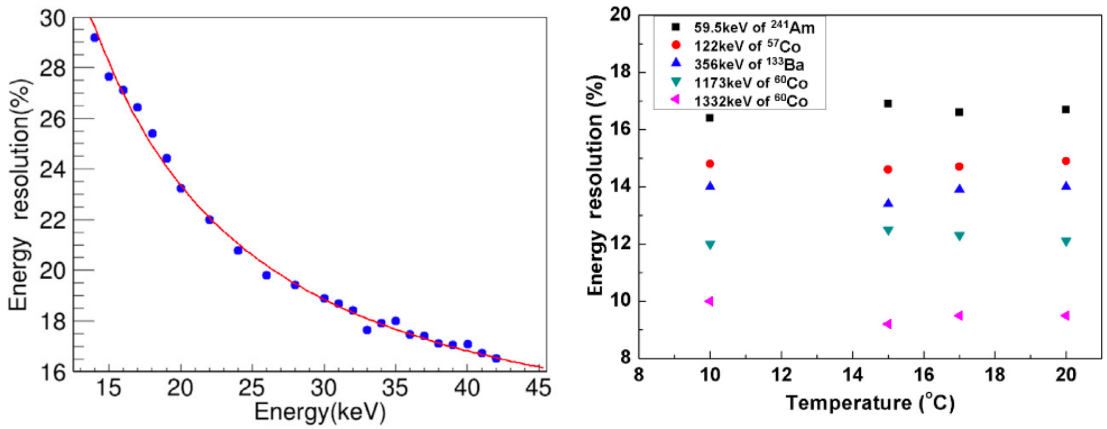

Figure 2.6: Energy resolution performance of the GRD qualification model measured during the calibration tests (Wen et al., 2021).

2.3.2 Trigger algorithm of GRM

The principle of the GRM's trigger algorithm is to detect an increase in the background counts. The SNR is determined by comparing the total counts (C) received by the detector to the background counts (B), calculated as Equation 2.1.

$$SNR = \frac{C - B}{\sqrt{B}} \tag{2.1}$$

When applying this formula specifically to the GRM scenario, the algorithm utilizes previous background counts to estimate the current background. Furthermore, to enhance the detection of various types of GRBs (categorized by their spectra as soft-hard and by their duration as long-short), the GRM's trigger algorithm segments the detection energy band into four strips (15–50 keV, 50–300 keV, 300–1000 keV, and 1000–5000 keV) and considers three different timescales (0.1 s, 1 s, and 4 s). Thus, the estimated background for one GRD (B_i) over a timescale interval $[t, t + \delta t]$ and within an energy strip δE is calculated as Equation 2.2. In the current parameter configuration, the timescale for the previous background estimation, denoted as δt_{bkg}, is set to 16 s.

$$B_i\left(t, \delta t, \delta E\right) = B_i\left(t - \delta t_{bkg}, \delta t_{bkg}, \delta E\right) \times \frac{\delta t}{\delta t_{bkg}} \tag{2.2}$$

GRM trigger requires that at least two GRDs have a SNR above a predefined threshold. For each GRD, a total of 4 x 3 adjustable thresholds are set in the 4 different time scales and the 3 different energy bands. Note that GRM could only have a crude localization (approximately 15 x 15 deg^2) if all three GRDs simultaneously trigger.

The simulated background of a single GRD is illustrated in Figure 2.7. The CXB is the predominant source of background for the GRD. When the Earth is outside the FOV of a GRD, the total background count amounts to $\sim$ 1300 counts/s in 15 keV - 5 MeV, with the CXB representing approximately 90% of this total. Conversely, when the Earth is positioned directly in front of the SVOM satellite, with an angle of 30 deg to the GRD's viewing direction, the total background count reduces to $\sim$ 800 counts/s (15 keV - 5 MeV), and the contribution of the CXB falls to about 50% (He et al., 2020).

GRM is anticipated to detect more than 90 GRBs annually and will provide lightcurves and spectrum information for GRBs in 15 keV–5 MeV (especially the peak energy). This complements the detection range of ECLAIRs, which covers 4–150 keV. Note that detecting a GRB with GRM does not initiate a slew request for the SVOM satellite due to its limited localization capability. However, the alert will be sent to ground stations and broadcast to the scientific community for further study or follow-up observations. Additionally, this trigger information can assist scientists on the SVOM team in cross-checking and identifying GRBs.

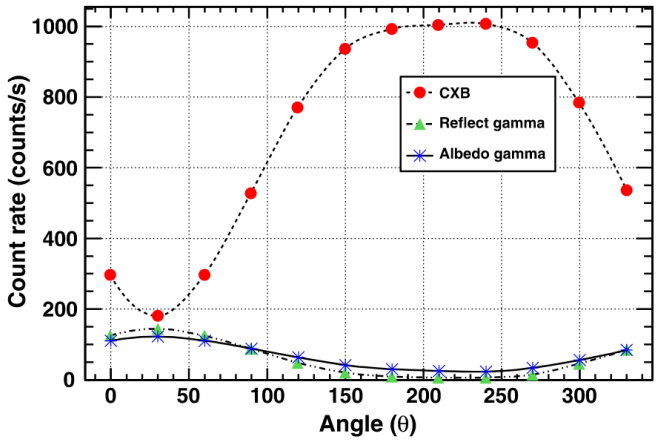

Figure 2.7: Simulated X-ray background of GRD, only considers the CXB, reflection, and albedo background, excluding the SAA delayed background $\sim$ 300 count/s. Credit:(He et al., 2020).

2.4 Microchannel X-ray Telescope

The Microchannel X-ray Telescope (MXT) is a focusing X-ray follow-up telescope onboard SVOM, with an energy band of 0.2–10 keV designed to detect the GRB afterglows within error boxes of ECLAIRs. This type of telescope is based on a "lobster-eye" optics. It mainly consists of a mosaic of Micropore Optics (MPO) and camera implementing a pnCCD (MCAM), as shown in Figure 2.8. There are also three other subsystems to support the whole telescope operation: the data processing units (MDPU), the carbon fiber structure, and the radiator to dissipate the heat. Those five subsystems compose a light and compact focusing X-ray telescope, with a weight of < 42 kg and a focal length of about 1.15 m.

The expected performance of MXT is illustrated in Table 2.2. A FOV equivalent to 58 x 58 arcmin^2 is sufficient to image the entire the error region provided by ECLAIRs (radius $\sim$ 13 arcmin). The effective area is approximately 35 cm^2 @ 1.5 keV which provides a sensitivity of ~ 10 mCrab (2 x 10^{-10} erg cm^{-2} s^{-1}) in 10 s of observation and ~150 μCrab (3x10^{-12} erg cm^{-2} s^{-1}) in 10 ks of observation. With such a sensitivity, the large majority of the GRB (80–90%) could be located to better than 2 arcmin by MXT. Furthermore, 50% of the GRB will be located within 60 arcsec in 5 min after a trigger (D. Götz, Boutelier, et al., 2023).

2.4.1 Micropore Optics and pnCCD camera

In general, the incident X-ray photons will be reflected by the MPO if they are directed at a small incident angle with the micropore walls. They will be collected at the focal plane and recorded by the X-ray camera. The MPO design is based on the new X-ray micropore "lobster-eye" optical technology which is inspired by the vision of some crustacean decapods, like the lobster. Different missions utilize nowadays the same technology, such as the Wide-Field X-ray telescope onboard Einstein-Probe mission (Yuan et al., 2022) which

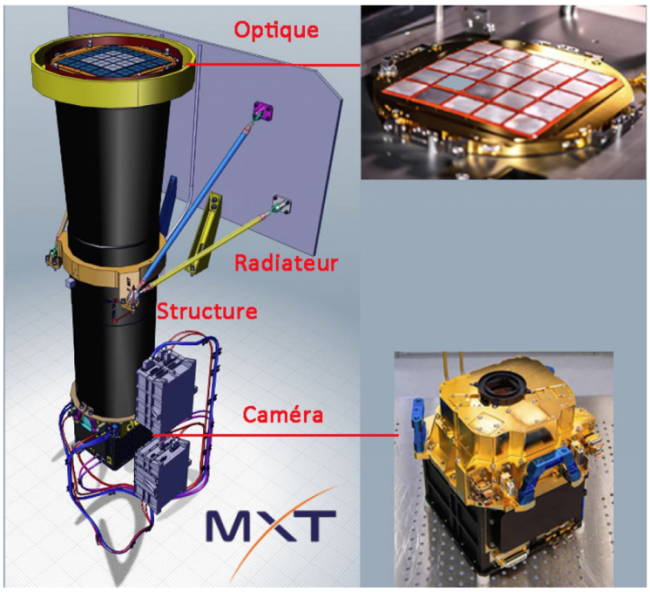

Figure 2.8: MXT instrument. Left: the overall instrument structure. Right: the optical segment and the X-ray camera. Ref: `https://www.svom.eu/mxt-microchannel-x-ray-telescope`.

Table 2.2: MXT expected scientific performance (D. Götz, Boutelier, et al., 2023).

Parameter	**Value**
Energy range	0.2 –10 keV
Field-of-view	58 x 58 arcmin
Angular resolution	10 arcmin at 1.5 keV
Source location accuracy	$<$ 120 arcsec for 90% GRBs
Effective area	$\sim$ 35 cm^2 at 1.5 keV
Sensitivity (5σ)	10 mCrab in 10 s
	150 μCrab in 10 ks
Energy resolution	$<$ 80 eV at 1.5 keV
Time resolution	100 ms

has been launched in January 2024.

The MPO is composed of 5×5 micro-channel plates, each plate is 40 mm wide with pores of 40 μm side. The "lobster-eye" results in a peculiar point spread function with a central peak and cross arms. The central peak is produced by the photons that are reflected twice on adjacent walls (approximately 50% of the incident photons for MXT), and the cross arms are produced by those photons that reflect only once (accounting for $2 \times 22\%$). There is also a small fraction of photons that, without interaction with the optical materials, contribute to a diffuse background.

Lobster-eye optics are very attractive for small space instruments with a wide FOV. Although the optical system has a lower performance in terms of effective area and angular resolution compared to the classical Wolter-I type optics, it provides a FOV of 1 deg, with a

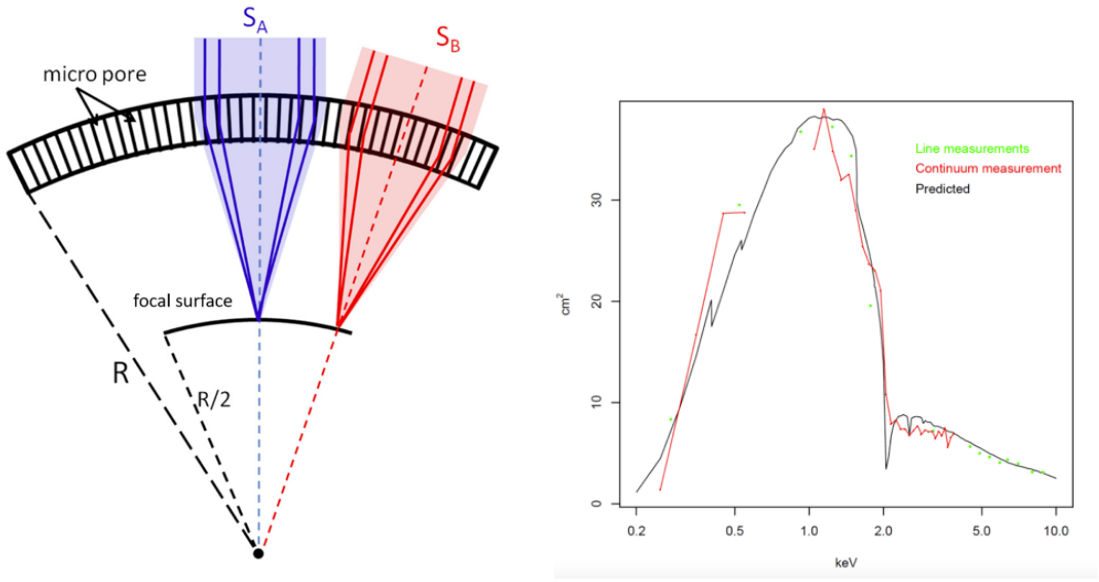

Figure 2.9: Left: imaging principle of lobster-eye optical (Yuan et al., 2022). Right: effective area of MXT as a function of energy: the black line represents the model, while the red line and green points the experimental data.

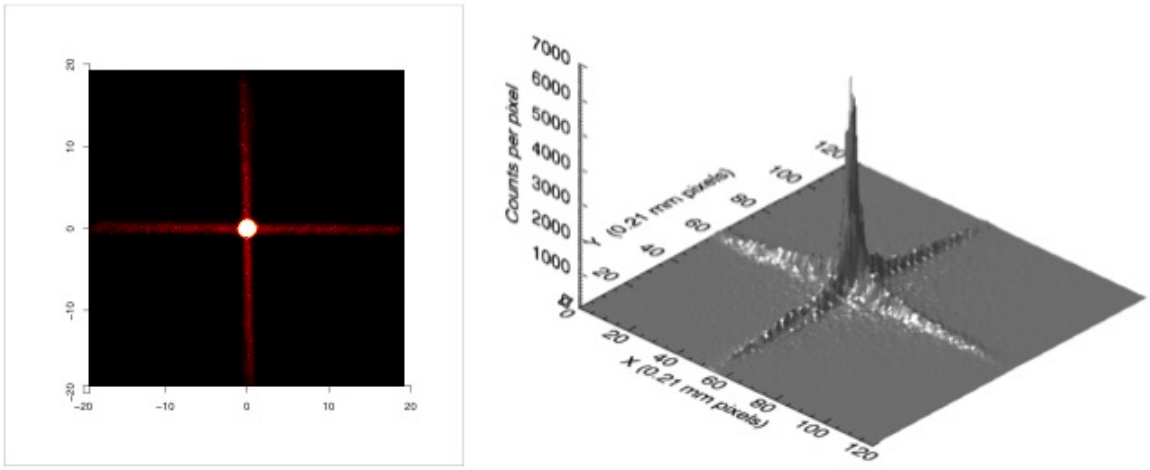

Figure 2.10: The point spread function describes the spatial distribution of the intensity of light of a point-like source in the focal plane of an optical system. Ref: `https://www.svom.eu/en/mxt-langouste-en/`

very light weight (< 2 kg), more than 1 order lighter compared to the Wolter-I type optics.

The pnCCD camera of MXT is developed by the Max Planck Institute für Extraterrestrische Physik (MPE) and uses the same detector technology as the eROSITA telescope (Friedrich et al., 2004; Meidinger et al., 2006), although on a smaller device (256×256 vs 384×384 pixels), and with a slower readout speed (100 ms vs 50 ms).

This frame store pnCCD consists of an image area and a frame store area, included the on-chip electronics. It has a 256 x 256 Si pixels of 75 μm in side length in the image area,

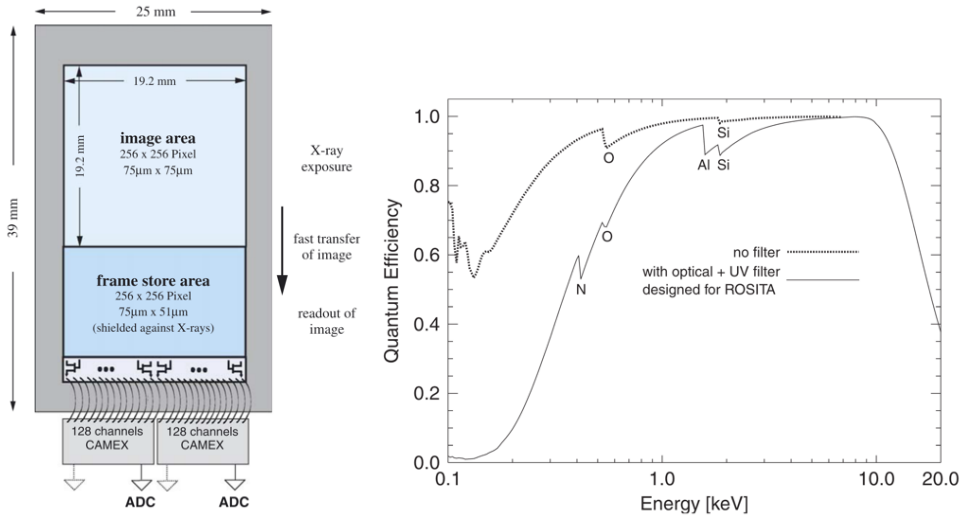

Figure 2.11: Left: schematic drawing of the MXT detector. Right: quantum efficiency of the MXT frame store pnCCD (Friedrich et al., 2004, Meidinger et al., 2006).

and a reduced frame store area with 75 × 51 μm pixels, as shown in Figure 2.11. The pnCCD pixels are fully depleted with a 450 μm depth.

The detector is actively cooled to -65° C to ensure low thermal noise and to reduce in-flight radiation damage effects. With the optimization as discussed above, the camera has an excellent low energy response down to 200 eV and energy resolution (48 eV FWHM @ 277 eV, 131 eV FWHM @ 5.9 keV), as detailed in Table 2.3. The quantum efficiency of this camera is shown in the right panel of Figure 2.11.

Table 2.3: Key performance of the new frame store pnCCDs.

Parameter	**Frame store pnCCD**
Pixel size	75 x 75 μm^2 or 51 x 51 μm^2
Depletion (= sensitive) depth	450 μm
Readout noise	2 e^- ENC (highest gain 1.8 e^-)
Quantum efficiency	$\geq$90% from 0.4–1 keV
Charge handling capacity	$>10^5$ electrons/pixel
Energy resolution	FWHM(5.9 keV) = 123 eV (singles)/131 eV (all events)

2.4.2 Summary of MXT

In summary, MXT is capable of significantly improve the ECLAIRs error boxes for SVOM GRBs to better than 2 arcmin, enhancing the probabilities to detect the GRB afterglows for the optical telescopes. Despite having a smaller effective area (35 cm^2) compared to the Swift/XRT (110 cm^2), MXT is able to detect most of SVOM GRB afterglows up to ~ 10^5 s after the trigger. Furthermore, MXT possesses the ability to measure the spectrum of the afterglow and, in some cases, the one of the GRB prompt emission, if the latter lasts long enough, thus providing broad-band measurements with ECLAIRs.

2.5 Visible Telescope

Visible Telescope (VT) is another follow-up telescope onboard SVOM. The main task for VT is to detect and observe the GRB optical afterglow, and localize the GRB position precisely in the sub-arcsec level.

The VT consists of five functional units: the VT optics and detector (main body), the image processing computer, the primary control box, the thermal control box, and the thermo-electric cooler control box.

The VT telescope, based on a Ritchey-Chretien design, features two light channels (red and blue). During observation, light is first reflected by the primary and secondary mirrors, and then divided into two channels by a dichroic beam-splitter. Finally, the light beams are captured by the red-channel CCD and blue-channel CCD simultaneously.

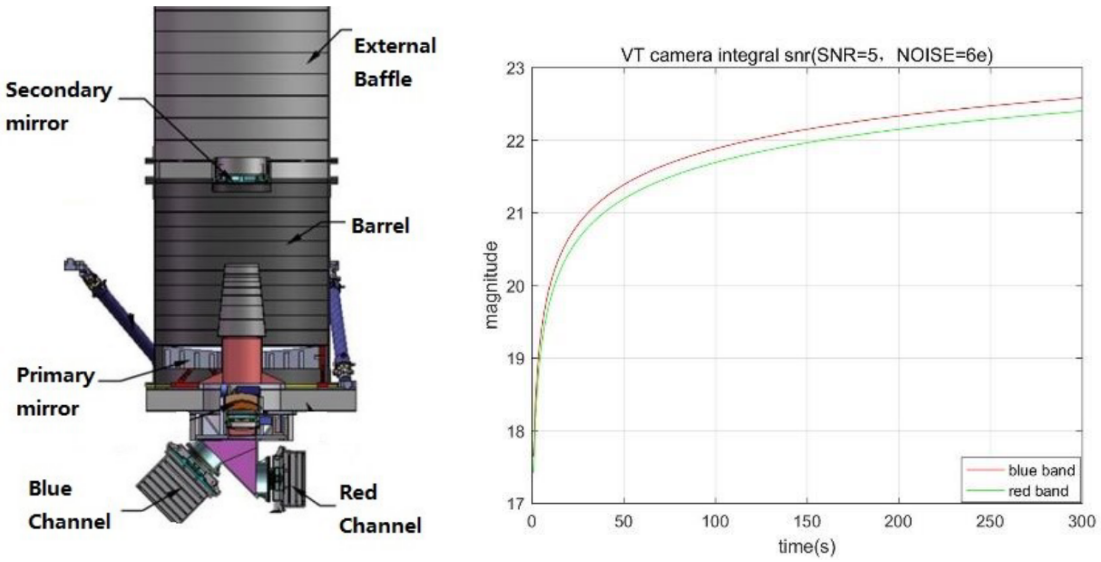

Figure 2.12: VT instrument. Left: schematic drawing of the telescope. Right: sensitivity versus observation time. Credit: NAOC

The sensitivity of VT reaches approximately Mv = 22.5 for an observation time of 300 s, as shown in the right panel of Figure 2.12. The FOV of VT spans 26 x 26 arcmin^2, sufficiently covering the error box of ECLAIRs in most cases. The main parameters of the VT telescope are detailed in Table 2.4.

2.5.1 VT components

The VT optical system contains a 440 mm diameter primary mirror and a 135 mm secondary mirror to collect the photons. There are three lenses behind to focus and adjust the light beam. The first two lenses (Focusing lenses) are servo-controlled to align the optical axis, aiming to adjust the focus during the VT operation onboard. The third lens is fixed to

Table 2.4: The key parameters of VT (X. Fan, Zou, Jianyan Wei, et al., 2020).

Parameters	**Description**
Sensitivity	Mv=22.5 (3 sigma, 300 s exposure)
Pixel resolution	0.77 arcsecond/pixel
Primary mirror diameter	440 mm
Focal length	3600 mm
Field-of-view	$\geq$26 arcmin$\times$26 arcmin
Spectral range	400 nm–650 nm (blue band):
	650 nm–1000 nm (red band)
Surface obscuration	0.18
Optical transmission	0.6 (average)
Detector	2048$\times$2048 pixels,13.5 um$\times$13.5 um
CCD working temperature	-65$\pm$2°C (blue band); -75$\pm$2°C(red band);
ADC	16bits
Readout noise	$<$ 8e-/pix (15 s, 30 s exposure time);
	$<$ 6e-/pix (100 s, 300 s exposure time)
Stray light	$<$1/3 sky background when the Moon is $>$ 30deg off axis.

make the light beam entrance to the ingenious dichroic beam-splitter prism. This beam-splitter prism is inserted before the focal plane to ensure the light beam is divided into two channels so that the telescope can make the observation in both channels simultaneously. The average transmission for the optical is around 60 % in VT.

For the camera, two main CCDs (E2V CCD42-80) are mounted in the focal plane of the two optical channels, the red one ranging from 650-1000 nm, and the blue one ranging from 400-650 nm. Each CCD consists of 2k $\times$ 2k pixels with 13.5μm $\times$ 13.5 μm size. Combined with the design optical structure, the pixel resolution achieves 0.77 arcsec/pixel, and the spectrum response for different wavelengths is shown in Figure 2.13.

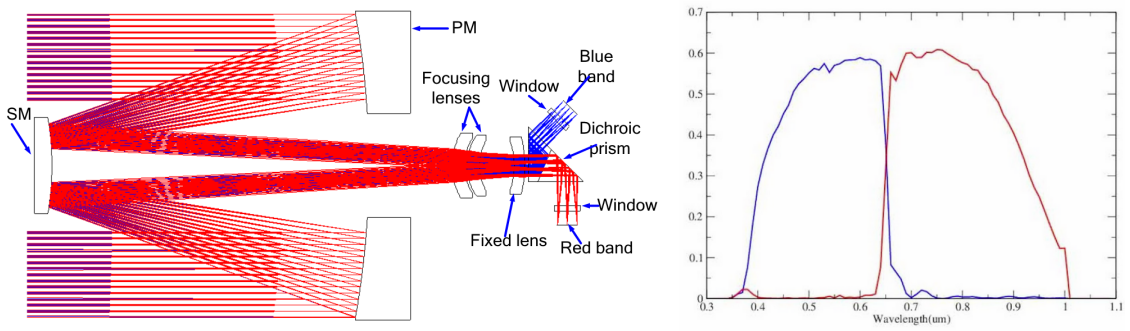

Figure 2.13: Left: VT optical scheme. Right: spectral responses of the red and blue channels of the VT telescope. Credit: NAOC, X. Fan, Zou, Jianyan Wei, et al. (2020).

Moreover, to enhance the pointing accuracy of the satellite's attitude control system, two fine guidance sensors (operating in the 400–650 nm range) have been mounted onto the blue channel's focal plane. The specifications of these sensors are detailed in Table 2.5.

Table 2.5: Specifications of the fine guidance sensors camera (X. Fan, Zou, Qiu, et al., 2020).

Parameters	Description
Field-of-view	12.7'x12.7'
Spectral range	400-650nm
Detector	1024x2048 pixels, 13umx13um
CCD working temperature	-20°C (blue band)
ADC	14bits
Readout noise	$<$ 10e-/pix

2.5.2 The potential science contribution of VT

VT conducts data processing onboard to enable rapid alerts. After a GRB is localized by MXT, VT will extract a list of potential sources from its sub-image surrounding the MXT localization. This list is then transmitted in real-time to the ground. Subsequently, these sources are compared with existing catalogs to identify potential GRB optical counterparts. Once a counterpart is identified, an alert is distributed to the global scientific community (Section 2.7.3. Following this alert, ground-based telescopes are used to carry out redshift measurement by spectroscopic observations of the identified counterpart.

The primary objective of VT is to refine GRB localization, as provided by ECLAIRs and MXT, to sub-arcsecond accuracy. With both the red and blue bands being detected simultaneously onboard, the VT telescope should capture optical images of approximately 70% of the SVOM GRBs during the first orbit. This capability could assist SVOM in constructing a comprehensive and uniform lightcurve afterglow sample. It enables scientists to explore the "dark GRBs" realm for the first time.

In theoretical predictions, approximately 5%–7% of GRBs are expected to be high-redshift events (J. Wei et al., 2016). However, Swift has rarely detected high-redshift GRBs, possibly due to the insufficient depth of early-time optical images for source identification. The VT telescope, with its high sensitivity, especially in the red band, is capable of detecting high-redshift GRB afterglows up to $z \sim 6.5$. By combining the fast optical-counterpart alerts generated by VT and the anti-solar pointing strategy of SVOM, we can expect to identify a larger fraction of high-redshifted GRBs for the SVOM mission.

2.6 Ground-based instruments

2.6.1 GWAC cameras network

The Ground-based Wide-Angle Cameras network (GWAC) aims to detect the GRB optical counterparts from the very early prompt emission phase to the early afterglow phase. To achieve this goal, the designed GWAC system has a large joint FOV $\sim$ 5400 deg^2 and the ability to monitor the same region of the sky as that observed by ECLAIRs.

The GWAC array consists of 9 GWAC-A cameras units and 3 follow-up telescopes named F60A, F60B, and F30. They are all installed in the GWAC dome located in the Xinglong Observatory in China (Figure 2.14). The parameters of each type of instruments are shown in Table 2.6.

Figure 2.14: Panoramic view of the GWAC setup at Xinglong Observatory, with the GWAC-A mounts on the right and the 60 cm and 30 cm telescopes on the left. Credit: NAOC.

Each GWAC-A unit is equipped with 4 Joint Field-of-View (JFOV) cameras and a Full Field-of-View (FFOV) camera. Each JFOV camera consists of a 4k × 4k CCD camera and a refractive lens with an aperture of 180 mm, with an individual FOV of $\sim$ 12.8 × 12.8 deg^2. These 4 cameras form a collective FOV of ~25 x 25 deg^2. The sensitivity of the JFOV camera is 16 mag for a 10 s exposure in the R-band, and could reach a typical 18 mag when stacking the images. The FFOV camera is used to guide and extend the detection flux to bright sources $\sim$ 6 mag in the R-band. This camera is equipped with a 3k x 3k CCD camera and an aperture of 3.5 cm. It has a FOV 25 × 25 deg^2, roughly covering the same FOV as JFOV cameras.

Table 2.6: GWAC instruments parameters (X. Han et al., 2021).

Telescope	Number	Aperture (cm)	FOV	Filter	Limiting Magnitude (single/stack)
GWAC-A	9	18 (JFOV)	12.5° x 12.5°	Clear	16/18
		3.5 (FFOV)	25° x 25°	Clear	12
F30	1	30	1.8° x 1.8°	Clear, UBVRI	16.5/17
F60A/B	2	60	18' x 18'	Clear, UBVRI	18/19

Note: the limiting magnitudes are measured in R-band in either a single 10 s image or in several 10 s stacked images.

In addition to the GWAC-A unit, three robotic follow-up telescopes, F60A, F60B telescopes and F30 are also installed in the GWAC dome. All three telescopes are equipped with Johnson UBVRI filters. The GWAC-F60A/B have a 60 cm aperture and are equipped with 2k × 2k CCDs. They have a FOV 18' × 18' and fast slewing speed $\sim$10 deg s^{-1} allowing them to quickly follow the potential targets. The GWAC-F30 telescope has a FOV of 1.8 x 1.8 deg^2, its sensitivity can complete the gaps of flux coverage between the GWAC-A and the GWAC-F60A/B.

In order for the system to run smoothly, the GWAC data processing and management system (Xu, L. P. Xin, X. H. Han, et al., 2021), the real-time automatic validation system and the automatic observation management system are built (Xu, L. P. Xin, Wang, et al., 2020). The hardware architecture of those systems is shown in Figure 2.15.

The GWAC system can incorporate external telescopes by using a customized data link to extend the network. Currently, two telescopes are included: the 80 cm Cassegrain reflecting TNT telescope located at the Xinglong Observatory and the 1.2 m CGFT at the Jilin Observatory of NAOC (X. Han et al., 2021).

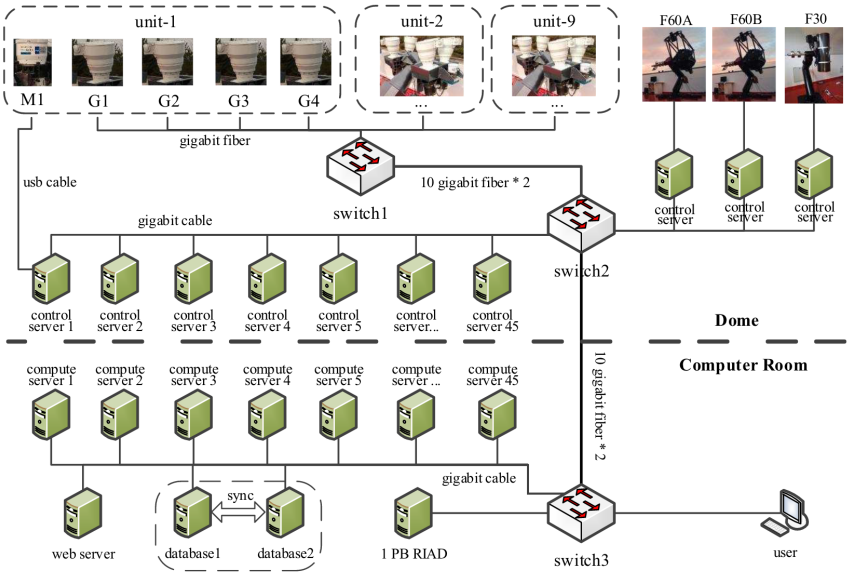

Figure 2.15: The hardware architecture of GWAC control system, including the GWAC telescopes, organized by a computer cluster (Xu, L. P. Xin, X. H. Han, et al., 2021).

To date, there are only a few cases of optical counterpart emissions detected before the end of the GRB prompt phase. GWAC has contributed to one of those cases, which detected the optical emission from the prompt phase to the afterglow (L. Xin et al., 2023).

After the launch of SVOM in 2024, simultaneous observations by GWAC and space instruments will be performed. It has the potential to provide essential optical data for GRB studies and build a large sample during the life of the SVOM mission. The system also will be used for ToO observations for searching optical counterparts of transient events or gravitational wave detection from LIGO/Virgo interferometers.

2.6.2 Follow-up telescopes

In order to perform quick follow-up on the high-energy transients detected by SVOM, China and France are responsible for developing dedicated ground follow-up telescopes: Chinese GFT (C-GFT) and French-Mexican GFT (Colibri, F-GFT). The two telescopes aim to precisely measure the GRB optical counterpart and its positions. They are located at complementary

longitudes to provide a quick and continuous follow-up of the GRBs. The main characteristics of the C-GFT and the F-GFT are given in Table 2.7.

Table 2.7: GFTs main characteristics (Atteia et al., 2022).

	C-GFT	**F-GFT/Colibri**
Diameter (mm)	1200	1300
Focal ratio	8	3.75
Number of channels	3 (g; r; i)	3 (g/r i; z/y ; J/H)
Field-of-view (arcmin)	21 x 21	26 x 26 (grizy) ; 21 x 21 (JH)
Sensitivity (r channel, 300 s, 10σ)	$m_{AB} \sim 20$	$m_{AB} \sim 22$

The Chinese Ground Follow-up Telescope (C-GFT) is a 1.2 m aperture telescope located in Jinlin Observatory (China). C-GFT has a sensitivity of 20 mag in r-band with 300-second exposures during the new moon night.

C-GFT is a Cassegrain telescope (Figure 2.16) where the primary and secondary mirrors of the telescope are hyperboloidal mirrors, with effective diameters of 1180 mm and 340 mm, respectively. It could also switch to a primary focus to have a wider FOV by removing the secondary mirror through a switching mechanism (1-day operation).

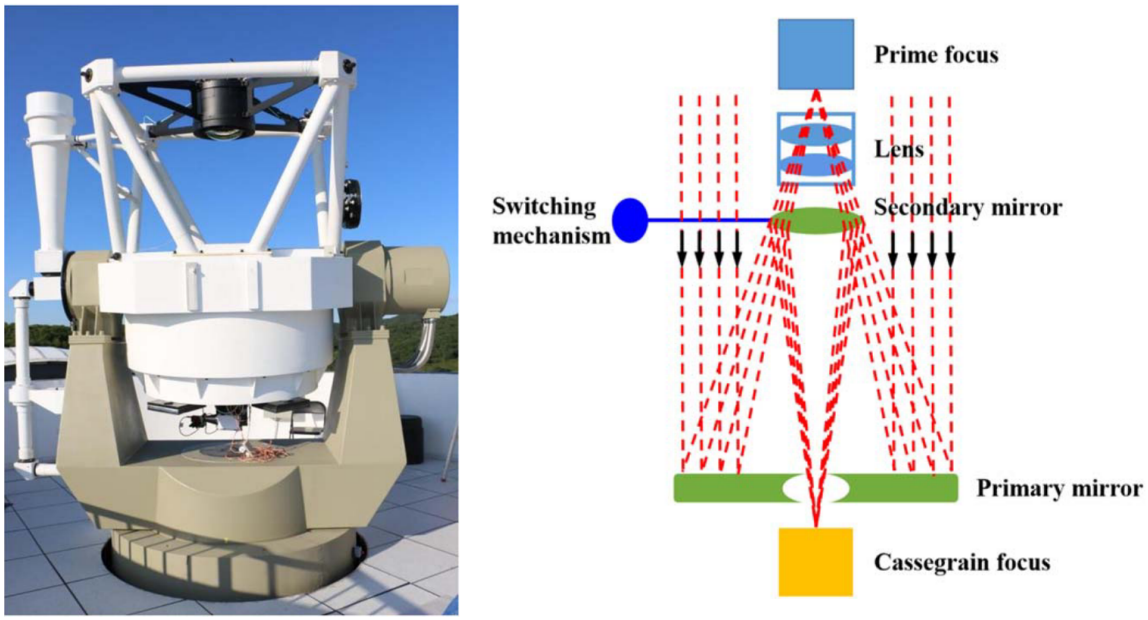

Figure 2.16: Chinese Ground Follow-up Telescope (left) and its optical scheme (right) (Niu et al., 2022).

A three-channel imaging system equipped the C-GFT Cassegrain focus as shown in Figure 2.17. This system enables simultaneous imaging in SDSS g, r, and i bands with an FOV 21' x 21'. Three CMOS-CCD cameras with a size of 2k × 2k are equipped in each channel. The imaging system is sensitive in the 400–950 nm wavelength range (Niu et al., 2022). In the primary focus, a 4k×4k pixel camera provides images on a FOV of 1.5 x 1.5 deg^2.

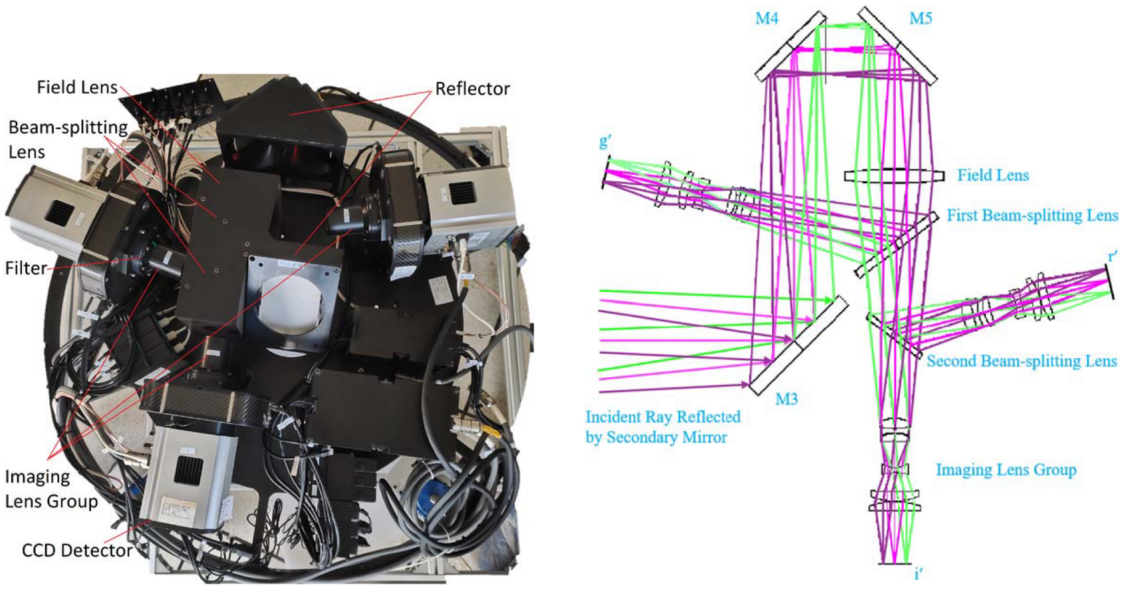

Figure 2.17: Photograph (left) and optical structure (right) of the three-channel CCD photometer (Niu et al., 2022).

During operation, once ECLAIRs detects a GRB, the C-GFT control system will follow the remote commands from the China Science Center (CSC) and point to the corresponding GRB position. It can also remotely change the pointing as needed. After the observation, the real-time data processing system will perform data reduction (bias, dark, and flat field correction), cosmic ray removal, and astrometric calibration, then search potential GRB counterparts in the 3 channel images.

Thanks to its large FOV and multiple bands of simultaneous photometry, C-GFT can quickly (< 1 min) track the GRB with an accuracy of 0.5 arcsec, and deliver alert messages within 5 minutes of receiving triggers. It is expected that C-GFT will observe more than 20% of the ECLAIRs GRBs during the life of the mission (J. Wei et al., 2016).

Colibri is the 1.3-meter robotic telescope jointly developed by French and Mexico (Basa et al., 2022; Fuentes-Fernández et al., 2020) located in San Pedro Mártir, Baja California, Mexico at an altitude of about 2800 meters. The schematic of the telescope and its optical path are displayed in Figure 2.18. Colibri can observe GRBs from visible to infrared, from the first minute to at least one day. It can locate the GRBs with an accuracy better than one arcsec in less than 5 minutes after receiving the alert. The sensitivity of Colibri is ~ 22 in the r-band for a 300 s exposure at 10 σ.

The telescope is equipped with two cameras, DDRAGO and CAGIRE. Those cameras will operate jointly thanks to a dichroic splitting of the beam between visible and NIR light. DDRAGO has two 4k × 4k CCD detectors that provide optical imaging in two channels: a blue one (with g, r, i filters) and a red one (with z, y filters). It has a FOV of 26 × 26 arcmin^2, with a spatial resolution of 0.38 arcsec.

CAGIRE is a 2k $\times$ 2k NIR camera located at the last focus of Colibri (Nouvel de la Flèche et al., 2023) allowing observation in 1.1 and 1.8 μm (with J, H filter). It has a FOV of 21 ×

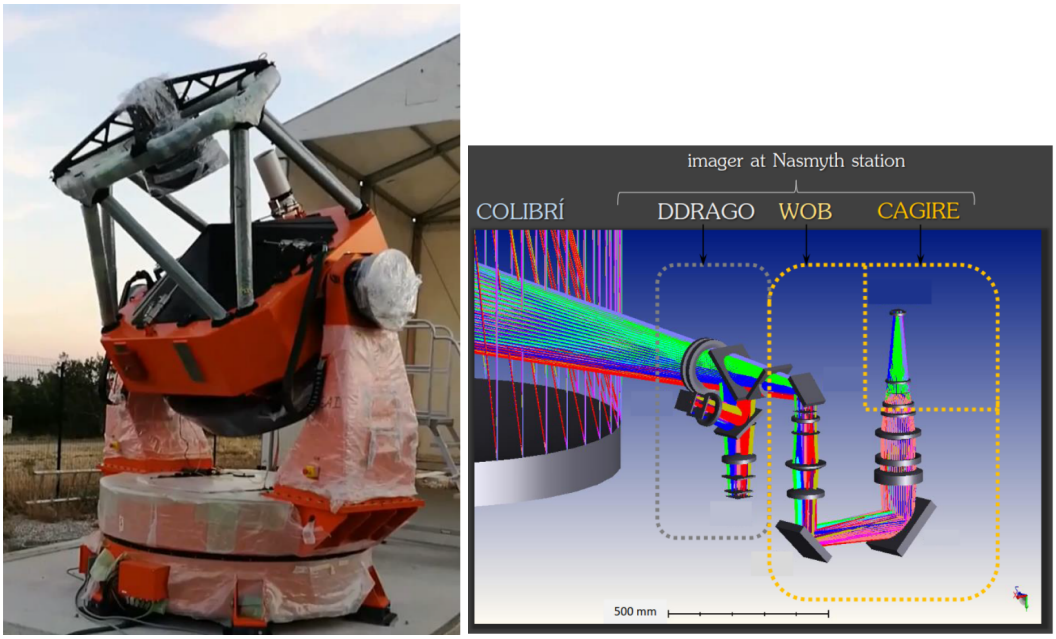

Figure 2.18: F-GFT/Colibri telescope and its optical scheme (Nouvel de la Flèche et al., 2023).

21 arcmin^2. To measure the reshift, two features in the spectrum need to be analyzed: the Lyman-break at 912×(1+z) Å and the Lyman-α at 1216×(1+z) Å. CAGIRE can detect and monitor GRB afterglows up to redshift $\sim$ 11, when the Lyman-break at λ = 912 Å is shifted towards the NIR bands. A combined observations of DDRAGO and CAGIRE will enable a photometric estimation of the wider range redshift of GRBs. The relative accuracy of redshift detection is found to be about 10% for 3.5 < z < 8 and 13-14% for z > 8 (Basa et al., 2022).

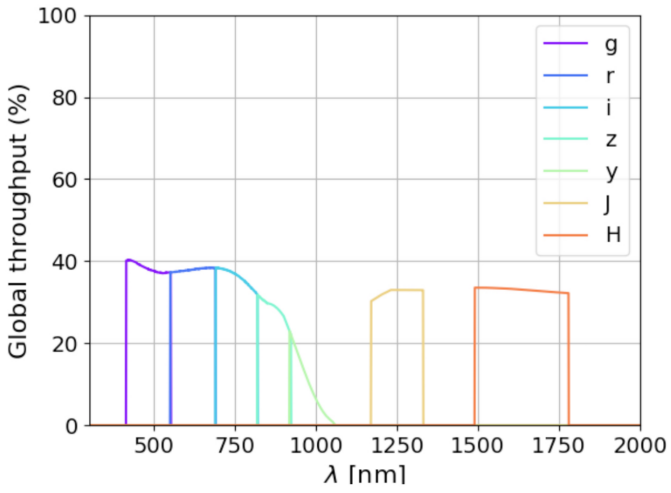

Figure 2.19: Global transmission curves for F-GFT/Colibri in different channels, taking into account the efficiency of all the optical elements and their coatings, and the detector quantum efficiency (Basa et al., 2022).

One notable ability of F-GFT/Colibri is its fast slew capability. It could point to any

source in the sky in less than 20 seconds, which is essential for studies of the first few minutes of the GRB prompt emission, a domain which is still largely unexplored.

2.7 Mission Operation

We have introduced the SVOM science instruments (onboard and ground-based) in the previous sections, here we will explain how those instruments are organized and the mission operations concept.

2.7.1 Satellite orbit and pointing strategy

The SVOM satellite is scheduled for launch in June 2024 with an LM-2C rocket from Xichang, China. It will be placed into a Low Earth Orbit (LEO) at an altitude of 625 km, with an orbital period of 96 minutes.

The satellite's is designed to be compatible with an inclination of 30 deg to the Earth equator. Throughout the majority of the year, the optical axis of the SVOM instrument will maintain an approximate angle of 45 deg off from the anti-solar direction, a pointing strategy named the B1 law.

The B1 law enhances the GRB detection capability of ECLAIRs, as this strategy effectively excludes the Sco-X1 bright source and the Galactic plane sources from ECLAIRs' FOV. Indeed, photons from these sources contribute to the background for the detection of new sources for ECLAIRs. Also, burst detection outside high extinction regions would help to observe the optical afterglows not absorbed by dust in the Galactic plane.

Moreover, this approach also improves the observations carried out from the ground since GRBs will be detected in the night hemisphere, within the observable sky area for major telescopes in Hawaii, Chile, or in the Canary Islands.

However, there are some disadvantages when combining the LEO with the B1 law. First, the SVOM satellite will encounter the South Atlantic Anomaly (SAA) region several times a day, which leads to an overall dead time of 13% to 17% (J. Wei et al., 2016). Then, the Earth appears in every orbit within the FOV of the SVOM instrument. As a result, the effective observing time is further reduced by about 35% for ECLAIRs and 50% for the narrow-FOV instruments MXT and VT.

2.7.2 Observation programs

There are three types of observation programs for SVOM: the Core Program (CP), the General Program (GP), the Target of Opportunity Program (ToO). The percentage of time allocated to these programs is shown in Figure 2.20.

- The Core Program (CP) encompasses all SVOM observational activities related to

high-energy transients detected on board. This includes the observation and characterization of both the prompt and afterglow emissions of GRBs. Given that the expected GRB detection rate by ECLAIRs is approximately 60-70 per year, the Core Program is allocated about 25% of the active mission time.

- The General Program (GP) deals with pre-planned observations. The GP is accessible to all scientists for proposal submission, and selections are made by the Chinese-French Time Allocation Committee (TAC) every six months. The GP considers the limitations set by the Core Program and typically permits observations of sources within 10 deg of the B1 attitude law. In the first three years (nominal mission), approximately 10% of the GP's effective time may be allocated to observe sources outside the B1 constraint, to foster interesting scientific outcomes.

- The Target of Opportunity (ToO) program handles unplanned active sources or transients observations upon request from the ground. All scientists are eligible to apply for ToOs; these applications will be reviewed by the Principal Investigators (PIs). The ToO program is divided into nominal ToOs and exceptional ToOs. Exceptional ToOs, such as counterparts of gravitational waves (GW), may be requested approximately once a month to facilitate rapid follow-up of significant astrophysical events. They will be executed within 12 hours after acceptance by the TAC. Normal ToOs will be executed within 48 hours.

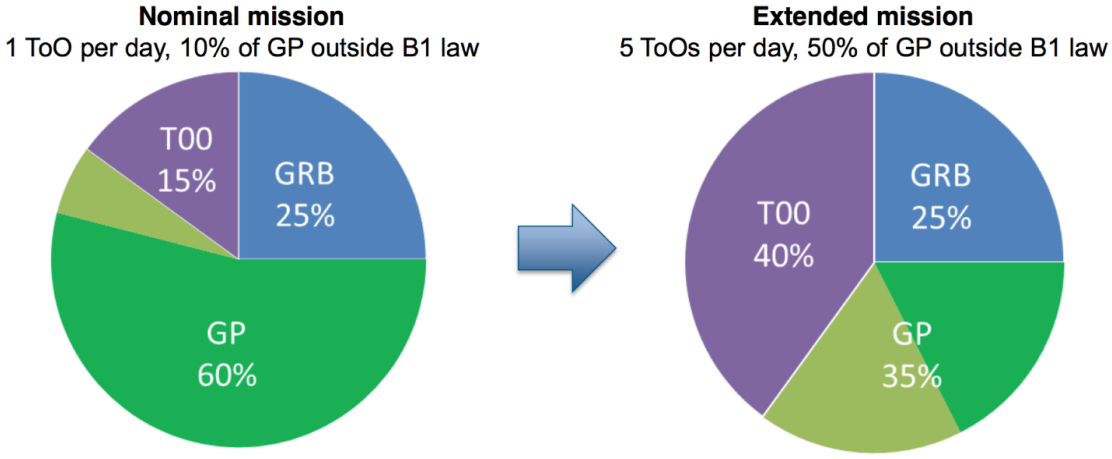

Figure 2.20: Time distribution of SVOM mission programs (Atteia et al., 2022).

Among these observation programs, the order of priority is as follows: exceptional ToO > Core Program > normal ToO > General Program. A higher priority program can interrupt a lower priority program. The original program will be resumed once the higher priority program is completed. For a one-year observation of SVOM, the planned observation durations and the pointings towards different sky regions are shown in Figure 2.21.

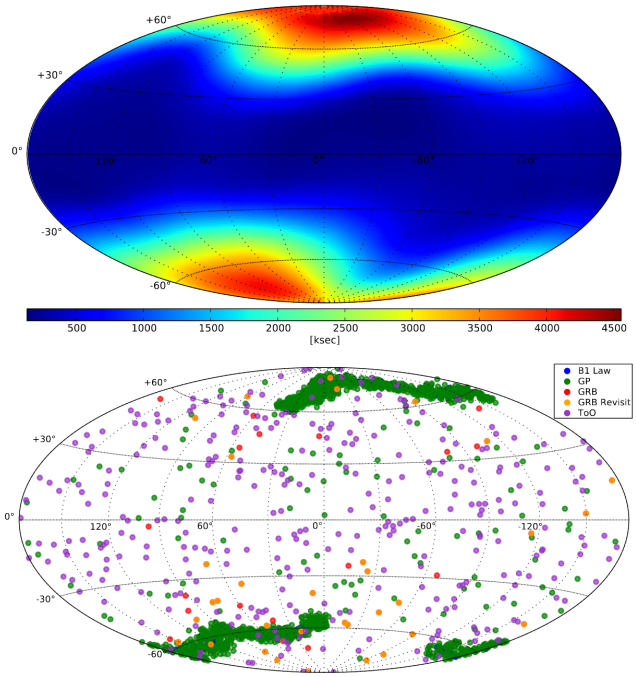

Figure 2.21: Simulation of a one-year observation of SVOM, simulating 65 GRBs and one ToO per day. Top: observation durations of ECLAIRs (kilo-seconds). Bottom: pointings distribution that correspond to targets observed by MXT and VT during each program (J. Wei et al., 2016).

2.7.3 Communication system

The VHF network (Figure 2.22), comprising approximately 50 VHF stations under French responsibility, is deployed worldwide to ensure GRB alerts reception on the ground within 30 seconds for 65% alerts. In addition, the VHF network serves to receive near real-time payload status updates and to facilitate monitoring of current satellite activity.

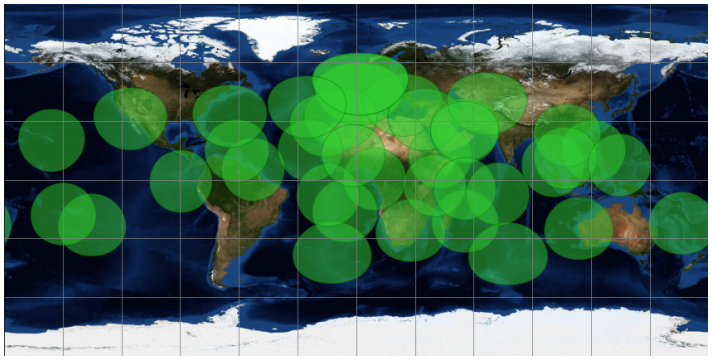

Figure 2.22: VHF station localization. Credit: `https://www.svom.eu/en/reseau-dalerte-en/`.

The S-band system includes two French and three Chinese stations, installed worldwide. Those stations are utilized to send telecommands to the satellite and to receive house-

keeping data. Moreover, it will also be used to upload ToO observation requests (maximum delay being 12 hours).

Additionally, SVOM may also communicate with the satellite through the Beidou system. It could be used to quickly receive alerts messages (with a delay of 1 min) or to send ToO plans (within a delay of less than few hours).

There are X-band stations including those located in Kourou, HBK, and Sanya. They are aimed at transmitting the science raw data from the onboard instruments as well as housekeeping telemetry. The satellite makes six passes over the X-band stations per day, allowing download of ∼18 Gbit of raw data to the stations. The maximum data delay for the X-band in the Core Program is 24 hours.

2.7.4 SVOM system architecture

The SVOM system relies on a scientific instrumentation setup that comprises four instruments onboard the satellite and ground-based telescopes. Rapid communication and data transmission between the satellite and the ground are facilitated by a small VHF emitter onboard along with a dedicated network of ground receivers, including VHF, S-band, and X-band stations. The observation program, pointing, and follow-up requests, as well as data analysis, are coordinated by the science centers, operation center, and instrument centers in both China and France. The whole SVOM system architecture is shown in Figure 2.23.

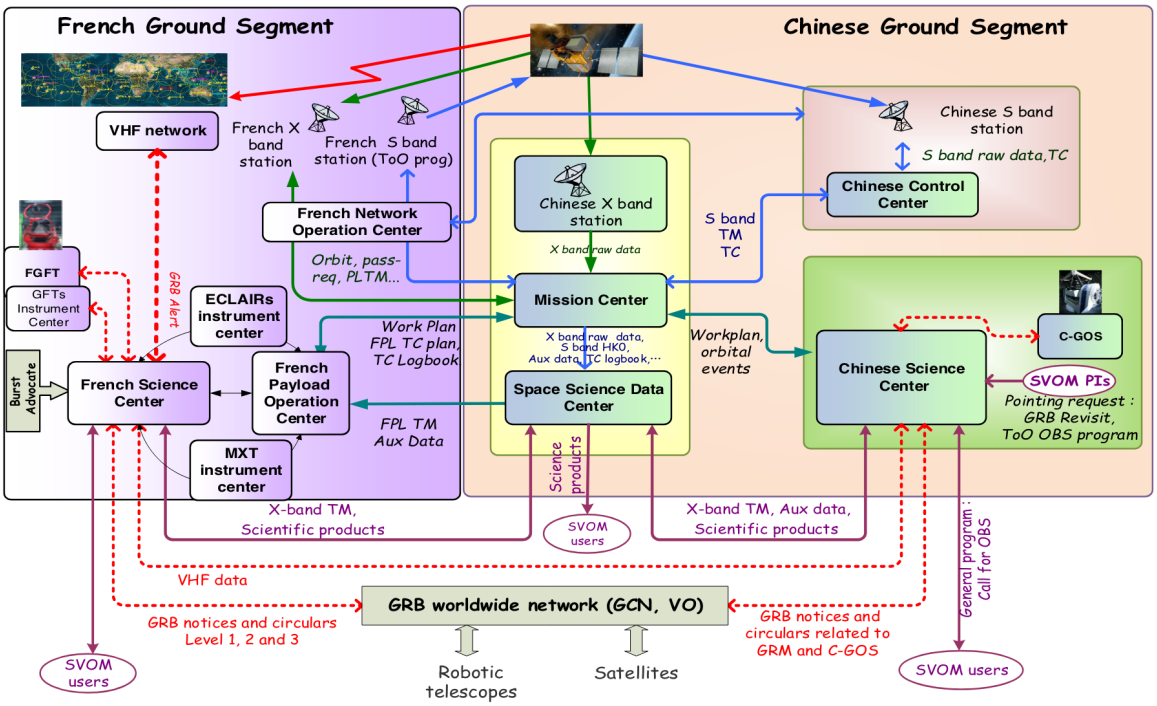

Figure 2.23: SVOM system architecture (Charmeau et al., 2018).

When ECLAIRs or GRM detects a candidate GRB event, The GRB's location and its main characteristics, as determined by ECLAIRs, are quickly transmitted to the ground via

the SVOM satellite's VHF transmitter and the VHF antennas on the ground (or via Beidou). Moreover, the refined positions of the X-ray counterparts identified by MXT are also swiftly downlinked to the VHF station.

This information is received by the French Science Center (FSC) and is automatically distributed to Burst Advocates (BAs) in France and China. The alerts information also distributed automatically to the ground-based telescopes and to the GCN and VOE systems.

The BAs have to ensure that the VHF scientific products are well processed by the FSC, and ensure the diffusion of the notices and circulars to the scientific community. They can send the high-energy circular and can request additional follow-up observations. The onboard instruments' raw data (including MXT and VT) are later downloaded through the X-band stations.

Chapter 3

The ECLAIRs telescope

Contents

3.1 Overview

3.1.1 Main components and characteristic parameters

ECLAIRs is the hard X-ray imager onboard SVOM designed to monitor and quickly localize the GRBs and other high-energy transients in an error of a dozen arcmin. It is developed by a consortium of French research organizations (CNES, CNRS, CEA).

ECLAIRs is mainly composed of a coded mask, a detection plane, an electronic readout system ("Electronique de Lecture Secteur", ELS), and a scientific trigger and control unit ("Unité de Gestion et de Traitement Scientifique", UGTS). Additionally, the instrument is also equipped with a thermal control system (cold plane and radiator), and a structured shell ensuring geometrical rigidity, shielding of X-ray photons from outside the FoV and optical opacity. The model and exploded view of the ECLAIRs is shown in Figure 3.1.

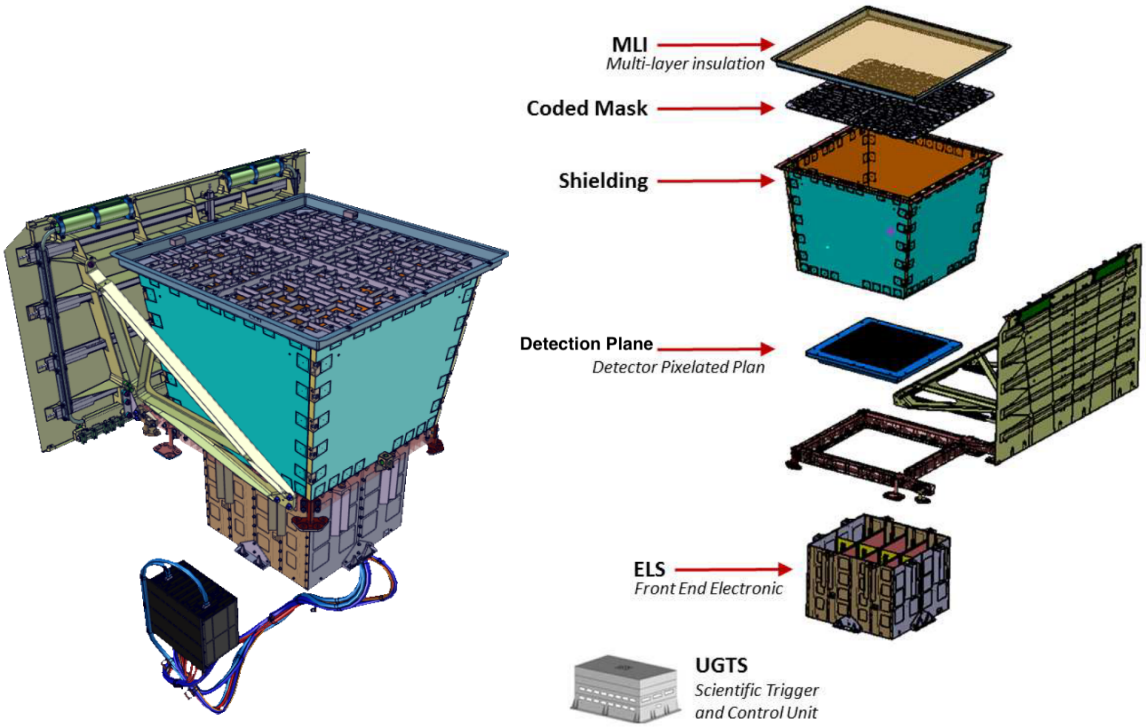

Figure 3.1: The ECLAIRs telescope. Credit: ECLAIRs instrument team.

The functions of the ECLAIRs subsystem are described below

- The detection plane and ELS are responsible for detecting incoming photons and measuring their energy, arrival time and position. They also preprocess the data before sending it to the ECLAIRs' on-board computer (Section 3.2).
- The coded mask is responsible for modulating the photon distribution on the detection plane. Due to the distribution of opaque and transparent elements (mask pattern), X-ray sources in the sky will project corresponding patterns on the detection

plane (shadowgram). By performing the deconvolution algorithm on the shadowgram, the sky image can be reconstructed (Section 3.3).

- The UGTS is responsible for detecting and localizing GRBs by applying trigger and deconvolution algorithms to the data sent by the ELS. It also oversees the operation of ECLAIRs, ensuring that the detection planes and ELSs are functioning properly (Section3.4).

The detection area of ECLAIRs is approximately 1000 cm^2, with an energy range spanning 4–150 keV, and a wide field of view of $89° \times 89°$ (2 sr, partially coded). The instrument characteristic parameters are shown in Table 3.1. ECLAIRs

Table 3.1: ECLAIRs instrument specifications.

Parameter	**Specification**
Energy range	4–150 keV
Detectors	6400 CdTe detectors
Detecting area	$\sim$1000 cm^2
Effective area in 10–70 keV	$\geq$340 cm^2
Effective area @ 6 keV	$\geq$200 cm^2
Field of view (half-coded/total)	0.9 sr / 2.06 sr
Sensitivity to 1 sec long GRB	2.5×10^{-8} erg cm^{-2} s^{-1} in [5–50] keV
Source Localization Error	12 arcmin
Energy resolution at 60 keV	$<$ 1.6 keV
Dead time	$<$5% for 10^5 cts/s
Expected GRB rate	$\approx$ 65 $year^{-1}$

3.1.2 Large field-of-view

The geometry of the ECLAIRs telescope is shown in Figure 3.2. The coded mask of ECLAIRs has a size of 54 × 54 cm^2 and is located 46 cm above the detection plane with a geometry of 36 x 36 cm^2. Based on this structural configuration, within a total FOV of 2 sr (89 × 89 deg^2), two different regions can be distinguished.

The first is the Fully Coded FOV (FCFOV). It corresponds to the central portion of the FOV and has a size of 0.15 sr or approximately 22 × 22 deg^2. Point sources located in this region will see a partial mask projected onto the entire detector surface.

The second region is the Partially Coded FOV (PCFOV), which is the FOV outside the FCFOV and inside the Zero Response FOV (ZRFOV), where the source will illuminate only a portion of the detector plane. Therefore, ECLAIRs telescopes are more sensitive in the FCFOV than in the PCFOV.

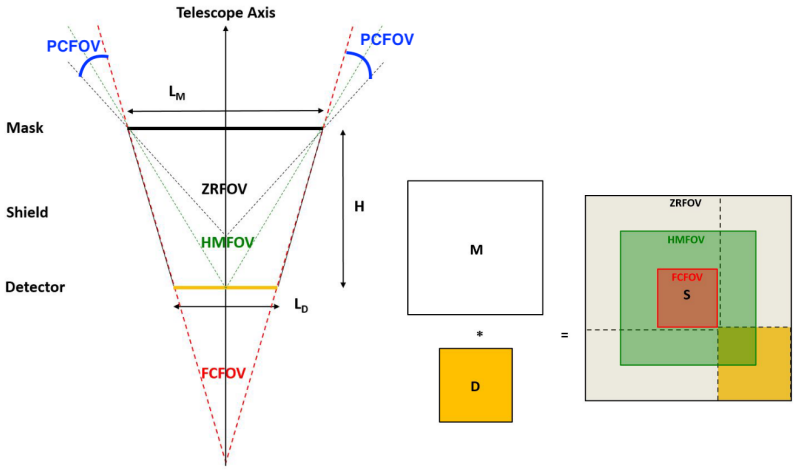

Figure 3.2: Geometry of a coded mask telescope with a mask larger than the detector and a shield attached to the detector. The FOV around the telescope axis is shown in the figure: Fully Coded FOV (FCFOV, red), Partially Coded FOV (PCFOV, blue), Half Modulated FOV (HMFOV, green), and Zero Response FOV (ZRFOV, black) (Goldwurm et al., 2023).

3.1.3 Detection band down to 4 keV

Coded-mask telescopes are efficient in surveying large fields of hard X-ray sky, as demonstrated by current instruments such as INTEGRAL/ISGRI and Swift/BAT. Although the detection areas of ECLAIRs are about a factor of 2 smaller than INTEGRAL/IBIS and about a factor of 4 smaller than Swift/BAT, ECLAIRs have a remarkable feature of low energy thresholds, down to about 4 keV. A comparison of the sensitivity of ECLAIRs with these instruments is shown in Figure 3.3.

The unique combination of a coded mask and a sensitive detection plane starting at 4 keV allows the ECLAIRs telescopes to achieve competitive sensitivities even with modest volume and mass constraints. Thanks to the low energy threshold of 4 keV, SVOM has the potential to unravel the mysteries of extragalactic soft X-ray transients, such as X-ray flashes, especially high-redshift GRBs, and supernova shock breakout bursts, which are relatively little explored areas.

Reaching the 4 keV threshold is a major technical challenge for detectors, readout electronics, masks, and trigger software. For masks, hole transparency is critical at these energies. At the detection plane, it is critical to deal with unexpected noise and efficiency inhomogeneities in the 4–8 keV band (as described in Chapters 4 and 5). In addition, the trigger software must efficiently manage the large number of non-GRB transient sources, the X-ray background, and low-energy detector noise (Chapter 5).

3.1.4 General detection process for ECLAIRs

For ECLAIRs to detect GRBs, the following factors affecting detection need to be considered. From far to near and based on the process of detection described below.

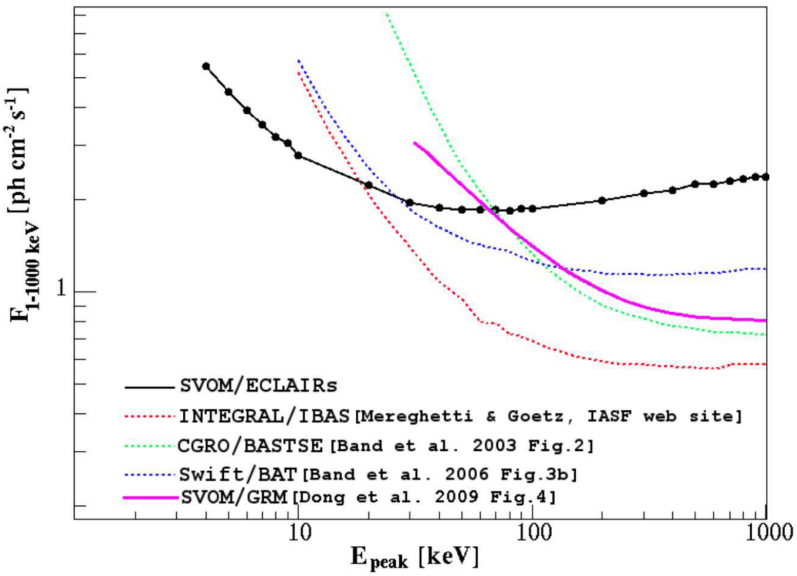

Figure 3.3: Simulated ECLAIRs sensitivity for GRB trigger as a function of the peak energy, and compared to other instruments. Assuming that the GRB is characterized as a Band function with α=-1 and β=-3. Here the detection band of ECLAIRs is 4–50 keV (O. Godet et al., 2014).

1. First the GRB has to occur within the FOV of the ECLAIRs. If it occurs outside the FOV of the ECLAIRs, it will not be detected. If the GRB occurs off-axis (within part of the FOV), the count rate decreases with increasing off-axis angle.

2. Secondly the GRB must appear not behind the Earth and the satellite has to be located outside the South Atlantic Anomaly (SAA) region. Since ECLAIRs will be off inside the SAA region.

3. The coded mask above the detector blocks a portion of the incident photons (about 40%).

4. The efficiency of the detector pixels and the energy response of the detector plane will have an impact on events count detection.

5. The X-ray background, which is dominated by CXB, needs to be subtracted from the onboard data analysis.

6. A deconvolution algorithm is used to reconstruct the sky image. The contribution of known X-ray sources then needs to be excluded from the reconstructed image.

7. Decide whether to request a follow-up observation based on the signal-to-noise ratio of the obtained GRB candidate sources.

3.2 Detection plane and sector readout electronics

The ECLAIRs detector plane is equipped with 6400 low-leakage-current Schottky cadmium telluride (CdTe) detectors, providing a detection area of $\sim$ 1000cm^2. These detectors are mounted on 200 modules, each containing 32 CdTe detectors, referred to as XRDPIX. Those XRDPIX modules are hybridized with the low-noise and low-consumption ASIC IDef-X from CEA (Gevin et al., 2009).

These 200 XRDPIX modules are mechanically fixed to a rigid cold plate structure, ensuring both their mechanical uniformity and cooling to approximately -20℃. The detection plane is electrically divided into 8 independent sectors, as shown in Figure 3.4, each comprising 5x5 XRDPIX modules, with dedicated sector readout electronics (ELS).

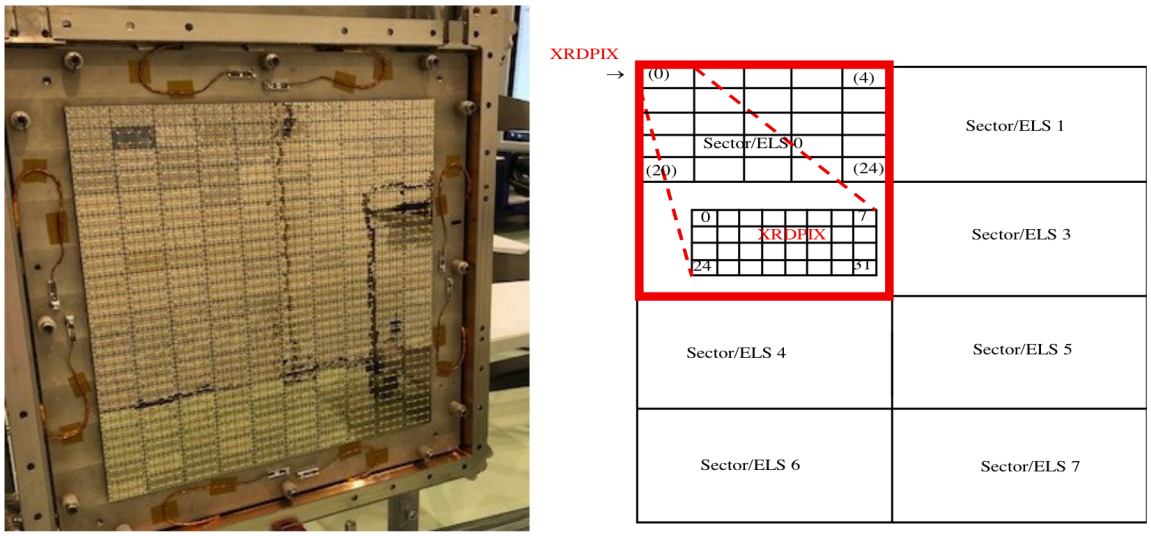

Figure 3.4: Physical and structural schematics of the ECLAIRs detection plane. Individual XRDPIX module with 32 CdTe pixels in an 8×4 arrangement. Image credit: ECLAIRs instrumentation team.

The total detecting area of ECLAIRs detection plane is around 1000 cm^2, while effective area not only depends on the size of the detection plane but also depends on both the CdTe detection efficiency and mask and multi-layer insulation (MLI) absorption in different photon energies. In the Geant4 Monte Carlo simulation, after considering the efficiency of detectors and the absorption of mask and MLI, the effective area is greater than 340 cm^2 in 10–70 keV, as shown in the Figure 3.5. The spectrum response of the ECLAIRs detection plane is depicted in the same figure.

3.2.1 CdTe pixels

There are three photon-matter interaction effects that play an important role in radiation detection, they are photoelectric effect, Compton scattering and pair production effect. The photoelectric effect is where the electron of an atom absorbs all the photon energy and escapes the atom with kinetic energy. Compton scattering is the photon transfers only part

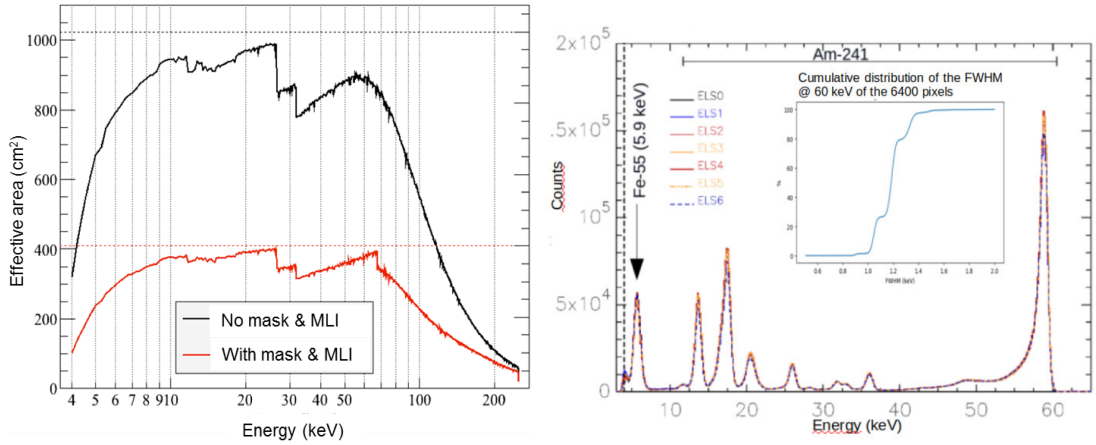

Figure 3.5: Left: effective area of ECLAIRs simulated by Geant4, the black line indicates the effective area of the detection plane only, and the red line indicates the effective area taking into account the mask-MLI absorption. Right: spectral response in the energy range of the ECLAIRs. Each sector is constructed from energy-calibrated ^{55}Fe+^{241}Am spectra (by stacking 800 individual spectra). Credit: ECLAIRs Instrumentation Team, Sizun (2011).

of its energy to the outer electrons, producing a hotter electron and an attenuated photon. The pair production effect occurs only when a photon with an energy higher than 1.02 MeV interacts within the Coulomb field of the nucleus and produces a new pair of electrons and positrons. In the energy range less than 200 keV, the photoelectric effect dominates among these three interactions, as show in Figure 3.6.

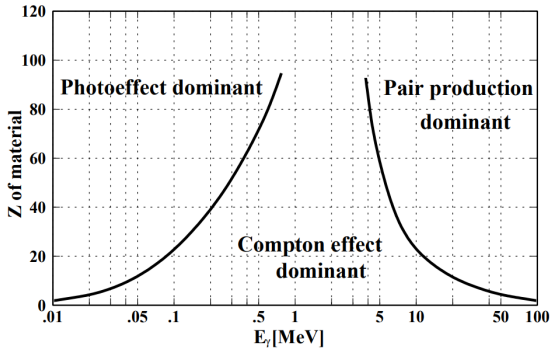

Figure 3.6: Cross-section for photon-matter interaction. Dominant region according to atomic number (Z) of material and photon energy. CdTe has a average Z value of 50.

CdTe has been considered a promising material for hard X-ray semiconductor detectors since the 1970s due to its high resistivity and large linear attenuation coefficient at room temperature. For the detection plane of ECLAIRs, the Schottky-type CdTe detectors were selected for their excellent spectral properties and good quantum efficiency between 4 and 150 keV. These ECLAIRs CdTe pixels were made in two different periods by the Acrorad Co., Ltd (Funaki et al., 2007). Two different batches of pixels were respectively received in 2008 (>12000 detectors) and 2016 (2000 detectors), respectively. After a series of performance tests (Remoué et al., 2010), 6400 of the selected CdTe pixels are mounted in the detection plane.

Each CdTe pixel in the modular design has a thickness of 1 mm and a size of 4x4 mm^2, placed on a grid with a pitch of 4.5 mm. The effective area for each pixel is around 0.147 cm^2 (Carine et al., 2011). The cathode is made of platinum (Pt) and the anode is made of indium (In). The CdTe pixels were designed to be illuminated from the cathode side (Pt contacts), as shown in Figure 3.7.

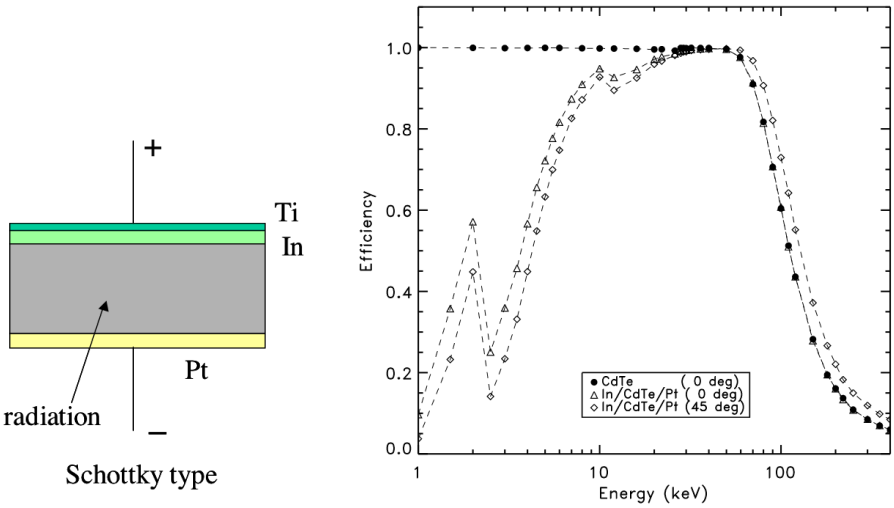

Figure 3.7: Left: schematic diagram of CdTe detector (Funaki et al., 2007). Right: simulated absorption efficiency of the In/CdTe/Pt detector. The simulation considers the absorption of the Pt layer (250 nm thickness), compared to bare CdTe, and compared with the beam injected at a 45 deg angle (Remoué et al., 2010).

A CdTe detector detects X-ray photons by the photoelectric effect, the X-ray photon transfers all its energy to an inner-shell electron of a Cd or Te atom, ejecting the electron from its orbit. Which then generates many pairs of electric charges - electrons and positively charged ”holes”.

In this process, the X-ray photons transfer all their energy to the inner-shell electrons of a cadmium or tellurium atom, causing the electrons to escape their bound orbits. Pairs of charges are then generated, including negatively charged electrons and positively charged ”holes.” An electric field inside the CdTe crystal separates these charges and moves them toward different electrodes. These charges are collected as small electrical impulsions, which are then amplified and converted into voltage signals. The voltage signal is finally analyzed to extract information about the X-rays, such as energy.

Before arriving at the CdTe crystal, some X-ray photons may be absorbed by the Pt layer. The thickness of the Pt layer for the CdTe pixels is around 200–300 nm. The photon absorption caused by a 250 nm Pt layer is shown in Figure 3.7. The absorption of X-ray photons by the Pt layer is mainly at energies below 8 keV.

3.2.2 XRDPIX module

The CdTe pixels are organized on the detector module (called "XRDPIX") in a 4x8 array. The XRDPIX module is an innovative hybrid combining two elements: the detector ceramic and the ASIC ceramic (Lacombe et al., 2018). The detector ceramic houses 32 Schottky CdTe detectors with a bias range of 0 to -450 V, thanks to a conductive grid of 8 metal circular pads glued to the detectors. The ASIC ceramic consists of one high-temperature co-fired ceramic (HTCC) as a substrate material supporting a low-noise, 32-channel ASIC chip in a sealed cavity. Two metal rods mechanically secure each XRDPIX module to the cold plate.

The exploded view of the XRDPIX module (Figure 3.8) shows the different components: the CdTe detector, the grid, the HTCC (ASIC) and thick-film ceramics, the cavity closed by the cover and the threaded shaft.

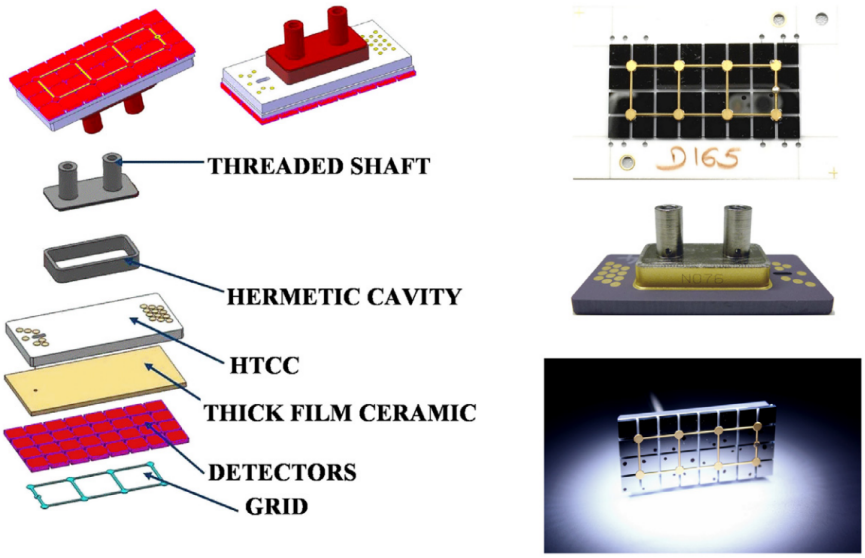

Figure 3.8: Left: Exploded view of the XRDPIX module. Right: Picture of "Detectors Ceramics" (top), picture of "ASIC Ceramics" (middle) and picture of flight model XRDPIX (bottom). Credit: Lacombe et al. (2018).

The charges generated by the CdTe detector through the photoelectric effect are collected on the anode, measured by the ASIC chip of the corresponding module. The charge is converted to a voltage by a charge preamplifier (PAC) inside the ASIC. Then this voltage is processed by the chip's filtering and shaping circuitry to facilitate the measurement of its peak value.

Then the voltage amplitude is compared to a threshold value: if the voltage generated by the collected charge exceeds this value, a signal trigger is activated. The trigger signal freezes the ASIC module during a freeze time of approximately 6.8 μs, so that the charge has time to be collected completely without any interference.

3.2.3 Readout sector electronics

ECLAIRs has 8 ELSs, each responsible for the operation of 25 XRDPIX modules. The 8 sectors work almost independently, as do their corresponding electronics. Each sector performs the following tasks:

- Managing 25 XRDPIX detection modules, including adjusting ASIC parameter configurations, supplying high and low voltages.
- Collect information of the detected photon events (position, energy, trigger data, multiplicity etc.).
- Pre-process photon events and send them to the science processing and control module (UGTS).

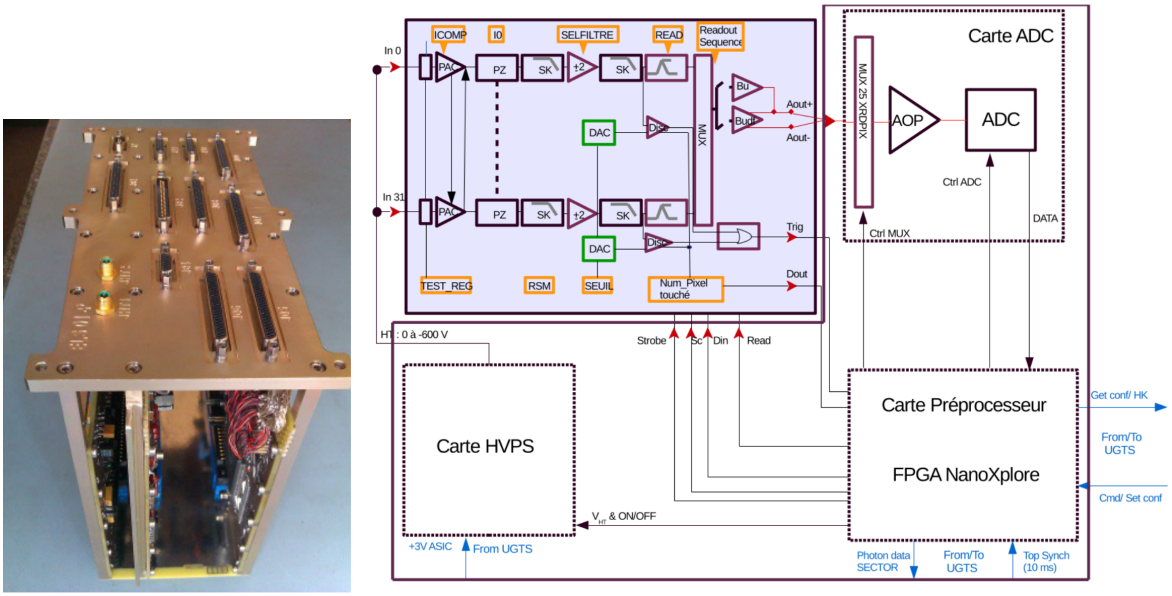

Figure 3.9: Left: picture of a readout sector electronics (ELS) module. Right: circuit diagram of the electronics sector, including the XRDPIX-ASIC (shaded in blue) and the ELS electronics with LV/HVPS, ADC, and preprocessor cards (Bajat, 2018).

In order to implement the above tasks, each sector module contains 3 electronic boards: Low-voltage / High-Voltage Power Supply (LV/HV PS) board, Analogic-Digital Convertor (ADC) board, and pre-processing board, as shown in Figure 3.9.

The analog voltage signals acquired at the XRDPIX-ASIC are read (A+ output, A- output) by the ADC board and digitized to encode the energy of the registered event. Then the pre-processing board collects the photon events information from ADC and XRDPIX-ASIC, and sends a coded frame containing information about the detected event to the UGTS.

3.3 Coded-mask and reconstruction of sky image

A coded mask is a screen consisting of opaque and transparent elements, usually of the same shape and size, arranged in a specific regular pattern (mask pattern). In a coded mask telescope, the coded mask is located in front of a position-sensitive detector. Photons emitted from celestial sources are encoded by a mask, which projects a unique pattern, called a "shadowgram", on the detection plane. By "decoding" the shadowgram through certain mathematical methods with the mask pattern , one can reconstruct the hard X-ray sky image, realizing the positioning capability.

3.3.1 ECLAIRs' coded-mask

ECLAIR's coded mask, designed by APC and CEA and manufactured by APC, consists primarily of a 0.6 mm tantalum foil inserted between two rigid titanium structures. The mask is self-supporting and its design ensures the efficiency of low-energy (X-ray) photon transmission.

Due to the imperative for the mask to withstand the mechanical vibrations experienced during the launch, a stringent requirement for its rigidity is essential. Consequently, two supplementary titanium masks sandwich the tantalum, as depicted in Figure 3.10. The upper mask, referred to as "Ti-Top," incorporates 10 mm ridges and a 16 mm cross, whereas the lower mask, labeled "Ti-Bottom," is thinner at 1 mm thickness, yet maintains the 16 mm cross configuration.

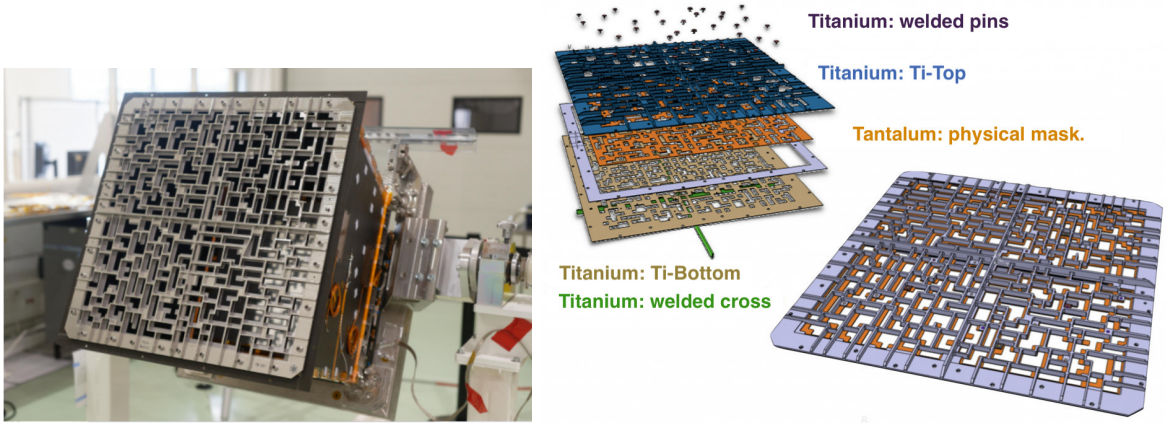

Figure 3.10: Left: coded mask and shield of the ECLAIRs during assembly and testing. Right: representation of the elements that make up the ECLAIRs coding mask. Source: APC, CEA.

To mitigate the vignetting effect caused by off-axis light sources, the apertures in the titanium foils are widened. Additionally, for enhanced structural integrity, titanium pins are welded between the Ti-Top and Ti-Bottom masks. These pins serve to reinforce the assembly, and tantalum pads are affixed to the pins ensure X-ray opacity.

The coded mask of ECLAIRs has a size of 54×54 cm^2, with a 40% open fraction located 46 cm above the detection plane. This configuration, mask pattern and the the detection

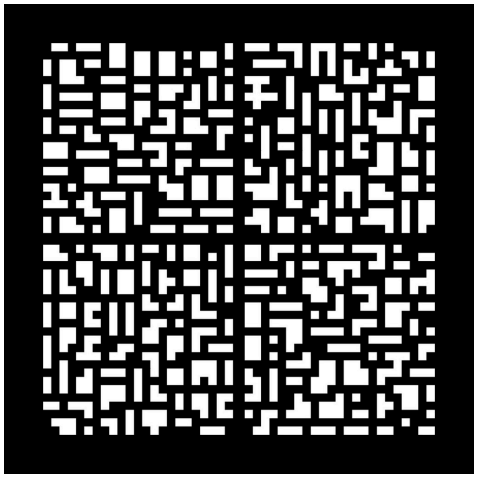

Figure 3.11: The mask pattern selected for ECLAIRs, which includes a 46×46 grid of holes and opaque elements. Credit APC, CEA.

plane determines a FoV of 2 sr (ZRFoV) and a point spread function of 52 arcmin (FWHM).

The mask parameters (aperture, element size) result from simulations carried out at CEA and APC. The 40% aperture fraction is optimized to improve the detection of short GRB by compromising the number of photons received from these sources and the background noise while retaining a low loss for long bursts.

The size ratio between the elements of the mask and the detector pixels is 2.53, offering optimum sensitivity at the cost of a poorer localization than theoretically achievable (Skinner, 2008). With this mask configuration, 90% of the bursts will be localized with an error of less than 12 arcmin. This location remains compatible with the FOV sizes of the MXT and VT instruments, which will provide a more precise position.

The size of the mask pixels is different from the size of the detector pixels, so the mask matrix must be interpolated to obtain pixels equal to the size of the mask and the detector to compute the deconvolution. The interpolated mask has the same aperture as the physical mask and contains 120 x 120 pixels (each pixel is equal in size to the detector grid step of 4.5 mm) with pixel values between 0 and 1 (Nicolas Dagoneau, 2020).

3.3.2 Shadowgram deconvolution and sky image reconstruction

The principle of deconvolution was described in Goldwurm, A. et al. (2003) and (Goldwurm et al., 2023), and is mathematically translated into Equation 3.1 for the ECLAIRs telescope. The equation can estimate the number of counts received from each sky pixel, and finally reconstruct the sky image (200x200 pixels).

$$C_{cnt}(i,j) = \left(\frac{G^{+} * (\tilde{D} \times W)}{A} - \frac{B \times [G^{-} * (\tilde{D} \times W)]}{A} \right)(i,j) \tag{3.1}$$

The first term corresponds to the contribution of the sources and the background noise under the transparent elements of the mask seen from the position (i, j) of the sky. The second term corresponds to the contribution of the background noise under the opaque elements of the mask for the same position. In the equations, the operator "$*$" denotes the convolution between two quantities, while the operator "$\times$" denotes the term-by-term product of two matrices.

The matrix D corresponds to the image recorded by the detector (without background correction), with dimensions 80 x 80, $\tilde{D}$ stands for the detector image corrected for non-uniformity defects and non-flat background noise (see section 3.3).

W is a matrix for adjusting the efficiency associated with each detector pixel. For example, the dead or noisy pixels could be ignored by setting their efficiency to 0 (detail in Section 3.4.5).

Matrices G^+ and G^- are decoding matrices constructed from the mask matrix M and the mean opening fraction of mask (a=40% for ECLAIRs). M is a 120 x 120 array filled with integers, with 0 for the opaque element and 1 for the transparent elements (linearly interpolated from a 46 × 46 array to have the same physical size as the detector pixel). $G^+ = M/a - 1$ for transparent elements and 0 elsewhere; $G^- = M/a - 1$ for opaque elements and 0 elsewhere.

The matrix B ensures a flat image if the noise is flat, with zero mean in the absence of sources. The matrix A is a normalization of counts to obtain a correct flux of sources located at the centers of sky pixels.

The variance of each sky pixel is given by Equation 3.2.

$$C_{\text{var}}(i,j) = \left(\left[\frac{G^{+2} * (\tilde{V_D} \times W^2)}{A^2} \right] - \frac{B^2 \times \left[G^{-2} * (\tilde{V_D} \times W^2) \right]}{A^2} \right) (i,j) \tag{3.2}$$

Where $\tilde{V_D}$ is the variance of the corrected detector image. By assuming that the number of counts on each pixel in the detection plane follows a Poisson distribution, $\tilde{V_D}$ can be assumed to be equal to that of the detector image, and thus $\tilde{V_D} \approx D$.

The signal-to-noise ratio (SNR) of the sky image can be calculated by the counts and variances obtained above using Equation 3.3.

$$SNR_{im}(i,j) = \frac{C_{cnt}(i,j)}{\sqrt{C_{var}(i,j)}} \tag{3.3}$$

The deconvolution process is implemented using Fourier transforms (via an FFT library) in the ECLAIRs UGTS. It takes around 1 second, independent of the count rate on the detector. The calculated sky SNR will be used in the triggering algorithms to search for transientS. This part is detailed in the next section.

3.4 Scientific Processing and Control Module (UGTS) and trigger algorithm

3.4.1 UGTS hardware

One important hardware module in ECLAIRs is the science processing and control module (UGTS, Figure 3.12). This module is mainly used to control various parameters of ECLAIRs, to perform real-time data processing and trigger functions onboard. The trigger function is capable of detecting and localizing GRBs, requesting satellite reorientation for follow-up observations by MXT and VT, and sending alert signals to ground-based follow-up instruments and burst advocates (Le Provost et al., 2013, Stéphane Schanne, Le Provost, et al., 2013).

The UGTS consists of 10 electronic boards that perform different functions. Four of these boards are used for detection plane power control. Two boards are used for the UGTS power supply. Two UGTS I/O boards with FPGAs are used for ELS management. Two CPU boards are used for data acquisition and trigger functions. The CPU boards each consist of an FPGA board for pre-processing trigger software data and a Leon3 Dual Core CPU board for running the complete ECLAIRs flight software, including triggers.

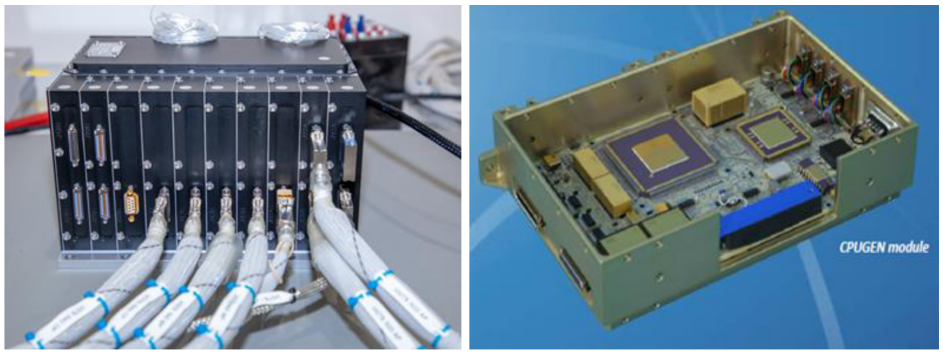

Figure 3.12: UGTS qualification model (Left) and view of the UGTS CPU card (Right), Credit: CEA/CNES.

3.4.2 Onboard trigger algorithm

The onboard trigger software aims to search and localize for high-energy transients, such as GRBs and outbursts from known X-ray sources (S. Schanne et al., 2019). If a new transient source is detected and the SNR exceeds a predefined threshold, the software will request the repositioning of the spacecraft for follow-up observations and alert the community in near real-time.

The duration of GRBs varies from very short (milliseconds) to very long (thousands of seconds), the lightcurves can be smooth or spike-like. To detect GRBs with various lightcurve shapes, the triggering software is divided into two different algorithms: Count-

Rate Trigger (CRT) and Image Trigger (IMT). Both trigger algorithms are simultaneously executed on the UGTS hardware.

3.4.3 Count-rate trigger

The Count-Rate Trigger (CRT) determines whether a new transient source has been detected by monitoring the change in the number of counts detected in the detector plane from 10 ms to 20.48 seconds. The CRT algorithm operates with a cycle time of 2.5 seconds, and its logic is as follows (Figure 3.13):

1. The detector counts are divided into four configurable energy intervals to increase sensitivity in detecting GRBs with different hardness ratios (e.g., 4–8, 8–50, 4–120 keV, and 50–120 keV) and nine detection regions (including the entire area, four semi-regions, and four corners) to detect GRBs seen by ECLAIRs away from its optical axis.

2. Counts are extracted for different reference time intervals ranging from 10 ms to 20 s.

3. The significance of the count-rate increase (count-significance) is calculated by predicting the background (B) and the true counts (C) using the following formula:

$$significance = \frac{C - B}{\sqrt{B}} \tag{3.4}$$

   The predicted background (B) is obtained by fitting the data from the previous duration ($\sim$ 1 minute) using a quadratic function.

4. If the significance value exceeds the predefined threshold for a given time interval, energy interval, and detection region, a corresponding shadowgram is constructed using counts stored in the memory.

5. Deconvolution is performed on the selected shadowgram (full plane) to reconstruct the sky SNR maps (deconvolution process is described in section 3.3.2). If a SNR exceeds the predefined dynamic trigger threshold: SNR ~ 6.5 σ_{SNR}, the position of that sky pixel is determined. Here the σ_{SNR} stand for the standard deviation of the SNR sky map.

6. If this position does not correspond to a known celestial source (such as Sco-X1 or Crab) and is not occulted by the Earth, the count rate trigger algorithm considers it as the detection of a new transient source and it produces an alert.

7. If this sky SNR value exceeds another higher threshold (~ 8 σ_{SNR}), ECLAIRs will request that the SVOM satellite be reoriented to allow for follow-up observations by the narrow-field telescopes (MXT, VT) on the platform.

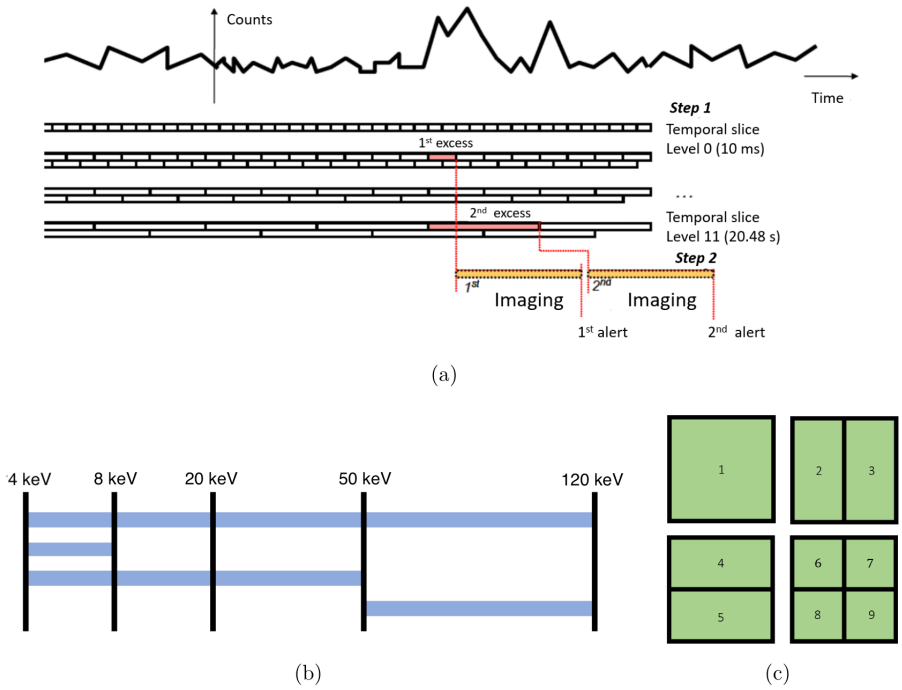

Figure 3.13: The diagram of the count-trigger algorithm. (a) The time scale of count accumulation. (b) Definition 4 energy bands (blue bar) using 5 specified energy boundaries. (c) Segmentation of the detector zones. Source: Nicolas Dagoneau (2020),Arcier (2022)

.

3.4.4 Image trigger

The Image Trigger (IMT) continuously stacks the sky image and searches for transients in the sky image from 20.48 seconds to 20 minutes. This trigger algorithm is suitable for detecting long transients. The IMT mode is designed to detect both weak and long GRBs and operates with the following logic:

1. In each of the four energy intervals, a detection count image (shadowgram) is generated every 20.48 seconds. The background of the shadowgram is subtracted by conventional fitting or or wavelet methods (Dagoneau et al., 2022). Then, the processed shadow maps are deconvoluted to obtain the SNR sky image.

2. The following image is stacked on the previous image. The process of stacking the images starts at 20.48 s and continues by multiplying by powers of 2 until nearby 20 min.

3. If a pixel point in the stacked image exceeds a predefined threshold (6.5 σ_{SNR}), the position of this pixel is identified.

4. If this sky pixel position does not coincide with the location of a known celestial source, such as Sco-X1 or a crab, and is not obscured by the Earth, the image-triggering algorithm treats it as a detection of a new transient candidate and sends an alert signal

(N. Dagoneau et al., 2021). Alternatively, if this position coincides with the location of a known celestial source and its SNR value exceeds a specially set threshold, it will be considered a new outburst of that known celestial source.

5. The SNR of that sky pixel in the stacked image may increase as the observation time is extended. If the SNR value exceeds the threshold (~ 8 σ_{SNR}), the ECLAIRs will send a message to the SVOM satellite requesting reorientation for subsequent observations.

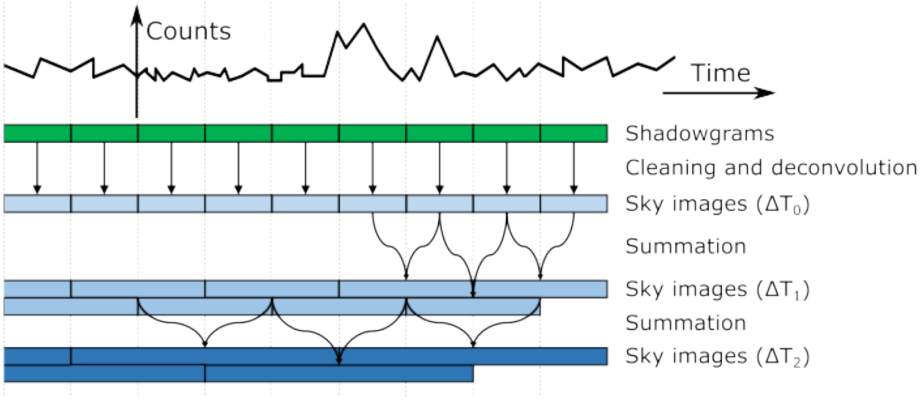

Figure 3.14: A diagrammatic overview of the image trigger algorithm. The green block corresponds to the detection plane count of 20.48 seconds. The blue block corresponds to the sky image and the deeper blue block represents the stacked sky image. Credit: Dagoneau et al. (2022)

3.4.5 Configuration parameters for trigger algorithm

The different steps of the CRT and IMT can be deeply configured with many parameters. Here we introduce the parameters related to the count-shadowgram preprocessing and the following deconvolution to build the sky images.

To adjust the contribution of each pixel in the trigger algorithm, three parameters per energy band are used in the onboard trigger software. They are the efficiency value, weight value, and efficiency limit.

- The efficiency value is the efficiency of the pixel. The detected count will be corrected for this efficiency value.
- The weight value is the pixel weight in the background subtraction and deconvolution process.
- The efficiency limit is a scalar value that is the criterion for deciding whether the pixel is used. When the efficiency of a pixel is below this value, this pixel is ignored in the trigger process.

From the efficiency value and weight value, two tables are built: the efficiency tables, and the weight tables (one of each per energy band). Each of these two tables can be selected by configuration for use in the following operations: for the pixel efficiency correction, for the pixel contribution for the background fit, and for the pixel contribution for the deconvolution (per energy band). Typically, the efficiency table is used for the pixel efficiency correction prior to the deconvolution. The contribution of each pixel for the background fit (IMT only) and the deconvolution is tuned by the weight table.

The efficiency correction is performed by dividing the detected counts by the efficiency to obtain the corrected shadowgram in counts and by the square of the efficiency to obtain the variance of the shadowgram. If the efficiency is 0, both counts and variances are set to 0. The count and the variance corrections can be activated or deactivated separately in the configuration. If the variance normalization is deactivated, the shadowgram in counts (possibly corrected by the efficiency) is also used as the variance. The way to set the pixel contribution for the deconvolution is presented in Goldwurm, A. et al. (2003).

The onboard software updates the initial values for the two tables. It sets the values to 0 for which the initial efficiency values are lower than or equal to the efficiency limits. As an example, with these configuration parameters (but with smaller matrices),

$$\text{efficiency configuration} = \begin{bmatrix} 1 & 0.2 \\ 0.5 & 0.9 \end{bmatrix}; \tag{3.5}$$

$$\text{weight configuration} = \begin{bmatrix} 1.0 & 1.0 \\ 1.0 & 1.0 \end{bmatrix}; \tag{3.6}$$

$$\text{efficiency limit} = 0.5. \tag{3.7}$$

The two tables used by the onboard software will be

$$\text{efficiency} = \begin{bmatrix} 1 & 0 \\ 0 & 0.9 \end{bmatrix}; \tag{3.8}$$

$$\text{weight} = \begin{bmatrix} 1.0 & 0 \\ 0 & 1.0 \end{bmatrix}. \tag{3.9}$$

3.5 ECLAIRs background and cleaning methods

3.5.1 CXB, Albedo, and reflection

The X-ray and γ-ray background of ECLAIRs is dominated by the cosmic X-ray background (CXB), additional reflected photons from the CXB reflected back to the Earth's atmosphere, and Albedo photons from the interaction of cosmic rays with the Earth's atmosphere.

Due to the anti-solar pointing strategy and the low-orbit altitude of the SVOM satellite, the Earth will appear in the ECLAIRs FOV during each orbit and will cover the entire FoV

(Mate et al., 2019a). The background count referenced above will change with Earth's occultation. As shown in Figure 3.15 and Figure 3.16. When ECLAIRs is pointed away from the Earth, CXB is the dominant background component, with about 3000 counts/s. For this orbit. When the Earth completely obscures the field of view, the CXB, reflection, and albedo strengths are comparable.

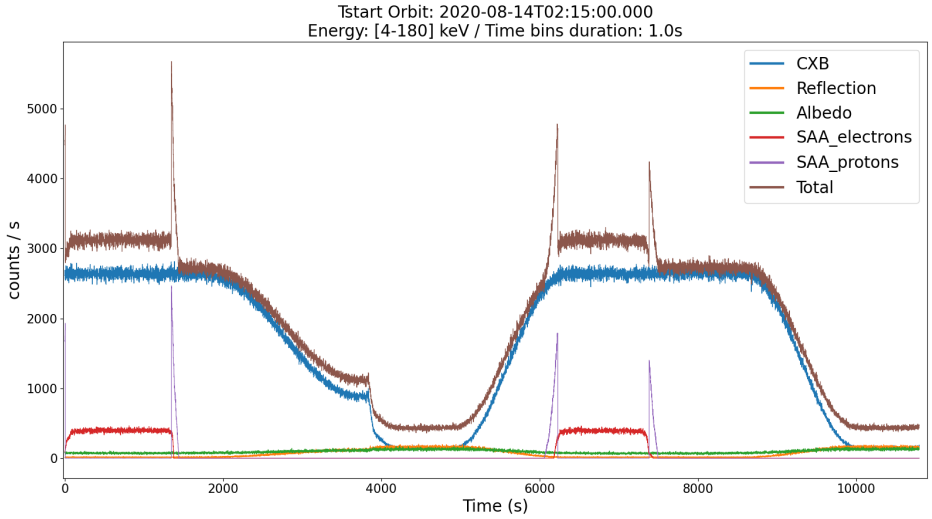

Figure 3.15: The simulated background of ECLAIRs in 4-150 keV for different components: CXB (blue), reflection (orange), albedo (green). SAA electrons (red) and protons (purple). The total duration is 11000 s.

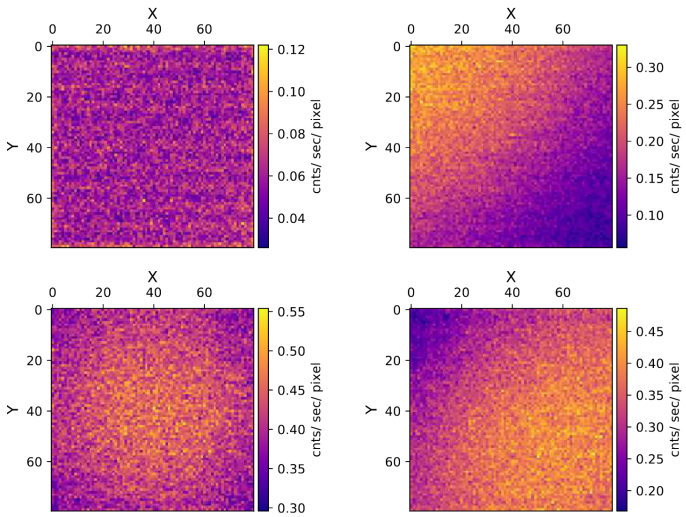

Figure 3.16: Simulated X-ray background of ECLAIRs. The panels show (clockwise, starting from the top left corner) the count rate detected for each pixel when the Earth is completely in the FoV, gradually moving away from the FOV, completely behind the FOV, and rising into the FOV, respectively. The background include CXB, Albedo, and reflection.(Mate et al., 2019a).

To reduce the influence of background on ECLAIRs trigger and image reconstruction,

it is necessary to correctly subtract those backgrounds (CXB, Albedo, and reflection background). The onboard software uses two methods (switchable by remote command): a 2D fitting algorithm and a wavelet algorithm (Dagoneau et al., 2022).

The default method used is the traditional one that has been used in the past and consists of subtracting a 2D polynomial shape after fitting a shadowgram. For the wavelet algorithm, it is the first time has been used to correct the background in detector images from coded mask telescopes before deconvolution. The main idea is that the background shape produced by the large FOV modulated by the presence of the Earth shows up as a large-scale structure on the shadowgram, while the point source contribution shows up as a small-scale structure on the shadow map due to the small scale of the coded mask elements. Thus, it is possible to decompose the shadowgram into different scales and reconstruct a background-corrected version of the shadowgram using only the smallest scales.

3.5.2 SAA region

The South Atlantic Anomaly (SAA) is a region of the Earth's magnetic field, located in the South Atlantic Ocean region, which is characterized by weaker magnetic than the rest of the Earth, and the magnetic anomalies in the SAA region may lead to an easier entry of solar wind and cosmic rays into the Earth's atmosphere. This causes an increase in particle radiation, which can cause damage to satellites and instruments on board.

When the SVOM satellite crosses the SAA region, the interaction of these particles with the instrument also produces background counts, and also causes an activation effect that generates the additional noise component. The simulated background counts produced in the SAA region could be raised to 10^4 counts/s within 5 minutes (Mate et al., 2019a). For safety reasons, ECLAIRs will not make observations when crossing the depths of the SAA region.

3.5.3 The known X-ray sources

Background counts of ECLAIRs are also increased when a known X-ray source is in the FOV. Figure 3.17 shows the distribution of known X-ray sources in the sky. The solid circles represent the 53 brightest sources in the catalog that ECLAIRs should be able to detect in 20 min (the sensitivity of ECLAIRs is about 0.05 ph/cm^2/s in 20 min). They are located mainly in the galactic plane. Most of these sources are accreting X-ray binaries whose main compact object is a neutron star or a black hole. The empty circles represent fainter sources (Mostly AGNs), which are evenly distributed across the sky.

The count rate added by these sources varies greatly with the pointing direction, ranging from about 100 counts/sec near the Galactic poles to about 5000 counts/sec near the Galactic center and Sco X-1 in the 4–120 keV band (N. Dagoneau et al., 2021).

To avoid false triggers caused by the bright known sources, ECLAIRs sets a specific threshold for each known X-ray source in the trigger algorithm. When the trigger algorithm searches for new sources in the sky map, it will compare the position of a transient candidate

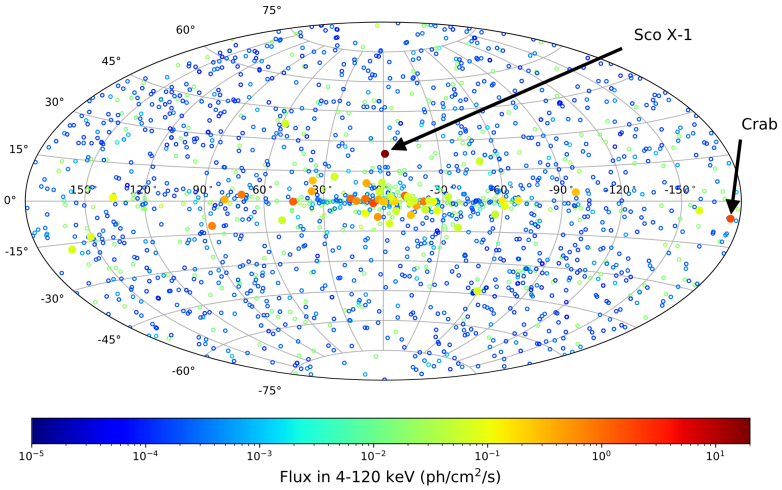

Figure 3.17: Distribution of the X-ray catalog sources in the sky in galactic coordinates (N. Dagoneau et al., 2021).

with those in the onboard catalog. If the two positions overlap, the SNR will be compared with the corresponding threshold value. If the SNR is below this threshold, the source is ignored. If the SNR is above this threshold, it indicates that the ECLAIRs have detected a new outburst from this known source. In this case ECLAIRs will send a catalog alert instead of a GRB candidate alert.

Chapter 4

Efficiency inhomogeneity of the ECLAIRs detection plane in 4–8 keV and its impact on the trigger performances

Contents

In 2021, a series of test campaigns were performed on the ECLAIRs flight model in a thermal vacuum chamber (TVAC) at the CNES and at Airbus Defense & Space (ADS) in Toulouse. The main goal of these campaigns was to meticulously study and assess the detailed performances of the ECLAIRs instrument. It started with measurements on the detection plane from January to March, and shifted to measurements on the cameras (both without and with the coded mask) from April to May. In October, the thermal vacuum test of the complete ECLAIRs instrument took place. Most of the performances and calibration measurements were conducted using a 2-meter diameter, 3-meter long TVAC chamber (hereafter called TVAC), situated in a clean room at CNES, as depicted in Figure 4.1. The comprehensive ECLAIRs calibration was performed in a larger TVAC at ADS.

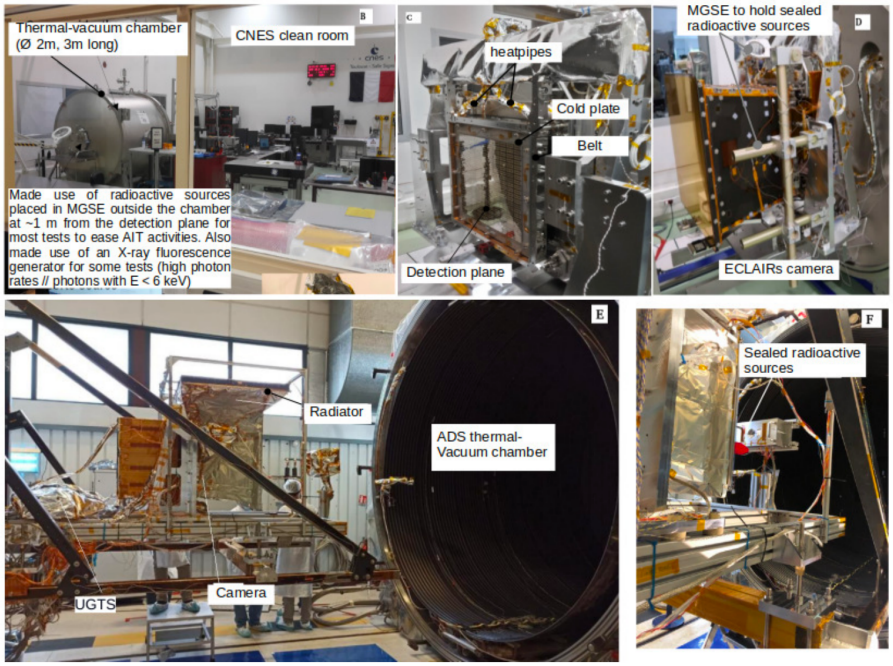

Figure 4.1: TVAC test in Toulouse. Panels (B) and (F) depict the test benches used for the instrument calibration at CNES and ADS, respectively. Panels (C), (D), and (E) represent the calibration measurements conducted on the detection plane, the entire camera assembled (including MLI, mask, shielding and supporting structure), and the complete ECLAIRs instrument (including radiator and UGTS). Credit: Olivier Godet et al. (2022).

The experimental sequences, setup, ground equipment, main performances and calibration results of the ECLAIRs instrument are comprehensively detailed in Olivier Godet et al. (2022). The TVAC tests of the instrument was carried out with different sources of X-ray photons as described below.

- To measure the relative efficiency (Section 4.1): a setup to generate beams of X-ray fluorescence photons using an X-ray generator radiating on metal targets, yielding to spectral lines ranging from 4 to 22 keV, depending on the target material. Here the relative efficiency of a given pixel is equal to the ratio of the pixel absolute efficiency to the average efficiency value of the entire pixel sample.

- To measure the absolute efficiency (Section 4.2): calibrated radioactive sources. The absolute efficiency here is the ratio of the number of detected photons to the incident photons for a pixel.

In this chapter, we show that the efficiency of the detection plane is inhomogeneous between 4 and 8 keV. Based on the efficiency variations within the 4–8 keV range, we have identified three distinct populations of pixels on the detection plane: the Low Efficiency Pixels (LEP), High Efficiency Pixels (HEP), and High Threshold Pixels (HTP). In this chapter, we will focus on the study of the characteristics of these inhomogeneities and analyze their impact on the ECLAIRs onboard triggers at low energies. Furthermore, we propose various strategies aimed at mitigating these impacts and enhancing the onboard trigger performance. Note that throughout Chatpter, the absolute efficiency of a pixel is count efficiency and equal to the ratio of photons detected by the pixel to incident photons. The relative efficiency is the normalized efficiency of the pixel and is equal to the absolute efficiency divided by a normalization constant.

4.1 Efficiency inhomogeneity in the 4–8 keV band

4.1.1 Experimental setup

In this section, we focus on the experiments carried out using the X-ray setup to generate fluorescence photons.

A simplified illustration of the setup is shown in Figure 4.2. During the experiment, the detection plane was situated inside a large TVAC. A high electrical voltage (of the order of 15 keV) is applied between two electrodes inside the X-ray generator. This produces a current of electrons from the cathode to the anode. The electrons are slowed down by the anode atoms, causing a continuous bremsstrahlung X-ray spectrum. These X-ray photons excite the target atoms, which re-emit characteristic X-rays by fluorescence.

The metal targets used in this setup are scandium (Sc), titanium (Ti), vanadium (V), chromium (Cr), manganese (Mn), and iron (^{56}Fe). The energies of the fluorescence X-ray photons produced by these different targets are given in Table 4.1. The collimated beam of fluorescence photons passes through a window of Beryllium to enter the TVAC. These fluorescence X-ray photons then reach the detection plane and are detected by the camera's pixels. It should be noted that this system is outside the TVAC and operates at the atmospheric pressure. The distance between the targets and the ECLAIRs detection plane was set to 1.0 m.

4.1.2 Relative efficiency: example for the chromium target

We detail the data analysis process on the chromium (5.41 keV) dataset as an example. From the raw data, we extracted the spectrum for each pixel of the detector. The lowest energy

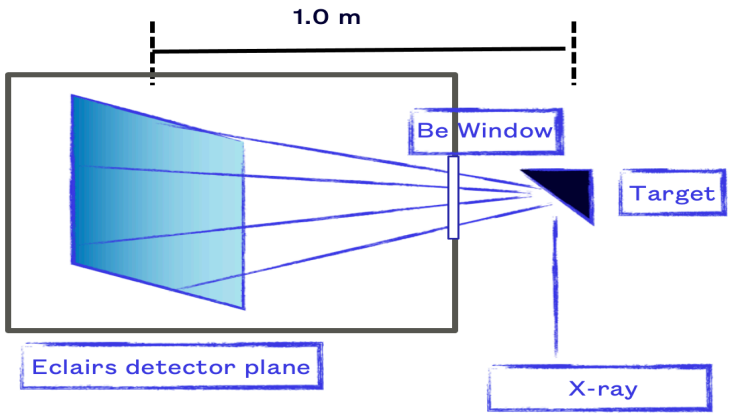

Figure 4.2: Schematic diagram of the experimental setup where the X-ray generator associated with a metal target project photons to the ECLAIRs detection plane.

Table 4.1: Characteristics of the X-ray fluorescence emission line (K lines) for the different targets.

Element	$K_{\alpha 1}$(keV)	$K_{\beta 1}$(keV)
Titanium (Ti)	4.51	4.93
Vanadium (V)	4.95	5.95
Chromium (Cr)	5.41	5.94
Manganese (Mn)	5.89	6.49
Iron (Fe^{56})	6.40	7.05
Copper (Cu)	8.05	8.90

Source: `https://xdb.lbl.gov/Section1/Table_1-2.pdf`

value found in these spectra determine the pixel's low-energy threshold (Figure 4.3). In this distribution, we observe that the vast majority of pixels have a threshold of 4 keV, corresponding to the expected low threshold (pixels in blue). There are other pixels with a higher threshold. Those include pixels aligned along dashed lines (pixels number 8 and 16 of each XRDPIX module, shown in orange, see 3.2).

Their threshold has been artificial set to 7 keV in order to avoid noise from cross-talk effect internal to the XRDPIX, we have designated these as the High Threshold Pixels (HTP). There is one whole XRDPIX module (number 12 of ELS 3) which shows an energy shift of about 4 keV, demonstrated by the observation of the Cr line at the wrong energy. This module therefore records no counts below 8 keV and appeared falsely with a higher low-energy threshold in Figure 4.3 (shown in dark red). The reason for this shift, which occurred randomly during the various tests, remains unclear and will be monitored in-flight. There were also a small number of switched-off pixels (shown in white) during the test.

In order to analyze the detector's behavior around the characteristic energy of the fluorescence line, it is necessary to identify an effective energy range for each dataset. We generated the spectrum for the entire detection plane, as depicted in Figure 4.4. We fit-

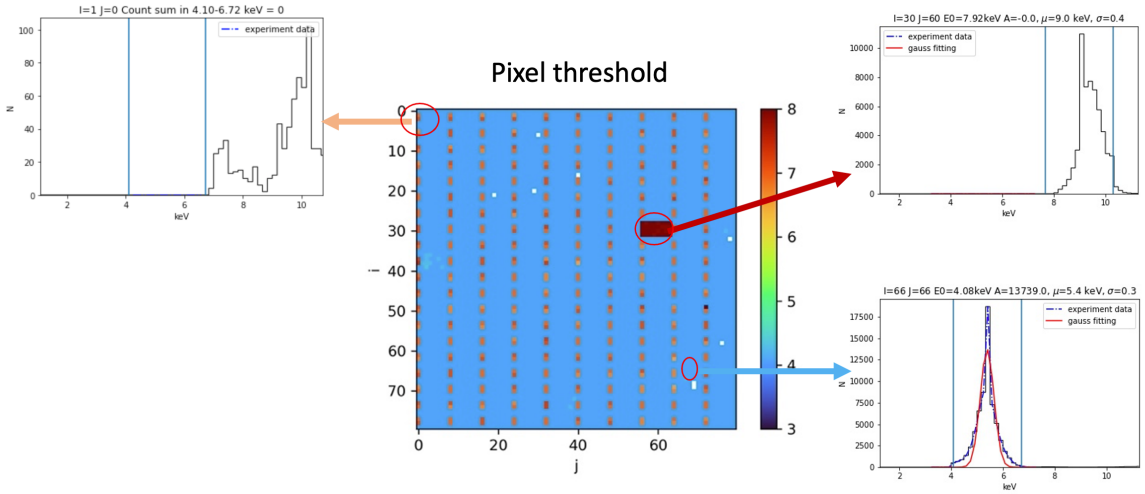

Figure 4.3: Pixel low energy threshold distribution for the Cr target. In this distribution, blue, orange and dark red pixels respectively represent normal pixels, 7 keV threshold pixels (to suppress cross-talk effect) and 8 keV threshold pixels (offset energy module) . For each category, we have selected one pixel and illustrated its spectrum in the figure.

ted the spectrum using a Gaussian function and selected the range within $\pm 3\sigma$ around the mean as the effective range. For the Cr target, the resulting interval is 4.1–6.7 keV. This approach is justified since the mean value in the spectrum (5.29 keV) exhibits a slight deviation compared to the theoretical value (5.41 keV). This discrepancy could be attributed to the deviation in the pixel's channel-to-energy law, which can be further refined during the commissioning phase.

Once the energy bounds have been found, we aggregated the counts to form an image of the detector plane in this energy range, as illustrated in Figure 4.5. The figure reveals that the pixel counts are inhomogeneous, with one part of the pixels (the Low Efficiency Pixels, LEP) having fewer counts than the other (the High Efficiency Pixels, HEP). There are also the aforementioned pixels, which do not count at low energy (they appear in black in Figure 4.5).

Finally, we calculated the relative number of counts on the detection plane, by dividing the number of counts in each pixel by the mean value of HEP plus LEP (Figure 4.6, left). To compare the differences between the two populations, we created a histogram for the pixels with relative counts ranging between 0.7 and 1.3. We fitted this bimodal distribution with two Gaussian functions to obtain the average relative efficiency of the two populations (Figure 4.6, right).

4.1.3 Relative efficiency: full low energy range (4–8 keV)

In this section, we present the result of the analysis on all the different metal targets that have been used during the calibration test (see Table 4.1).

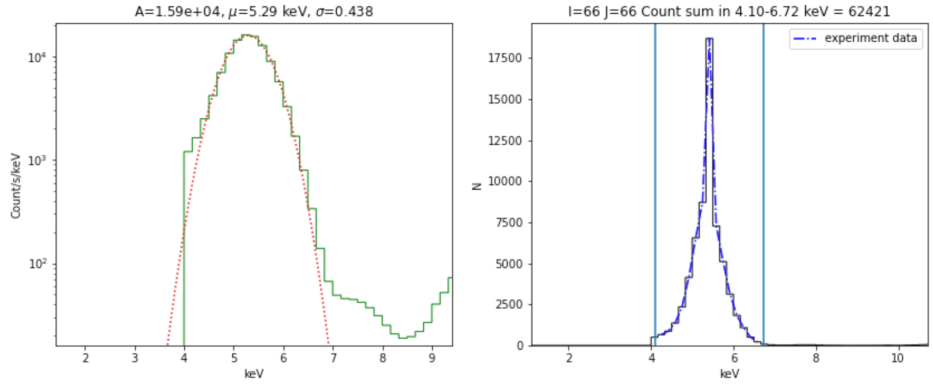

Figure 4.4: Left: spectrum for the full detection plane and the Cr target. The red dashed line is a Gaussian fit to the count spectrum (green histogram), and the title of the figure indicates the result of the fit. Right: example of a single pixel spectrum. It is a HEP with coordinate i=66 and j=66 in the detection plane.

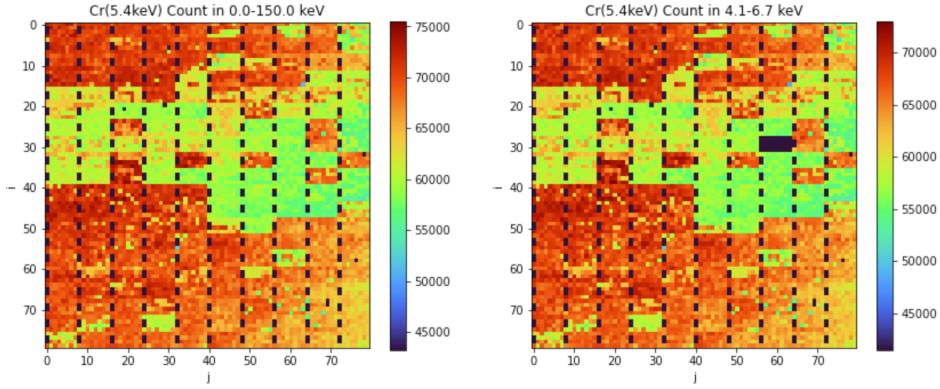

Figure 4.5: Left: image of the detected number of counts per pixel for the entire energy band (4–150 keV). Right: image of the detected number of counts per pixel in the selected energy band (4.1–6.7 keV).

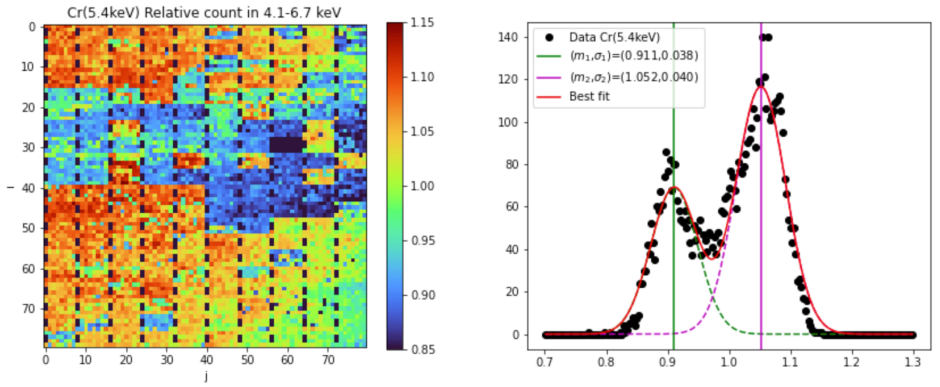

Figure 4.6: Left: image of the relative number of counts within the selected energy band (4.1–6.7 keV in the chromium case). Right: relative count distribution fitted with two Gaussian functions for the two populations.

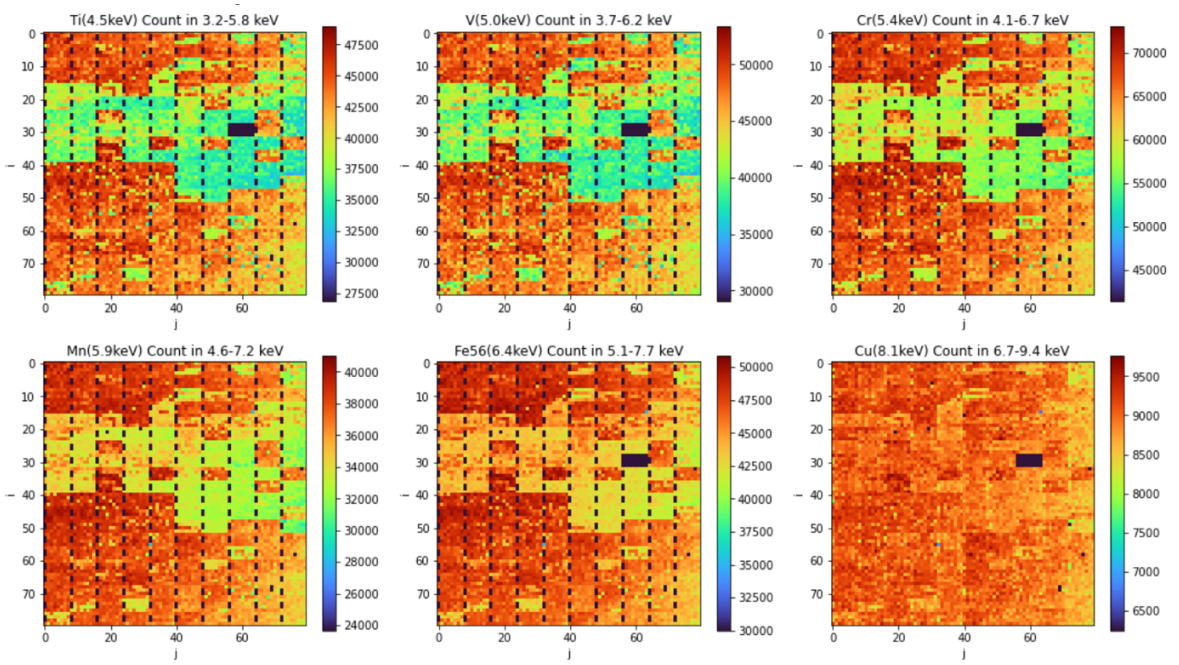

Figure 4.7: Images of the detected number of counts per pixel on the detection plane between 4.5 and 8.0 keV, obtained with 6 metal targets, producing X-ray fluorescence lines): ^{22}Ti (4.5 keV), ^{23}V (5.0 keV), ^{24}Cr (5.4 keV), ^{25}Mn (5.9 keV), ^{26}Fe (6.4 keV) and ^{29}Cu (8.0 keV). The energy bands are determined to be $\pm 3\sigma$ around the fitted Gaussian mean value for each line.

The count distributions on the detection plane for the different targets are shown in Figure 4.7 for fluorescence energies ranging from 4.5 keV to 8.1 keV. As presented in the previous section with the chromium example, the count of each pixel is obtained by summing the counts for which the energy is included in the $\pm 3\sigma$ interval around the mean value of the Gaussian fit of the energy spectrum (over the entire test duration). The corresponding relative counts distributions are given in Figure 4.8.

The count distribution clearly shows that the detection plane is inhomogeneous in 4–8 keV.

Based on the difference in counting efficiency, we identify three populations of pixels, hence confirming the observations detailed in the previous section.

- The first population, referred to as High Efficiency Pixels (HEP), comprises the majority of the pixels ($\sim$2/3).
- The second population, named Low Efficiency Pixels (LEP), represents approximately $\sim$ 1/3 of the total pixels.
- The third population, named High Threshold Pixels (HTP), corresponds to the pixels 8 an 16 of each XRDPIX module (black dashed lines of pixels seen in Figure 4.7). The energy threshold of these pixels was increased to 7 keV (against 3.8 keV for the others) in order to reduce the noise from the cross-talk effects that they induce on

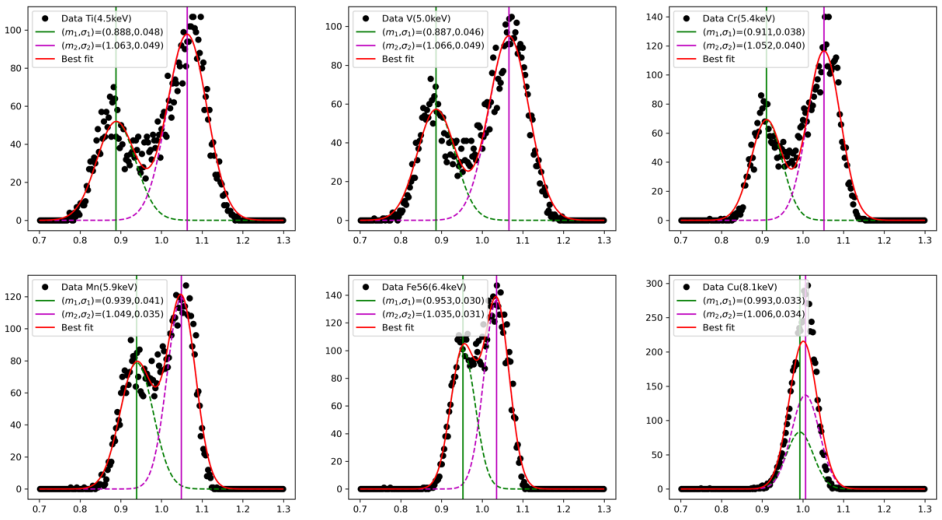

Figure 4.8: Distribution of the relative number of counts in the 6 images of Figure 4.7 (corresponding to the 6 energy bands). HTPs have been excluded from these histograms. The x-axis represents the relative count value of the pixel, which is obtained by dividing the count of the pixel by the average count of all pixels (excluding high threshold pixels). The y-axis is the number of corresponding pixels.

their neighbors (Olivier Godet et al., 2022).

The counting discrepancy between HEP and LEP tends to decrease when the energy increases. At 8 keV, the two populations of pixels exhibit a homogeneous efficiency distribution and thus cannot be distinguished. This trend is more distinctly illustrated in the combined plots in Figure 4.9.

Figure 4.10 (left) shows the evolution of the difference of relative efficiency between HEP and LEP according to the energy. The differences can be fitted with a simple linear equation. When we randomly pick some detector pixels and plot their relative count versus the energy, the result is presented in the right panel of Figure 4.10. As the energy increases, the single-pixel relative count approaches the mean value ($= 1$) of the whole distribution.

4.1.4 Discussion: possible cause of this efficiency inhomogeneity?

Previously, we show that the pixel efficiency is inhomogeneous below 8 keV. This could be caused by different reasons.

The CdTe pixels in ECLAIRs detection plane were manufactured during two different periods in 2008 and 2016 (Table 4.2). The detectors counting less on the detection plane, the LEP, mainly come from the 2016 batch.

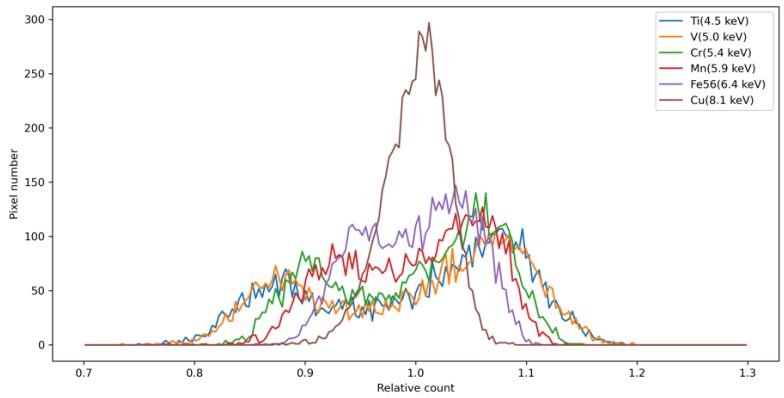

Figure 4.9: Relative count distribution of HEP and LEP. The colors represent the different metal targets used in the experiment.

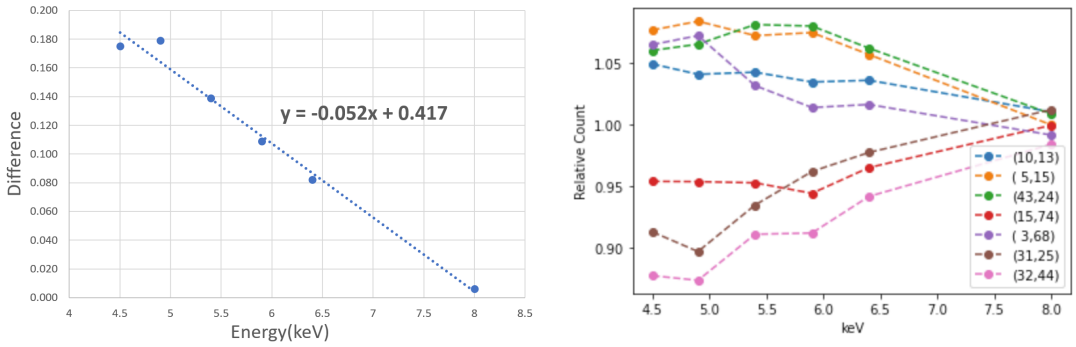

Figure 4.10: Left: Efficiency difference between two batches of pixels at different energy. Right: Relative count of pixels versus energy. Different colors indicate randomly selected pixels, while the numbers denote the position of the pixel in the plane.

The difference between the two batches may be due to some variations in the detector parameters. The CdTe detector bare element is composed of a platinum (Pt) cathode and an indium (In)/titanium (Ti) anode surrounding the CdTe crystal. There may also be a dead layer composed of tellurium dioxide (TeO_2) at the interface between the cathode and the sensitive bulk of CdTe (Dubos et al., 2013). In this case, photons have to pass through the Pt cathode and the dead layer prior to deposit their energy in the scintillator. This is illustrated in Figure 4.11.

The efficiency difference between the two batches changes with the energy. This indicates that the difference may come from a thickness variation for the Pt and/or for the TeO_2 layers between the two batches. This would result in a different absorption intensity.

If we assume that there is only one material that is likely to have a different thickness between the two batches (either Pt or TeO_2), this difference can be calculated according to Equation 4.1, where $\boldsymbol{x_2 - x_1}$ stands for the thickness difference between the two populations, $\boldsymbol{I_1}$ and $\boldsymbol{I_2}$ represent the mean counts from the Gaussian fits of the two populations in

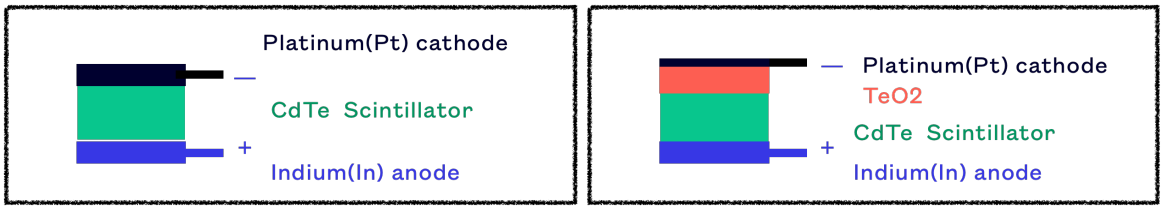

Figure 4.11: Simplified scheme of pixel structure.

Table 4.2: Geometric parameters of the detector plane and CdTe pixels.

Manufactoring batch	2008 (12500)	2016 (2000)
Size	4×4 mm^2 (-50 μm / +0 μm)	4($\pm$50μm)×4($\pm$50μm) mm^2
Thickness	1 mm (-0 μm / +50 μm)	1 mm ($\pm$20 μm)
Pt layer thickness (cathode)	200–300 nm (Remoué et al., 2010)	200–300 nm

Figure 4.8 and $\boldsymbol{\mu}$ represents the linear attenuation factor of the material, the value of which is related to the energy of the photon. The results of the calculations are shown in Table 4.3.

$$\frac{I(x)}{I_0} = e^{-\mu x} \tag{4.1}$$

$$\frac{I_1}{I_2} = e^{\mu(x_2 - x_1)} \tag{4.2}$$

$$x_2 - x_1 = \frac{\ln\left(\frac{I_1}{I_2}\right)}{\mu} \tag{4.3}$$

If we suppose that the Pt layer is the only one to have a different thickness between the two populations, then Equation 4.3 gives a mean difference of $\sim$ 123 nm for the different metal targets. If we now assume that it is the TeO_2 that changes thickness, then the average difference is $\sim$ 460 nm. In both cases, the consistency of thickness difference values found at different energies (Table 4.3) supports the hypothesis of a thicker layer of either Pt or TeO_2 in the 2016 batch.

A more realistic possibility is that the difference in the pixel efficiency between the two populations is the result of the combined effect of different thicknesses of Pt and TeO_2.

In a recent test dedicated to studying the Pt/TeO_n thickness performed at CNES (Toulouse, Emmanuel, 2022), the Pt/TeO_n thicknesses were measured for one pixel of each batch. It was found that the thicknesses of the Pt layer and the oxide (TeO_n) of the pixel belonging to LEP was greater than the one belonging to HEP. As a larger thickness indicates more absorption for the layer, this test gives results which are in line with what we observe with the PFM test in the low-energy band.

Table 4.3: Estimated difference in thickness of the Pt or TeO_2 material. These results are deduced from Equation 4.3 in a model where the efficiency difference between LEP and HEP population is due to the Pt thickness differences alone or to the TeO_2 thickness differences alone.

Energy (keV)	Peak1	Peak2	Peak difference	μPt (/nm)	Pt thickness difference (nm)	μ_{TeO_2} (/nm)	TeO_2 thickness difference (nm)
4.5	0.888 (±5.41%)	1.063 (±4.63%)	0.175 (±0.069)	0.00171	105 (±42)	0.000337	534 (±210)
4.9	0.887 (±5.19%)	1.066 (±4.52%)	0.179 (±0.067)	0.00138	133 (±50)	0.000367	501 (±189)
5.4	0.911 (±4.17%)	1.052 (±3.80%)	0.141 (±0.055)	0.00109	132 (±52)	0.000335	430 (±168)
5.9	0.939 (±4.37%)	1.049 (±3.33%)	0.110 (±0.054)	0.000871	127 (±63)	0.00025	443 (±220)
6.4	0.953 (±3.15%)	1.035 (±2.99%)	0.082 (±0.043)	0.000713	116 (±61)	0.000211	391 (±206)

1. Peak1 and Peak2 correspond to the mean values of the Gaussian fit in Figure 4.8.
2. Attenuation coefficient values come from: https://physics.nist.gov/PhysRefData/FFast/html/form.html.

4.2 Absolute efficiency of the ECLAIRs detector plane in 4–8 keV

In this chapter we will calculate the absolute overall effective area of ECLAIRS in the 4–8 keV band. By overall effective area, we mean the number of effective square centimeters left after all the effects have been taken into account: pixels efficiency, overall transparency of the insulation layers (MLI) and overall transparency of the mask.

4.2.1 Towards the absolute calibration

The inhomogeneity study presented in the previous section was carried out using an X-ray generator. However, an X-ray generator cannot be used to calculate an absolute efficiency because the photon flux emitted by the system is very difficult to quantify. The flux emitted will depend on the characteristics of the X-ray tube, the stability of the power supply and the geometry of the system.

But the X-ray generator can be used to estimate a relative efficiency between the different energies produced by the different targets. If we are able to perform an absolute calibration with a calibrated radioactive source, at an energy within the range covered by the X-ray generator, then we can re-normalize the values measured with the generator and estimate the efficiency over the whole energy range. We propose to apply this principle by using the ^{55}Fe source to estimate the efficiency of ECLAIRs in the 4–8 keV range.

In addition, in order to estimate the overall efficiency of the detection plane, we need to calibrate all the pixels. This is why the measurements were carried out without the mask, in order to have access to all the detectors and not just those illuminated through the holes of the the mask. Subsequently, to estimate the overall efficiency of the ECLAIRs telescope,

it will be necessary to reintroduce the mask. This last step will be done virtually and will be discussed in Section 4.2.6.

The path to the absolute efficiency and the global effective area in 4–8 keV can be summarized as follows.

1. Relative calibration of the full detection plane (presented in Section 4.1).
2. Full detection plane absolute calibration with a radioactive source.
3. Re-normalization after the absolute calibration with a radioactive source.
4. compute the detection plane global effective area.
5. Testing and calculation of MLI transmission rates.
6. Compute the ECLAIRs global effective area in 4–8 keV （include MLI and Mask).

4.2.2 Description of the experimental setup and radioactive sources

The experimental setup employed is consistent with that detailed in subsection 4.1.1, with two notable distinctions. First, a radioactive reference source served as the X-ray source, replacing the previously used X-ray generator. Secondly, the tests have been expanded to include not only the single detection plane but also the fully assembled ECLAIRs instrument, including the detection plane, its protective shielding and the MLI.

To obtain the absolute efficiency of the detector pixels, different radioactive elements were used as X-ray sources in the irradiation experiments: Iron (^{55}Fe), Cobalt(^{57}CO), Barium(^{133}Ba) and Americium (^{241}Am).

In our analysis, we specifically focused on the low energy range and selected only the dataset with the ^{55}Fe source. Detailed information about the radioactive source is shown in Table 4.4.

Table 4.4: ^{55}Fe radioactive source parameters.

Source	A_0 (MBq)	Uncertainty %	T_0 Date	$T_1 - T_0$ (days)	$T_{1/2}$	A_1 (MBq)
^{55}Fe	2.18	(3.67%)	2019-03-15	315.087	2.737 years	1.752 (2021-02-12)

At low energies, the use of a radioactive source is not simple because everything surrounding the source will contribute to absorbing photons, in particular the material supporting the radioactive product.

The parameters of the source holder are shown in Figure 4.12. The holder's substrate material for ^{55}Fe consists of a 0.254 mm aluminized Mylar layer and a 0.0064 mm Kapton polyimide layer.

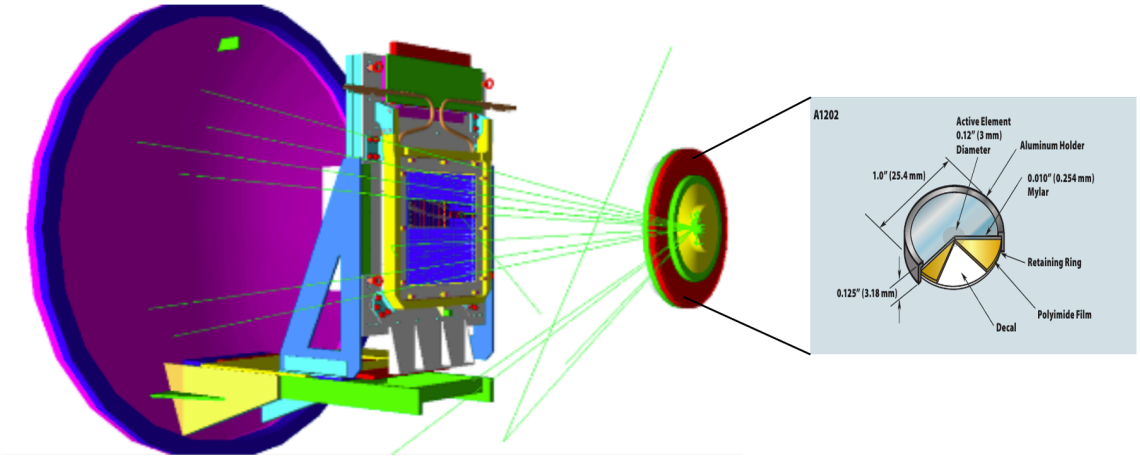

Figure 4.12: Experiment simulated with GEANT4: the radioactive source is placed in front of the camera, housed in a source holder at one end of the TVAC. The green rays illustrate the photons emitted by the radioactive source. The sources were placed as far as possible on the optical axis (from Laurent Bouchet, IRAP).

There were two experimental configurations with the ^{55}Fe source, both without the mask so that all the pixels in the camera could be calibrated and not just those illuminated by the source if the mask had been present. The experimental parameters are outlined in Table 4.5.

- Configuration 1 consists of the detection plane only (Figure 4.13, left).
- Configuration 2 consists of the integrated telescope including the detection plane, the MLI, the mechanical structure and the shield but still without the mask (4.13, right).

Table 4.5: Experimental parameters with the ^{55}Fe source (from IRAP, CNRS)

Experiment	Date	^{55}Fe Activities (MBq)[a]	Exposed Time (s)	Distance (m)
Without MLI	2021-02-12	1.344	59500.35	1.00
With MLI	2021-04-07	1.295	44192.53	1.14

[a] The ^{55}Fe initial activities was 2.18 MBq (3.67%) measured on 2019-03-15 and the half-period is 2.747 years. Emission information taken from www.lnhb.fr/Laraweb/index.php.

The parameters of the MLI are detailed in Figure 4.13. On top the ECLAIRs instrument, there is the SLI +X screen, which is comprised of one film of 25 µm thick Kapton (polyimide, $[C_{22}H_{10}O_5N_2]_n$), with 130 nm of SiO_2 on the external side and 0.1 µm of aluminum on the internal side. Additionally, inside the ECLAIRs, above the detection plane, there is the SLI–X Screen, which is composed of two films made of Mylar (ethyl glycol polyterephtalate, $[C_{10}H_8O_4]_n$), each 12.5 µm thick with 0.1 µm of aluminum (Al) on each side. These parameters are guaranteed by the supplier with a tolerance of about ±10%.

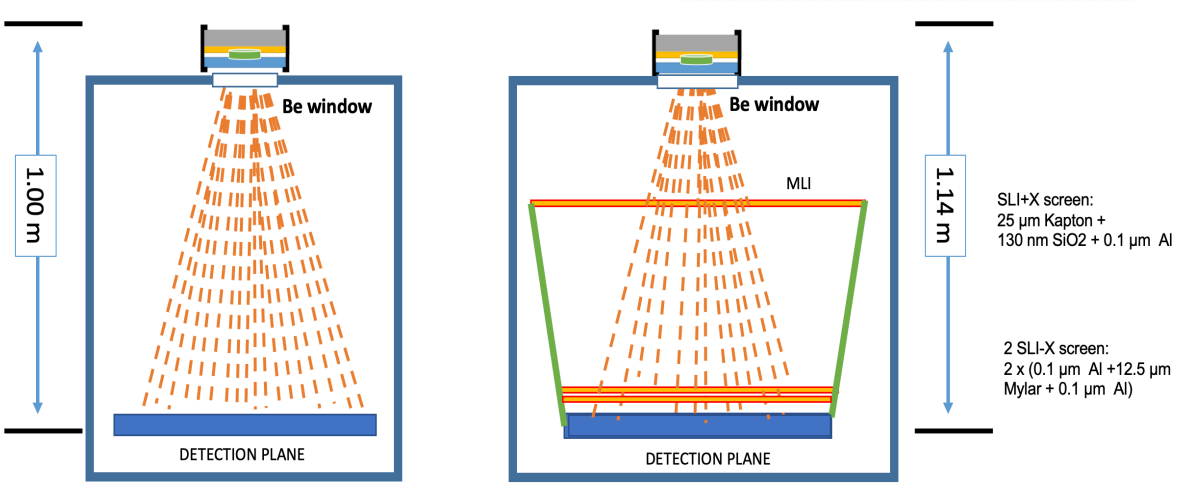

Figure 4.13: Schematic diagram of the experiment using a radioactive source for both configurations, top view, so that the detection plane and the source are placed in the vertical position as shown in Figure 4.12

4.2.3 Analysis of the ^{55}Fe datasets

Configuration 1

For the scenario where ^{55}Fe serves as the X-ray photons source without MLI installed above the detection plane (configuration 1), an overview of the data is provided in Figure 4.14. The mean count rate of the detection plane is 0.16 count/s/pixel. HTP and LEP (Section 4.1), can still be observed in the counts map and the relative counts map.

The relative counts map reveals a notably lower count rate on the bottom right corner. This discrepancy might be attributed to the radiation source not being centrally placed, with part of the emission possibly obstructed by the holder edge material. There is also a noticeable trend of the number of counts decreasing from the center to the edge. This phenomenon can be explained by the increasing distance between the ^{55}Fe source and the pixels from the center to the edge, which affects the count rate as described below.

1. The closer to the edge of the detection plane, the greater the distance, the lower the count rate per unit area.

2. The closer you get to the edge of the detection plane, the thicker the material the source photons have to pass through, resulting in increased absorption of X-ray photons.

3. The closer you get to the edge of the detection plane, the greater the angle of inclination between the pixels and the source, reducing the effective area available to receive photons.

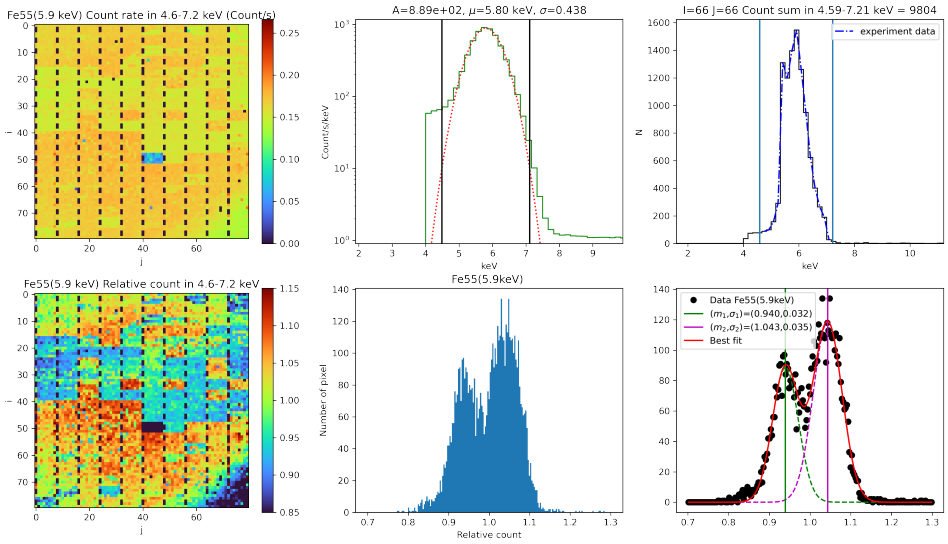

Figure 4.14: Analysis of the detection plane data for ^{55}Fe without MLI (configuration 1). Top, from left to right: count maps for the detection plane in the 4.6–7.2 keV range, entire spectrum of the detection plane, and an example of a pixel spectrum (HEP). Bottom, from left to right: relative count map and its histogram distribution, result of the fit of the histogram by a double Gaussian function.

Configuration 2

Figure 4.15 presents the data analysis results from the ECLAIRs test (configuration 2, with MLI). The mean count rate in this setup is 0.078 count/s/pixel. An abnormally higher count rate is observed in the bottom right corner. This anomaly is unexpected since we observed a deficit of counts without the MLI. Its precise cause remains unclear but could potentially be attributed to an inappropriate position and orientation of the radioactive source.

4.2.4 Absolute efficiency of the ECLAIRs pixels at 5.9 keV using the Fe^{55} radioactive source

Mathematical formalism

In this section, we will describe in detail how the efficiency of the pixels was calculated using the data presented in the last section.

The efficiency of a given pixel ϵ is equal to the ratio between the number of detected counts N_{det} and the theoretical number of photons reaching the pixels N_{th} (Equation 4.4.

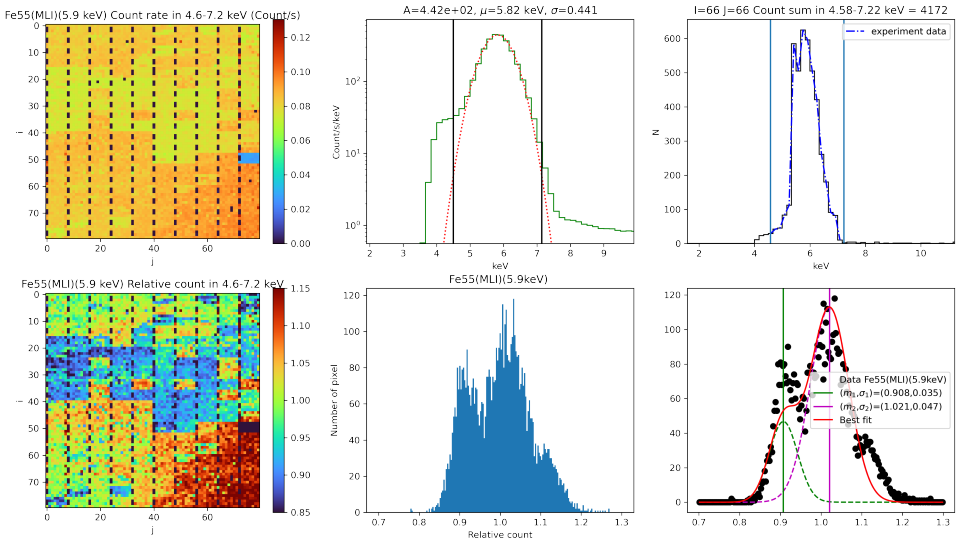

Figure 4.15: Similar to Figure 4.14, but in configuration 2 (with the MLI installed above the detection plane).

$$\epsilon = \frac{N_{det}}{N_{th}} \tag{4.4}$$

The theoretical number of photons on the pixels (N_{th}) is given by Equation 4.5. S stands for the X-ray source radioactive activity during the experiment. E_{holder} represents the transmission of the source holder. Ω_{pixel} is the solid angle of the pixel on a sphere centered on the radiation source and t is the exposure time. E_{Be} represents the transmission of the beryllium window.

$$N_{th} = S \times E_{\text{holder}} \times E_{Be} \times \frac{\Omega_{\text{pixel}}}{4\pi} \times t \tag{4.5}$$

The X-ray source activity S is given by Equation 4.6 where S_0 stands for the initial activity of ^{55}Fe, which is 2.18 MBq. The half-period τ is 2.747 year. The radiation percentage distribution of ^{55}Fe in 5.9 keV and 6.5 keV are 0.250 and 0.034, respectively.[1]

$$S = S_0 \left(\frac{1}{2}\right)^{\frac{T_1 - T_0}{\tau_{1/2}}} (0.25 + 0.034) \tag{4.6}$$

For a given pixel, the holder transparency E_{holder} is given by Equation 4.7 and depends on the substrate materials, the absorption coefficient μ of the materials, their thickness x and the angle θ. θ is the angle between the source and the pixel in the vertical direction.

[1] `http://www.lnhb.fr/Laraweb/index.php`

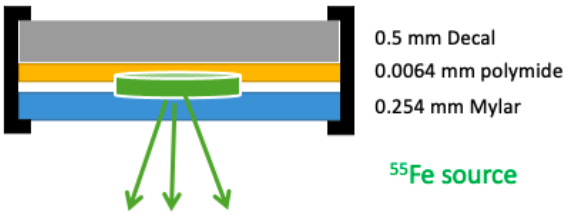

Figure 4.16: Simple diagram of ^{55}Fe source holder structure

The composition of the ^{55}Fe source substrate is presented in Figure 4.16. From this figure we can see that only the Mylar film will absorb the photon from the source.

$$E_{\text{holder}} = e^{-\frac{(x_1\mu_1 + x_{Be}\mu_{Be})}{\cos(\theta)})} \tag{4.7}$$

The beryllium window that separates the radioactive source from the vacuum in the tank must also be taken into account. Finally, considering 0.254 mm of aluminized Mylar, and 0.125 mm of Beryllium window, with the corresponding attenuation coefficient (μ) 24.9 cm^{-1} and 4.68 cm^{-1} at 5.9 keV[2], we obtain a transparency of 53.7% for the Mylar layer and 94.9% for the Be window at 5.9 keV for the central pixel (θ = 0).

Ω_{pixel} is given by Equation 4.8. A_{pixel} represents the pixel average area, which is 0.147cm^2. l stands for the distance between the radioactive source and the detection plane center. As the detection plane is made up of an 80x80 pixel array, the angle θ varies from 0 to 11 deg.

$$\Omega_{\text{pixel}} = \frac{A_{\text{pixel}} \times \cos\theta}{l^2} \tag{4.8}$$

Application: configuration 1

Following the calculation process described above, we obtain the absolute efficiency distribution of pixels, which is shown in Figure 4.17. HEP have a Gaussian mean value of about 0.777, the simulated efficiency value of $\sim$ 0.804 at 5.9 keV from Remoué et al. (2010). For the LEP, the mean value of efficiency we obtained here is 0.694 at 5.9 keV.

Application: configuration 2

By using the same method, we studied the detection plane integrated into the telescope with the presence of MLI. We obtained the ECLAIRs pixels efficiency distribution. As shown in figure 4.18, which have a Gaussian mean value of 0.518 and 0.459 for HEP and LEP respectively.

In this study we obtained an abnormally high efficiency in the lower right corner (also mentioned in Section 4.2.3) for configuration 2. This over-efficiency in the lower right corner can be explained by a higher number of photons detected in this area. This is very

[2] `https://physics.nist.gov/PhysRefData/FFast/html/form.html`

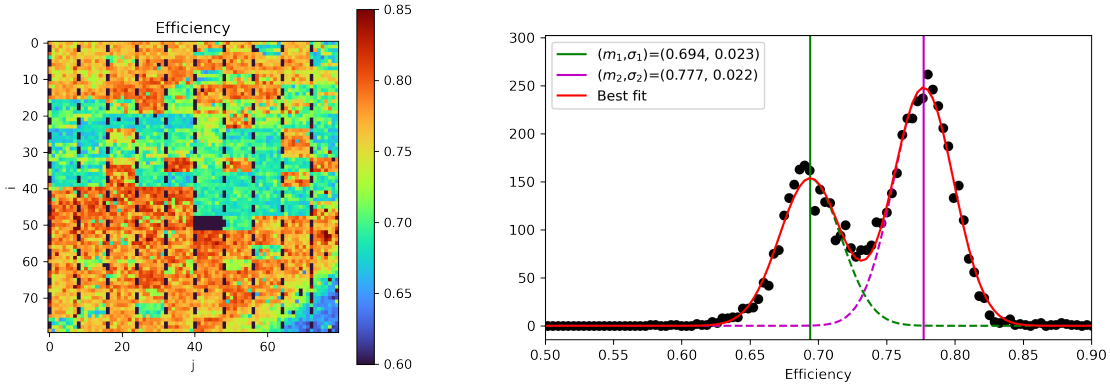

Figure 4.17: Left: counts distribution obtained in the configuration 1 (without MLI). Right: absolute efficiency distribution.

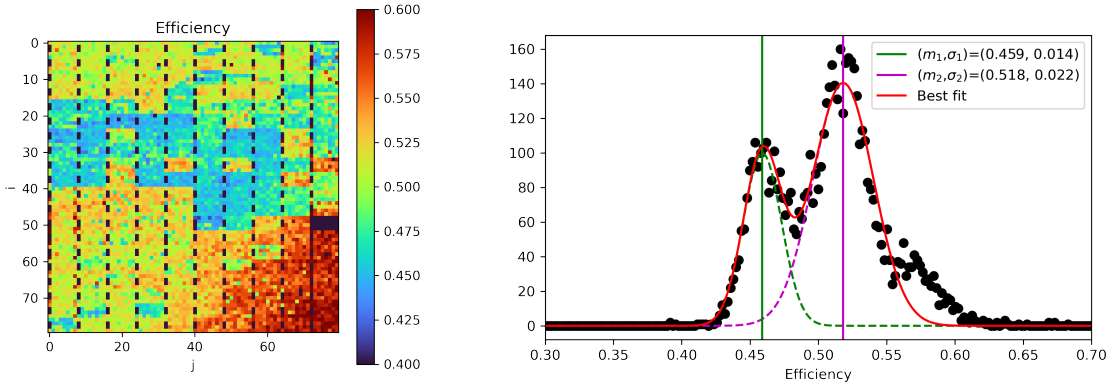

Figure 4.18: Left: counts distribution obtained in the configuration 2 (with MLI). Right: absolute efficiency distribution.

strange because we had observed exactly the opposite in the configuration 1 (without MLI). We still don't understand what happened.

4.2.5 The problem of MLI transparency

As a result of a lack of understanding of the results obtained from measurements with and without MLI, we decided to study the aborption of MLI more precisely, firstly by a theoretical approach based on the composition supplied by the manufacturer, secondly by carefully analyzing the measurements with the ^{55}Fe source in CNES and finally by carrying out an alternative measure in CEA on a sample of the flight MLI.

Theoretical calculation

The theoretical MLI transparency value can be calculated using the component information and thickness detailed in Figure 4.13. This calculation utilizes the detailed structure information of MLI, as well as the linear attenuation coefficient data summarized in Table 4.6. Consequently, we obtain a theoretical transparency value for MLI $\epsilon_{MLI} = 88.7\%$ as calculated in Equation 4.9 where 1, 2, 3 and 4 represents different layers. In a Geant4 simulation performed by Olivier Godet et al., 2022, the simulated transparency at 5.9 keV was approximately 88%, aligning closely with our calculated result.

$$\epsilon_{MLI} = e^{(-x_1\mu_1 - x_2\mu_2 - x_3\mu_3 - x_4\mu_4)} \tag{4.9}$$

Table 4.6: MLI parameters.

Material	**Attenuation Coefficient (μ, cm^{-1})**[a]	**Length (μm)**
Kapton – $(C_{22}H_{10}O_5N_2)_n$	20	25
SiO_2	200	0.13
Al	300	$(1+4)\times 0.1$
Mylar – $(C_{10}H_8O_4)_n$	21	2×12.5

[a] Attenuation coefficient is taken from `https://physics.nist.gov/PhysRefData/FFast/html/form.html`.

Experiments with the 55Fe source in CNES

To verify the theoretical value of the MLI transparency, we proposed to test it through the analysis of datasets both with and without MLI. We calculated the MLI transparency (ϵ_{MLI}) according to the Equation 4.10.

$$\epsilon_{MLI} = \frac{e_{DP+MLI}}{e_{DP}} \tag{4.10}$$

In the equation, e_{DP+MLI} represents the efficiency of the detection plane with the presence of MLI. This efficiency is calculated to be 0.501 for HEP and 0.440 for LEP. e_{DP} denotes the efficiency of detector pixels only, which is determined to be 0.777 for HEP and 0.672 for LEP, as previously discussed.

The MLI transparency value we obtained is $66.5\%^{+1.6\%}_{-1.6\%}$. The spatial distribution of this value is illustrated in Figure 4.19. It is observed that the MLI's transparency is uniformly distributed, with the exception of a specific area in the bottom right corner, indicating a notable deviation.

The calculated transparency value of 66.5% is significantly different from the theoretical value of 88.7%. To verify and cross-validate this discrepancy, a dedicated experiment was conducted in our laboratory (CEA).

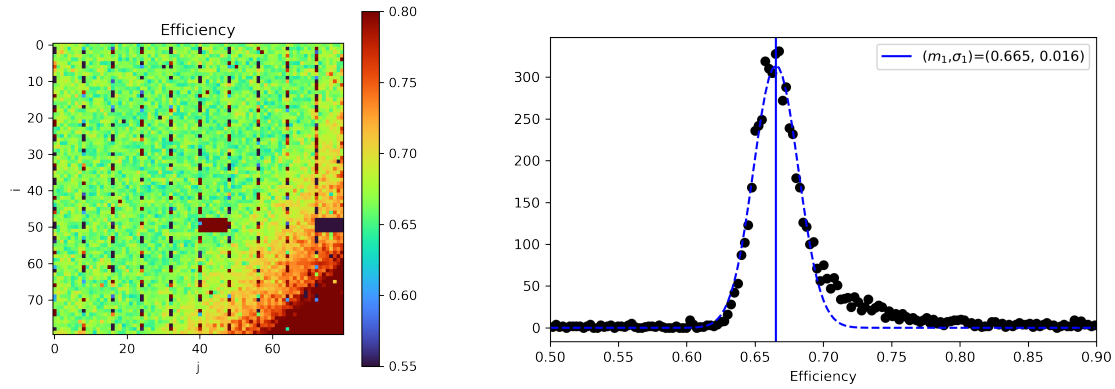

Figure 4.19: Left: distribution map of MLI efficiency. Left: corresponding histogram.

Alternative measure in CEA

To conduct a laboratory test of MLI transparency, we obtained a piece of MLI layer identical to the flight model from the project team (CNES, Toulouse). Our experimental setup, as depicted in Figure 4.20, included several components: radioactive sources (^{55}Fe, ^{241}Am and ^{60}Co), the MLI layer, a germanium detector, a high voltage power supply, a preamplifier module, an ADC module and data acquisition software on a computer.

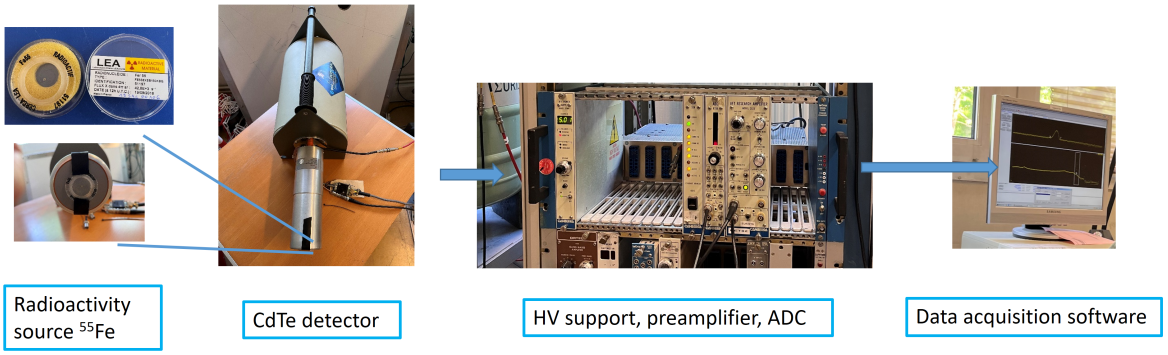

Figure 4.20: Schematic of the Experimental Setup for the MLI transparency test: From left to right, the components include the ^{55}Fe source, the germanium detector, the electronic module, and the data acquisition computer.

The detailed procedure of the MLI transparency measurement at CEA was executed as described below.

1. We conducted a channel-energy calibration test for the germanium detector using ^{241}Am and ^{60}Co radioactive sources. The established calibration relation is: $E_{\text{keV}} = 0.01 \times E_{\text{channel}} + 0.808$ (keV).

2. Subsequently, we performed a 300 s test using ^{55}Fe to record its spectrum, as shown in Figure 4.20.

3. We then placed the MLI layer between the ^{55}Fe source and the germanium detector, maintaining the same test duration (300 s) to record the source spectrum while accounting for the MLI layer's absorption (Figure 4.21).

4. To mitigate the impact of thickness variations in the MLI, we replicated steps 2 and 3 at two different positions on the MLI.

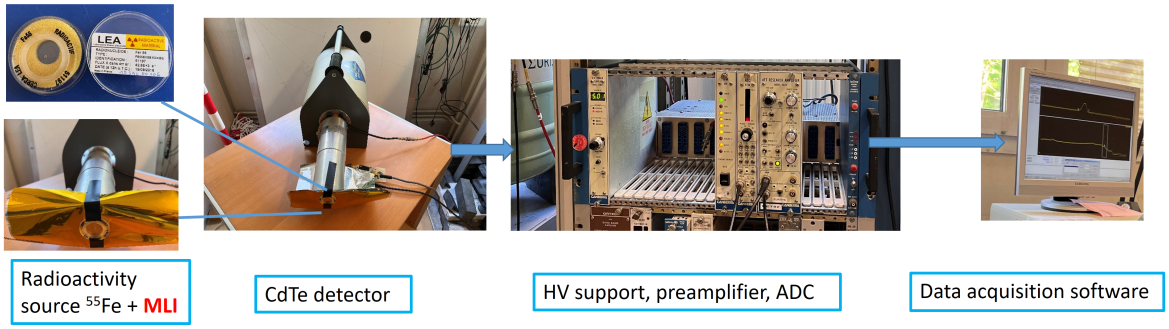

Figure 4.21: Similar to Figure 4.20, with the MLI layer inserted between the germanium detector and the ^{55}Fe source.

Table 4.7 presents a summary of the MLI transparency test results for both positions. The average MLI transparency value we derived was approximately $84.5\% \pm 0.3\%$.

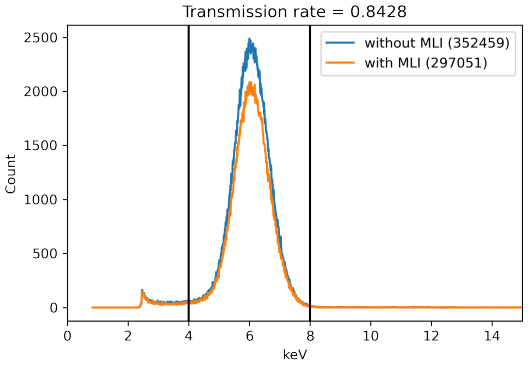

Figure 4.22: Spectra recorded with the germanium detector (first position). The blue line illustrates the ^{55}Fe spectrum obtained without MLI absorption, and the orange line with MLI absorption. Numbers in the legend indicate the integrated counts detected within 4–8 keV.

In summary, the measurement if the MLI transparency has not reached a clear conclusion. The theoretical calculations and Geant4 simulation suggest a value of approximately 88%, the measurement in CEA give a transparency of 84.5% and the measurement with the ^{55}Fe source performed in CNES indicated an MLI transparency of only 66.5%. This last result is surprising and clearly diverges from the other two estimates. We hypothesize that the experimental procedures in Toulouse may have encountered unrecorded issues, or there might have been errors in our data handling process. Further investigation and a thorough

Table 4.7: Summary of MLI transparency tests result.

Position	Count (Ge only)	Count (Ge + MLI)	Transparency
1 (300 s)	352459	297051	0.8428
2 (300 s)	354208	300469	0.8483
Average	353333.5	298760.0	0.8455 ± 0.003

Note: Both positions have a dead time $\sim$ 3 %.

review of the experimental processes are necessary. Given these difficulties, the MLI transparency value that we will use for the rest of this work is the one we measured at CEA on the flight sample, because it is the only one that we can control.

4.2.6 Global effective area of ECLAIRs in 4–8 keV

In this section, using the absolute measurements made with the ^{55}Fe source at 5.9 keV on the detection plane and on the MLI, we will calculate the global effective area in the 4–8 keV band. By global effective area we mean the number of effective square centimeters that remain after all the effects have been taken into account: the efficiency of the pixels, the overall transparency of the MLI and the overall transparency of the mask.

Due to the existence of HTP and LEP in 4–8 keV, the effective area of the ECLAIRs detection plane is inevitably decreased in this energy band. We calculated the global effective area and the loss area due to LEP and HTP in 4–8 keV as described below.

1. **Absolute efficiency of HEP pixels in the 4–8 keV range**

   We assumed that the HEP population represented the normal pixels, and that their average efficiency as a function of energy is consistent with the efficiency of the CdTe pixel with a Pt layer of 250 nm, as suggested by Remoué et al. (2010). However, we observed a small difference between the absolute efficiency value measured at 5.9 keV (0.777) and that theoretical calculation at the same energy (0.8). In the next steps we will explain how we correct and propagate this difference over the 4–8 keV range.

   To tune the efficiency ratio between the experiment and the numerical simulated one, an absorbing element was introduced to bring the numerical simulation value in line with the measurement at 5.9 keV. The idea is to introduce an additional layer of TeO_2, as found in Dubos et al. (2013).

   We kept the 250 nm of platinum and introduced a thickness of TeO_2 to obtain the drop in efficiency observed at 5.9 keV. We found a TeO_2 thickness of 127 nm. Once the models had been tuned at 5.9 KeV, we computed the estimated HEP absolute efficiency in 4–8 keV.

   The results are shown in Figure 4.23. In the blue line, we have the simulated efficiency with a Pt thickness of 250 nm. The green curve represents the efficiency of the Pt+TeO_2 model presented above. It can be seen that this model converges well

towards the absolute efficiency measured at 5.9 keV. The results are presented in table 4.8.

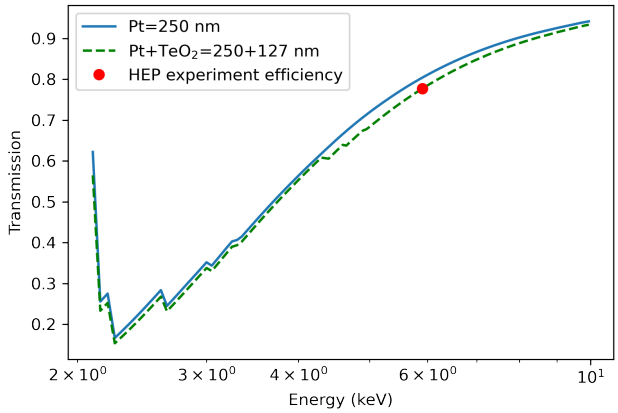

Figure 4.23: The blue lines represent the efficiency of a detector pixel with 250 nm Pt layer. The green line represents the efficiency of the Pt+TeO_2 model, which is based on the efficiency = 0.777 @ 5.9 keV obtained in the experiment.

2. **Absolute efficiency of all pixels in the 4–8 keV range**

   We have decided that the average absolute HEP efficiency ($\overline{\xi_{\mathrm{HEP}}(\mathrm{E})}$) calculated previously at different energies is our reference. To obtain the efficiency of each pixel from the distributions of the relative efficiency (Figure 4.8), for each energy bin of the distribution we applied Equation 4.11 where we divide the number of counts C_i by the mean count of HEP population ($\overline{C_{\mathrm{HEP}}}$) and we normalize by $\overline{\xi_{\mathrm{HEP}}(\mathrm{E})}$. This gives the pixel efficiency distributions shown in Figure 4.24.

$$\xi_i(\mathrm{E}) = \overline{\xi_{\mathrm{HEP}}(\mathrm{E})} \times \left(\frac{C_i}{\overline{C_{\mathrm{HEP}}}} \right) \tag{4.11}$$

3. **Absolute effective area of the ECLAIRs detector plane in 4–8 keV**

   In order to compute the absolute effective area of the detection plane ($A_{DP}(\mathrm{E})$), we applied Equation 4.12. For each energy and for each bin of the efficiency distributions in Figure 4.24 we multiply the absolute efficiency by the number of pixels and by the average area of a pixel (0.147 cm^2,). The results are shown in Figure 4.26 and Table 4.26.

$$A_{DP}(\mathrm{E}) = \sum_i \xi_i(\mathrm{E}) \times 0.147 \tag{4.12}$$

4. **Absolute effective area of the ECLAIRs telescope in 4–8 keV**

   To calculate the absolute effective area of the ECLAIRs telescope, we reintroduced the absorption of the MLI and the absorption of the mask.

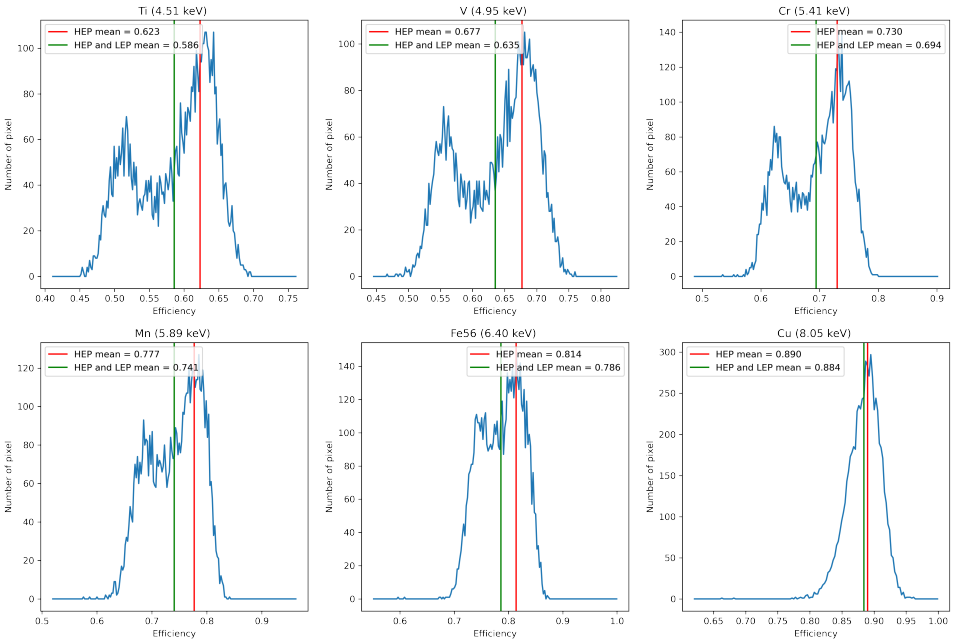

Figure 4.24: ECLAIRs CdTe pixels efficiency histogram (blue line) from 4.5 to 8.1 keV. The red line represents the means absolute efficiency of HEP, and the green line stands for the mean efficiency values of all pixels.

For the absorption of the MLI, we will use the model adjusted from our measurements carried out in CEA. In view of the lack of understanding of the various estimates presented in Section 4.2.5, we decided to retain the values for which we were most confident, as they were derived from a controlled measurement of a sample of the flight MLI. We recalculated the thickness of the MLI based on the transparency value obtained in CEA, then we got the adjusted thickness of MLI equal to 1.35 times that described in Table 4.6. The transparency of MLI ($\xi_{MLI}(E)$) we adopted finally is shown in Figure 4.25.

For the overall absorption of the mask we simply apply the aperture factor (0.60), which in the energy range under consideration (4–8 keV) represents the overall effective surface loss. The results are shown in Figure 4.26 and Table 4.26.

$$A_{ECLAIRs}(E) = A_{DP}(E) \times \xi_{MLI}(E) \times 0.4 \tag{4.13}$$

5. **Errors estimation**

Following the calculation process, the errors come from the ^{55}Fe source and MLI.

- Error of ^{55}Fe source ($\mathrm{err_{Fe}}$) ~ 3.7% at 95% confidence level.
- Error in MLI ($\mathrm{err_{MLI}}$) ~ 10% in thickness error in transmission ~ 1.2 % in 5.9 keV.

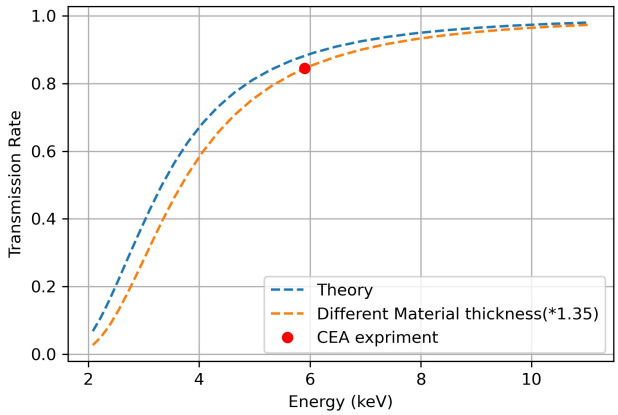

Figure 4.25: MLI transmission rate in 4–8 keV. The theoretical curve in blue is calculated based on the material component. The red point is the experiment result from CEA. The orange line is the model adjusted to the measurement point.

$$\text{Err} = \sqrt{\text{err}_{\text{Fe}}^2 + \text{err}_{\text{MLI}}^2} = \sqrt{0.037^2 + 0.012^2} = 3.9\% \tag{4.14}$$

6. **Result of global effective area**

   Finally, we got the effective area of the detection plane and the whole ECLAIRs, and compared it with the simulation result in Sizun (2011) and Olivier Godet et al. (2022). We summarized those results and presented them in Figure 4.26. We found that the effective area was reduced ∼100 cm^2 due to the HTP and LEP.

- HTP: 400 pixels in total, which lead to a loss of about 58.8 cm^2. Each pixel has an area of 0.147 cm^2 (Carine et al., 2011). We also took into account some ”dead pixels” and non-working XRDPIX (38 pixels), in total lost about 64 cm^2.
- LEP: the loss area related to the energy that they introduce, compared to the case where all pixels are HEP: 4.51 keV: 32.37 cm^2, 4.95 keV: 36.59 cm^2, 5.41 keV: 31.58 cm^2, 5.89 keV: 31.93cm^2, 6.40 keV: 24.43 cm^2, 8.05 keV: 5.36 cm^2.
- Difference between Geant4 simulation and experiment: the difference between the efficiency calculated using the Fe^{55} dataset and the one from the simulation in Remoué et al. (2010) is : (1-0.777/0.804)= 3.4 %; about 0.034*6400*0.147 cm^2 ~ 32 cm^2

Compared to the ideal detection plane with only HEP (without inhomogeneity effect), the HTP reduces the effective detection area by 6.25%. The LEP reduces the effective detection area by 5.93%, 6.17%, 4.94%, 4.67% and 3.42% at 4.5 keV, 5.0 keV, 5.4 keV, 5.9 keV and 6.4 keV, respectively.

Although we can configure the trigger software to mitigate the impact from the inhomogeneities of the detection plane in the 4–8 keV band, the effective area of the ECLAIRs detection plane is inevitably decreased by approximately 100 cm^2 in this energy band.

Table 4.8: The absolute effective area of ECLAIRs in 4-8 keV

Energy (keV)	4.51	4.95	5.41	5.89	6.40	8.05
Pixels theoretical Efficiency (Pt = 250 nm)	0.652	0.714	0.761	0.804	0.837	0.904
Mean efficiency of HEP	0.630	0.690	0.735	**0.777**	0.809	0.873
Mean value of efficiency for detection plane	0.592	0.647	0.683	**0.740**	0.781	0.868
Involved number of pixels	5962	5962	5962	5992	5962	6359
Effective area of detection plane (cm^2)	513.63	556.75	608.2	652.47	688.97	826.59
Effective area of ECLAIRs (cm^2)	141.87	168.65	196.56	219.93	242.72	310.59

Note: here ECLAIRs means the detection plane with the MLI (with transparency measured in CEA) and the mask (40% fraction). Bold numbers are derived from the ^{55}Fe measurements.

As a consequence, the detection sensitivity will decrease by a few percent in this energy band, and the detection rate of soft GRBs (for example X-Ray flashes) might be reduced. More detailed studies need to be conducted in the future to quantify this rate.

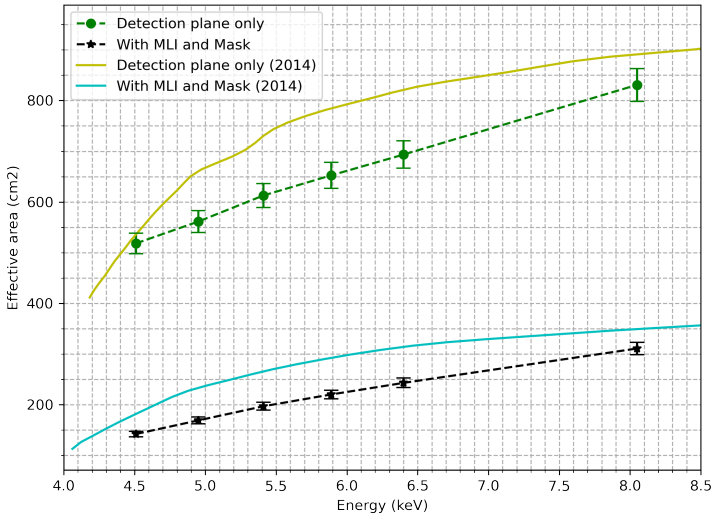

Figure 4.26: Effective area of ECLAIRs in 4–8 keV for different situations: the light blue and orange lines represent the ideal results of the simulation in Stéphane Schanne, Bertrand Cordier, et al. (2014). The dash-dotted lines in green represent our results. The green lines represent the effective area in the scenario where the CdTe pixels surface layer is 250 nm Pt plus 127 nm TeO_2.

The effective area comparation between ECLAIRs and other GRB telescopes could be

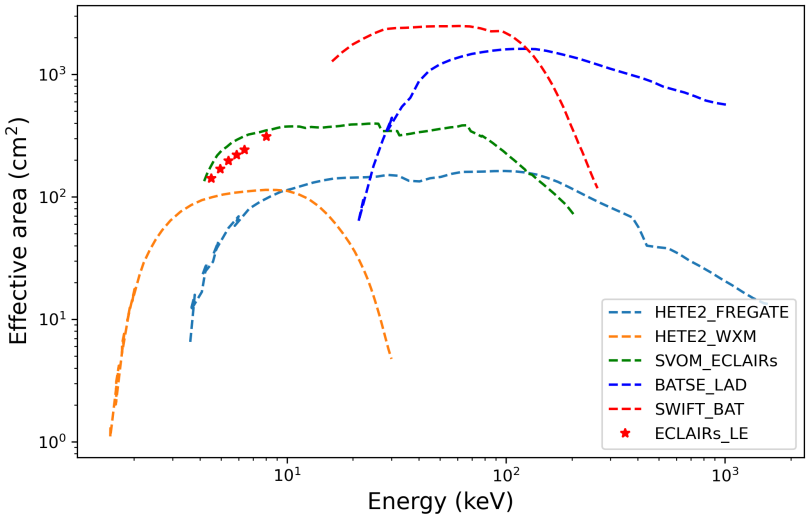

Figure 4.27: ECLAIRs Effective area compare with other missions. Including Wide X-ray Monitor (WXM) and FREGATE telescope in HETE-2 mission, Large Area Detector (LAD) in BATSE, Burst Alert Telescope (BAT) in Swift satellite. The red stars are the effective area values measured in this work in the 4-8 keV band, the green dashed line represents the simulated effective area of ECLAIRs. The plot adapted from Sakamoto et al. (2011).

found in the Figure 4.27. For the energy band above 15 keV, ECLAIRs have less effective area ($\sim$ 400 cm^2) compare to BAT/Swift ($\sim$2000 cm^2) and LAD/BATSE ($\sim$ 1000 cm^2). However, ECLAIRs has greater effective area (1.5 time up to 3 time) in the 4-15 keV band compare to the WXM/HETE-2 and FREGATE/HETE-2. This will provide a unique advantage for SVOM mission in detecting the soft GRB with lower peak energy from few keV to several decades of keV.

4.3 Impact of the efficiency inhomogeneity

To study the impact of LEP and HTP on the onboard imaging trigger performances and on the detection of sources, we built a dedicated simulation process.

1. Simulate the orbital background seen by ECLAIRs due to the CXB (Moretti, 2009) assuming perfect performances for the detection plane in the 4–8 keV band (This CXB Model was adjusted with data from 1.5-200 keV energy band using XRT and BAT). The simulation is processed with a Python library wrapping the same C++ code (named ssbpy package) as the one used for the onboard trigger. 64 shadowgrams are simulated, each exposed for 20.48 s. These shadowgrams are deconvolved, and the 64 sky images are stacked together to reach a total exposure time of 1310.72 s. In this simulation, all pixels are assumed to have an efficiency of 1.0.

2. Conduct the same CXB simulation as in step 1 but with LEP or HTP. In this case, the

HEP pixels are assumed to have an efficiency of 1, and the efficiency of LEP is set to a value in each 1 keV bin, which depends on the ratio shown in Figure 4.28. The HTP efficiency is set to 0 in 4–8 keV.

We choose the dataset of the Cr target (5.4 keV) to associate each pixel of the detection plane to one of the three populations, since it is easier to separate the two Gaussian peaks, as shown in the left panel of Figure 4.28. The ratio of the Gaussian mean value between the HEP and LEP populations in the 4–8 keV band is also shown in the right panel of Figure 4.28. The relationship between the efficiency ratio of the LEP compared to the HEP population versus energy could be fitted with a simple linear equation.

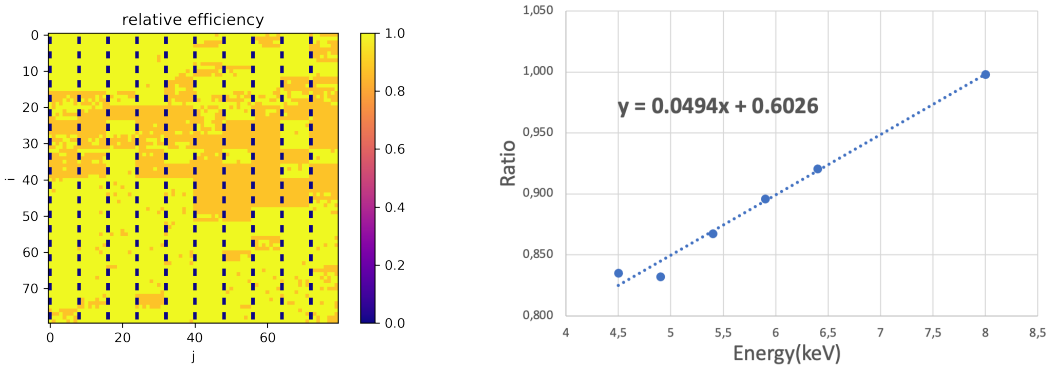

Figure 4.28: The three populations of pixels found in the ECLAIRs detection plane are shown on the left (HTP: black, LEP: orange, HEP: yellow). The ratio of the mean number of relative counts between the LEP and the HEP as a function of energy is shown on the right, and fitted with a linear function.

In an ideal situation, where the shadowgram is filled with a flat background observed for a sufficient time, the sky signal-to-noise ratio (SNR) produced by the deconvolution follows a normal distribution with $\sigma_{\mathrm{SNR}} = 1$. In this case, the canonical 3σ detection threshold in one of the pixels of the sky becomes 5.4 when the entire image of the sky is considered Nicolas Dagoneau, 2020. In practice, the background, which is not flat, is subtracted and previous studies have set the detection threshold to $6.5 \times \sigma_{\mathrm{SNR}}$ in order to dynamically adapt the threshold according to the distribution of SNR (Dagoneau et al., 2022).

One of the simulation results with a perfect detection plane only exposed to the CXB, as well as the impact of LEP and HTP, is shown in Figure 4.29. In the case of the perfect detection plane (first row), a normal distribution of SNR is obtained after the deconvolution and σ_{SNR} equal 0.984, which is close to the ideal theoretical value of 1. In the second, when the LEP attenuation effect is included in the simulation, the σ_{SNR} value of the sky image is equal to 1.436. This means that the trigger threshold in 4-8 keV would increase by 43.6% due to the LEP impact. If we consider only the HTP, some stripes appear in the sky image, as shown in the third row. These stripes strongly reduce the quality of the sky image, and the threshold will increase by a factor of 5.753 since σ_{SNR}= 5.753.

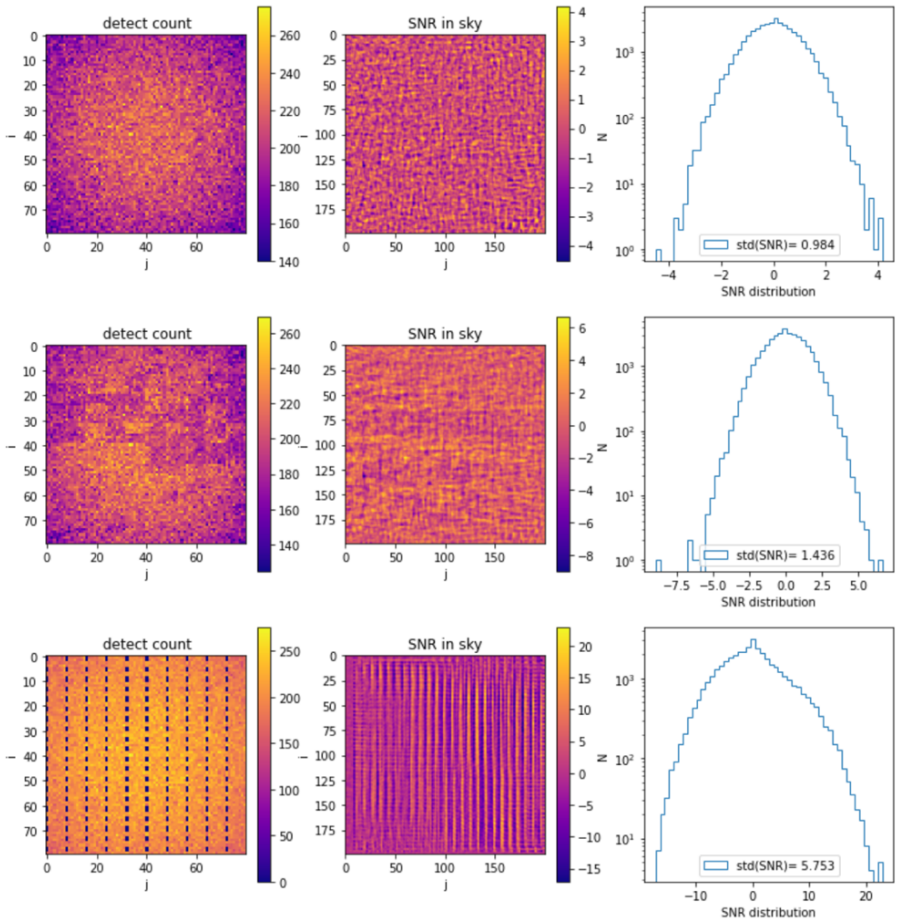

Figure 4.29: Simulation of the CXB on a perfect detector (row 1), with simulated LEP attenuation (row 2), and with HTP switched off in the simulation (row 3). Left: simulated detector-count distributions. Middle: deconvolved sky images in SNR without applying any correction. Right: distribution of the SNR of all pixels for the images shown in the middle column.

4.4 Onboard trigger mitigation method

To mitigate the impact of the attenuation caused by LEP and HTP, different solutions have been developed and applied in the processing, as shown in Figure 4.30. For HTP, the solution involves setting the weight of those pixels to 0 for the background fitting table and for the deconvolution table in the trigger algorithm (described in Chapter 3). This means that the HTP counts are ignored in the trigger algorithm in the 4–8 keV energy band. For LEP, since the attenuation effect is taken into account, an efficiency correction based on the background photon spectrum has been applied in order to estimate the detection counts without the LEP attenuation, which is the shadowgram subsequently used in the deconvolution process.

The trigger algorithm works in four configurable energy bands. Therefore, the key is to determine the correction factor to be applied in each specific energy band. This correction

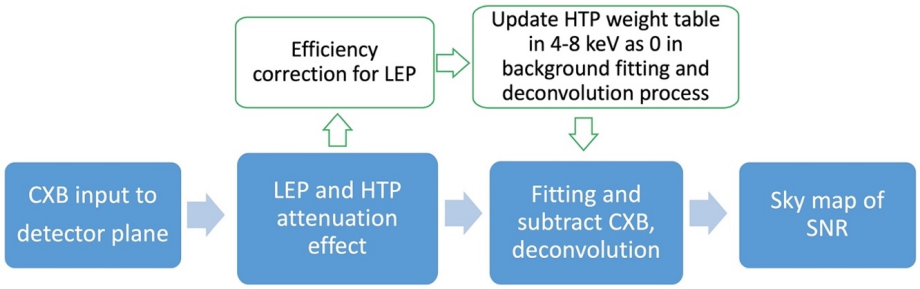

Figure 4.30: Simulation process after applying the mitigation methods for LEP and HTP. The blue blocks represent the standard imaging process without correcting the inhomogeneity effects. The white upper blocks represent the additional actions to mitigate the impact of the LEP and HTP.

factor depends on the spectrum of the observed source and the efficiency of the pixels computed in this band. To compute this efficiency, we choose 1 keV bins in which the efficiency is constant. We calculated this correction factor by using Equation 4.15.

$$f_{E_{\rm low},E_{\rm high}} = \frac{\sum_i \varepsilon_i N_i}{\sum_i N_i} \tag{4.15}$$

In Equation 4.15, $f_{E_{\rm low},E_{\rm high}}$ is the correction factor in the specified energy band, i is the index of the 1 keV energy bin, ε_i represents the efficiency of the pixel in the bin i. N_i stands for the source counts in the bin i given by Equation 4.16.

$$N_i = \int_{i_{\rm low}}^{i_{\rm high}} N(E)dE \tag{4.16}$$

In Equation 4.16, i_{low} and i_{high} indicate the low and high boundary of the energy bin i. $N(E)$ represents the CXB spectrum (Moretti, 2009). We choose the CXB spectrum because the CXB counts are dominant compared to the point-like sources, and because the homogeneity of the detection plane has to be primarily ensured during periods without GRBs (most of the time) in order to avoid false alerts. Also in the case of a weak GRB, the background will be dominant. In the case of a strong GRB, a slight inhomogeneity does not impact its detection and localization. As a result, the average efficiency correction factor $f_{4,8}$ we obtained is 0.875 in 4–8 keV.

After the methods discussed above have been applied in the simulation, the result of sky SNR distribution is shown in Figure 4.31. The distribution of sky SNR becomes uniform, and the σ_{SNR} value decreases to 1.012, which is close to the theoretical value of 1. Therefore the method we used is sufficient to mitigate the impact caused by the efficiency inhomogeneity on the detection plane.

In order to demonstrate the impact of the efficiency inhomogeneity more clearly, we conducted another simulation by setting the background value equal to 10 times the value of the CXB. The results are shown in Table 4.9. We found that the solution we proposed

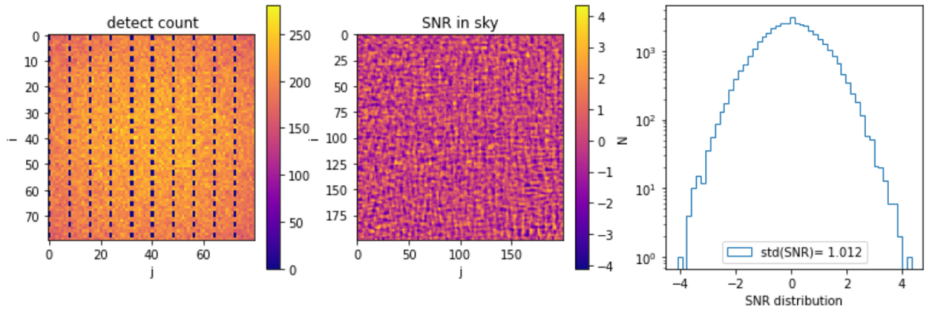

Figure 4.31: Simulation result in the 4–8 keV band for a 20 min exposure after applying the efficiency correction on the detector-plane image for LEP and ignoring the counts from HTP during the deconvolution process.

Table 4.9: Simulation result of sky σSNR which involved the LEP and HTP impact (without correction) and after applying the mitigation methods (with correction). $10 \times$ CXB indicates that the background value of CXB is set to 10 times the true value.

Background	Include effect	Std (SNR) without correction	Std (SNR) after correction
CXB	LEP	1.436	0.997
	HTP	5.753	0.997
	LEP and HTP	5.785	1.012
10*CXB	LEP	3.128	1.138
	HTP	16.059	1.035
	LEP and HTP	16.135	1.138

could effectively mitigate the impact induced by HTP and LEP, even in a situation where the background was equal to 10 times CXB counts. After applying the correction method, the σ_{SNR} decreased from 16.13 to approximately 1.13.

4.5 Conclusion and future perspective

In 2021, ECLAIRs was under serious calibration testes in Toulouse, we took the raw data out and performed the analysis. Those datasets we selected are using the X-ray photon source with an energy in the 4-8 keV range.

1. I analyzed the inhomogeneity of the detection plane in different energies. There are three population pixels we named High Threshold Pixels (HTP, 400 pixels), High Efficiency Pixels (HEP, $\sim$ 4000 pixels) and Low Efficiency Pixels (LEP, $\sim$ 2000 pixels). We found that the efficiency difference between LEP and HEP decreases with the energy in 4–8 keV, the difference could be described with a liner function: $\Delta_{\text{eff}} = -0.052 \times E_{\text{keV}} + 0.417$. Above 8 keV, those two populations show the homogeneity properties.

2. For the reason of the efficiency difference between LEP and HEP, we proposed it may be due to the thickness difference of the surface material between different population CdTe pixels. We calculated the thickness difference value for several possible models: if only one material component is different, we have a thickness different value for Pt $\sim$123 nm , for TeO2 $\sim$ 460 nm. A more realistic possibility is due to the combined effect of the thickness difference of both materials.

3. We analyzed the dataset with Fe^{55} as an X-ray source, and obtained the absolute efficiency of CdTe pixels. For the HEP, the efficiency is 0.777 $\pm$ 0.022 and for LEP, the efficiency is 0.694 $\pm$ 0.023.

4. We got the transparency of MLI layer = 0.665 in Fe55 dataset, However, the theoretical transparency = 0.887. We conducted a dedicated MLI test in CEA, finally we got MLI transparency is 0.845 $\pm$ 0.003, in agreement with the theoretical value.

5. Based on the detection plane efficiency in 5.9 keV, we extended the efficiency value to the 4-8 keV range based on the transparency of Pt=250 nm for the CdTe pixels, and the relative count distribution in 4–8 keV. Finally, we got the photopeak effective area for ECLAIRs of 219.93 cm^2 in 5.89 keV, which concerns the impact of LEP and HTP.

6. We performed the simulation to study the impact of LEP and HTP on the onboard trigger performance. Ideally, the SNR of sky maps is normally distributed with $\sigma_{SNR} \sim 1$ in a 20 min observation timescale. After introducing the effect of efficiency inhomogeneity, the σ_{SNR} in the 4–8 keV band increased to 5.75 and 1.43 for HTP and LEP, respectively.

7. We developed the approach to mitigate the impact of efficiency inhomogeneity. Most of the impact of HTP can be corrected by setting their weights to 0 in the background fitting table and in the deconvolution table of the trigger algorithm, which means excluding those pixels during the data processing in the trigger. To correct the impact of LEP, the efficiency correction in the shadowgram before the deconvolution could be a good solution.

Outlook: how to determine the absolute efficiency of the detection plane during the commissioning phase

SVOM satellite is scheduled for launch in June 2024. During the initial months post-launch, a commissioning phase will be undertaken to adjust the satellite and its instruments, ensuring they function as expected. The absolute efficiency of these instruments is crucial for detecting GRBs and conducting other scientific research. To ensure having the accurate efficiency across all pixels of the ECLAIRs detection plane, we propose several solutions to be implemented during the commissioning phase and future observations.

- Utilizing Crab as the calibration source, we can accurately calculate the absolute efficiency of illuminated pixels. This is feasible because the exact observation time and the spectrum of Crab are known. Comparing these calculations with our relative efficiency table, we can then determine the absolute efficiencies for all pixels.

- By conducting multiple observations of Crab in various pointing directions, we can illuminate different pixels each time. This method allows us to calculate the absolute efficiency of the pixels illuminated during each observation. Subsequently, we can combine these calculations to create a comprehensive efficiency profile for all pixels.
- Using only the Cosmic X-ray Background (CXB) as a reference, we can calculate the absolute efficiency of pixels. This method requires a highly accurate CXB spectrum model. By selecting data that exclusively contains CXB, excluding any X-ray sources and avoiding earth obstruction, we can accurately determine the efficiency of each pixel.
- Utilizing prolonged exposure to reflection and Albedo background during the earth occultation phase enables us to determine pixel efficiencies. A significant advantage of this method is that it eliminates the need to account for the background of the X-ray source. However, it is crucial to have a highly accurate spectrum model for these backgrounds to ensure precise efficiency calculations.

Chapter 5

Heat-pipes noise in the ECLAIRs detector plane

Contents

5.1 Heat-pipes noise in the thermal vacuum chamber test

In 2021, a series of test campaigns were performed on the ECLAIRs flight model in a thermal vacuum test chamber (hereafter TVAC) at the French Space Agency (CNES) in Toulouse. The test was performed on the complete Flight Model (FM) (detector plane, MLI, coded mask, shield) that will be carried on the SVOM satellite.

There were two scenarios during the test. Firstly, no X-ray source was used to simulate the instrument's operation in a space vacuum. Secondly, an X-ray source (either Fe^{55} or X-ray generator, see 4) was installed in front of the telescope for a certain period of time to simulate a constant source or a GRB in the sky.

The TVAC data (counts position, time and energy) was divided into 20 s time-bins and count images of the entire detector plane were created for each time-bin. The total number of counts in the images changed over the time during the experiment, as shown in Figure 5.1 (right).

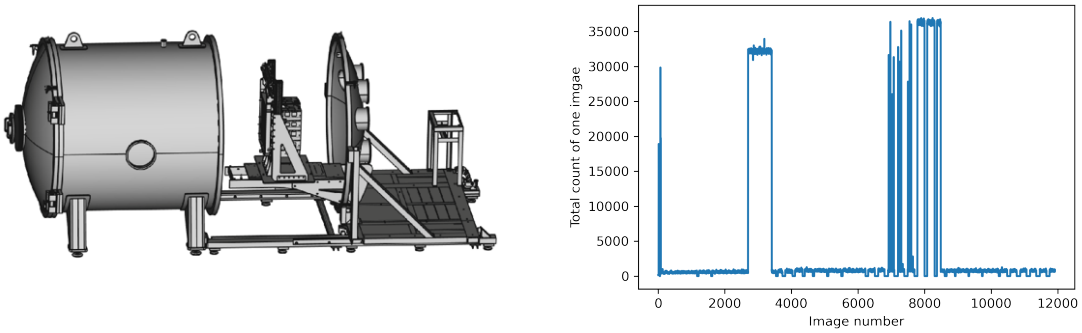

Figure 5.1: Left: configuration of TVAC test. Right: count lightcurve of TVAC data in 20 s time-bin.

Figure 5.2 displays an example of a detector image with and without an X-ray source in different energy bins: 4–10 keV, 10–15 keV, 15–30 keV, and 30–50 keV, respectively. The mask pattern becomes evident when the X-ray source is present. However, in the absence of an X-ray source, some unusual counts appear in the left columns of the detector plane in the 4–10 keV images compared to the random distribution in the 10–30 keV.

This high noise count-rate below 10 keV, which appears in an unexpected way, has been named "heat-pipe noise" (as described in Arcier, 2022). It is located in the heat-pipe area and appears to be connected to the heat-pipe operations, though the underlying physics remains unclear. It is important to note that one of the key features of the SVOM mission is that ECLAIRs aims to extend the detected energy band down to 4 keV. Therefore, it is critical to thoroughly study the heat-pipe noise characteristics and to find ways to reduce its impact on the detection of faint GRB sources.

(Arcier, 2022) has studied the characteristics of the heat-pipe noise based on the spectral,

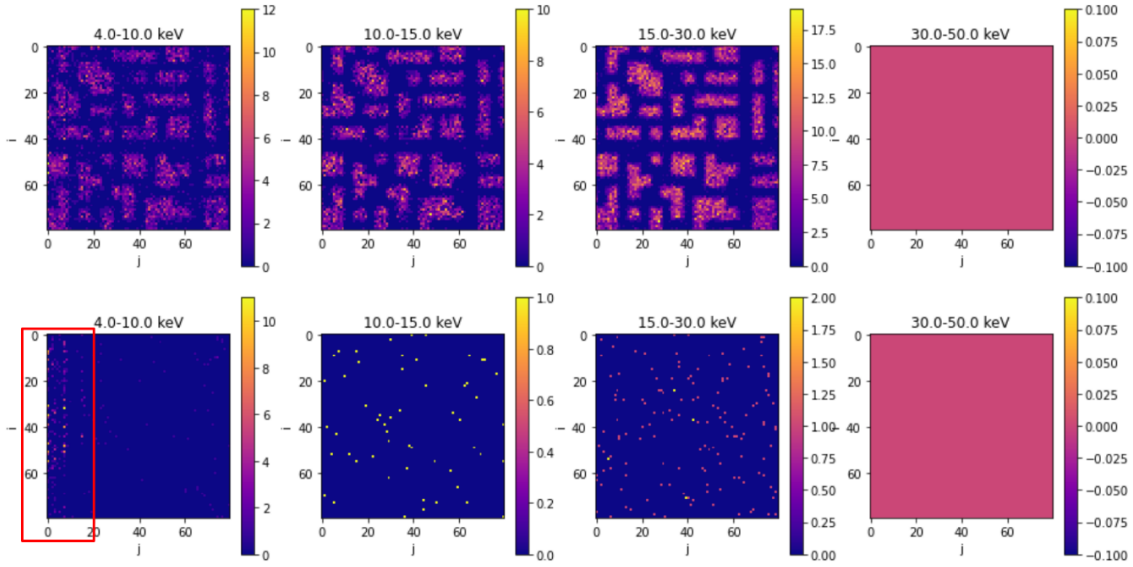

Figure 5.2: 20 s image example of count distribution with X-ray source (top) and without X-ray source (bottom) TVAC data in different energy bins, from left to right: 4–10 keV, 10–15 keV, 15–30 keV, 30–50 keV.

spatial, and temporal aspects. Based on the characters (time difference distribution, energy distribution and the pixel position distribution), he developed a method to clean this noise a posteriori for ground data exploitation. Here I focus on the detailed impact of the noisy pixels on the ECLAIRs trigger performance, and develop mitigation methods which operate in real time and which could be implement in the on-board trigger.

5.2 Characteristics of the heat-pipes noise

In this subsection, we will focus on the data without X-ray source in TVAC and analyze the heat-pipe noise. we are only interested in the noise images that display the heat-pipes noise without the presence of an X-ray source. We selected images with a total count between 100 and 1500, excluding the period during which the X-ray source was present and the switch-off state. Ultimately, 8690 images, representing approximately two days of data, were selected and the lightcurve is displayed in Figure 5.3.

5.2.1 Energy distribution

To determine the precise energy distribution in which the heat-pipes noise occurs, we divided the selected data into energy bins ranging from 4–15 keV. As shown in Figure 5.4, the heat-pipes noise is clearly evident in the 4–8 keV range, with a few counts present between 8 keV and 9 keV. Above 9 keV, the count distribution in the detector plane is uniform and has almost no effect. With respect to counts in the 4–8 keV range, the heat-pipes noise increases as the energy decreases and is strongest in the 4–5 keV range in our data.

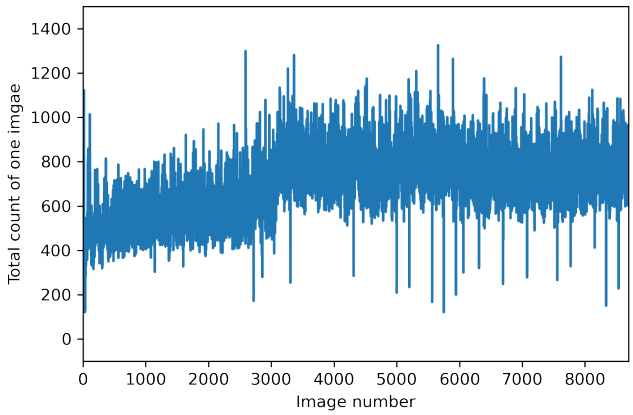

Figure 5.3: 20 s time bin lightcurve of TVAC data after removing period of time with X-ray source and where SVOM is simulated in SAA.

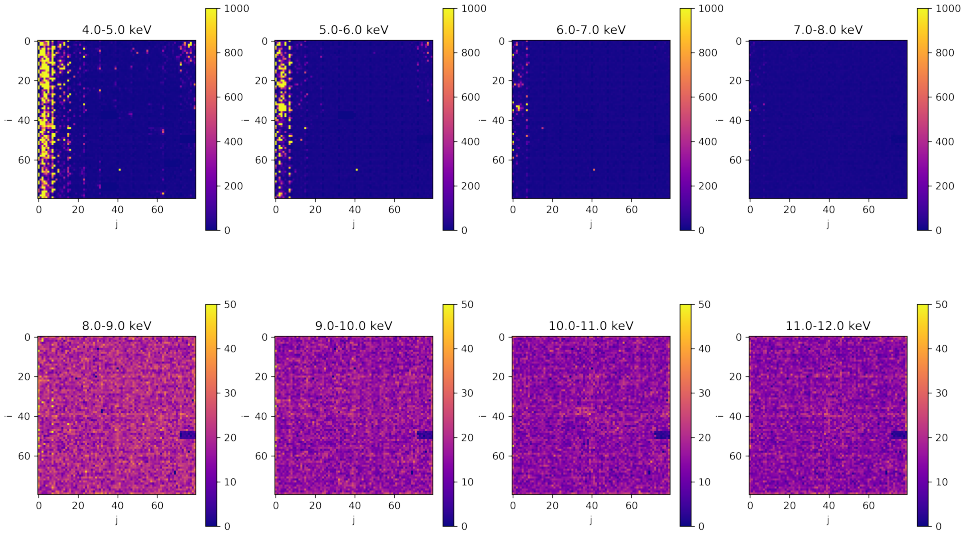

Figure 5.4: Images of the detected number of counts per pixel in 8 energy bands (from 4 to 12 keV) integrated over all 1.74×10^5 s of TVAC data where no X-ray source is present (background exposures only). The heat-pipe noise appears in the 4 to 8 keV energy band as pixels with abnormally high count-rates. Note: there is one detector module of 4×8 pixels on the right not working nominally, showing zero counts.

5.2.2 Time distribution

We divided 20 second images into smaller time-bins (1 s and 10 ms) and generated lightcurves in different energy bins to study the heat-pipes noise in various time frames. As shown in Figure 5.5, as we went into smaller time-bins, for example 1 s in Figure 5.5(b), we found that the sudden increase in counts was primarily due to the 4–8 keV range. This phenomenon could be clearly observed in the 10 ms time-bin lightcurve in Figure 5.5(c). In the 10 ms

time-bin, counts are always between 0 and 2 in the 8–50 keV range. However, counts in the 4–8 keV range often exceed 2 and reach 5–25 counts in the 10 ms time-bin. This means that we may be able to separate the heat-pipe noise from the normal background in the 10 ms time-bin counts based on this characteristic.

5.2.3 Spatial distribution

To determine the spatial distribution of the heat-pipes noise, the total count of pixels in the 8690 selected images in the 4-50 keV range was calculated. The pixels were ranked by total count events and the 500 pixels with the highest counts were selected and displayed in Figure 5.6. We found that the heat-pipes noise primarily occurs on the left side of the detector plane in this TVAC test, with a few pixels in the upper right corner of the detector plane also exhibiting abnormal counts.

We selected three pixels as examples, ranked 1, 2, and 100 on the right side of Figure 5.6, for further analysis to understand what occurred in the individual pixels during the experiment. The 20 s image count lightcurves of these pixels are shown and their 20 s count statistics distributions are presented on the left side of Figure 5.6.

For the pixel ranked 1, it is sometimes quiet with no noise, but sometimes it experiences a sudden increase in count, which we have named a Highly count-rate Noisy (HCRN) pixel. Two HCRN pixels were found in the TVAC data and these will be automatically excluded during onboard operations in the new version of the onboard software.

For the pixel ranked 2, the count in the images is relatively stable over time and its statistical distribution is approximately a Poisson distribution with a mean value of 6 counts per image.

For the pixel ranked 100, the count in each image is also stable with a value ranging from 0 to 1 count per frame.

5.3 Impact of heat-pipe noise and mitigation solution

The heat-pipe noise observed in TVAC experiments may also occur in onboard observations and may impact source detection. To determine the effect of the heat-pipe noise on observations, dedicated simulations are conducted using the onboard trigger software.

5.3.1 Impact of heat-pipes noises on the trigger performance

In this section, we carried out simulations using the onboard software and TVAC data to assess the potential impact of the heat-pipe noise on the detection of ECLAIRs sources. The principle of the simulations was to add heat-pipe noise data into the detector plane while simulating the onboard X-ray background, then to process the data to obtain the sky's SNR

Figure 5.5: From top to bottom, lightcurve figure of TVAC test in 10 ms, 1.0 s, 20 s time-bin in different energy bands.

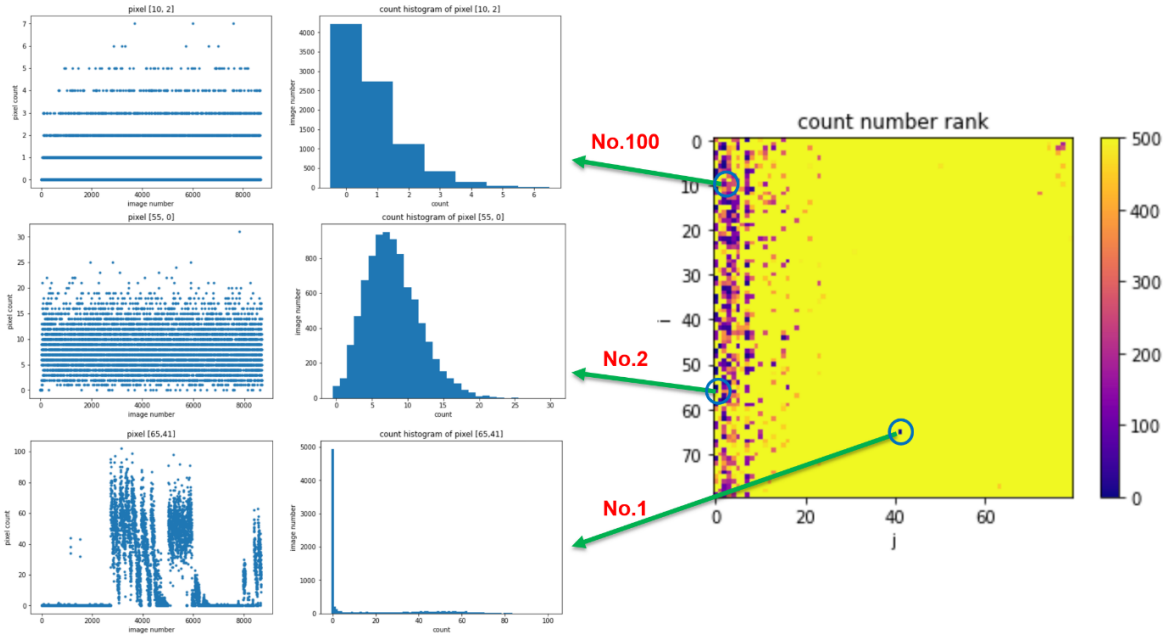

Figure 5.6: Right panel: rank spatial distribution total count in 4–8 keV. The total counts are in descending order from 1 to 500. Left panel: count lightcurve and histogram statistics of few detected pixels. The total count of pixels ranked from top to bottom is 1, 2 and 100, and the positions of the pixels in the detector plane are (65,41), (55,0), (10,2), respectively.

distribution, and finally to calculate the maximum SNR in the sky and the trigger threshold, which is 6.5 times the standard deviation of SNR (σ_{SNR}). The simulation process is as follows.

1. Simulate the CXB background and project the CXB count into the detection plane in the 4–8 keV range.
2. Add the TVAC counts of 4–8 keV in the detection plane for the same duration as the CXB background.
3. Process the combined data using the count-rate trigger (10 ms to 20.48 s) or the image trigger (20.48 s to 20 min) for different timescales. For the image trigger, in addition there is a background fitting and subtraction operation for each timescale image. Save the data of the standard deviation of sky SNR, the value of the maximum SNR and the related position in the sky image.
4. Repeat steps 2 and 3 until all TVAC data is used, and compute the statistical results with the impact from the heat-pipe noise.

Figure 5.7 shows simulation examples of the impact of the heat-pipe noise on ECLAIRs in 10 ms, 20.48 s, and 20 min observations, from top to bottom in different rows. The left three columns represent the detector count distribution of CXB, TVAC, and CXB mixed with TVAC, respectively. It can be seen from the TVAC mixed with CXB images that the impact of the heat-pipe noise increases over time. As a result, the distribution of SNR widens as the timescale increases. In the 20-minute SNR distribution, although the trigger threshold

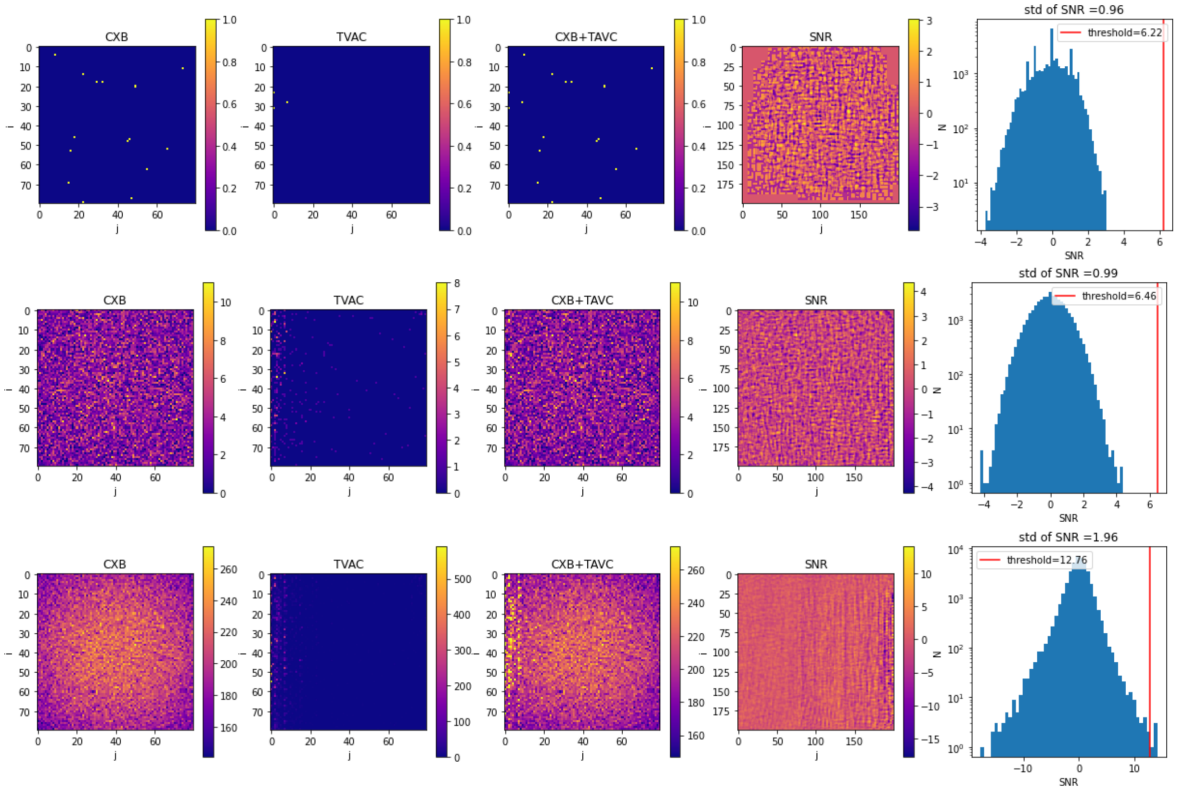

Figure 5.7: Impact of heat-pipes noise on ECLAIRs observation in different timescales. From top to bottom: 10 ms, 20.48 s, and 20 min observation simulation, respectively. The panels from left to right correspond to CXB count, TVAC count, CXB mixed with TVAC count, SNR sky map, and SNR distribution. The red line on the rightmost image is the trigger threshold, the trigger threshold of ECLAIRs is equal to 6.5 stdSNR here.

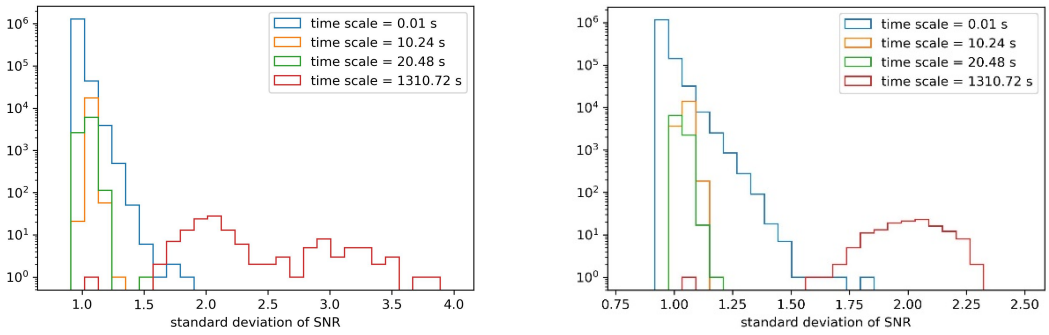

Figure 5.8: Left: relative threshold (σ_{SNR}) after taking the TVAC data into account in different timescales. Right: relative threshold distribution after removing 2 high count-rate noisy (HCRN) pixels.

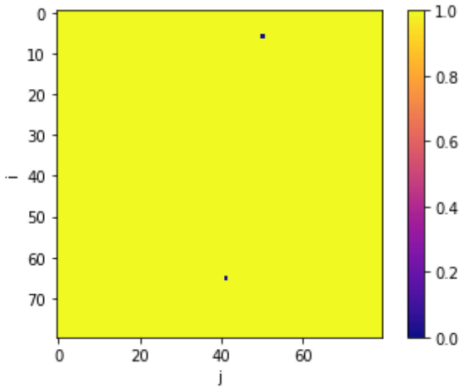

Figure 5.9: Two high count-rate noisy (HCRN) pixels selected in the TVAC data

value increases to 1.96 times, there are still some SNR points in the sky that exceed the threshold. This indicates that heat-pipe noise not only increases the trigger threshold, but also can cause false triggers.

5.3.2 Impact on the trigger threshold

Ideally, the standard deviation of the sky SNR should be close to 1.0 in the absence of heat-pipe noise. After adding the heat-pipe noise from the TVAC data in the simulation, the effect on the detection threshold is depicted in Figure 5.8(a). There are some high count-rate noisy (HCRN) pixels that exhibit abnormal behavior, as discussed in Section 5.2.3. We found that the standard deviation of SNR is mainly affected by those HCRN pixels over a long timescale, such as 20 minutes. Since their count-rate increases irregularly and they are not located on the column where the heat-pipes are situated, their impact is not part of the heat-pipe noise we are discussing here. During in-orbit operations, these HCRN pixels counts will be discarded and will be removed from the algorithm. There are 2 HCRN pixels found in the TVAC data, as shown in Figure 5.9.

We ran the simulation again after removing the 2 HCRN pixels. The result is shown in

Figure 5.8(b). In a 10 ms count trigger, the trigger threshold may increase by up to 80%. As time progresses, both CXB counts and TVAC counts increase, but CXB counts increase more rapidly than TVAC counts. In the simulation, the CXB counts detected by the detector plane steadily increase at a rate of approximately 15 counts per 10 ms. TVAC counts are usually 0 or 1 every 10 ms. As a result, the impact of heat-pipe noise on the trigger threshold will be reduced by the CXB counts as the timescale increases. With a count-rate trigger timescale of 10.24 s, the trigger threshold can increase by a maximum of 15%.

In the timescale of image trigger, ranging from 20.48 s to 20 min, there are background fitting and subtraction processes, as well as a deconvolution for each 20.48 s image. With the background counts removed and the accumulation of heat-pipe noise counts, the effect of the heat-pipe noise gradually becomes noticeable. As shown in Figure 5.8(b), the maximum increase in the threshold in 20.48 seconds is around 20%. However, in the timescale of 20 min, the maximum increase in the threshold value becomes 120%.

5.3.3 False trigger caused by the heat-pipe noise

The false trigger rate is also an important parameter for evaluating the impact of heat-pipe noise. A false trigger occurs when the instrument generates a trigger signal despite there being no transient source in the sky. It can be caused by the intrinsic noise of the instrument or the surrounding background. The simulation of the false trigger rate with the addition of heat-pipe noise is the same as discussed in Section 5.3.1. The occurrence of a false trigger in each simulation depends on the ratio of the maximum value to the standard deviation ($\max_{SNR}/\sigma_{SNR}$) of the sky images. If $\max_{SNR}/\sigma_{SNR} > 6.5$ (trigger threshold), a false trigger will occur. The results of the false trigger simulation are shown in the following Figure 5.10.

In the 4–8 keV energy range, we found no cases of false triggering within the timescales of 10 ms to 0.64 seconds. However, in the timescale of 1.28 s to 163 s, we observe some cases where the significance is above the trigger threshold. For timescales greater than 163 seconds, the $\max_{SNR}/\sigma_{SNR}$ values are distributed like a Gaussian, as shown in Figure 5.11(c), and a significant part of the right wing of the Gaussian is above the threshold. The false trigger rate in the 4–120 keV energy range, impacted by heat-pipes noise, is displayed in Figure 5.11. This result is similar to the one in the 4–8 keV range for timescales less than 81.92 s. However, for the timescale > 81.92 s, the mean value of the $\max_{SNR}/\sigma_{SNR}$ distribution in the 4–120 keV range is smaller than in the 4–8 keV range, due to the uniform distribution of 8–120 keV CXB photons reducing the impact of heat-pipe noise.

We utilized the TVAC data (1.7×10^5 s) to simulate the false trigger rate caused by heat-pipe noise in all timescales for both 4–8 keV and 4–120 keV energy ranges. The results are presented in Table 5.1 and Table 5.2. We calculate the false trigger rate as false trigger cases divided by total cases. In the 4–8 keV range, there will be false triggers when the timescale exceeds 1.28 s. In timescales from 1.28 s to 81.92 s, the probability of false triggers is relatively random and irregular. When the timescale is greater than 81.92 s, the false trigger rate increases steadily with time.

At a timescale of 20 min, the false trigger rate is equal to 99.26%, indicating that almost all cases have false triggers when heat-pipe noise is present. In the 4–120 keV range, there

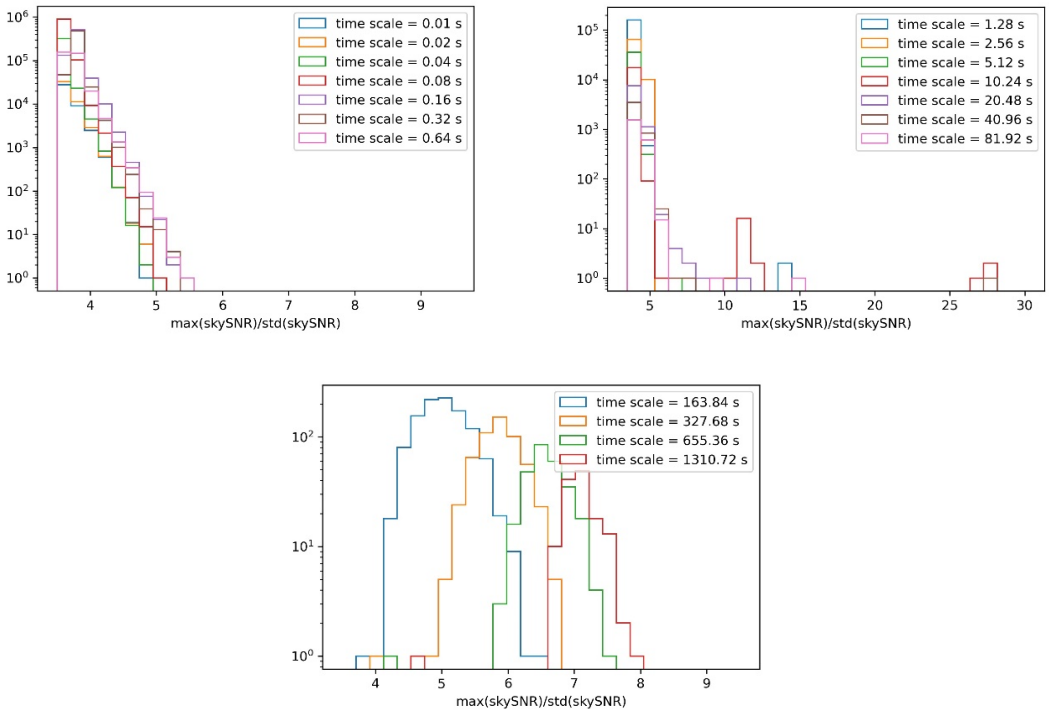

Figure 5.10: $\max_{\mathrm{SNR}}/\sigma_{\mathrm{SNR}}$ distribution in different timescales in 4–8 keV

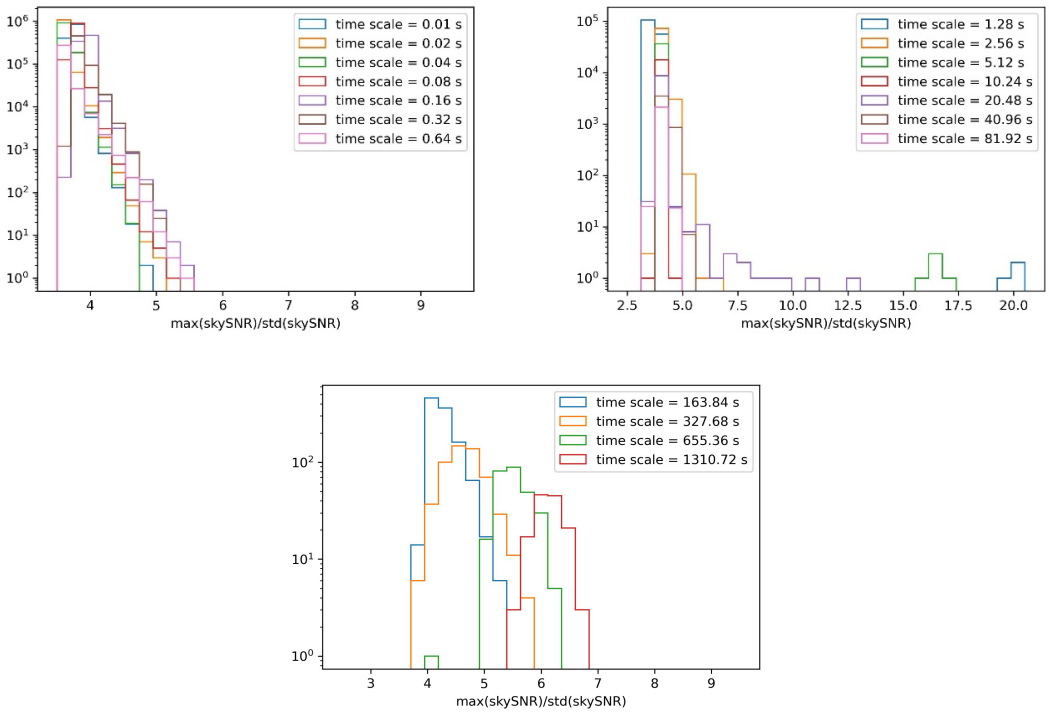

Figure 5.11: $\max_{\mathrm{SNR}}/\sigma_{\mathrm{SNR}}$ distribution in different timescales in 4–120 keV

is a lower false trigger rate compared to the 4–8 keV range, as the background photons in

Table 5.1: False trigger rate resulting from heat-pipes noise in the count-rate trigger, the result from the simulation combines the simulated CXB with 1.74×10^5 s of TVAC data. As for example, the false trigger rate is 0.136% for a timescale of 10.24 s with a energy range of 4-8 keV. We can have 10 false (fake) triggers per day with a trigger with for this timescale, which is not acceptable for the mission.

Timescale (s)	**0.01**	**0.02**	**0.04**	**0.08**	**0.16**
4–8 keV	0% (0/1340000)	0% (0/1280000)	0% (0/1190000)	0% (0/1040000)	0% (0/824375)
4–120 keV	0% (0/1340000)	0% (0/1280000)	0% (0/1190000)	0% (0/1040000)	0% (0/824375)
Timescale (s)	**0.64**	**1.28**	**2.56**	**5.12**	**10.24**
4–8 keV	0% (0/327188)	0.001% (2/160686)	0% (0/750400)	0.006% (2/36040)	0.136% (24/17670)
4–120 keV	0% (0/327188)	0.002% (3/160686)	0% (0/750400)	0.006% (5/36040)	0% (0) (0/17670)

Table 5.2: False trigger rate after involving heat-pipes noise in image trigger ($1.7\text{x}10^5$s TVAC data simulation)

Timescale (s)	**20.48**	**40.96**	**81.92**	**163.84**	**327.68**	**655.36**	**1310.72**
4–8 keV	0.091% (8/8750)	0.069% (3/4352)	0.092% (2/2170)	0% (0/1084)	2.399% (13/542)	60.886% (165/271)	99.259% (134/135)
4–120 keV	0.126% (11/8750)	0% (0/4352)	0% (0/2170)	0% (0/1084)	0% (0/542)	0% (0/271)	4.444% (6/135)

8–120 keV help to smooth out the heat-pipe noise. However, there are still some random false trigger cases, such as at a timescale of 20.48 s with a false trigger rate of 0.16%. With time increasing to 20 minutes, the false trigger rate caused by the accumulation of heat-pipe noise in the 4–120 keV range is 4.44%.

The sky position of false triggers in the 4–8 keV energy range at various timescales is depicted in Figure 5.12. For the case of less than 82.92 s, the false trigger is always located in the same pixel in the upper right corner of the sky map. The cause for this is currently unclear. For timescales greater than 82.92 s, false triggers caused by heat-pipe noise appear over several pixels on the right side of the sky map due to the noise originating from the left side of the detector. In the 4–120 keV energy range, we observe a similar localization of false triggers to that seen in the 4–8 keV energy range.

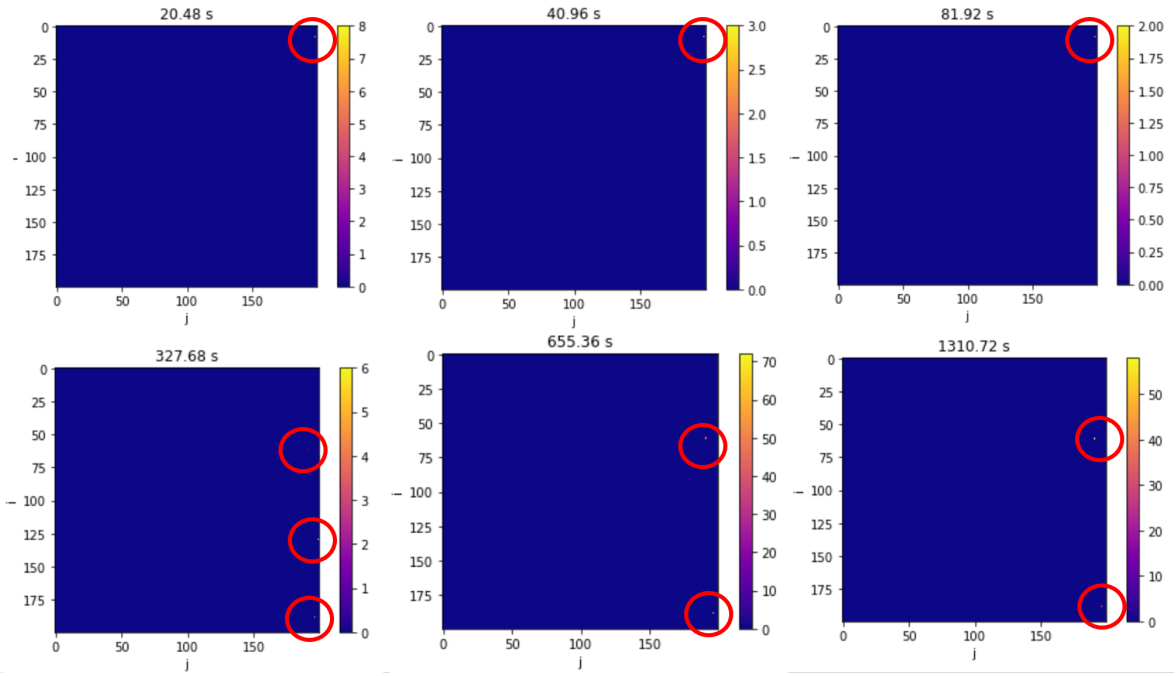

Figure 5.12: False trigger position distribution in different timescales in 4–8 keV.

5.4 Methods to reduce the impact of the heat-pipes noise

In order to mitigate the impact of heat-pipe noise, we can focus on the statistical characteristics of three dimensions: time, space, and energy. In terms of energy, the heat-pipe noise occurs in the 4–8 keV range, so we need to concentrate on that energy band. From a spatial perspective, the heat-pipe noise primarily occurs at the two edges of the detector where there are heating pipes. In terms of time, when a heat-pipe noise occurs, a large number of counts appear within 10 ms across the entire detector plane.

The general solution idea is to exclude data from the potential pixels, energy bands, and time periods where heat-pipe noise may occur. Excluding data from potential pixels in an energy band can be implemented in onboard software by setting the weight to 0 for these particular pixels in the specified energy band. However, real-time analysis of heat-pipe noise in 10 ms timescales is not possible onboard. The onboard software also does not allow us to set real-time changing weights for pixels. So, the onboard solution is to select specific pixels where heat-pipe noise may occur and ignore their data within 4–8 keV during data processing in the algorithms.

5.4.1 Different selection criteria for heat-pipes noise pixels

An effective solution for heat-pipes noise is to select the noisy pixels and ignore their data in the 4–8 keV range. This approach mitigates the impact of heat-pipe noise by removing affected pixels from the analysis. We identified two methods for selecting noisy pixels based on the count frequency in 10 ms time-bins: frequency selection (Figure 5.13 and distribution

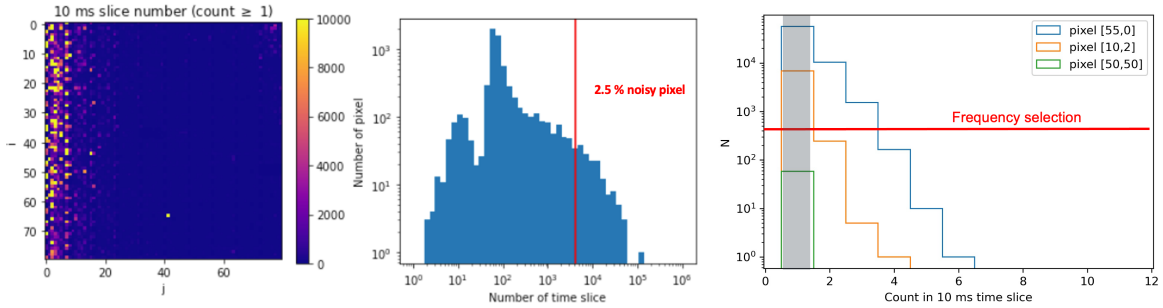

Figure 5.13: Frequency selection example. Left: 10 ms slice number (N) distribution of pixels with a count ≥ 1. Middle: histogram of N for 6400 pixels, the red line is the threshold of N to select 2.5% noisy pixels. Right: for 3 example pixels: histogram of 10 ms time slice number (N) versus minimum count inside 10 ms. The pixel (55,0]) and pixels (10, 2) are identified as noisy pixel since they have a frequency above the selection threshold.

selection (Figure 5.14).

Frequency selection

For a given pixel, we counted the number of 10ms time slices (N) in which the pixel detected photons, regardless of the number of photons detected. We set a threshold to identify noisy pixels as pixels having a high number of detected time slices. For example, we remove pixels that have a frequency higher than 4200 times over the 1340000 intervals.

Distribution selection

For each pixel, we count the number of photons in each 10 ms time slice (N). Then we build the integral distribution of N. To identify noisy pixels, we first choose a minimum value for the number of photons detected in 10 ms (a bin value of the distribution of N) and then set a threshold on the number of timeslices in this distribution. The noisy pixels are those with a value for the chosen bin above the threshold. For example, we remove all pixels that have a frequency more that 4 times with a counting ≥ 3 photons in 10 ms interval.

In both selection methods, by adjusting the value of the threshold we can tune the number of rejected pixels. By selecting a loss of 2.5% – 5%, we can prevent false triggers (false trigger rate = 0%) caused by heat-pipes noise and reduce the threshold increment to around 20% for 20 min timescales, as shown in Figure 5.15.

Based on the selection methods discussed above, two different sets of noisy pixels were chosen for comparison, each containing 161 pixels (~2.5% of the total). The specific selection criteria for the distribution selection (Figure 5.15, left) was that pixels had to have 3 counts within a 10 ms interval and appear more than 4 times. The second table was chosen using the frequency selection criteria: pixels had to have a non-zero count frequency of more than 4200 times (Figure 5.15, right).

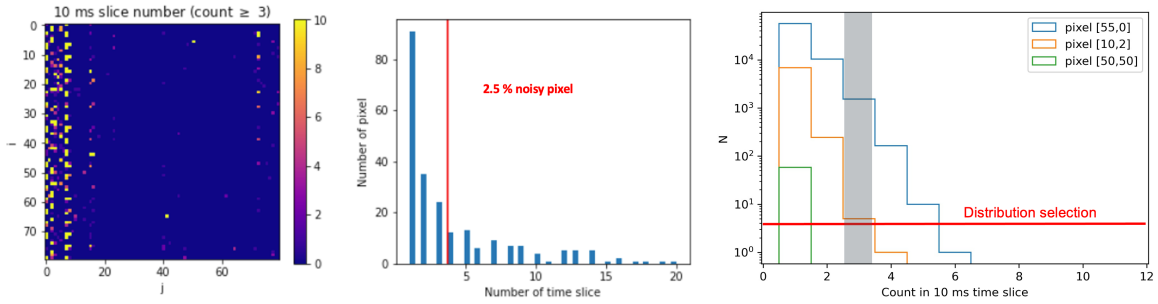

Figure 5.14: Distribution selection example. Left: 10 ms slice number (N) distribution of pixels with a count ≥ 3. Middle: histogram of N for 6400 pixels, the red line is the threshold of N to select 2.5% noisy pixels. Right: for 3 example pixels: histogram of 10 ms time slice number (N) verse minimum count inside 10 ms, the pixel (55,0) and pixels (10, 2) are identified as noisy pixel since they have a frequency above the selection threshold.

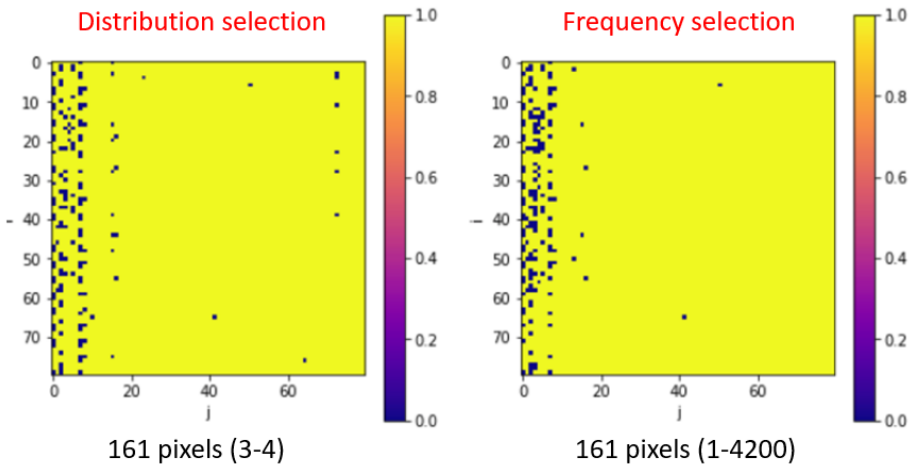

Figure 5.15: Example of 161 heat-pipes noisy pixels selected through the two selection methods. Left: distribution selection method. Right: frequency selection method.

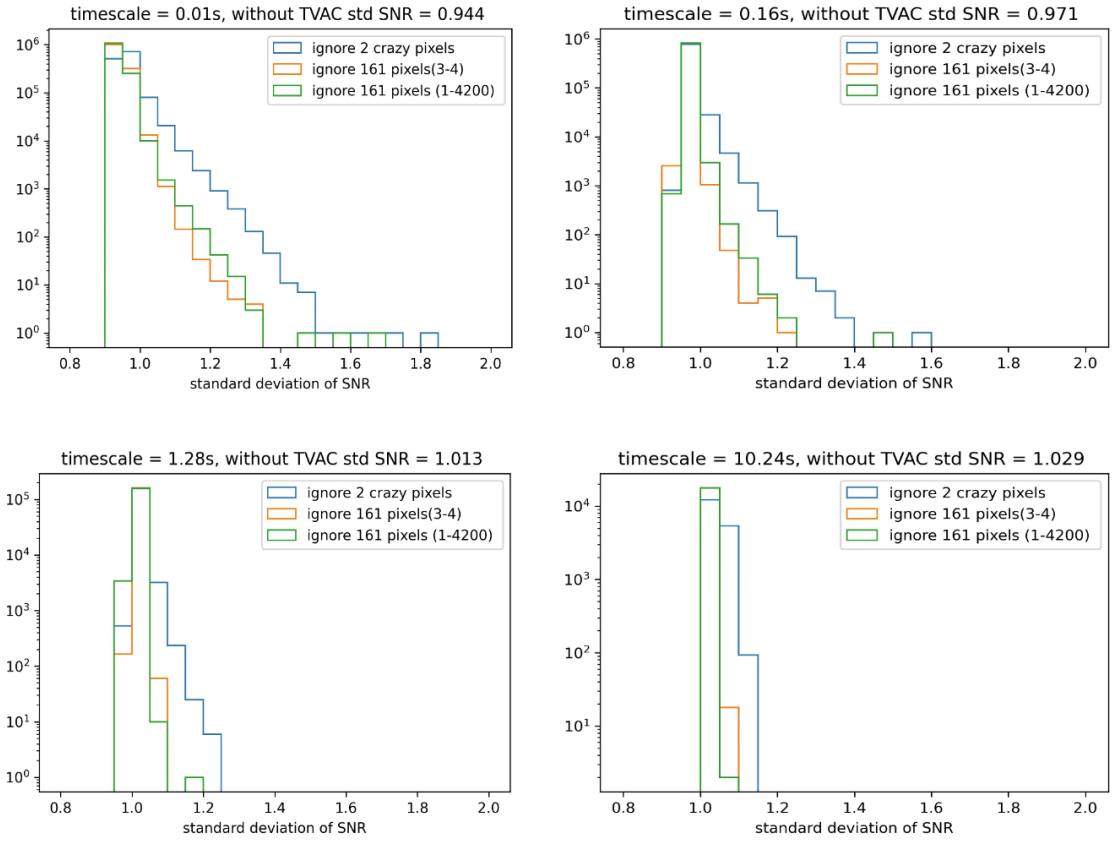

Figure 5.16: σ_{SNR} distribution for different timescales when using the count-rate trigger algorithm and mixing CXB with TVAC data. The figure titles display information about the timescale and initial σ_{SNR} when there is no TVAC data (only CXB). The blue line represents the result when ignoring the data of two HCRN pixels. The orange (distribution selection) and green lines (frequency selection) represent the result of ignoring 2.5% of pixels in Figure 5.15, respectively.

5.4.2 Trigger threshold increment after removing the noise pixels

To verify the effectiveness of the selection methods discussed above and compare the differences between them, we performed the same simulation process in 4–8 keV as described in Section 5.3.1, but we set the weights of the selected noise pixels to 0 during the background fitting and deconvolution process for all trigger timescales. This means that the data from those pixels will be ignored by the algorithm. The distributions of σ_{SNR} after removing the data from those noise pixels are shown in Figures 5.16 and Figure 5.17. Note that in the simulation, the trigger threshold is proportional to the σ_{SNR}.

In the timescales from 10 ms to 10.24 s. Both selection methods could help to reduce the impact of heat-pipes noises. There was little difference between the results of the two selection methods, in the case of timescale < 0.5 s, the result of the distribution selection is slightly better than the frequency selection.

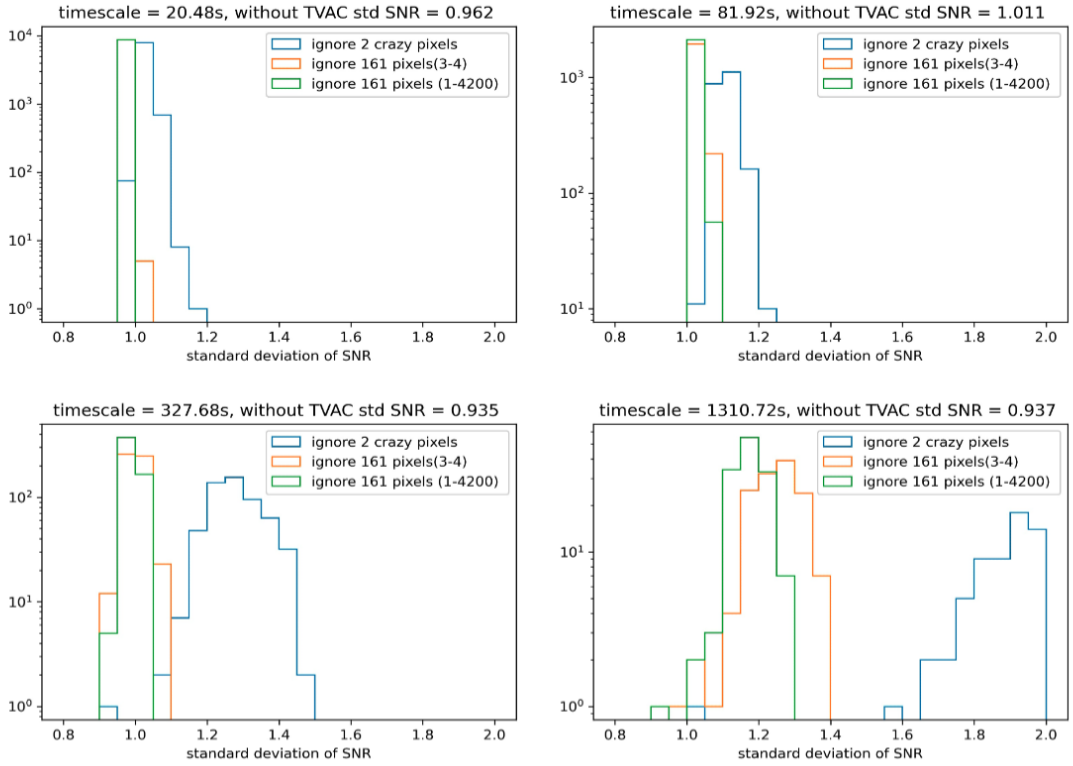

Figure 5.17: σ_{SNR} distribution for different timescales when using the image trigger algorithm and mixing CXB with TVAC data. The figure titles display information about the timescale and initial σ_{SNR} when there is no TVAC data (only CXB). The blue line represents the result when ignoring the data of two HCRN pixels. The orange (distribution selection) and green lines (frequency selection) represent the result of ignoring 2.5% of pixels in Figure 5.15, respectively.

In the imaging trigger with timescales ranging from 20.48 s to 20 min, the impact of heat-pipe noise increases with the trigger time scale. However, after removing the 161 noise pixels in the data processing, the impact of heat-pipe noise decreases rapidly. In the 20 min timescale, σ_{SNR} decreases from $\sim$2.0 down to $\sim$1.2. In this long-time exposed simulation, the frequency selection method performs better since the mean value of σ_{SNR} after removing the selected noise pixels (green) is lower than the one from the distribution selection method (orange).

While our current approach has successfully reduced the impact of noise pixels in our simulation, we recognize that there is still room for improvement. We have explored the possibility of selecting and disregarding additional noise pixels, but this may result in a trade-off with sensitivity.

In order to quantitatively compare the effectiveness of the two different selection methods with different percentage selected pixels, we selected the top 100 cases with maximal σ_{SNR} in each timescale simulation and calculated the mean value of the increment by assuming an initial σ_{SNR}=1. We found that the timescales with the maximal mean increment

Table 5.3: Mean value of σ_{SNR} "increment" of top 100 cases with maximal σ_{SNR} in each timescale simulation (assuming initial σ_{SNR}=1).

Selection method	Percentage of pixel loss	0%	∼2.50%	∼5.00%	∼7.50%	∼10.00%
	Pixels number	2	161	322	472	645
Distribution selection	0.01 s	39%	18%	16%	11%	8%
	1310.72 s	107%	28%	19%	18%	18%
Frequency selection	0.01 s	39%	23%	20%	18%	14%
	1310.72 s	107%	20%	18%	17%	17%
Counts rank selection	0.01 s	39%	22%	20%	18%	14%
	1310.72 s	107%	21%	18%	18%	17%

value in the top 100 cases caused by heat-pipes noise in the count-rate trigger and image trigger are 10 ms and 20 min, respectively. Therefore, we use these two timescales σ_{SNR} increment values to compare the effectiveness of the selection methods. The results are shown in Table 5.3.

In Table 5.3, we also added another simple selection method called "counts rank selection" for comparison, which selects the noise pixels based on their total count ranking over the entire period. For the noise pixel selection, the count ranking method and the frequency method gave similar results, with the difference in their selections being within 10 pixels. The simulation result of the increment of σ_{SNR} was quite similar, with only a 1% disparity.

When we ignore the 161 noisy pixels (2.5%), the top 100 most impacted cases show an increment of 18% for the distribution selection method and 23% for the frequency selection method in the 10 ms timescale simulation. In contrast, in the 20 min simulation, the increment is 28% for the distribution selection method and 20% for the frequency selection method. This suggests that the distribution selection method performs better in short timescale observations, while the frequency selection method works better for long-time observations. This conclusion is also applicable in the case of losing a higher percentage of noise pixels in the 4–8 keV range, as shown in Table 5.3.

5.4.3 False trigger after removing noisy pixels

After removing the data from 2.5%-10% selected pixels using either the frequency or distribution method, there were no false triggers for all timescales in the 4–8 keV and 4–120 keV energy bands. Figure 5.18 shows the distribution of $\max_{SNR}/\sigma_{SNR}$ in the 4–8 keV band after removing 2.5% (161) selected pixels based on the frequency selection method, with the left and right panels showing the results for count-rate trigger and image trigger, respectively. None of the simulated cases in the timescales from 10 ms to 20.48 s had a value above 6.5, which is the onboard trigger threshold value for $\max_{SNR}/\sigma_{SNR}$. Similarly, there were no false triggers for timescales from 20.48 s to 20 min. The same situation applied to the 4–120 keV energy band, as shown in Figure 5.19.

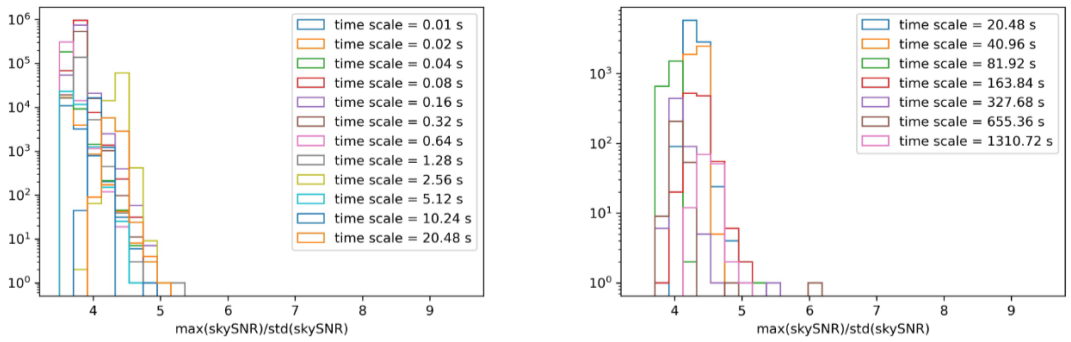

(a) (b)

Figure 5.18: Distribution of $\max_{SNR}/\sigma_{SNR}$ after removing 161 noisy pixels by frequency selection method in different timescales in 4–8 keV. Left: count-rate trigger. Right: image trigger.

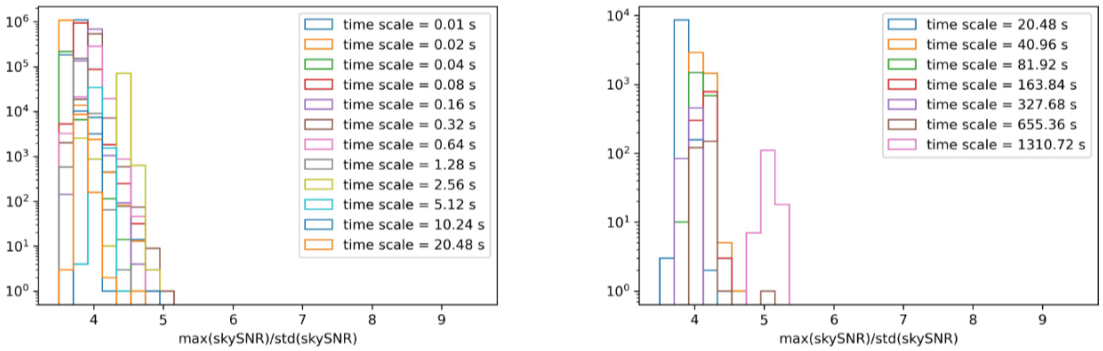

(a) (b)

Figure 5.19: Distribution of $\max_{SNR}/\sigma_{SNR}$ after removing 161 noisy pixels by frequency selection method in different timescales in 4–120 keV.

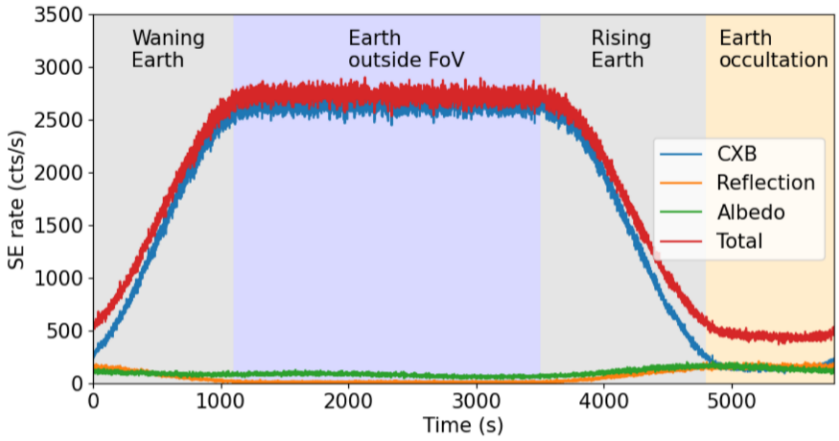

Figure 5.20: Example of ECLAIRs X-ray background in 4–150 keV (Mate et al., 2019b)

5.5 Identification of the heat-pipes noise pixels with CXB background

If heat-pipe noise occurs during ECLAIRs operation in space, it will be accompanied by a background mainly dominated by CXB. This background changes with Earth's occultation, as shown in Figure 5.20. The challenge is to identify heat-pipe noise pixels in the presence of CXB. During the Earth's waning and rising phases, the CXB count number and distribution on the detector plane change over time. Therefore, we propose to select the noise pixels using the data during the duration when the CXB count is stable, which is when the Earth is outside the FOV or during the Earth's occultation.

To investigate the selection of noise pixels in the presence of the CXB when the Earth is outside the FOV, we conducted a dedicated simulation. We combined 55000 seconds of TVAC data with simulated CXB counts over the same period. The results, shown in the left panel of Figure 5.21, indicate that the CXB counts in the central area can be as high as those from pixels affected by heat-pipe noise. Consequently, when we attempted to select 5% of noise pixels using the frequency selection method, some unexpected pixels were chosen in the central region, as seen in the right panel of Figure 5.21. Thus, we cannot directly apply the selection method we proposed when the CXB is present.

We carried out a background fitting and subtraction operation to correct the CXB count, as depicted in Figure 5.22. We assigned a weight of 1 to all pixels during the fitting and subtraction process. However, the CXB subtraction did not work as expected since the heat-pipe noise region on the left exhibited a higher count-rate. Consequently, more background was subtracted on the left side and less on the right side, as shown in the middle panel of Figure 5.22. If we apply the selection method in this scenario, we may choose some pixels in the middle-right area that are not related to the heat-pipe noise.

To prevent the selection of incorrect pixels, we could limit the region considered for CXB fitting. For instance, we could employ a 40 x 40 pixels region for the fitting and subsequently perform the subtraction for all pixels on the detector plane. This approach is

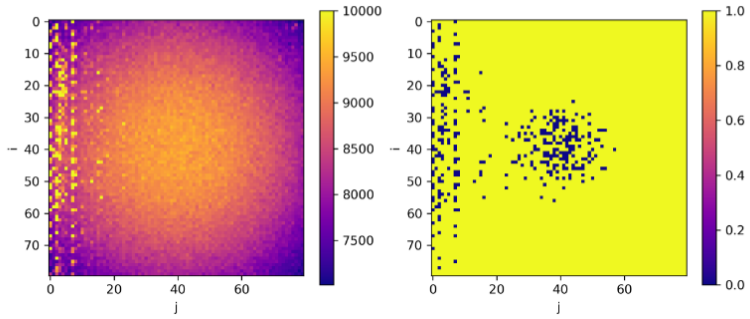

Figure 5.21: Left: simulated shadowgram over 55000 s with TVAC and CXB in 4–8 keV. Right: 5% selected pixels without subtracting the CXB.

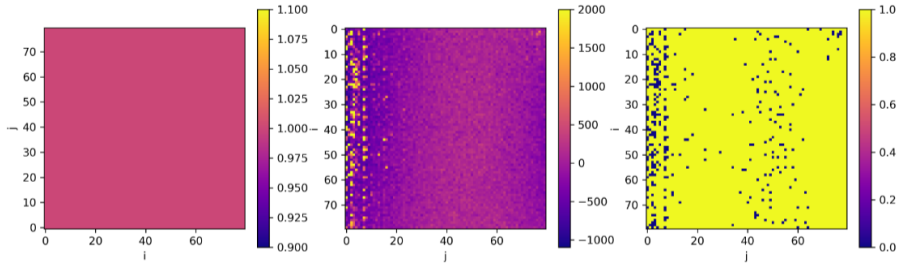

Figure 5.22: Left: Weight map for fitting the CXB. Middle: shadowgram of the 55000 s with TVAC and CXB in the 4–8 keV range after subtracting the CXB. Right: 5% of selected pixels after cleaning the CXB.

illustrated in Figure 5.23, where the background is well fitted and subtracted, and the noise pixels can be selected correctly, as shown in the right panel.

Another solution to identify noisy pixels during operations is to use data from the Earth occultation phase. This method is simpler and more practical for several reasons. Firstly, during Earth's occultation, the contribution from CXB should be suppressed. Consequently, we will be more sensitive to the weak signature of heat-pipe noise pixels since we will have less background. Secondly, we will not be polluted by the presence of an X-ray source in the partial FOV of ECLAIRs.

With this approach, we can directly select the heat-pipe noise pixels using the selection method. If necessary, we can also apply CXB subtraction, as discussed above, before selecting the noise pixels. In the future, we propose using this solution in SVOM commissioning and operational phase to select the noise pixels in this way.

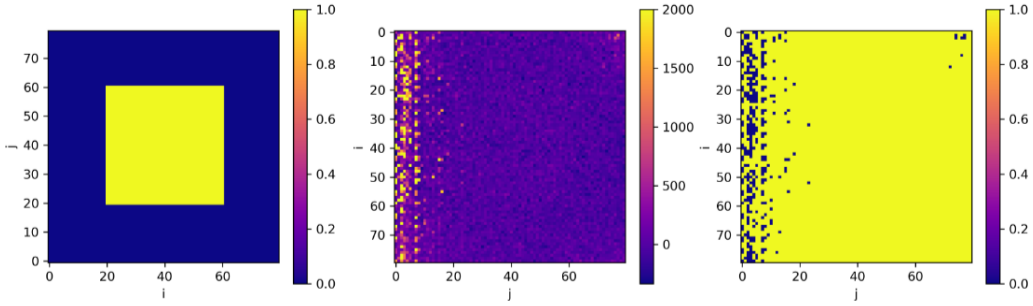

Figure 5.23: Left: Weight map for fitting the CXB. Middle: shadowgram of the 55000 s with TVAC and CXB in the 4–8 keV range after subtracting the CXB. Right: 5% of selected pixels after cleaning the CXB.

5.6 Data analysis and trigger simulation with TVAC test in Shanghai (2023)

The Shanghai TVAC test was conducted over a period spanning from 28th September to 8th October 2023. We derived our dataset from both the initial run test and the final end-to-end test, which was conducted on the entire satellite flight model. During these two tests, the ECLAIRs detection plane was positioned horizontally inside the chamber. This setup was maintained with a regulated temperature of -25℃ to ensure optimal operating conditions.

5.6.1 End-to-end test dataset

The total duration of this end-to-end test was approximately 1.18×10^5 s. A portion of this time involved ECLAIRs being in the switch-off state, simulating the satellite's passage through the SAA region. The time during which ECLAIRs was in the acquisition mode (actively counting) was 3.96×10^4 s.

The top panel of Figure 5.24 presents the counts lightcurve for different energy bands, each represented with an image unit of 20.48 seconds. In this test, the count-rate in the 4–8 keV energy band remains quite stable, contrasting with the irregular count-rate observed in Toulouse in 2021 (Figure 5.5).

Figure 5.25 shows the count-rate distribution in different energy bands. In this distribution, we only selected the duration when the detention plane is in operation mode. Overall, the counts exhibit a uniform distribution across the entire detection plane for energies above 8 keV. For 4–8 keV, there are some low count-rate pixels due to the threshold set to start at 7 keV (HTP mentioned in Chapter 4). Significantly, the heat-pipe noise observed in the Toulouse TVAC test is absent in the end-to-end TVAC test conducted in Shanghai.

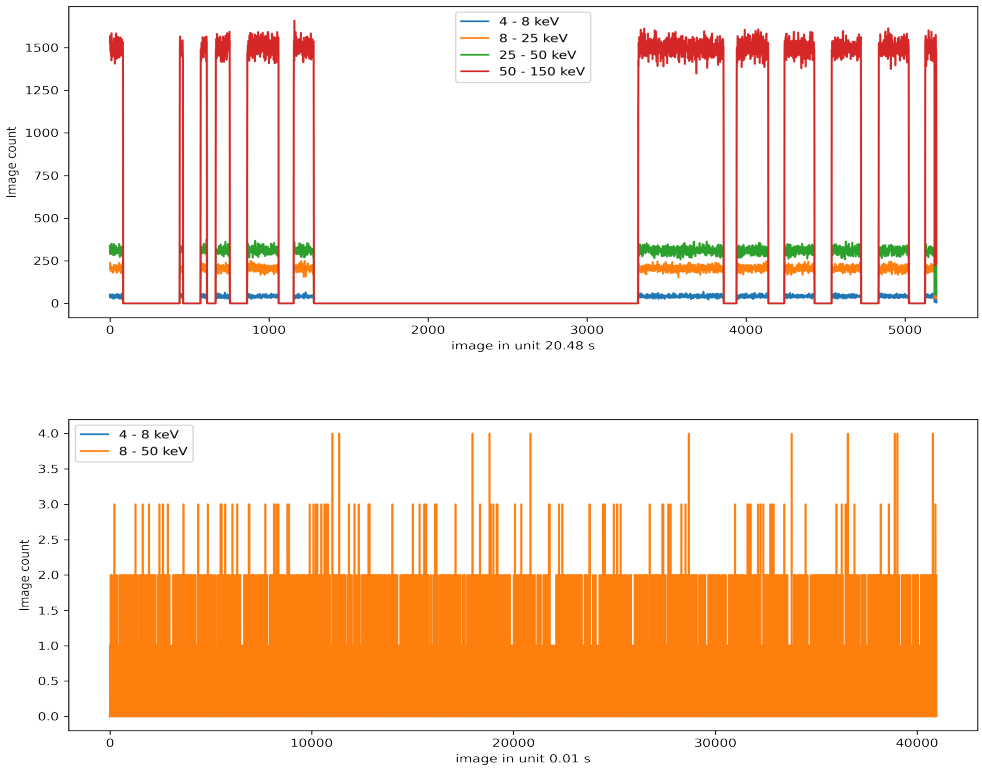

Figure 5.24: Top: ECLAIRs count lightcurve of the end-to-end TVAC test (6th October, 2023). The different colored lines indicate energy bands of 4–8, 8–25, 25–50, and 50–150 keV. The overall duration of the test is 1.18×10^5 s. Bottom: A selected 200 s segment of the lightcurve, segmented into 10 ms time-bins.

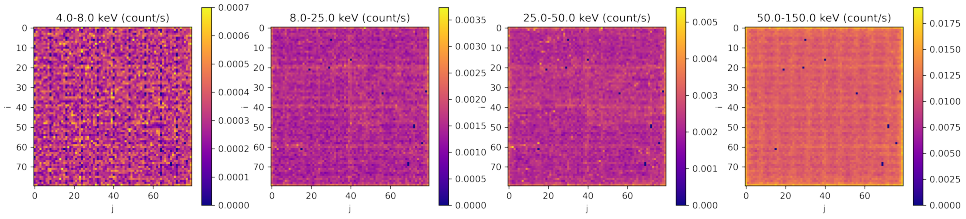

Figure 5.25: Count-rate distribution of detection plane pixels across different energy bands. In this figure, a specific duration of 3.96×10^4 s was chosen from the whole end-to-end TVAC test, during which ECLAIRs was in operation mode.

5.6.2 First cold-state cycle dataset

We also analyzed the data from the initial cycle test conducted on September 28, 2023, which took place a few days earlier than the end-to-end test. In this test, the whole SVOM satellite was located in the TVAC the ECLAIRs detection plane was placed horizontally, and the temperature of the chamber was regulated at -25℃. The corresponding lightcurve is depicted at the top of Figure 5.26. In the figure's bottom panel, sporadic spark counts are

noticeable in some 10 ms time-bins, characterized by several count spikes within the same time-bin.

Figure 5.26: Top: lightcurve of the detection plane in the TVAC test conducted in Shanghai on September 28, 2023. This part of the figure illustrates the lightcurve over a duration of 12963.84 seconds. Bottom: a selected segment of the lightcurve spanning 400 seconds, divided into 10 ms time-bins.

The count-rate distribution map shown in Figure 5.27 indicated there are still some noisy pixels and noisy modules in this test. In 4–25 keV, several pixels had dozens of times the noise compared to the others. But the count-rate in those several pixels is about 0.05 count/s in 4–25 keV, with the same level in most pixels count-rate in 50–150 keV. It is not the same level as the noise we found in Toulouse 2021.

5.6.3 False trigger and the increase of threshold

We performed the simulation to study the trigger influence of the noise found in Shanghai TVAC test. The simulation process is the same as in Section 5.3. The impact includes two aspects: the increment of the trigger threshold (which is equal to 6.5 times the standard deviation of sky SNR), and the false trigger rate.

To examine the impact of noise identified in the Shanghai tests on the trigger algorithms, we conducted a simulation mirroring the process described in Section 5.3. This simulation

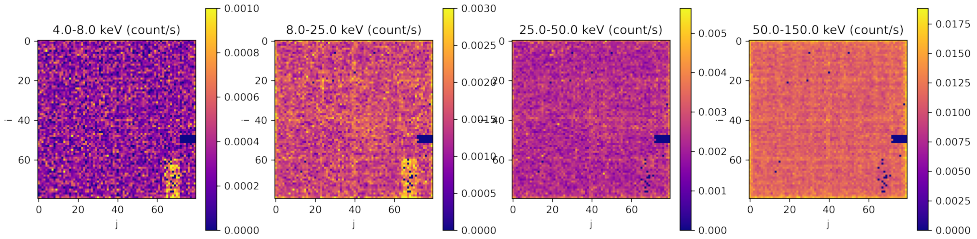

Figure 5.27: Count-rate distribution of detection plane during the TVAC test in Shanghai (28th September 2023). The duration is 12963.84 s.

also focused on two aspects: firstly, the increment of the trigger threshold ($6.5 \times \sigma_{\mathrm{SNR}}$), and secondly, the false triggers rate.

For the noise detected during the Shanghai cold-state first cycle TVAC test, the simulation results demonstrating its impact on the onboard trigger are illustrated in Figure 5.28. By incorporating this noise into the CXB across various timescales, we observed that the trigger threshold increased by approximately 1% to 12% over a 20.48 s timescale. Only one instance showed a significant increase, with the threshold which is incremented by approximately 30%. The right panel of Figure 5.28 reveals that after incorporating the noise data from the cold-state first cycle test into our analysis, no false triggers were identified.

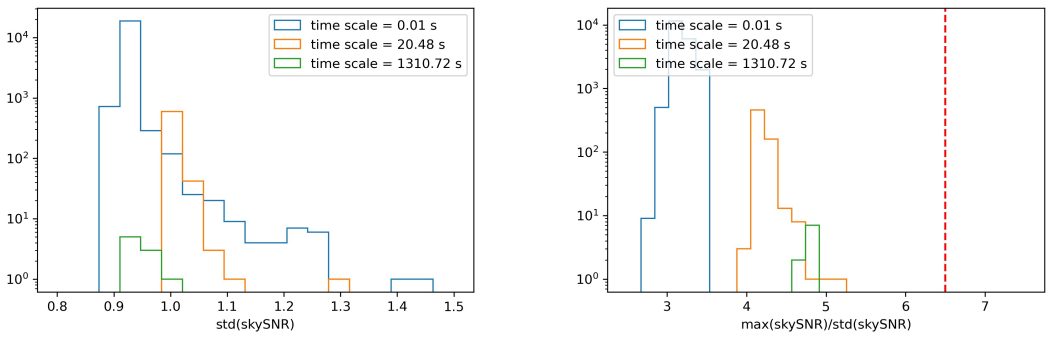

Figure 5.28: Result of the ECLAIRs trigger performance in 4–8 keV after considering the background from the Shanghai cold-state first cycle TVAC test. The various colors in the figure depict different timescales used in the simulation. Left: standard deviation of the sky map (σ_{SNR}), which reflects the impact on the trigger threshold, calculated as $6.5\times \sigma_{\mathrm{SNR}}$. Right: distribution $\mathrm{max}_{\mathrm{SNR}}/\sigma_{\mathrm{SNR}}$, with the red line representing the trigger threshold set at 6.5.

Figure 5.29 presents the trigger simulation results after incorporating the noise from the detection plane of the end-to-end test. Remarkably, ECLAIRs demonstrated excellent performance, attributable to the low count-rate of noise in the 4–8 keV range (as shown in Figure 5.25). There were no false triggers throughout the entire duration of 1.18×10^5 seconds, and the increase in the threshold remained under 10% across all timescales.

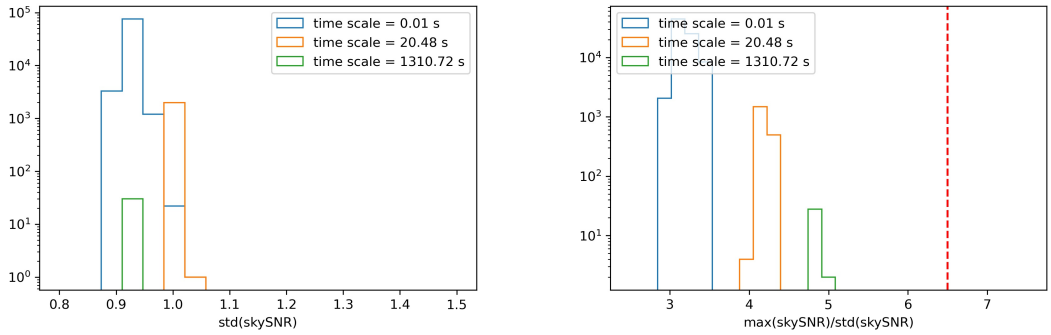

Figure 5.29: Result of the ECLAIRs trigger performance in 4–8 keV after considering the background counts from Shanghai end-to-end TVAC test. The various colors in the figure depict different timescales used in the simulation. Left: standard deviation of the sky map (σ_{SNR}), which reflects the impact on the trigger threshold, calculated as $6.5\times\ \sigma_{\mathrm{SNR}}$. Right: distribution $\mathrm{max}_{\mathrm{SNR}}/\sigma_{\mathrm{SNR}}$, with the red line representing the trigger threshold set at 6.5.

5.7 Discussion and conclusion

We have investigated the characteristics of the heat-pipe noise, its impact on the GRB detection, and studied methods to mitigate its effects. Although the cause of heat-pipe noise is unclear, it has been observed in areas close to the heat-pipes. Pixels affected by heat-pipe noise display a relatively high count-rate in the 4–8 keV range. This effect not only increases the trigger threshold for GRB detection, but also leads to false triggers, thereby reducing the GRB trigger sensitivity, particularly during long-term observations in image trigger mode.

Introducing heat-pipe noise counts from Toulouse TVAC data in a simulation of a 20 min observation results in an increase in the trigger threshold ($6.5 \times \sigma_{\mathrm{SNR}}$) of approximately 100%, compared to observations without heat-pipe noise. Even though we increased the trigger threshold, it still caused a false trigger rate of 99.26% in the 4–8 keV range and 4.44% in the 4–120 keV range in 20 min timescales.

The impact of the heat-pipes noise can be mitigated by removing the affected pixels. We have identified two methods for selecting pixels affected by heat-pipe noise in TVAC data: distribution selection for observation timescales of <0.5 s, and frequency selection for observation timescales $\geq$0.5 s. By using the frequency selection method and sacrificing 2.5% of pixels, false triggers caused by heat-pipe noise can be avoided. This reduces the threshold increment for 20-minutes image trigger observations to around 20% in 4–8 keV.

In practice, when heat-pipe noise occurs, it is often accompanied by the CXB, which can bias the noise pixel selection. To address this issue, we have developed two solutions. The first solution uses data when the Earth is outside the ECLAIRs FOV. The second solution uses data when the Earth fully occults the FOV. We propose to use the second method to select noise pixels in the future commissioning and operational phases, as it should be more efficient and more reliable.

When ECLAIRs is operating onboard, only a single weight table can be used in the software for CXB fitting and image deconvolution across all observation timescales, from 10 ms to 20 min. Our goal is to reduce the impact of heat-pipe noise by sacrificing no more than 5% of the pixels. We chose the frequency selection method to identify the 5% of pixels as the noise pixel in the 4–8 keV range. We have several reasons for this.

1. The onboard software automatically removes data from pixels that have a significant count excess in a short timescale (10 ms), which is equivalent to the distribution selection method.

2. Heat-pipe noise mainly affects long-term observations, and our simulations show that the frequency selection method performs better, particularly in 20-min observations.

In 2023, the fully integrated SVOM satellite underwent a TVAC test in Shanghai. We meticulously examined and analyzed the dataset from the initial test on September 28th, 2023 (first cold-state cycle), and the end-to-end test conducted on October 6th, 2023. Notably, some noisy pixels were identified in the Shanghai first test's data in the 4–25 keV range, which were absent in the final end-to-end test. Through simulations where we added the TVAC noise counts with the simulated CXB in the trigger process, it was observed that these noises marginally affected the trigger threshold, typically resulting in an increment of 1% to 12%. Importantly, these noises did not result in any false triggers. Furthermore, even if these noisy pixels exhibit high count-rates during the commissioning phase, they will be effectively selected and excluded in the deconvolution process.

Chapter 6

Detection of X-ray rich GRBs with ECLAIRs

Contents

In this chapter, we study the ECLAIRs detection performance for the X-ray rich GRBs using a simulation software named ECLGRM, described in Section 6.1. In Section 6.2, we made the simulations to estimate the ECLAIRs sensitivity for different kinds of GRB (with classical parameters) with different positions in the FOV. We tried to assess the SNR improvement for detecting the GRBs thanks to the 4–8 keV band. In Section 6.3 and Section 6.4 more accurate simulations are performed using real data from the HETE-2 GRB sample. In Section 6.5, we simulated the ECLAIRs detection using the real trigger hardware (UGTS) and the trigger parameter that will be used at the beginning of the mission. Finally, we compared the trigger results with the one obtained by using the ECLGRM software. The discussion and conclusion are presented in Section 6.6.

6.1 The ECLGRM simulation software

6.1.1 Overview of ECLGRM

The ECLGRM software[1] aims to perform the end-to-end gamma-ray source detection simulation of ECLAIRs and GRM. It consists of several packages that have been jointly developed by the SVOM collaboration team for several years. We introduce several key packages used in this work. For more detailed information about ECLGRM software, please refer to Arcier (2022). The simulation workflow is described in Figure 6.1.

- grb-simulator: simulates GRBs using lightcurve and spectrum information collected from other GRBs missions such as HETE-2, Swift, Fermi (Antier-Farfar, 2016).
- PIRA: generate the satellite attitude file and the background event file (Zhao et al., 2012; Mate et al., 2019b).
- event-simulator: simulates the X-ray known sources events and GRB events into the background event file created by PIRA.
- dpix-effect: applies the detection plane effects to the simulation. Those effects like are those observed during the calibration, such as the efficiency inhomogeneity or the heat-pipe noise.
- eclgrm-trigger: applies the count-rate trigger algorithm (10 ms - 20.48 s) on the event file.

6.1.2 grb-simulator

To generate the GRB photons list using grb-simulator, the information of GRB is needed. The input data for the grb-simulator consists of a light curve file (photon/timebin) and a spectrum file.

[1] https://drf-gitlab.cea.fr/eclgrm-fr

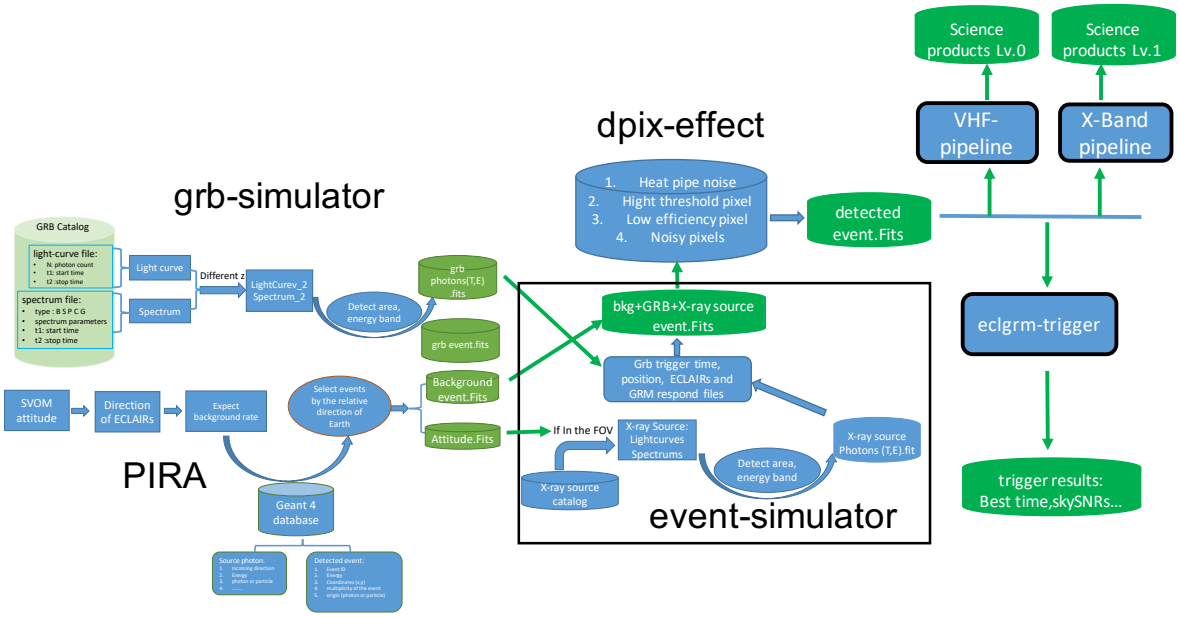

Figure 6.1: Workflow of the GRB detection simulation of ECLAIRs and GRM in the framework of the ECLGRM pipeline. Detailed information can be found in Arcier (2022).

The spectrum file provides detailed information, including the time-resolved energy spectrum that encompasses the start and stop time, the spectrum type (S, P, C, B, and G, representing the single broken power-law, the power-law, the Compton, the Band respectively), and the various spectral parameters such as the normalization factor, alpha, beta, the peak energy, etc. In this package, the input lightcurve file only contains information about the relative distribution of photons with respect to time, rather than the absolute count rate. Consequently, the absolute count is determined using the Anorm (ph/s/cm2/keV) parameter given in the spectrum file. Several GRB catalog data from various missions, such as HETE-2, BATSE, Swift/BAT, Fermi/GBM and others, are incorporated into the software. The output of the grb-simulator software includes the GRB photons list file and the GRB counts file (also called events file). Detected counts have been processed through the instrument (ECLAIRs and GRM) response matrix inside the ECLGRM software. Figure 6.2 shows the workflow of the grb-simulator package.

My contribution to the grb-simulator package was to develop a customized GRB generation tool. This tool is specifically designed to generate dedicated GRB lightcurve and spectrum files based on key input GRB information. Including fluence, duration, and spectrum parameters. These generated files are then compatible with the input of the grb-simulator software. It realizes the user's function of simulating custom GRBs in the ECLGRM framework.

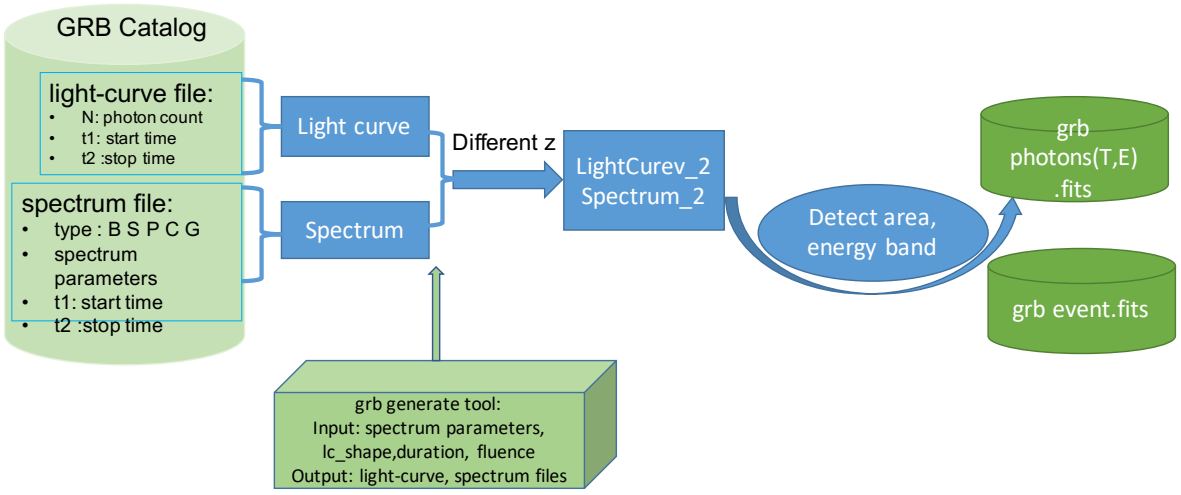

Figure 6.2: Overview of grb-simulator package.

6.1.3 Trigger algorithm in ECLGRM and comparison with the UGTS

After the simulated event file (GRB plus background) has been generated, the count-rate trigger algorithm in ECLGRM-trigger package (ECLGRM-CRT) is used to obtain the trigger results. The ECLGRM-CRT is inspired by the UGTS process and tries to reproduce its count-rate trigger (UGTS-CRT).

In ECLGRM-CRT, the algorithm first calculates the significance of the increase in count rate relative to the background for different time scales, energy bands and areas of the detection plane. It then identifies a subset of the data (best time slice) corresponding to the best count significance. From this best subset of data, it then subtract the background, deconvolves the shadowgram, generates the image of the sky and searches for the sky pixel with the maximum SNR.

These results encompass both an array of the count-significance and a sky SNR map for the best time slice. If the maximum sky SNR exceeds a specified threshold (set to SNR = 6.5, representing an ideal background scenario, as referenced in Chapter 3), then it means that the ECLAIRs has detected the simulated burst.

Note that the trigger algorithm implemented in the ECLGRM pipeline is not exactly the same as the real onboard trigger system. As introduced in Chapter 3, in the UGTS trigger system (same as the onboard trigger system), there is another trigger algorithm named the image-trigger (UGTS-IMT) that operates simultaneously on intervals of 20.48 s $\times$ 2^n, with n = 0, 1, 2..., 6, and processes all the data recorded on the detection plane (Dagoneau et al., 2022, S. Schanne et al., 2019).

There are also differences between the ECLGRM-CRT and UGTS-CRT. The main difference is that UGTS-CRT is a real-time trigger working on cycles of 2.56 s. In the real-time data flow, it analyzes all time slices for each timescale from 10 ms to 20 s, and computes the SNR of the counts in the time slice compared to a running background model. Then at

each cycle of 2.56 s, it selects the best time slice found in the past 1 minute (typically) and performs its deconvolution. In the resulting sky image, a sky excess is searched.

The ECLGRM-CRT is a global trigger. It reads all the data and picks only the best time slice over the whole lightcurve and performs a deconvolution only for this time slice. In this sky image an excess is then searched.

6.1.4 A simulation example performed by ECLGRM software

Here is a simulation example of a self-custom GRB shown in Figure 6.3. The lightcurve exhibits a typical one-pulse burst, characterized by a fast-rising and exponential-decay pattern. The duration of the burst is 100 s, and it has a fluence of 1.8 $\times$ 10^{-7} erg/cm^2. This event is classified as an X-ray Flash GRB, featuring a Band spectrum with parameters: E_p = 20 keV, α = -1.0, and β = -2.0 (Takanori Sakamoto et al., 2008).

Then we incorporate additional background events generated from PIRA package, such as CXB, reflection, and albedo. These background components are modeled assuming that the Earth is located outside ECLAIRs' FOV. In this case, the maximum detected SNR is 6.24, which couldn't trigger.

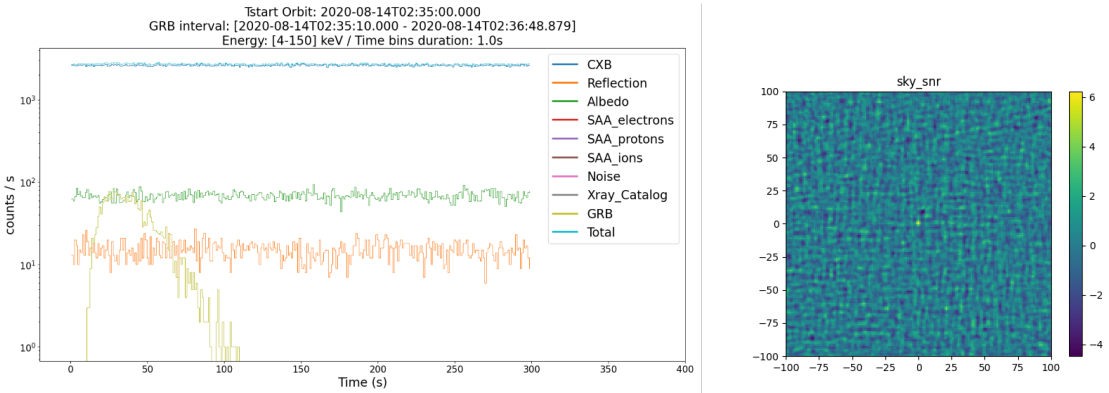

Figure 6.3: A GRB simulation example performed by the eclgrm-simulation software. Left: GRB and background events lightcurves generated by grb-simulator and PIRA. Right: the sky SNR map after running ECLGRM-CRT. In this sky image, the maximum SNR value is 6.24, which leads to no trigger in ECLAIRs.

6.2 Trigger sensitivity of ECLAIRs for different types of GRB

6.2.1 GRB distribution across different positions within the ECLAIRs FOV

To study how different GRB locations impact ECLAIRs' detection performance, we conducted a simulation of this GRB sample 1000 times at various sky positions within ECLAIRs' FOV. The full FOV of ECLAIRs, measuring 89 $\times$ 89 deg ^{2}, was segmented into 200 $\times$ 200 sky pixels for this simulation. We used the same X-ray Flash GRB and background as previously described but with a ten times higher fluence of 1.8 $\times$ 10^{-6} erg/cm^2. The positions of the GRBs were randomly generated within the FOV.

Figure 6.4 illustrates the best SNR results from the ECLGRM-CRT. In both figures, the SNR values show a gradual decrease from the center towards the edges. This trend is attributed to the fact that a more oblique angle results in fewer photons from the GRB reaching the detection plane. We also observe a circular symmetry with respect to the optical axis of ECLAIRs. The highest SNR is observed at the center of the FOV. The SNR value then decreased sharply once the sky pixel exceeded 25 ($\sim$ 11.4 deg), marking the transition from FCFOV to PCFOV. The outermost detectable angle for this burst is estimated at around sky pixel = 75 (25 deg from the optical axis).

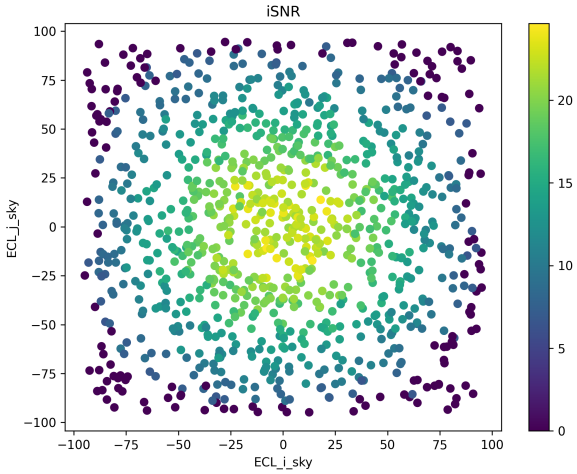

Figure 6.4: Simulated SNR distribution for an X-ray Flash GRB occurring in different FOV positions of ECLAIRs. The maximum SNR are shown in the reconstructed image for each position. The SNR values are set to 0 if it is smaller than 6.5. This simulation utilizes a GRB with a Band spectrum: E_p = 20 keV, α = -1.0, and β = -2.0, fluence = 1.8 $\times$ 10^{-6} erg/cm^2, t = 100 s.

6.2.2 ECLAIRs sensitivity for different types of GRB

To estimate ECLAIRs' performance in detecting various types of GRBs, we conducted dedicated simulations using ECLGRM software. Each simulation was designed to determine ECLAIRs' sensitivity to a GRB with different peak energy, such as long X-ray rich GRBs. These simulations involve entering the position of the GRB in the FOV and computing the flux at the sensitivity limit corresponding to the ECLAIRS default trigger with a SNR threshold = 6.5 (See Section 6.1.3.)

1. Simulate a fast-rising exponential-decay (classical pulse) GRB based on the classical spectrum parameter. In this step, simulated GRB data were input into ECLGRM software, using the parameters previously described. We also set the initial flux of the GRB to ensure it could trigger ECLAIRs, even if its position was at the edge of the FOV.

2. set the GRB position within the ECLAIRs FOV, simulate the GRB events, and combine it with background data simulated by PIRA into a detection shadowgram. Then process the ECLGRM-trigger algorithm for this shadowgram.

3. Determine the sensitivity for this GRB type.

   (a) Set the SNR trigger threshold at 6.5 and define an error range equal to 0.5. This gives an interval of SNR to detect a GRB of $[6, 7]$.

   (b) Get the best image SNR value, if SNR > 7.0, decrease the flux by half the difference between the two iterations and simulate again; if SNR < 6.0, increase the flux by half the difference between the two iterations and simulate again.

   (c) If the last two SNR values obtained are not included in the trigger range $[6, 7]$, repeat step (b) until the last two SNR are included. Then go to step (d).

   (d) Set the flux value to the median value of the flux for the last two tries. We identify this value as the sensitivity limit of ECLAIRs.

   (e) Add a random error to the flux. Pick up the flux value that the corresponding SNR in the trigger region $[6, 7]$. Repeat 3 times then calculate the mean value of flux as the ECLAIRs sensitivity limit for this kind of GRB.

4. Change the GRB position and repeat steps 1–3 to determine ECLAIRs sensitivity limit at various positions.

5. Collect the SNR, position, and sensitive flux to plot the figure.

6. Modify the trigger energy band from 4–150 keV to 8–150 keV and redo steps 1–5. By comparing these results, we can determine the impact of the 4-—8 keV band on different GRB types.

Figure 6.5 shows the simulation result of ECLAIRs' sensitivity to an X-ray Flash GRB (E_p = 20 keV) in the 4–120 keV range. To save simulation time, we have only simulated the diagonal of the FOV, as the axial symmetry of ECLAIRs' detection was already established

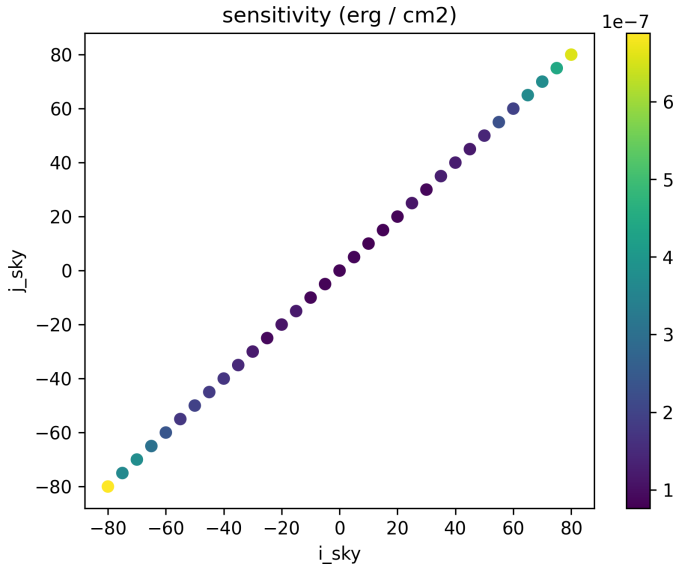

Figure 6.5: ECLAIRs flux sensitivity (4–120 keV) in different sky positions for a 30 s long GRB with Band spectrum: E_p = 20 keV, α = -1.0, and β = -2.0.

from Figure 6.4. It indicates that ECLAIRs is more sensitive in the center compared to the edge.

Figure 6.6 illustrates the trigger sensitivity for various types of long GRBs, each with a duration of 30 s. This includes X-ray flash GRBs ($E_p \leq 30$ keV), X-ray rich GRBs ($30 < E_p \leq 100$ keV), and classical GRBs ($E_p > 100$ keV). For all the simulations, it is found that the ECLAIRs sensitivity is better in the FCFOV, which spans over 22×22 deg^2, corresponding to approximately $[-25, 25]$ sky pixels in the figure.

For the classical long GRB (LGRB) with E_p = 200 keV, ECLAIRs exhibited a trigger sensitivity of 2.5×10^{-7} erg/cm^2 when the GRB is within the FCFOV. In contrast, a GRB fluence of approximately 10^{-6} erg/cm^2 is required for ECLAIRs to detect an LGRB occurring in the PCFOV.

Equation 6.1 gives a rough estimate of the sensitivity with respect to exposure time (Peterson, 1975). Here S represents the sensitivity observed in t second, S_1 stands for the 1 second sensitivity. Using the time adjustment based on Equation 6.1, the on-axis sensitivity of ECLAIRs in one second for a classical LGRB is 4.5×10^{-8} erg/cm^2/s.

$$S = S_1 \times \sqrt{t} \tag{6.1}$$

For the long X-ray rich GRB example with E_p = 50 keV, ECLAIRs exhibited a variation in trigger sensitivity from 10^{-7} erg/cm^2 in the FCFOV to approximately 10^{-6} erg/cm^2 in the PCFOV. In the case of the X-ray flash with E_p = 20 keV, ECLAIRs demonstrated a trigger sensitivity of around 9×10^{-8} erg/cm^2 for the FCFOV, and 2×10^{-7} erg/cm^2 for the PCFOV.

The 4-–8 keV bonus is particularly significant for the softer X-ray flash with E_p = 5 keV.

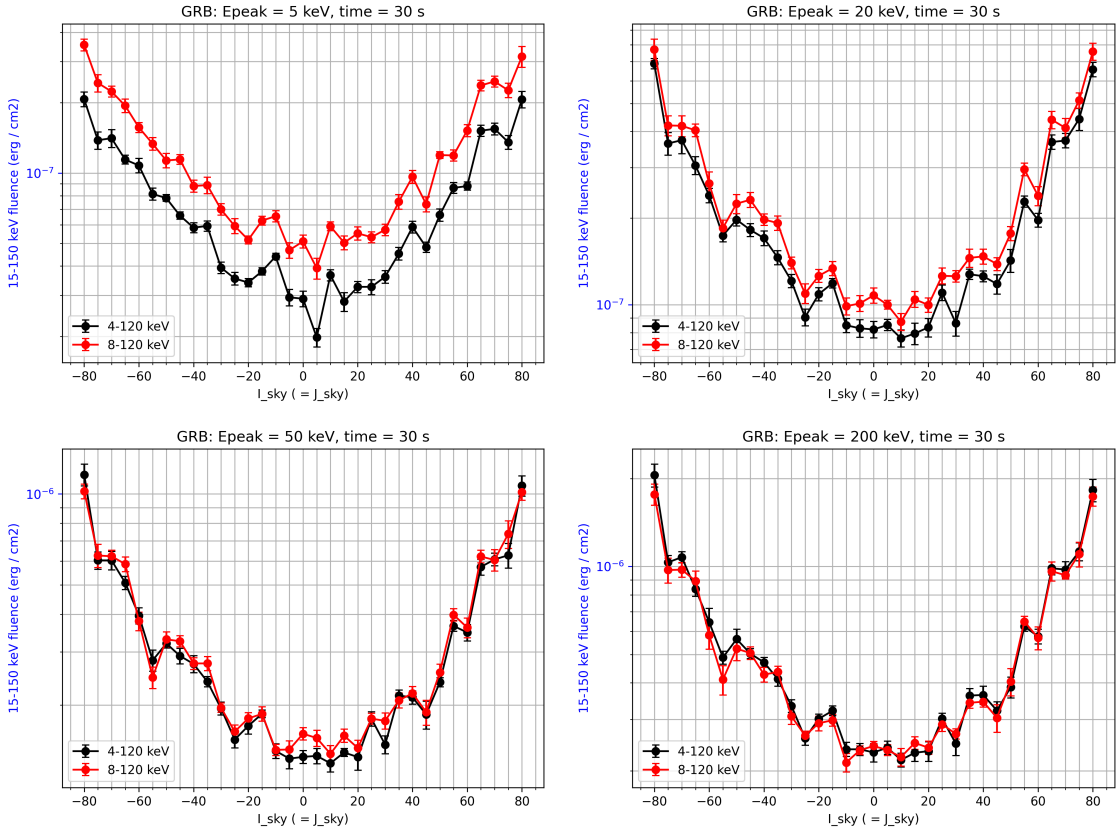

Figure 6.6: ECLAIRs trigger sensitivity for different positions in the FOV for various types of long GRBs. From the upper left panel to the lower right panel, the corresponding simulated GRBs have a Band spectrum with parameters: E_p= 5, 20, 50, 200 keV respectively. Classical indexes $\alpha = -1.0, \beta = -2.3$ are applied across these spectra. The GRB light curve is characterized by a duration of 30 s with a fast-rising exponential-decay shape. The red lines represent the trigger in the energy band 8–120 keV, and the black lines stand for a wider band 4–120 keV, starting from a threshold at 4 kev.

Within the 8–150 keV range, the trigger sensitivity is 5 $\times$ 10^{-8} erg/cm^2 for the FCFOV, which is equal to $\sim$ 10^{-8} erg/cm^2/s. Introducing the low energy band starting 4–8 keV, coupled with the 8–150 keV band, enhances the on-axis trigger sensitivity to 3 $\times$ 10^{-8} erg/cm^2. The sensitivity limits are detailed in Table 6.1 and Table 6.2.

Figure 6.7 illustrates approximately same result from a photon flux sensitivity perspective. The black lines represent the photon count necessary to trigger ECLAIRs within the 4–120 keV range. The on-axis photon sensitivity for a 30 s LGRB is approximately 5 counts/cm^2 in the 4–150 keV range, which corresponds to 0.91 count/cm^2/s, derived from the principle that sensitivity is inversely proportional to the square of time (Peterson, 1975), as outlined in the simplified Equation 6.1.

If the 4–8 keV band does not contribute to the trigger, as the red lines show in Figure 6.7, more additional high-energy photons in 8–120 keV are needed to trigger on the softest GRB with E_p = 5 keV, in order to compensate for the loss of photons in 4–8 keV.

Table 6.1: ECLAIRs trigger fluence sensitivity in different energy bands for 30 s long GRB. The GRB Band spectrum has indexes $\alpha = -1.0, \beta = -2.3$. The sensitivity fluxes are in the range of 15–150 keV (to compare with Swift/BAT).

E_p(keV)	On-axis (10^{-8} erg/cm^2)		Off-axis (10^{-8} erg/cm^2)	
	4–150 keV	8–150 keV	4–150 keV	8–150 keV
5	3	5	9	15
20	8	10	20	25
50	15	15	40	40
200	25	25	60	60

Table 6.2: ECLAIRs trigger flux sensitivity for 30 s long GRB. The sensitivity is normalized according to Table 6.1, by dividing the square root by the GRB duration (30 s), as expressed in Equation 6.1. The GRB Band spectrum has indexes $\alpha = -1.0, \beta = -2.3$.

E_p(keV)	On-axis (10^{-8} erg/cm^2/s)		Off-axis (10^{-8} erg/cm^2/s)	
	4–150 keV	8–150 keV	4–150 keV	8–150 keV
5	0.55	0.91	1.64	2.74
20	1.46	1.83	3.65	4.56
50	2.74	2.74	7.30	7.30
200	4.56	4.56	10.95	10.95

6.2.3 Bonus of the 4–8 keV band

The ECLAIRs telescope is particularly effective in detecting softer GRBs, owing to its lower energy threshold that extends down to 4 keV. With decreasing peak energy in GRBs, the relevance of the 4–8 keV energy band becomes increasingly significant. To quantify this advantage, we have determined the flux sensitivity improvement (I_f) by employing Equation 6.3.

$$I_f = \frac{f_{8-120}}{f_{4-120}} - 1 \tag{6.2}$$

f_{8-120} and f_{4-120} denote the trigger sensitivity for ECLAIRs in 8–120 keV and 4–120 keV, respectively. For instance, Figure 6.8 illustrates the trigger flux ratio between 8–120 keV and 4–120 keV for a GRB with Band function with E_p = 5 keV, $\alpha = -1.0, \beta = -2.3$. The ratio is 163.3%, indicating that the trigger sensitivity improves by 63.3% due to the 4–8 keV contribution. Furthermore, the ratio's consistency regardless of the on-axis or off-axis orientation also suggests that the advantage of the 4–8 keV band remains weakly affected by the GRB positions in the FOV.

We applied the same methodology as in Figure 6.8 to derive the mean sensitivity im-

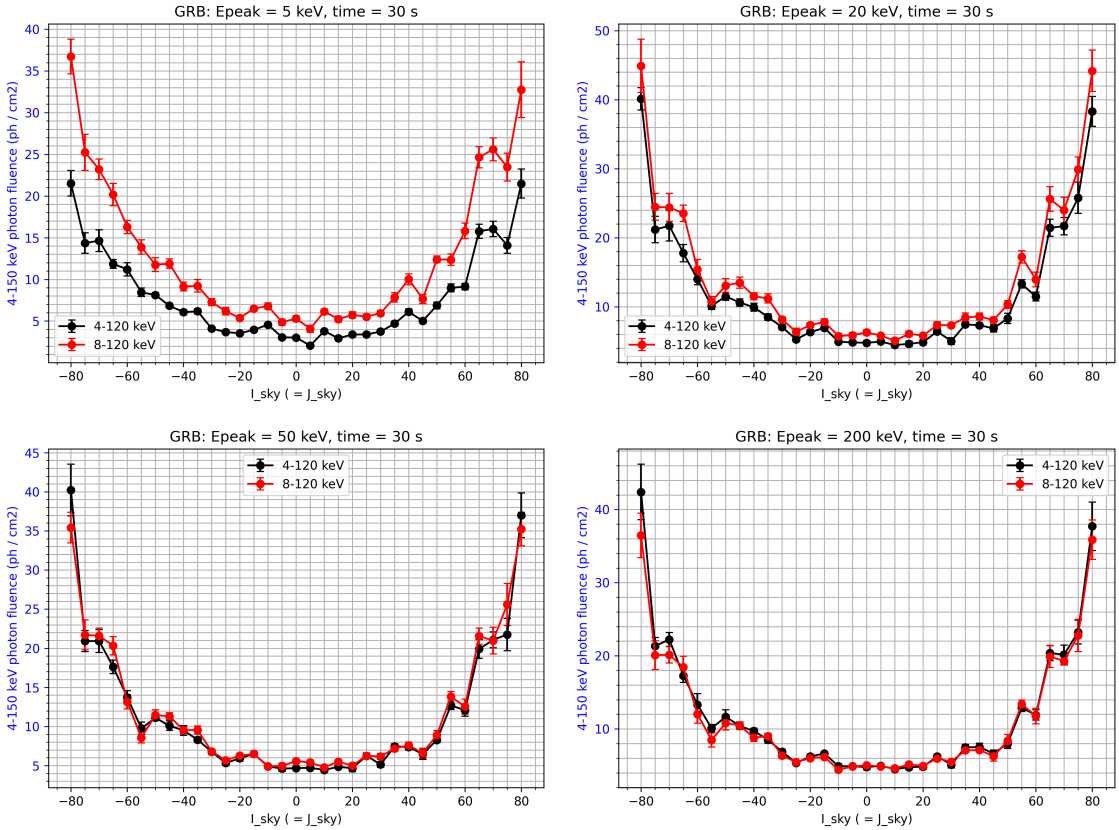

Figure 6.7: ECLAIRs trigger sensitivity, as in Figure 6.6 but expressed in ph/cm^2.The red lines represent the trigger in the energy band 8–120 keV, and the black lines stand for a wider band 4–120 keV, starting from a threshold at 4 keV.

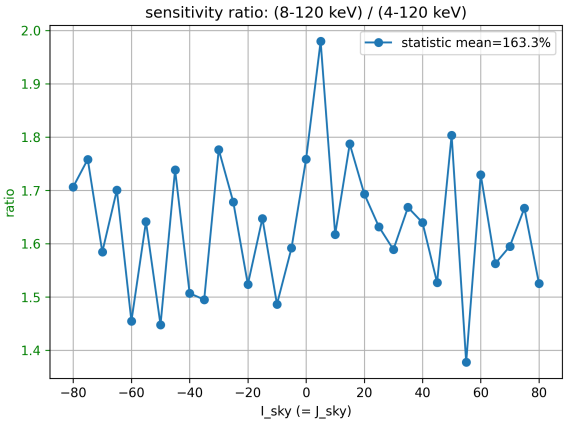

Figure 6.8: ECLAIRs sensitivity ratio between 8–120 keV and 4–120 keV for a GRB with E_p = 5 keV. The x-axis represents the source position in the sky, and the y-axis indicates the ratio of the trigger flux for 8–120 keV and 4–120 keV. The mean value of the ratio across all positions is 163.3%.

provement for different E_p GRBs, attributable to the 4–8 keV band bonus. The results are depicted in Figure 6.9. As the E_p of GRB increases, the contribution of the 4–8 keV band

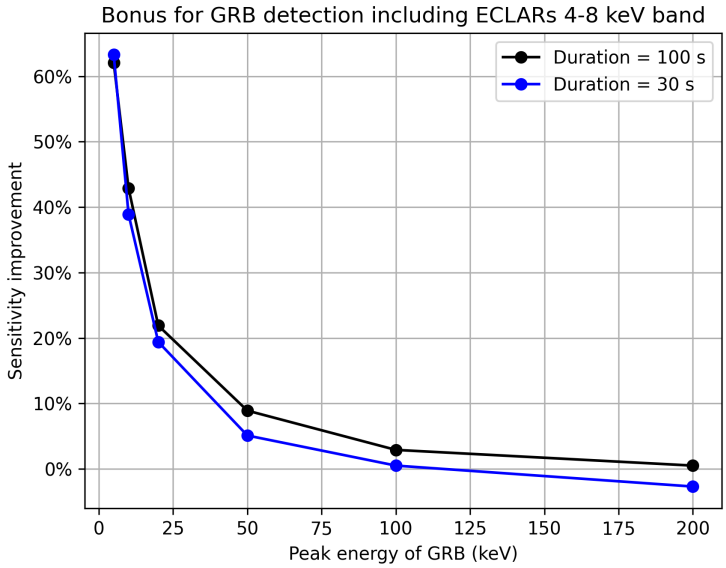

Figure 6.9: This graph illustrates the sensitivity improvement bonus achieved by including the 4–8 keV energy band. The X-axis represents the peak energy of GRB (5, 10, 20, 50, 100, and 200 keV), while the Y-axis shows the improvement in flux sensitivity. For all GRBs analyzed, a Band spectrum with indices $\alpha = -1.0, \beta = -2.3$ has been used.

diminishes. Additionally, we extended our simulation to include Longer GRBs with a duration of 100 s. These results mirror the trend observed with the classical 30 s duration, revealing a consistent pattern.

Sensitivity improvements are approximately 60% at 5 keV and 20% at 20 keV. Above 100 keV, the improvement is negligible. This trend is logical, considering that with higher E_p values in GRBs, there are comparatively fewer photons in the 4–8 keV range for the same GRB fluence, diminishing the relative impact of this energy band. Note that it is complicated to translate this sensitivity improvement in number of GRBs, because we do not know the true population of soft GRBs.

6.3 Simulation of the ECLGRM trigger using X-ray flash sample of HETE-2

To further verify the importance of the 4–8 keV energy band in detecting soft GRBs, a more detailed ECLGRM simulation was conducted utilizing the HETE-2 catalog dataset (Pélangeon, A. et al., 2008). In this section, we focused on the X-ray flash (E_p < 30 keV) bursts sample in the HETE-2 catalog (Pélangeon, A. et al., 2008). A total of 12 X-ray flash (XRF) events were selected.

Using the spectrum parameters, we first expanded the fluence of each burst from the HETE-2/WXM band (2–30 keV) to the ECLAIRs detectable band (4–150 keV). Then by hy-

pothesizing that these XRFs occur in the central FOV of ECLAIRs, we merged the XRF lightcurves with the X-ray background (CXB, albedo, reflection) to generate the detection events. Subsequently, the ECLGRM-CRT algorithm was applied, allowing the best sub-dataset (maximum count-significance) to be selected, followed by background subtraction and deconvolution, to obtain the sky image SNR values.

The detailed information of the XRF sample and the corresponding simulated fluence results are presented in Table 6.3. The best count-significances and the best sky SNRs were obtained in the 4–120 keV and 8–120 keV ranges. These results are also summarized in Table 6.3.

Table 6.3: Results of the simulation of the ECLGRM count-rate trigger for the HETE-2 X-ray flash sample. The selection criteria for the sample is $E_p < 30$ keV in the catalog.

GRB	E_p (keV)	T90_cat (s)	Spectrum type [a]	A_norm	Alpha	Beta	2–30 keV fluence[b]	4–150 keV fluence	4–120 keV count-significance	4–120 keV SNR	8–120 keV count-significance	8–120 keV SNR
11130	3.9	10.64	B	0.0047	-1.74	-2.7	5.90e-7	5.16e-7	67.69	62.39	39.81	38.28
11212	3.74	39.62	B	0.0086	-1.23	-2.15	4.85e-7	5.64e-7	12.75	14.1	8.51	9.09
20317	28.0	7.14	C	0.0337	-0.60	-999.0	2.20e-7	3.32e-7	29.63	28.01	27.3	24.75
20625	8.5	13.98	C	0.0114	-1.10	-999.0	2.40e-7	1.98e-7	27.32	28.79	17.98	19.12
21021	15.0	18.9	C	0.0029	-1.30	-999.0	2.50e-7	2.64e-7	16.38	17.93	12.8	13.49
21104	28.0	21.18	C	0.0137	-1.10	-999.0	1.00e-6	1.45e-6	56.88	50.83	48.71	42.94
30416	2.6	14.29	B	0.0029	-1.89	-2.3	9.00e-7	9.32e-7	95.07	82.12	61.82	55.36
30723	8.9	9.63	B	0.0014	-1.79	-1.9	2.80e-7	4.23e-7	26.34	27.56	19.42	20.13
30824	6.1	10.13	B	0.0056	-1.75	-2.1	8.90e-7	1.11e-6	83.22	73.87	57.47	52.7
031111B	6.01	27.34	B	0.0027	-1.71	-2.2	9.85e-7	1.15e-6	39.91	39.33	26.53	26.59
40701	3.44	11.67	B	0.0025	-1.84	-2.3	5.44e-7	5.70e-7	61.5	56.55	39.22	38.2
040825B	25.1	15.8	C	0.0079	-1.48	-999.0	1.20e-6	1.61e-6	98.76	84.38	78.41	66.86

[a] "B" represents the Band function, "C" represents the cut-off power law function.

[b] In the unit of erg/cm^2.

Figure 6.10 illustrates the best sky SNR results obtained from the ECLGRM-CRT. All the 12 XRFs listed in the HETE-2 catalog were found to be detectable by ECLAIRs. This outcome is reasonable, since the ECLAIRs has a larger effective area and a broader detection energy band than the HETE-2 Wide Field X-ray Monitor (WXM). In our analysis, we compare the ECLAIRs 4–120 keV SNR and 8–120 keV SNR for each burst. The contribution of the 4–8 keV range to the SNR increment is quantified using Equation 6.3.

$$I_{SNR} = \frac{\mathrm{SNR}_{4-120} - \mathrm{SNR}_{8-120}}{\mathrm{SNR}_{8-120}} \tag{6.3}$$

SNR_{4-120} and SNR_{8-120} represent the best sky SNR in the 4–120 keV and 8–120 keV band. The SNR improvement results are shown in Figure 6.10.

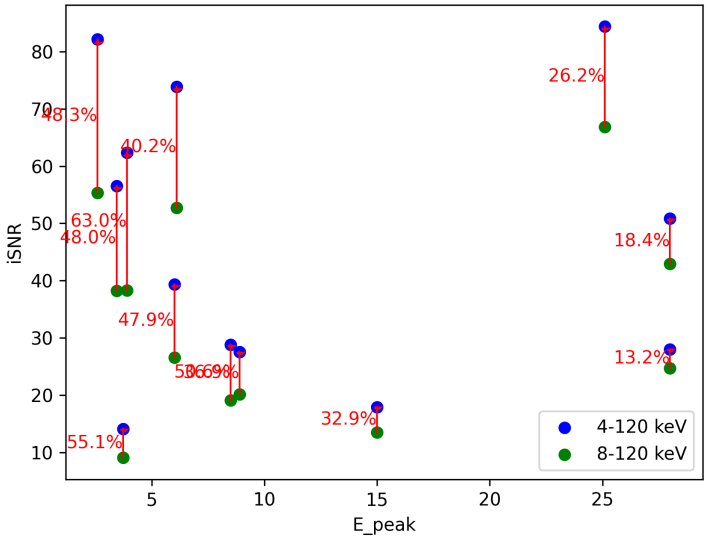

Figure 6.10: The best image SNR is presented for each X-Ray flash burst in the figure, obtained from the 8–120 keV band (green) and the 4–120 keV band (blue). The SNR improvements for each burst are quantitatively calculated and marked.

Figure 6.11 highlights the image SNR improvement attributable to the 4–8 keV range, observed across different peak energies in the selected XRFs. It demonstrates a trend where the lower the peak energy, the more significant the improvement in SNR, which agrees with the results for the customized GRB simulation in Figure 6.9. Specifically, for an E_p = 5 keV, the SNR shows an approximate improvement of 60%, and for an E_p = 25 keV, the SNR exhibits an approximate improvement of 20%. This trend aligns with our previous analysis: as the peak energy of a GRB increases, the proportion of 4–8 keV photons decreases in the total photon count, leading to a reduced influence of this band on the detection of the GRB.

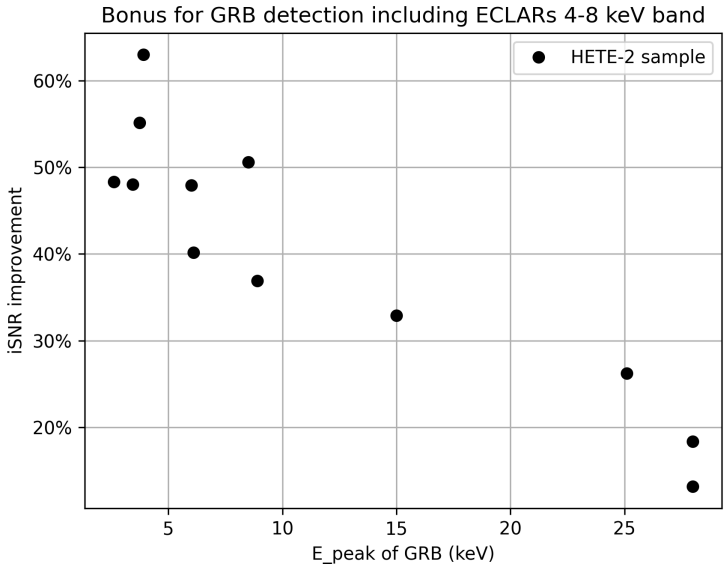

Figure 6.11: The image SNR improvement after involving the 4–8 keV band. The GRBs selected from the HETE-2 sample with peak energy < 30 keV.

6.4 Simulation of ECLGRM trigger using the HETE-2 catalog

In this section, we present the simulations of the ECLGRM trigger using the HETE-2 sample (Pélangeon, A. et al., 2008) composed of 57 GRBs. The simulation process follows the methodology described in section 6.3, but in this section we have extended the GRB sample to include both X-ray rich and classical GRBs.

We first converted the HETE-2 catalog fluence from the HETE-2/WXM band (2–30 keV) to the ECLAIRs detection band (4–150 keV), relying on each GRB's spectrum information. The outcomes are illustrated in Figure 6.12. There is a positive correlation between the fluence of the GRB in the HETE-2/WXM band and that in the ECLAIRs band, which can be explained by the fact that the energy range detectable by ECLAIRs largely overlaps the HETE-2/WXM range.

We integrated the GRB sample into the simulation, incorporating the same flat background (CXB, albedo, reflection) as demonstrated in Figure 6.3. Subsequently, the ECLGRM-CRT algorithm was executed. Additionally, we employed different trigger energy bands: 4–120 keV and 8–120 keV, aiming to assess the importance of the 4–8 keV band for detecting different GRB classes.

Figure 6.13 presents the simulation results. Generally speaking, the best image SNR obtained from ECLGRM-CRT correlates directly with the GRB fluence. Of the 57 GRBs simulated, 56 successfully triggered ECLAIRs, with one exception: GRB031109B did not trigger ECLAIRs.

GRB031109B exhibited a weak fluence of 8.16×10^{-7} erg/cm^2 and a long T_{90} duration of

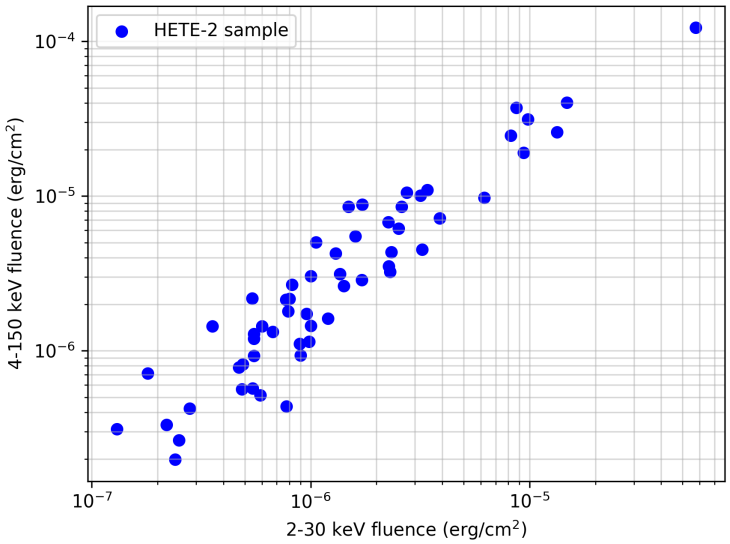

Figure 6.12: Fluence value of HETE-2 GRB samples in 2–30 keV band (WXM) versus their corresponding fluence converted in the 4–150 keV band (ECLAIRs).

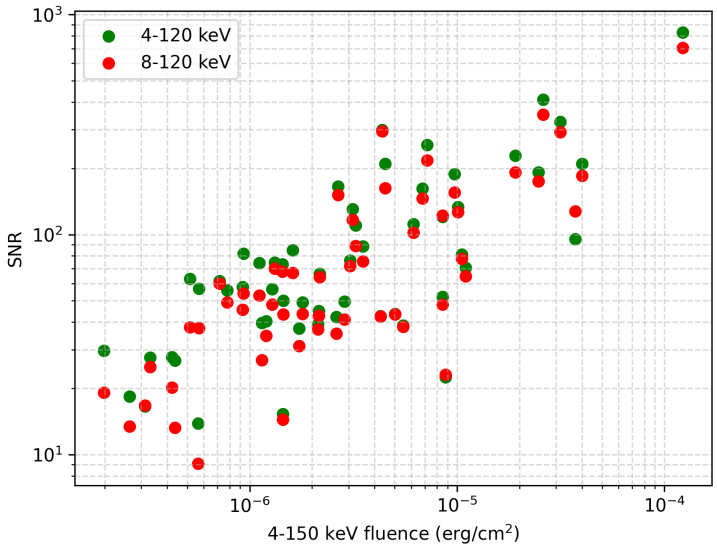

Figure 6.13: This figure represents the simulation of ECLAIRs detection for the HETE-2 GRB sample. On the x-axis is the fluence of the GRB sample in the 4–150 keV range, while the y-axis depicts the best image SNR obtained from ECLGRM-CRT in the simulation. Points colored in red represent the ECLAIRs trigger energy band of 8–120 keV, and those in green indicate a band of 4–120 keV.

51.8 s with a platform-like shape, as shown in the right panel of Figure 6.14. The ECLGRM-CRT is limited to selecting time slices of less than 20.48 s. This limitation coupled with the time dispersion of photons in this GRB could be the reason why ECLGRM-CRT couldn't

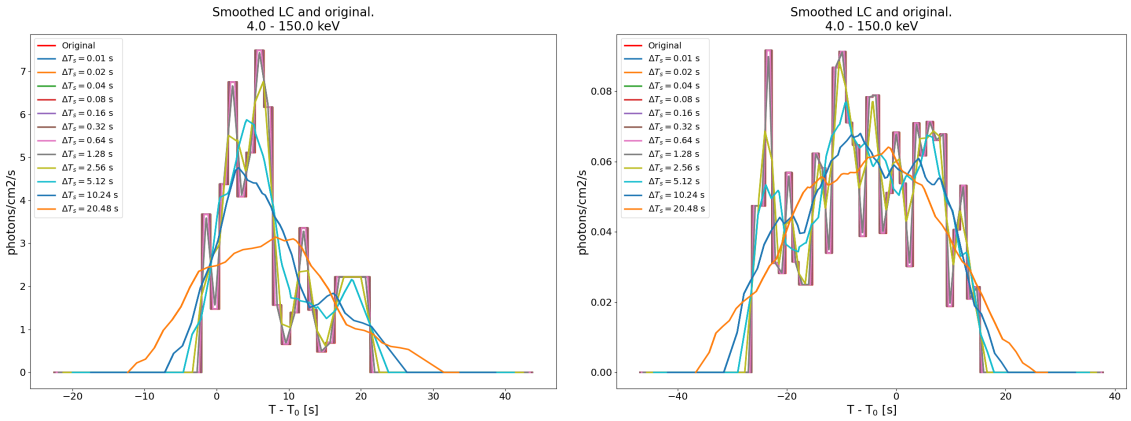

Figure 6.14: HETE-2 GRB lightcurve example. Left: GRB011130. Right: GRB031109B.

produce an SNR $\geq$ 6.5.

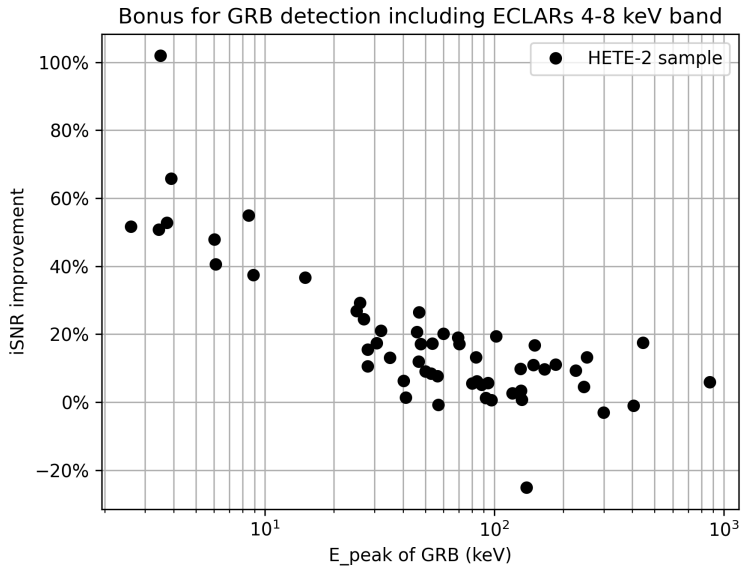

Figure 6.15: ECLGRM-CRT image SNR improvement after involving the 4–8 keV band for HETE-2 57 GRBs sample.

The bonus of SNR improvement after involving the 4–8 keV band is illustrated in Figure 6.15. Generally, the best image SNR obtained from 4–120 keV exceeds that from 8–120 keV. The simulation results in Figure 6.15 also demonstrates the consistent trend that the image SNR improvement attributable to the 4–-8 keV bonus is more pronounced for X-Ray Flashes with E_p < 30 keV, ranging between 20% - 60 %, compared to GRBs with E_p > 30 keV, in which image SNR improvement is generally between 0% – 20%.

There is a burst, GRB030519, which exhibited a lower SNR in the 4–120 keV range (SNR = 95.56) compared to the 8–120 keV range (SNR = 127.63). This particular GRB has a band spectrum with E_p = 138 keV, $\alpha = -0.8$, $\beta = -1.7$. For this burst, the optimal trigger energy band was found to be 25–120 keV. The observed decrease in SNR in the 4-120 keV

GRB name	T90 (s)	E_p (keV)	fluence in 2–30keV (erg_cm^2)	fluence in 4–150keV (erg_cm^2)	best trigger timescale (s)	SNR_4_120keV	SNR_8_120keV
011130	10.64	3.9	5.900e-7	5.160e-7	20.48	62.96	37.98
011212	39.62	3.74	4.850e-7	5.640e-7	20.48	13.89	9.09
020305	39.06	245.1	2.750e-6	1.060e-5	20.48	81.38	77.85
020317	7.14	28.0	2.200e-7	3.320e-7	5.12	27.67	25.03
020331	179.4	92.0	1.600e-6	5.510e-6	20.48	38.6	38.13
020625	13.98	8.5	2.400e-7	1.980e-7	20.48	29.68	19.15
020801	460.33	53.0	2.600e-6	8.530e-6	20.48	52.26	48.22
020812	18.28	88.0	8.000e-7	2.160e-6	10.24	45.01	42.79
020813	87.34	253.4	1.480e-5	4.010e-5	20.48	209.88	185.43
020819	28.8	50.0	2.520e-6	6.150e-6	20.48	111.45	102.17
021004	48.94	80.0	7.700e-7	2.130e-6	20.48	39.14	37.08
021016	80.63	226.2	3.420e-6	1.100e-5	20.48	70.62	64.61
021021	18.9	15.0	2.500e-7	2.640e-7	20.48	18.37	13.44
021104	21.18	28.0	1.000e-6	1.450e-6	10.24	50.15	43.4
021112	3.24	57.0	1.300e-7	3.120e-7	2.56	16.58	16.71
021211	4.23	46.8	1.360e-6	3.130e-6	2.56	130.77	116.83
030115	20.33	83.0	7.900e-7	1.800e-6	20.48	49.31	43.56
030226	76.23	97.0	1.300e-6	4.270e-6	20.48	42.67	42.42
030324	10.98	150.0	5.500e-7	1.200e-6	5.12	40.46	34.66
030328	138.27	130.0	8.200e-6	2.460e-5	20.48	191.59	174.46
030329	25.91	70.2	5.760e-5	1.230e-4	20.48	829.19	707.75
030416	14.29	2.6	9.000e-7	9.320e-7	20.48	82.0	54.08
030418	139.23	46.0	1.710e-6	2.870e-6	20.48	49.62	41.11
030429	12.95	35.0	4.700e-7	7.800e-7	20.48	55.79	49.3
030519	12.85	138.0	8.710e-6	3.720e-5	2.56	95.56	127.63
030528	62.8	32.0	6.200e-6	9.740e-6	20.48	188.69	155.86
030723	9.63	8.9	2.800e-7	4.230e-7	20.48	27.69	20.15
030725	174.31	102.0	9.400e-6	1.910e-5	20.48	228.95	191.81
030821	19.42	84.0	1.000e-6	3.040e-6	20.48	76.35	71.95
030823	50.39	27.0	2.310e-6	3.240e-6	20.48	110.38	88.69
030824	10.13	6.1	8.900e-7	1.110e-6	20.48	74.4	52.9
030913	6.58	120.0	1.800e-7	7.160e-7	5.12	61.66	60.05
031026	65.58	870.3	3.560e-7	1.440e-6	20.48	15.28	14.43
031109A	57.32	185.2	9.830e-6	3.140e-5	20.48	324.88	292.45
031109B	51.8	37.7	4.900e-7	8.160e-7	20.48	0.0	0.0
031111A	7.94	404.4	1.490e-6	8.510e-6	5.12	120.64	121.96
031111B	27.34	6.01	9.850e-7	1.150e-6	20.48	39.77	26.9
031203	10.38	148.2	2.270e-6	6.800e-6	10.24	162.16	146.16
031220	9.69	46.9	5.500e-7	9.250e-7	10.24	57.73	45.63
040319	6.1	56.6	6.000e-7	1.440e-6	10.24	73.15	67.96
040423	45.87	30.7	2.270e-6	3.520e-6	20.48	88.61	75.52
040425	138.81	299.9	1.720e-6	8.800e-6	10.24	22.43	23.13
040511	45.8	93.9	3.170e-6	1.010e-5	20.48	133.74	126.6
040701	11.67	3.44	5.440e-7	5.700e-7	20.48	56.84	37.68
040825A	39.2	60.0	9.600e-7	1.730e-6	20.48	37.44	31.15
040825B	15.8	25.1	1.200e-6	1.610e-6	20.48	85.09	67.05
040916	349.0	3.5	7.740e-7	4.370e-7	20.48	26.72	13.23
040924	3.37	41.1	2.340e-6	4.350e-6	5.12	298.8	294.89
041004	50.13	53.7	1.340e-5	2.590e-5	20.48	411.82	351.25
041006	22.08	47.7	3.890e-6	7.170e-6	20.48	255.14	217.72
041016	21.96	165.3	8.210e-7	2.670e-6	20.48	165.82	151.12
041211	113.84	132.0	1.060e-6	5.020e-6	20.48	43.63	43.32
050123	14.72	40.2	6.700e-7	1.320e-6	20.48	74.61	70.19
050209	18.38	445.0	5.500e-7	1.290e-6	20.48	56.56	48.11
050408	28.39	25.9	3.240e-6	4.500e-6	10.24	209.82	162.29
050807	10.32	69.47	1.410e-6	2.620e-6	1.28	42.17	35.44
050922	6.13	130.5	5.400e-7	2.170e-6	5.12	66.38	64.23

Table 6.4: HETE-2 GRB catalog information (Pélangeon, A. et al., 2008) and simulation results.

range can likely be attributed to the background count's impact being more significant than the effect of this GRB counts in the 4–25 keV range.

6.5 Assessment of the UGTS trigger performance using HETE-2 catalog

The SVOM satellite will be launched in June 2024. Over the first few months, the satellite will go through a commissioning phase to test the performance of the instruments and adjust their parameters. During this phase, the ECLAIRs trigger strips will be set to 5–8, 8–20, 20–50, 50–120 keV and the predefined trigger bands will then be 8–120, 8–50, 20–120, 5–8 keV.

The trigger threshold is preset to 5 keV to avoid noisy counting in the 4–5 keV band. A separate 5–8 keV energy band is set to avoid the impacts of pixel inhomogeneity and heat pipe noise that we have observed in the 4–8 keV band. If, despite the corrections presented in Chapter 5, this band significantly affects the normal trigger function, we can drop the data from this band and select only the data from 8 to 120 keV.

Based on this energy band setting, we ran simulations using ECLGRM software. We also played the same dataset with the ground test bench, which uses the same real-time triggering hardware as the UGTS system implemented on board, and compared these two results. Since the real-time dynamic behavior of this ground hardware test bench is identical to the UGTS system on board SVOM (see Chapter 3), we will refer to this test bench trigger as the UGTS trigger in the remainder of this chapter.

The simulation sample is the same as in Section 6.4 (with the same 57 GRBs). The trigger results of ECLGRM-CRT, UGTS-CRT, UGTS-IMT are summarized in Table 6.5.

6.5.1 Comparation the count-rate trigger in ECLGRM and UGTS

First, we compare the results of ECLGRM-CRT and UGTS-CRT. Given that their underlying logic is to select the best time slice for deconvolution and search for the highest excess in the deconvolved image, their results should be similar. Figure 6.16 shows the comparison of maximum SNR between ECLGRM-CRT and UGTS-CRT for each GRB. It shows a high degree of consistency between the triggering results obtained by ECLGRM-CRT and the UGTS-CRT method.

The histograms of the maximum SNR values extracted from various trigger methods are shown in Figure 6.17. These methods encompass ECLGRM-CRT, UGTS-CRT, and UGTS-IMT. The mean value of the histogram between ECLGRM-CRT and UGTS-CRT is quite similar with 92.6 and 92.2, respectively.

Suppose we have a trigger threshold of 6.5 (ideal flat background and no systematic residual errors in the image), among the 57 simulated burst triggers analyzed, all bursts could be triggered by the UGTS-IMT, and 55 of these were also triggered by both UGTS-

Table 6.5: ECLAIRs trigger result summary of 57 HETE-2 GRBs sample.

GRB information [1]				ECLGRM count-rate trigger			UGTS count-rate trigger			UGTS image trigger		
GRB	E_p	T90	fluence	SNR[2]	Time[3]	Energy[4]	SNR	Time	Energy	SNR	Time	Energy
011130	3.90	10.64	5.16e-07	41.09	20.48	5–8	37.47	10.24	5–8	34.28	40.96	5–8
011212	3.74	39.62	5.64e-07	7.34	20.48	8–50	7.66	10.24	8–120	10.48	655.36	5–8
020305	245.10	39.06	1.06e-05	75.25	20.48	8–120	70.71	20.48	8–120	60.79	40.96	8–120
020317	28.00	7.14	3.32e-07	24.97	5.12	8–50	23.99	2.56	8–50	15.54	20.48	8–50
020331	92.00	179.40	5.51e-06	35.54	20.48	8–120	31.33	20.48	8–120	32.45	40.96	8–120
020625	8.50	13.98	1.98e-07	18.05	20.48	5–8	17.88	20.48	5–8	18.85	20.48	5–8
020801	53.00	460.33	8.53e-06	33.54	20.48	8–120	33.48	20.48	8–120	43.45	81.92	8–120
020812	88.00	18.28	2.16e-06	43.21	10.24	8–120	41.42	10.24	8–120	28.54	20.48	8–120
020813	253.40	87.34	4.01e-05	182.72	20.48	8–120	123.20	20.48	8–120	233.20	40.96	8–120
020819	50.00	28.80	6.15e-06	100.60	20.48	8–120	90.53	20.48	8–120	85.12	40.96	8–120
021004	80.00	48.94	2.13e-06	36.62	20.48	8–120	35.01	20.48	8–120	43.52	40.96	8–120
021016	226.20	80.63	1.10e-05	62.70	20.48	8–120	56.73	20.48	8–120	76.50	81.92	8–120
021021	15.00	18.90	2.64e-07	10.69	20.48	8–50	11.21	10.24	8–50	10.51	655.36	5–8
021104	28.00	21.18	1.45e-06	41.32	10.24	8–50	40.01	20.48	8–120	31.87	20.48	8–50
021112	57.00	3.24	3.12e-07	13.05	2.56	8–120	12.86	2.56	8–120	10.40	655.36	5–8
021211	46.80	4.23	3.13e-06	102.83	1.28	8–120	103.58	20.48	8–120	103.43	20.48	8–120
030115	83.00	20.33	1.80e-06	44.38	10.24	8–120	39.33	20.48	8–120	31.80	40.96	8–120
030226	97.00	76.23	4.27e-06	42.52	20.48	8–120	41.35	20.48	8–120	59.92	81.92	8–120
030324	150.00	10.98	1.20e-06	30.08	5.12	8–120	32.19	10.24	8–120	24.67	20.48	8–120
030328	130.00	138.27	2.46e-05	173.37	20.48	8–120	125.46	20.48	8–120	265.68	163.84	8–120
030329	70.20	25.91	1.23e-04	726.43	20.48	8–120	137.27	5.12	8–120	673.96	40.96	8–120
030416	2.60	14.29	9.32e-07	52.45	20.48	5–8	55.88	20.48	8–120	53.54	20.48	8–120
030418	46.00	139.23	2.87e-06	32.07	20.48	8–120	34.21	20.48	8–120	50.48	163.84	8–120
030429	35.00	12.95	7.80e-07	48.29	20.48	8–120	47.02	20.48	8–120	41.98	40.96	8–120
030519	138.00	12.85	3.72e-05	123.34	2.56	20-120	109.80	20.48	8–120	109.69	20.48	8–120
030528	32.00	62.80	9.74e-06	154.42	20.48	8–120	97.94	20.48	8–120	193.82	81.92	8–120
030723	8.90	9.63	4.23e-07	18.28	20.48	8–120	21.01	10.24	8–120	13.66	40.96	8–120
030725	102.00	174.31	1.91e-05	193.34	20.48	8–120	0.00	0.32	8–120	196.87	40.96	8–120
030821	84.00	19.42	3.04e-06	72.63	20.48	8–120	72.31	20.48	8–120	62.16	40.96	8–120
030823	27.00	50.39	3.24e-06	89.72	20.48	8–50	89.91	20.48	8–120	109.92	81.92	8–120
030824	6.10	10.13	1.11e-06	49.93	20.48	8–50	53.69	10.24	8–120	39.07	40.96	8–120
030913	120.00	6.58	7.16e-07	53.06	5.12	8–120	54.47	20.48	8–120	45.85	40.96	8–120
031026	870.30	65.58	1.44e-06	13.14	20.48	8–120	12.83	20.48	20-120	13.75	81.92	8–120
031109A	185.20	57.32	3.14e-05	292.13	20.48	8–120	102.50	20.48	8–120	297.33	40.96	8–120
031109B	37.70	51.80	8.16e-07	4.17	20.48	8–120	4.98	1.28	5–8	10.38	655.36	5–8
031111A	404.40	7.94	8.51e-06	155.50	5.12	20-120	136.22	20.48	8–120	141.79	20.48	8–120
031111B	6.01	27.34	1.15e-06	25.14	20.48	8–50	26.52	10.24	8–120	18.10	40.96	8–120
031203	148.20	10.38	6.80e-06	140.36	10.24	8–120	82.20	20.48	8–120	126.95	20.48	8–120
031220	46.90	9.69	9.25e-07	46.58	10.24	8–120	43.41	10.24	8–120	34.02	20.48	8–120
040319	56.60	6.10	1.44e-06	64.61	5.12	8–120	66.94	10.24	8–120	54.70	20.48	8–120
040423	30.70	45.87	3.52e-06	75.83	20.48	8–50	77.72	20.48	8–120	79.20	40.96	8–120
040425	299.90	138.81	8.80e-06	22.23	10.24	20-120	23.54	10.24	8–120	17.80	20.48	20-120
040511	93.90	45.80	1.01e-05	126.11	20.48	8–120	121.92	20.48	8–120	149.32	40.96	8–120
040701	3.44	11.67	5.70e-07	38.68	20.48	5–8	39.49	20.48	8–120	64.59	81.92	8–50
040825A	60.00	39.20	1.73e-06	30.35	20.48	8–120	29.85	20.48	8–120	29.90	20.48	8–120
040825B	25.10	15.80	1.61e-06	65.12	20.48	8–50	61.53	20.48	8–120	53.16	40.96	8–120
040916	3.50	349.00	4.37e-07	4.11	20.48	5–8	4.98	1.28	5–8	11.04	327.68	5–8
040924	41.10	3.37	4.35e-06	291.35	5.12	8–120	277.32	20.48	8–120	271.81	20.48	8–120
041004	53.70	50.13	2.59e-05	354.10	20.48	8–120	100.26	20.48	8–120	430.20	81.92	8–120
041006	47.70	22.08	7.17e-06	216.13	20.48	8–120	125.25	20.48	8–120	214.05	20.48	8–120
041016	165.30	21.96	2.67e-06	153.16	20.48	8–120	109.86	20.48	8–120	172.27	163.84	8–120
041211	132.00	113.84	5.02e-06	49.00	20.48	20-120	47.85	20.48	8–120	50.04	40.96	8–120
050123	40.20	14.72	1.32e-06	67.65	10.24	8–120	64.15	20.48	8–120	58.07	40.96	8–120
050209	445.00	18.38	1.29e-06	46.70	20.48	8–120	48.99	20.48	8–120	42.90	40.96	8–120
050408	25.90	28.39	4.50e-06	159.08	10.24	8–120	132.81	20.48	8–120	159.40	40.96	8–120
050807	69.47	10.32	2.62e-06	38.05	1.28	8–120	39.52	1.28	8–120	27.40	20.48	8–120
050922	130.50	6.13	2.17e-06	64.30	5.12	8–120	54.37	10.24	8–120	43.57	20.48	8–120

1. The units of GRB E_p, T90 and fluence are Kev, s, and erg/cm^2 in 4–150 keV, respectively. The detailed spectrum parameter can be found in Pélangeon, A. et al. (2008). 2. SNR represents the best SNR (largest) of all obtained in the trigger algorithm. 3. Time is the timescale (second) corresponding to the best SNR. 4. Energy is the energy band (keV) corresponding to the best SNR.

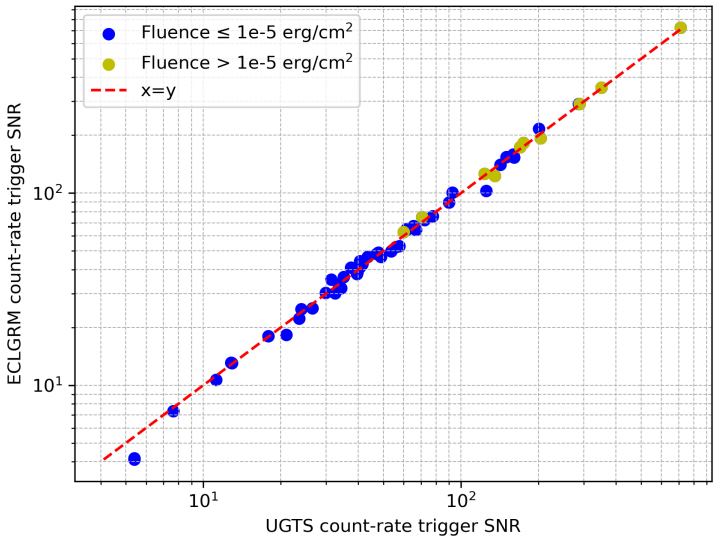

Figure 6.16: Comparison of maximum SNRs between the ECLGRM-CRT and UGTS-CRT. Bright GRBs, identified by yellow points, are those with a fluence greater than 10^{-5} erg/cm^2.

CRT and ECLGRM-CRT. These two fail GRBs are GRB040916 and GRB031109B. We will analyze these two cases in detail in the next section.

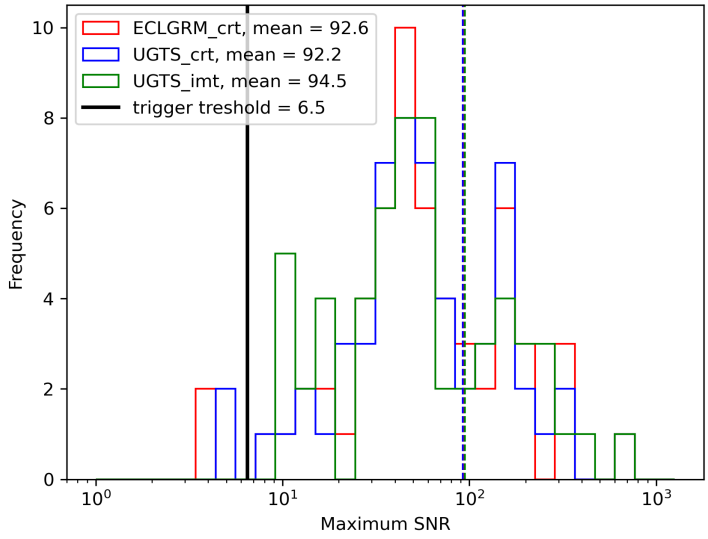

Figure 6.17: ECLAIRs trigger performance for 57 HETE-2 GRB sample. The red color represents the maximum SNR obtained from the ECLGRM-CRT, and the blue and green histograms are obtained from the UGTS-CRT and UGTS-IMT respectively. The black line stands for the trigger threshold of 6.5.

6.5.2 UGTS trigger result with a dynamical threshold

In an ideal situation, in which the shadowgram is filled with a flat background observed for a sufficiently long time, the sky SNR produced by the deconvolution follows a normal distribution with a standard deviation of the sky map (std, σ_{SNR}) of 1. That's why we set the threshold to 6.5 in ECLGRM.

However, in a practice situation, as presented in Chapter 3, the imperfect correction of the background could cause SNR higher than 6.5 when stacking images up to 20 min. The quality of the resulted sky images is measured by computing the standard deviation of the SNR which can reach values greater than 1. Previous studies (Dagoneau et al., 2022) have suggested that to avoid false triggers, we could set the trigger threshold as 6.5 $\times$ σ_{SNR} to have a dynamic threshold according to the SNR distribution (Section 3.4). This is the criteria used in UGTS trigger to detect new transients.

Therefore, in the next analyses, we will only focus on the performance of the UGTS triggers, based on a trigger threshold set as SNR/σ_{SNR} = 6.5. We summarize the trigger results for UGTS in Table 6.6. These results include the best SNR of the GRB obtained by the trigger, the std corresponding to the time slice containing the best SNR, and the SNR/σ_{SNR}.

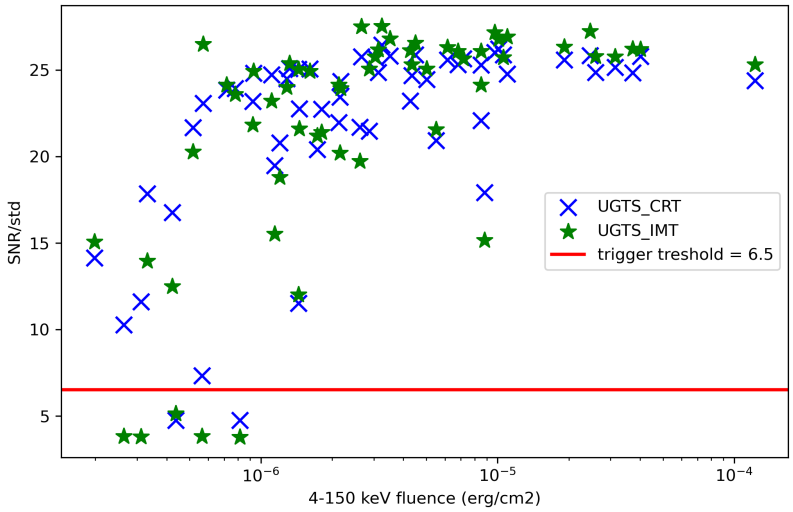

Figure 6.18: SNR/σ_{SNR} versus GRB fluence for different trigger methods. The blue crosses and green indicate the best SNR/σ_{SNR} from the UGTS-CRT and UGTS-IMT respectively.

Figure 6.18 shows the relationship between the GRB fluence and the detected SNR/σ_{SNR} in UGTS. The fluence of the GRBs samples ranges from 10^{-7} to 10^{-4} erg/cm^{-2}. The figure shows a trend whereby the higher the fluence of a GRB, the higher the SNR/σ_{SNR} detected. But after the GRB fluence reaches a certain value ($\sim 3 \times 10^{-4}$ erg/cm^{-2}), the maximum SNR/σ_{SNR} ends up centered $\sim$ 26 and does not continue to increase higher.

There are 5 undetected GRBs for UGTS-IMT. However, 3 of them could be triggered by UGTS-CRT. All these bursts are weak bursts with a fluence smaller than 10^{-6} erg/cm^2. The

Table 6.6: UGTS trigger result summary of 57 HETE-2 GRBs sample.

GRB information [1]				UGTS-CRT			UGTS-IMT		
GRB	E_p	T90	fluence	SNR[2]	σ_{SNR}[3]	SNR/σ_{SNR}	SNR	σ_{SNR}	SNR/σ_{SNR}
011130	3.90	10.64	5.16e-07	37.47	1.73	21.67	34.28	1.69	20.28
011212	3.74	39.62	5.64e-07	7.66	1.05	7.32	10.48	2.74	3.82
020305	245.10	39.06	1.06e-05	70.71	2.73	25.88	60.79	2.36	25.73
020317	28.00	7.14	3.32e-07	23.99	1.34	17.85	15.54	1.11	13.95
020331	92.00	179.40	5.51e-06	31.33	1.50	20.93	32.45	1.51	21.56
020625	8.50	13.98	1.98e-07	17.88	1.26	14.14	18.85	1.25	15.06
020801	53.00	460.33	8.53e-06	33.48	1.52	22.08	43.45	1.80	24.15
020812	88.00	18.28	2.16e-06	41.42	1.77	23.44	28.54	1.41	20.20
020813	253.40	87.34	4.01e-05	174.74	6.78	25.79	233.20	8.90	26.21
020819	50.00	28.80	6.15e-06	92.70	3.62	25.60	85.12	3.23	26.32
021004	80.00	48.94	2.13e-06	35.01	1.59	21.96	43.52	1.80	24.15
021016	226.20	80.63	1.10e-05	59.84	2.41	24.78	76.50	2.84	26.93
021021	15.00	18.90	2.64e-07	11.22	1.09	10.27	10.51	2.75	3.82
021104	28.00	21.18	1.45e-06	40.58	1.78	22.77	31.87	1.47	21.61
021112	57.00	3.24	3.12e-07	12.94	1.12	11.60	10.40	2.74	3.79
021211	46.80	4.23	3.13e-06	125.43	5.05	24.86	103.43	3.95	26.17
030115	83.00	20.33	1.80e-06	40.51	1.78	22.73	31.80	1.49	21.41
030226	97.00	76.23	4.27e-06	41.35	1.78	23.22	59.92	2.29	26.13
030324	150.00	10.98	1.20e-06	32.43	1.56	20.79	24.67	1.31	18.81
030328	130.00	138.27	2.46e-05	169.85	6.57	25.84	265.68	9.75	27.24
030329	70.20	25.91	1.23e-04	710.84	29.13	24.40	673.96	26.61	25.33
030416	2.60	14.29	9.32e-07	55.88	2.25	24.83	53.54	2.15	24.94
030418	46.00	139.23	2.87e-06	34.21	1.59	21.48	50.48	2.01	25.08
030429	35.00	12.95	7.80e-07	47.02	1.96	23.93	41.98	1.78	23.59
030519	138.00	12.85	3.72e-05	135.32	5.45	24.85	109.69	4.18	26.22
030528	32.00	62.80	9.74e-06	149.88	5.76	26.02	193.82	7.13	27.17
030723	8.90	9.63	4.23e-07	21.01	1.25	16.76	13.66	1.09	12.48
030725	102.00	174.31	1.91e-05	203.99	7.97	25.60	196.87	7.47	26.34
030821	84.00	19.42	3.04e-06	72.31	2.81	25.73	62.16	2.41	25.78
030823	27.00	50.39	3.24e-06	89.91	3.40	26.46	109.92	3.99	27.55
030824	6.10	10.13	1.11e-06	53.69	2.17	24.73	39.07	1.68	23.22
030913	120.00	6.58	7.16e-07	57.72	2.42	23.84	45.85	1.90	24.15
031026	870.30	65.58	1.44e-06	12.83	1.12	11.50	13.75	1.15	12.00
031109A	185.20	57.32	3.14e-05	288.91	11.48	25.17	297.33	11.54	25.77
031109B	37.70	51.80	8.16e-07	5.40	1.14	4.75	10.38	2.75	3.78
031111A	404.40	7.94	8.51e-06	157.00	6.21	25.30	141.79	5.44	26.08
031111B	6.01	27.34	1.15e-06	26.52	1.36	19.48	18.10	1.17	15.52
031203	148.20	10.38	6.80e-06	142.25	5.62	25.31	126.95	4.87	26.09
031220	46.90	9.69	9.25e-07	43.41	1.87	23.20	34.02	1.56	21.84
040319	56.60	6.10	1.44e-06	66.94	2.67	25.05	54.70	2.18	25.05
040423	30.70	45.87	3.52e-06	77.72	3.01	25.81	79.20	2.95	26.81
040425	299.90	138.81	8.80e-06	23.54	1.31	17.91	17.80	1.17	15.16
040511	93.90	45.80	1.01e-05	123.30	4.70	26.22	149.32	5.57	26.79
040701	3.44	11.67	5.70e-07	39.65	1.72	23.07	64.59	2.44	26.50
040825A	60.00	39.20	1.73e-06	29.85	1.46	20.40	29.90	1.41	21.21
040825B	25.10	15.80	1.61e-06	61.53	2.45	25.07	53.16	2.13	24.93
040916	3.50	349.00	4.37e-07	5.40	1.14	4.75	11.04	2.15	5.13
040924	41.10	3.37	4.35e-06	286.84	11.62	24.69	271.81	10.74	25.31
041004	53.70	50.13	2.59e-05	350.57	14.10	24.87	430.20	16.67	25.80
041006	47.70	22.08	7.17e-06	200.96	7.83	25.65	214.05	8.35	25.65
041016	165.30	21.96	2.67e-06	160.52	6.23	25.78	172.27	6.26	27.52
041211	132.00	113.84	5.02e-06	47.85	1.96	24.47	50.04	2.00	25.07
050123	40.20	14.72	1.32e-06	65.41	2.61	25.09	58.07	2.29	25.39
050209	445.00	18.38	1.29e-06	48.99	2.00	24.50	42.90	1.79	24.00
050408	25.90	28.39	4.50e-06	159.44	6.16	25.89	159.40	6.00	26.57
050807	69.47	10.32	2.62e-06	39.52	1.82	21.70	27.40	1.39	19.73
050922	130.50	6.13	2.17e-06	61.44	2.52	24.35	43.57	1.82	23.94

1. The units of GRB E_p, T90 and fluence are keV, s, and erg/cm^2 in 4–150 keV, respectively. The detailed spectrum parameter can be found in Pélangeon, A. et al. (2008). 2. SNR is the maximum signal-to-noise ratio obtained from the trigger. 3. σ_{SNR} is the standard deviation of the sky image.

two GRBs that can't be triggered in either method are GRB 031109B and GRB 040916. Both of them are long bursts with a T_{90} equal to 531.2 s and 349.0 s, respectively. The other three GRBs (GRB 011212, GRB 021021, GRB 021112) that only could be detected by UGTS-CRT have a shorter duration $T_{90} < 40$ s.

In the case of weak and very long bursts, one might think that the image trigger is an advantage. However, stacking a large number of images after deconvolution increases the standard deviation of the resulting sky image and consequently increases the trigger threshold. This is why, for weak GRBs of intermediate duration, the count rate trigger seems to perform better.

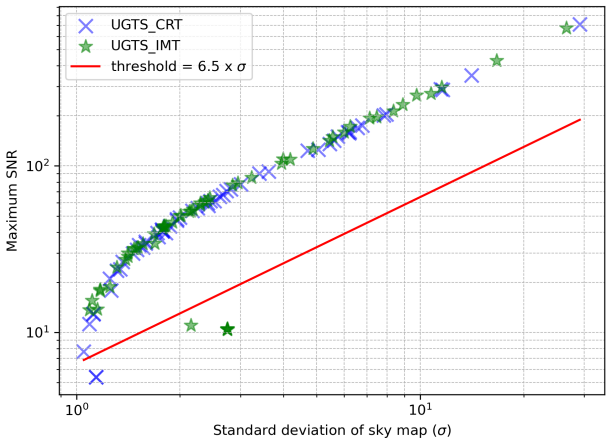

Figure 6.19: UGTS trigger result for 57 GRBs. The best image SNR versue the standard deviation of the sky image obtained from different trigger algorithm.

In order to investigate why $\mathrm{SNR}/\sigma_{\mathrm{SNR}}$ did not continue to rise as the fluence of the GRB increased, we made a plot comparing the best SNR and σ_{SNR} obtained by triggering, as shown in Figure 6.19. From the figure, we find that the maximum SNR value is increasing with the GRB fluence. However the value of σ_{SNR} also increases, this can be explained by the so called "coding noise" which increases the SNR elsewhere in the image, which will result in an increasing Std of the SNR in the whole image. The "coding noise" is due to the fact that the projection of the mask on the detection plane does not only correlate at the position of the source, but a little bit also elsewhere in the image (this is unavoidable, it is related to the mask pattern). This is the reason why although GRB fluence continues to increase while $\mathrm{SNR}/\sigma_{\mathrm{SNR}}$ remain similar.

The comparison of $\mathrm{SNR}/\sigma_{\mathrm{SNR}}$ obtained from UGTS-CRT and UGTS-IMT is depicted in Figure 6.20. Their distributions are similar overall in the histogram, with a mean value of 22.0 for UGTS-CRT and 21.8 for UGTS-IMT. From the right panel, the main difference of these two trigger methods is on the weak and related short GRBs.

For bursts with duration less than 20.48 s, the UGTS-CRT performs much better than the UGTS-IMT. For example, GRB 021112 has a duration 3.24 s. For this burst UGTS-CRT has a SNR of 12.94, σ_{SNR} of 1.12, and a $\mathrm{SNR}/\sigma_{\mathrm{SNR}}$ of 11.60. UGTS-IMT has a SNR of 10.40 but a σ_{SNR} of 2.74, and a final $\mathrm{SNR}/\sigma_{\mathrm{SNR}}$ of 3.79, so this burst could not be detected by UGTS-

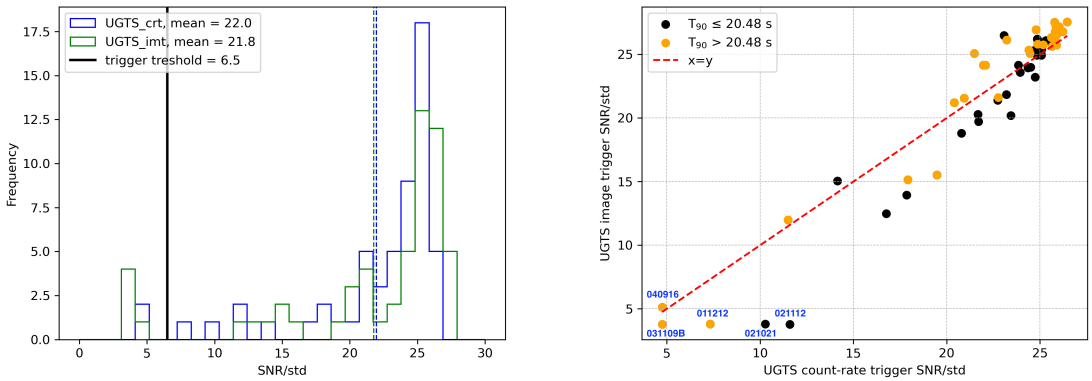

Figure 6.20: SNR/$\sigma_{\rm SNR}$ results. Histogram distribution of the two trigger methods within UGTS (left) and their comparison scatterplot (right). The black and orange scatter points in the right panel indicate GRBs with T_{90} durations less than 20.48 s and greater than 20.48 s, respectively.

IMT. This is because the minimum trigger time for UGTS-IMT is 20.48 s. So a lot of useless background counts outside of the GRB burst time window are collected, causing an increase in $\sigma_{\rm SNR}$.

Another example is GRB 011212, which has a duration 39.62 s. For this burst, the SNRs obtain from UGTS-CRT and UGTS-IMT are 7.66 and 10.48, the $\sigma_{\rm SNR}$ values are 1.05 and 2.74, respectively. Finally the the SNR/$\sigma_{\rm SNR}$ are 7.32 (trigger) and 3.82 (untriggered). The duration of this burst is larger than 20.48s, but the energy of the GRB is mainly concentrated in a certain pulse interval rather than uniformly distributed with time (this burst detail in next section). Therefore, the GRB photons collected outside the main pulse cannot compensate for the fluctuation caused by the background. UGTS-CRT still outperforms UGTS-IMT in this case.

6.5.3 Trigger details of some GRB cases

In our sample, five of 57 GRBs have peak energies less than 5 keV, we mark them as "very soft GRB". We select two of them as examples for detailed UGTS trigger performance.

GRB011130: very soft GRB with E_p < 5 keV

GRB 011130 has a fluence as 5.9 x 10^{-7} erg/cm^2 in 4–150 keV with a T_{90} = 10.6 s. The peak energy is 3.90 keV with Band spectrum parameters α = -1.74 and β = -2.70. Figure 6.21 shows the input event generated by the ECLGRM tool. We still see the GRB above the background.

The best trigger SNR/$\sigma_{\rm SNR}$ for this burst is around 21.5, in the 5–8 keV band for UGTS-IMT, and in the 8–120 keV band for UGTS-CRT. We detect it in all energy bands except in

the 20–120 keV band of the UGTS-CRT. This could be explained by the fact that this burst is bright but its photon flux is concentrated in the low-energy band.

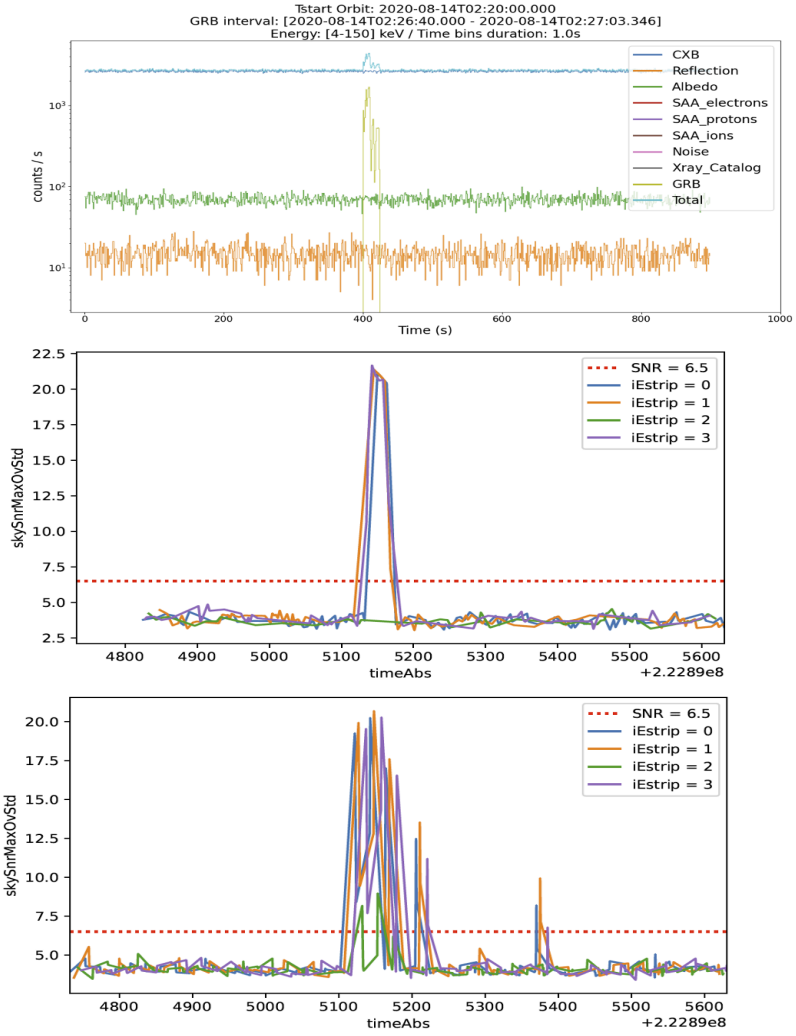

Figure 6.21: Trigger result for simulated GRB011130. (a) Events simulated by ECLGRM software. SNR results in different energy bands performed by UGTS CRT algorithm (b) and UGTS IMT algorithm (c), the iEstrip 0, 1, 2, 3 represent the energy band 8–120, 8–50, 20–120, 5–8 keV, respectively.

GRB 011212, very soft GRBs with E_p < 5 keV

GRB011212 is a weaker and longer burst compared the GRB011130. This burst has a fluence as 4.8 x 10^{-7} erg/cm^2 in 4-150 keV with a T_{90} = 39.6 s. Its spectrum could be described as a Band function with E_p = 3.74 keV, α=-1.23 and β = -2.15. Figure 6.21 shows the input event generated by the ECLGRM tool. The GRB can barely be seen above the background.

Due to the weaker fluence and longer duration, the average flux of this burst is lower. As a result, the SNR obtained from the triggers is much lower than that of the GRB 011130.

Notably, this burst only could be detected via the UGTS-CRT, in the 8–120 and 8–50 keV energy bands. The maximum SNR/$\sigma_{\rm SNR}$ is 7.6 for UGTS-CRT and 5.5 for UGTS-IMT (undetected).

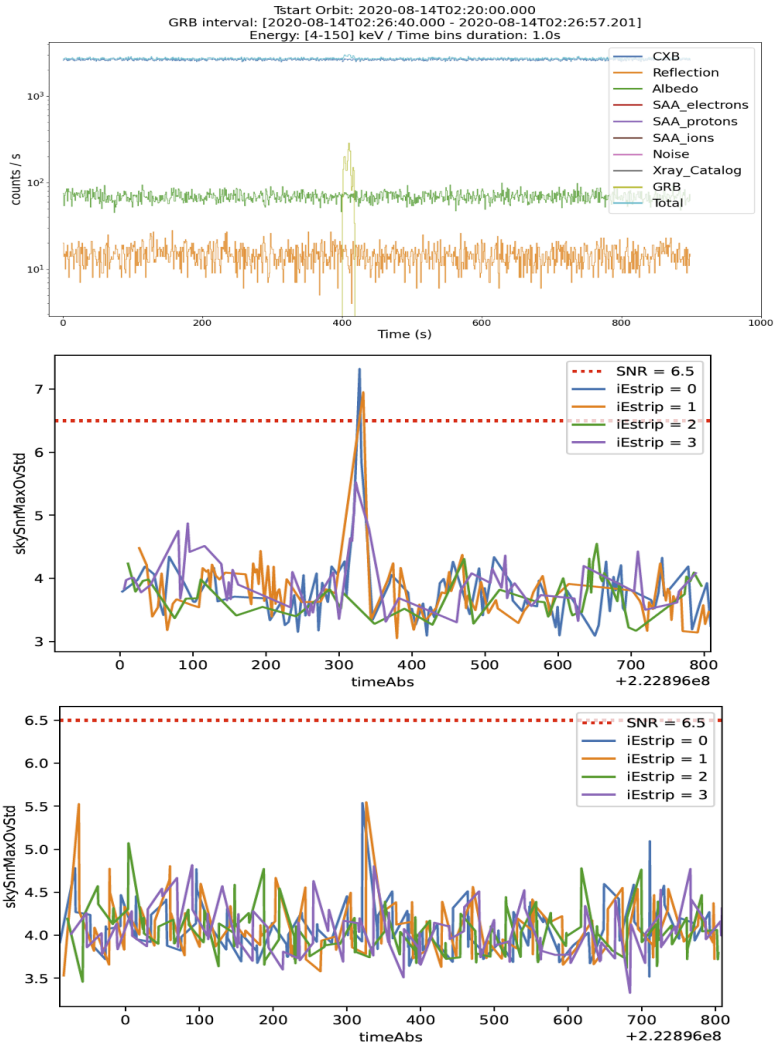

Figure 6.22: Trigger results of simulated GRB 011212. (a) Events simulated by ECLGRM software. SNR results in different energy bands performed by UGTS-CRT algorithm (b) and UGTS-IMT algorithm (c), the iEstrip 0, 1, 2, 3 represent the energy band 8–120, 8–50, 20–120, 5–8 keV, respectively.

GRB 020801: very long GRBs (T90 > 200 s)

GRB 020801 is a long burst with a T_{90} = 460.3 s. This burst has a fluence as 8.5 x 10^{-6} erg/cm^2 in 4-150 keV and its spectrum could be described with a Band function with E_p = 53.0 keV, α=-0.30 and β = -2.00.

The best trigger SNR/$\sigma_{\rm SNR}$ for this burst is 24.0, which was obtained from UGTS-IMT with the best timescale of 81.92 s in 8–120 keV. This can be explained by the long duration

of this burst and the bimodal structure of the lightcurve. The peak energy of the spectrum is relatively high, which means that the photons are concentrated on the high-energy band. Figure 6.23 shows that the SNRs obtained from both triggers in UGTS follow the shape of the lightcurve flux.

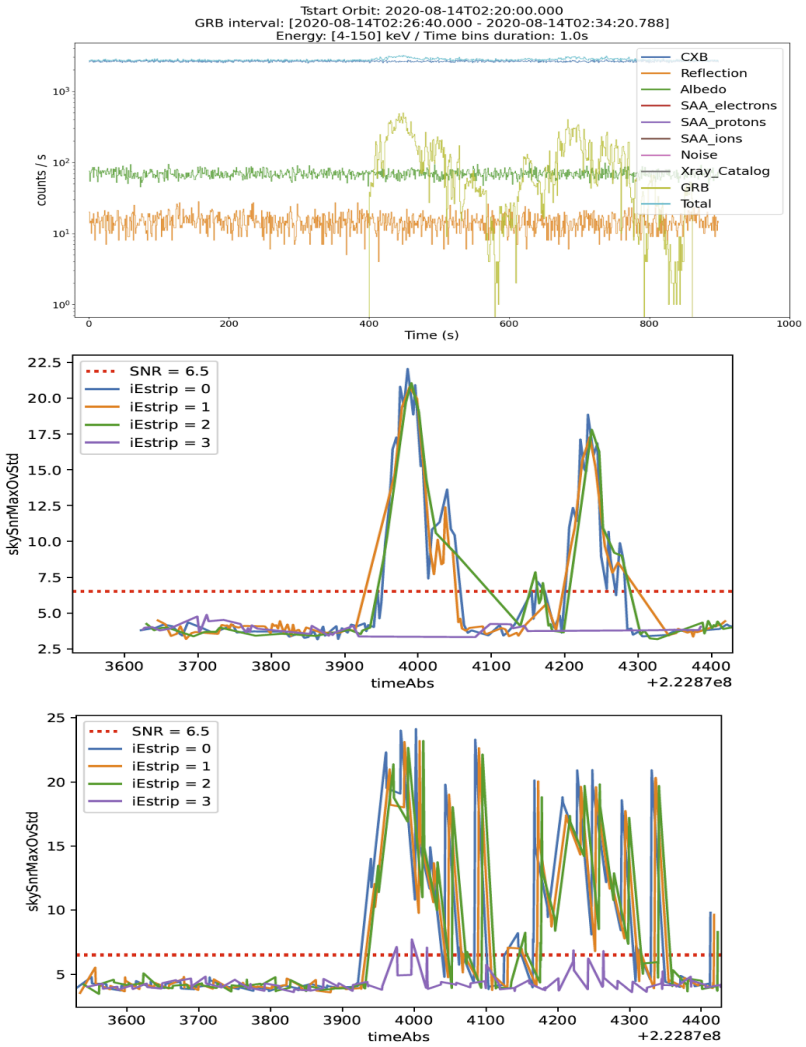

Figure 6.23: Trigger results of simulated GRB 020801. (a) Events simulated by ECLGRM software. SNR results in different energy bands performed by UGTS CRT algorithm (b) and UGTS-IMT algorithm (c), the iEstrip 0, 1, 2, 3 represent the energy band 8–120, 8–50, 20–120, 5–8 keV, respectively.

GRB 040916: weak and long GRB, failed trigger

GRB 040916 is a very long (T_{90} = 349 s), very soft (E_p = 3.5 keV) and weak burst, which was detected by the WXM. The total fluence of this burst is 4.4 x 10^{-7} erg/cm^2 in 4–150 keV, which means that the average flux of this burst is 1.26 x 10^{-9} erg/cm^2.

The trigger results are shown in Figure 6.24. UGTS can't detect this burst. It's a very

long burst stretched out over time which could explain the poor performance of the UGTS-CRT. In the other hand, the UGTS-IMT doesn't do much better. The stacking of images in the IMT process, which is useful for integrating GRB events, does not compensate the increase of the dynamic threshold correction, which takes into account the standard deviation of the summed sky images.

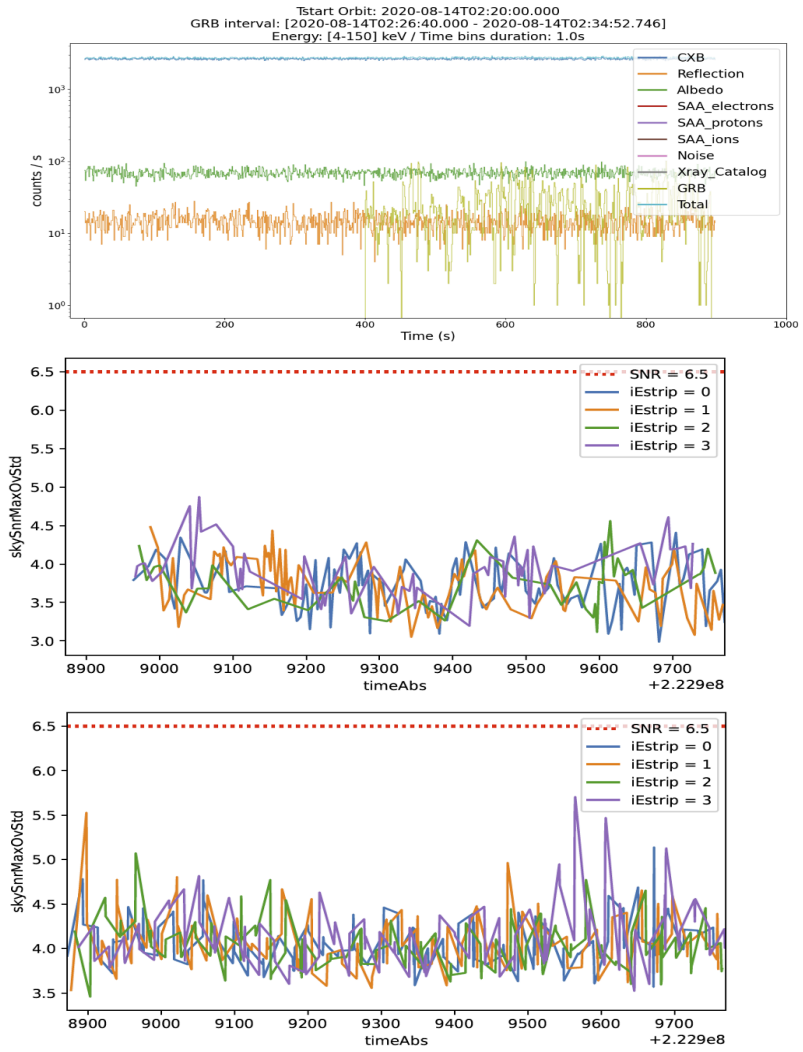

Figure 6.24: Trigger results of simulated GRB 040916. (a) Events simulated by ECLGRM software. SNR results in different energy bands performed by UGTS CRT algorithm (b) and UGTS IMT algorithm (c), the iEstrip 0, 1, 2, 3 represent the energy band 8–120, 8–50, 20–120, 5–8 keV, respectively.

6.5.4 Simulation summary

In this section, trigger simulations of a sample of 57 HETE-2 GRBs are performed by the UGTS test bench, using trigger band configurations predefined during the commissioning phase, and dynamic thresholds that take into account the standard deviation of the sky image sum. We compared the results obtained by the two methods, UGTS-CRT and

ECLGRM-CRT. We found that the SNR results obtained by UGTS and ECLGRM's CRT are consistent.

We then compared the triggering performance of CRT and IMT in UGTS and found that CRT could trigger 55 out of 57 GRBs in the sample and IMT could trigger 52. This result suggests that count rate triggering is more sensitive than image triggering for weakly long GRBs (< 40 seconds). This may be due to the stacking of images during the processing of the IMT, which is useful for integrating GRB events but does not compensate for the increase in dynamic threshold correction. Note that these conclusions apply to the population of GRBs detected by HETE-2, which is a biased sample of the full GRB population.

6.6 Conclusion and Outlook

6.6.1 Summary

In this chapter, we have studied the ECLAIRs trigger performance for different kinds of GRBs by utilizing ECLGRM software and UGTS test bench. ECLGRM is a simulation tool for the instruments ECLAIRs and GRM. It could generate the GRB event file required by the triggering software with the input GRB information (lightcurve and spectrum files). The GRBs we simulated included 57 GRBs from HETE-2 catalog with different peak energies.

We first conducted a simulation for the classical long GRBs, focusing on how the GRB positions affect the detection capabilities of ECLAIRs. The SNR values exhibited a gradual decrease from the center to the periphery. Then we tried to assess the trigger sensitivity for long GRBs (LGRBs) with varying peak energies (E_p) by utilizing the ECLGRM CRT. It is found that the sensitivity of ECLAIRs is around 10^{-8}–10^{-7} erg/cm^2/s in the 4–150 keV band for bursts with different peak energy and different positions of GRBs. For example, for a classical 30s LGRB with E_p = 200 keV, the on-axis sensitivity of ECLAIRs is 4.5×10^{-8} erg/cm^2/s for 4–150 keV, which correlates to approximately 0.91 count/cm^2/s. For an X-ray Flash with E_p = 20 keV, the on-axis and the off-axis sensitivity in the 4–150 keV band are 1.5×10^{-8} erg/cm^2/s and 3.7×10^{-8} erg/cm^2/s, respectively

We also explored the contribution of the 4–8 keV band for enhancing the trigger sensitivity for GRBs with varied peak energies. We found that this sensitivity improvement is significant for soft GRB detection, which is approximately 60% for GRB with peak energy equal to 5 keV and 20% for GRB with peak energy equal to 20 keV. For the GRB with a peak energy above 100 keV, the contribution of the 4–8 keV band becomes negligible.

We conducted the same simulations by using the HETE-2 GRB sample. In this process, the 57 GRBs with background were simulated by ECLGRM software. We found that 56 of these GRBs could successfully trigger ECLAIRs in the simulation, each with a minimum SNR > 10 in the 4–120 keV range. The bonus of the 4–8 keV band in improving detected SNR appears to increase inversely with the E_p of the GRB. It is ∼50% for GRB with E_p= 5 keV, and ∼20% for E_p = 30 keV, compared to GRBs with E_p > 30 keV, where SNR improvement is generally between 0%–20%.

Finally, to simulate a more realistic scenario, we performed trigger simulations on 57 HETE-2 GRBs using the UGTS test bench with the selected trigger band configuration used to begin the commissioning phase (5–8, 8–50, 8–120, 20–120 keV), as well as a dynamic threshold that takes into account the total sum standard deviation of the sky images. We compared the triggering performance of CRT and IMT in UGTS and found that CRT could trigger 55 out of 57 GRB of the sample and IMT could trigger 52. This result suggests that count rate triggering is more sensitive than image triggering for weakly long GRBs (< 40 seconds). This may be due to the fact that IMT' s image stacking processing, while helpful in integrating GRB events, does not compensate for the increase in dynamic threshold used to avoid false triggers induced by background residuals.

To further enhance and refine our research, the following points can be considered in the next steps.

1. In our current simulations to assess the sensitivity of ECLAIRs, we have only considered long GRBs. extending our simulations to short bursts with a duration of 1.0 s would provide more accurate sensitivity results.
2. In our GRB samples, we only used the HETE-2 sample from Pélangeon, A. et al. (2008). Those burst are Long GRBs with relative high fluence (> 10^{-7} erg/cm^2). It would be interesting to estimate the sensitivity of ECLAIRs to the weak and short GRB.
3. Throughout the simulations presented in this chapter, we have taken into account background factors like CXB, reflection, and albedo. However, to enhance accuracy, it would be more interesting to consider additional elements such as sky X-ray sources, detection plane noise as well as the impact of efficiency inhomogeneity in the 4–8 keV band, and see if, after applying the mitigation methods, we see a loss of sensitivity.

6.6.2 Discussion and Prospect

This work proves the importance of the 4–8 keV band of ECLAIRs in detecting soft GRBs. Particularly those with $E_p < 30$ keV. Although challenges such as efficiency inhomogeneity (discussed in Chapter 4) and heat-pipe noise (addressed in Chapter 5) have been identified in the 4–8 keV band, which may lead us to abandon the band in the trigger process if it impacts the whole trigger system. Our research demonstrates that the contribution of the 4–8 keV band in detecting soft GRBs is substantial. Therefore, it is worth investing in efforts to ensure the operational functionality of this energy band within the onboard trigger system.

Since ECLAIRs is more sensitive in 4–20 keV (1.9 ph/cm^2/s; N. Dagoneau et al., 2021) compared to the HETE-2/WXM (WXM: ~ 4 ph/cm^2/s; Shirasaki et al., 2000) and has a bigger FOV (ECLAIRs = 2 sr, WXM = 0.91 sr), it is expected to detect more soft GRB (like X-ray Flash) compared to the HETE-2 mission.

Compared to Swift/BAT, ECLAIRs is capable of detecting in the 4–15 keV band, whereas BAT is not, although the detection area of BAT is five times larger than that of ECLAIRs, as shown in Figure 6.25.

This is why we expect the ECLAIRs burst catalog to contain a higher proportion of X-ray-rich bursts in the future than previous missions.

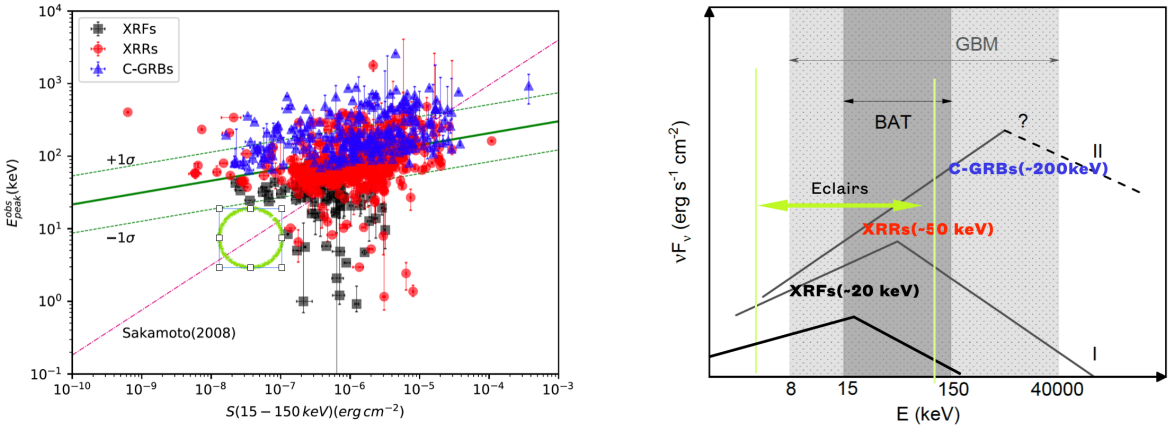

Figure 6.25: Left: scatter plot between flux and peak energy of different GRB bursts. Right: peak energy of GRBs prompt emission and energy coverage intervals for the Swift/BAT, Fermi/GBM and SVOM/ECLAIRs. Left panel from (Bi et al., 2018).

To date, only a few soft-weak GRBs have been detected (Figure 6.25). This may be because previous GRB telescopes were not sensitive enough to detect and trigger this kind of GRBs. Due to the very few detected cases, and even scarcer follow-up observations, the physical origin of this kind of GRB is also currently unknown. This kind of soft weak GRB is very interesting for SVOM, since ECLAIRs instrument has an advantage in the detection of X-ray-rich transients compared to other GRB missions. The green circle in the left panel indicates the potential discovery region for ECLAIRs to detect very soft X-ray flashes, which is determined based on the trigger sensitivity we obtained in Section 6.2.

With sensitive triggering for soft GRBs and simultaneous observations with the other SVOM telescopes on board (GRM, XRT, VT) and on the ground (GWAC, GFTs), there should be more soft GRBs (such as XRF) detected with associated high-performance multi-wavelength observation. This could be a discovery space that the SVOM mission could open up and explore.

Chapter 7

Conclusion and prospect

The SVOM mission is a combination of space and ground-based instruments designed to study gamma-ray bursts and other high-energy transients by observing them at several wavelengths. The SVOM satellite will be launched in June 2024. ECLAIRs is one of the most important telescopes on board the SVOM satellite. It works in the 4–150 kev energy range and its main task is to alert the community by transmitting the location, light curve and spectrum of new sources as quickly as possible.

In 2021, the ECLAIRs telescope underwent various calibration campaigns in vacuum test chambers to evaluate its performance. I made a detailed analysis of the datasets of the 2021 campaigns. Intriguingly, I found some effects that degrade the performances in the 4–8 keV band. These effects include some inhomogeneities in the detector pixels efficiency, and an additional noise on two regions of the detection plane, in proximity to the heat pipes. Due to this spatial proximity, we call it the heat-pipe noise.

7.1 Inhomogeneity of the detection plane

This part is detailed in Chapter 4 and led to the writing of a paper published in the A&A journal (Xie et al., 2024).

- I studied the details of the inhomogeneity property, and identify three populations of the pixels in the detection plane: Low Efficiency Pixels (LEP, $\sim$ 2000 pixels), High Efficiency Pixels (HEP, $\sim$ 4000 pixels), and High Threshold Pixels (HTP, 400 pixels).
- I analyzed the inhomogeneity of the detection plane in different energies, and found that the efficiency difference between LEP and HEP decreases with the energy in the 4–8 keV band, the difference could be described with a linear function.
- Based on the dataset from the experiment, I calculated the pixel efficiency of both LEP and HEP populations at 5.9 keV. And for the first time, obtain the ECLAIRs effective area in 4–8 keV taking into account the degradation of efficiency inhomogeneity.

- There was some confusion in the transmission of MLI when I analyzed the dataset from Toulouse. I clarified the transmission of MLI by performing a dedicated test in CEA and combining it with theoretical calculations.

- I performed a dedicated simulation to study the impact of the inhomogeneity on the onboard trigger performance. To solve the impact of the inhomogeneity, I proposed an efficiency compensation based on the spectrum of CXB, and verified this method by the simulation.

- To better understand the ECLAIRs performance in space, I proposed several approaches to acquire the absolute efficiency of ECLAIRs during the commission phase.

7.2 Heat-pipe noise

This part is detailed in Chapter 5 and led to the writing of a paper published in the A&A journal (Xie et al., 2024).

- I studied the energetic, temporal and spatial character of heat pipe noise by analyzing the TVAC data set, which only includes background.

- I made a dedicated simulation to study the heat-pipe noise impact on ECLAIRs trigger performance in different timescales from 10 ms to 20 min, focused on the false trigger rate and the increment of the trigger threshold. This simulation mainly combined the heat-pipe noise data with the simulated CXB background and then performed the trigger algorithm.

- I proposed a mitigation solution for the impact of the heat-pipes noise, which is to find the noisy pixels and ignore them in the trigger algorithm. I developed two algorithms to select the noisy pixels onboard, named frequency selection and distribution selection. By applying the mitigation methods in the simulation of the 4-8 keV band, the false trigger rate from 99.26% was reduced to 0%, the increment of the trigger threshold from $\sim$ 100% to $\sim$ 10 %

- To apply this method in the future when ECLAIRs operates in space. I worked with Nathan Van Hille (CEA) to integrate this selection method into the ECLAIRs instrument center toolbox. This tool could be used to select the noisy pixels and generate the pixel weight matrix that applies in the ECLAIRs triggering system. Related to this subject, I also proposed and developed a strategy to select the heat-pipe noisy pixels when ECLAIRs is operating in space, during periods of earth occultation when the CXB background noise is absent, which increases our sensitivity for detecting noisy pixels.

- From September to October 2023, the SVOM flight model was undergoing a series of thermal vacuum tests in Shanghai. I analyzed this recent data and found that the heat pipe noise observed in 2021 in Toulouse was not present at that time. I used the

Shanghai data combined with a simulated CXB background to run the trigger simulation. It turned out that the level of the background noise during the Shanghai tests could not cause false triggers and had a negligible impact on the trigger threshold.

Between these two campaigns, the ECLAIRs telescope was not in the same configuration. In Toulouse, the telescope's heat pipes were in a vertical configuration, whereas in Shanghai the heat pipes were in a horizontal configuration. As a result, the absence of noise observed in Shanghai could suggest that the problem is linked to the impact of gravity on the fluid circulating in the heat pipes.

7.3 ECLAIRs detection simulation for different kinds of GRBs

This part is detailed in Chapter 6. In this work, I mainly make the simulation of ECLAIRs detection by utilizing the ECLGRM tools developed by different institutions (CNRS, CEA, CNES) and the real trigger hardware UGTS. To evaluate the ECLAIRs trigger performance, I generated the classical GRBs with different peak energies and the HETE-2 GRBs, Then combined them with the simulated background. The main objective is to estimate the advantage of the 4–8 keV band in the detection of soft GRBs.

- I have developed the package to generate the customized GRBs, with different spectrum and light curve parameters that the users wanted. I embedded this tool into the ECLGRM framework. With this tool, the user could generate GRB input files necessary by ECLGRM.
- I simulated Long GRBs detected by ECLAIRs with different peak energy, which represents the different types of GRBs: Classical GRBs (Ep > 100 keV), X-ray rich GRBs (XRRs, 30 keV > E_p > 100 keV) and X-ray flashs (XRFs, E_p < 30 keV). With this simulation, I estimated the trigger sensitivity for those GRBs in different positions in the FOV.
- I got the improvement of ECLAIRs trigger sensitivity thanks to the 4–8 keV band for different types of GRBs. It is notable that the lower the peak energy of GRB, the more bonus of sensitivity improvement given by the 4–8 keV band. If ECLAIRs detected a GRB with E_p = 5 keV, the 4–8 keV band could improve sensitivity by 60%.
- To have a more accurate simulation, I used the HETE-2 GRBs sample to replace the customized GRBs in the simulation. In this way, we can estimate the detection performance of HETE-2 GRBs with ECLAIRs. We can also get an idea of how the 4–8 keV band might improve the detection of individual bursts. As expected, we find that with the softest GRB, the SNR improves more significantly after involving the 4–8 keV band.
- Finally, I used the UGTS test bench to perform the real trigger for the simulated HETE-2 GRB samples (both count-rate trigger and image trigger), with a trigger band

configuration pre-determined during the commissioning phase (5–8, 8–50, 8–120, 20–120 keV), as well as a dynamic threshold that takes into account the background fluctuations. We compared the performance of count-rate trigger and image trigger in UGTS and found that count-rate trigger could detect 55 out of 57 GRBs and image trigger could detect 52 GRBs. This result suggests that count rate trigger is more sensitive than image trigger for weak-medium-long GRBs (< 40 seconds).

7.4 Prospects

- **Preparing tools for the operation of ECLAIRs instruments in the commissioning phase**

  During the recent tests in Shanghai (October 2023), we did not observe the appearance of heat pipe noise, but it may appear in orbit in the future. It is therefore necessary to prepare tools for this purpose in order to ensure the scientific results of SVOM. This tool is capable of removing the effects of potential heat-pipe noise in orbit by the methods I have proposed.

- **Combined detection of SVOM and EP can detect prompt emissions down to 0.5 keV.**

  In January 2024, China launched a wide-field X-ray telescope called Einstein Probe (EP). The aim of the EP mission is to detect transient sources in the 0.5–5 keV band using a set of wide-field X-ray cameras and to study the afterglow emission in the 0.3–10 keV band using two follow-up X-ray telescopes. However, it will be difficult to determine the nature of the transient source using the EP mission alone. A cooperative detection between SVOM and EP could be set up to solve this problem. This joint detection could improve the detection capabilities of both and lead to more interesting scientific discoveries. The advantage for SVOM would be to extend the detection range for transient emission down to 0.5 keV, and EP could benefit from SVOM's multi-wavelength observations.

- **Scientific exploitation based on observations from ECLAIRs**

  In the future, based on the sensitivity advantage of ECLAIRs in the 4–15 keV band (compared to HETE-2 and Swift) and the combination of simultaneous multi-wavelength observations with both on-board telescopes and ground-based telescopes, it will be possible to make breakthroughs in the study of the soft GRBs. For example, the center engine of the X-ray flash, the jet structure, and the outburst environment.

  The SVOM project was delayed for various reasons, but mainly because of the Covid-19 epidemic, which penalized developments in France and China. Initially I should have processed and analyzed real ECLAIRS data collected from the sky.

  With my thesis supervisor, we reoriented my work, which was finally based on the analysis of ground calibrations and associated numerical simulations. The results obtained make me even more enthusiastic about processing the real data and taking part in the SVOM scientific adventure.

On a personal note, if I can remain in the SVOM collaboration after my thesis, I would like to go in the direction studied in this thesis and set up a research project focusing on the study of X-ray rich bursts.

References

Abbott, B et al. (Oct. 2017). "Gravitational Waves and Gamma-Rays from a Binary Neutron Star Merger: GW170817 and GRB 170817A". In: *The Astrophysical Journal Letters* 848.2, p. L13. ISSN: 2041-8205. DOI: 10.3847/2041-8213/aa920c. URL: https://dx.doi.org/10.3847/2041-8213/aa920c (visited on 03/05/2024).

Abbott, B. et al. (June 2009). "LIGO: The Laser Interferometer Gravitational-Wave Observatory". In: *Reports on Progress in Physics* 72.7, p. 076901. ISSN: 0034-4885. DOI: 10.1088/0034-4885/72/7/076901. (Visited on 03/08/2024).

Abbott, Benjamin P et al. (2017). "Gravitational waves and gamma-rays from a binary neutron star merger: GW170817 and GRB 170817A". In: *The Astrophysical Journal Letters* 848.2, p. L13.

Acernese, F. et al. (Jan. 2015). "Advanced Virgo: A Second-Generation Interferometric Gravitational Wave Detector". In: *Classical and Quantum Gravity* 32, p. 024001. ISSN: 0264-9381. DOI: 10.1088/0264-9381/32/2/024001. (Visited on 03/08/2024).

Amati, Lorenzo (Oct. 1, 2006). "The Ep,i-Eiso Correlation in Gamma-Ray Bursts: Updated Observational Status, Re-Analysis and Main Implications". In: *Monthly Notices of the Royal Astronomical Society* 372, pp. 233–245. ISSN: 0035-8711. DOI: 10.1111/j.1365-2966.2006.10840.x. URL: https://ui.adsabs.harvard.edu/abs/2006MNRAS.372..233A (visited on 03/05/2024).

An, Zheng-Hua et al. (Mar. 1, 2023). *Insight-HXMT and GECAM-C Observations of the Brightest-of-All-Time GRB 221009A*. arXiv e-prints. DOI: 10.48550/arXiv.2303.01203. URL: https://ui.adsabs.harvard.edu/abs/2023arXiv230301203A (visited on 03/05/2024). preprint.

Antier-Farfar, Mme Sarah (2016). "La détection des sursauts gamma par le télescope ECLAIRs pour la mission spatiale SVOM". l' Université Paris-Sud. URL: https://theses.hal.science/tel-01456239.

Arcier, B. (Oct. 2022). "Detection of High-Energy Transients with SVOM/ECLAIRs". URL: https://theses.hal.science/tel-04147209/document (visited on 02/16/2024).

Atteia, J.-L., B. Cordier, and J. Wei (Apr. 2022). "The SVOM Mission". In: *International Journal of Modern Physics D* 31.05, p. 2230008. ISSN: 0218-2718. DOI: 10.1142/S0218271822300087. URL: https://www.worldscientific.com/doi/abs/10.1142/S0218271822300087 (visited on 09/23/2023).

Atwood, W. B. et al. (May 2009). "THE LARGE AREA TELESCOPE ON THE FERMI GAMMA-RAY SPACE TELESCOPE MISSION". In: *The Astrophysical Journal* 697.2, p. 1071. ISSN: 0004-637X. DOI: 10.1088/0004-637X/697/2/1071. URL: https://dx.doi.org/10.1088/0004-637X/697/2/1071 (visited on 01/29/2024).

Bajat, Armelle (2018). "2018_Bajat_Thesis.Pdf". URL: http://thesesups.ups-tlse.fr/4060/1/2018TOU30151.pdf.

Band, D. et al. (Aug. 1, 1993). "BATSE Observations of Gamma-Ray Burst Spectra. I. Spectral Diversity". In: *The Astrophysical Journal* 413, p. 281. ISSN: 0004-637X. DOI: 10.1086/172995. URL: https://ui.adsabs.harvard.edu/abs/1993ApJ...413..281B (visited on 02/25/2024).

Basa, Stéphane et al. (Aug. 26, 2022). "COLIBRI, a Wide-Field 1.3 m Robotic Telescope Dedicated to the Transient Sky". In: *Ground-Based and Airborne Telescopes IX*. Ground-Based and Airborne Telescopes IX. Vol. 12182. SPIE, pp. 602–613. DOI: 10.1117/12.2627139. URL: https://www.spiedigitallibrary.org/conference-proceedings-of-spie/12182/121821S/COLIBRI-a-wide-field-13-m-robotic-telescope-dedicated-to/10.1117/12.2627139.full (visited on 02/10/2024).

Bi, Xiongwei et al. (Oct. 2018). "Statistical Study of the Swift X-Ray Flash and X-Ray Rich Gamma-Ray Bursts". In: *The Astrophysical Journal* 866, p. 97. ISSN: 0004-637X. DOI: 10.3847/1538-4357/aadcf8. (Visited on 03/07/2024).

Blandford, R. D. and R. L. Znajek (May 1, 1977). "Electromagnetic Extraction of Energy from Kerr Black Holes." In: *Monthly Notices of the Royal Astronomical Society* 179, pp. 433–456. ISSN: 0035-8711. DOI: 10.1093/mnras/179.3.433. URL: https://ui.adsabs.harvard.edu/abs/1977MNRAS.179..433B (visited on 03/01/2024).

Boella, G. et al. (Apr. 1997). "BeppoSAX, the Wide Band Mission for X-ray Astronomy". In: *Astronomy and Astrophysics Supplement Series* 122.2, pp. 299–307. ISSN: 0365-0138, 1286-4846. DOI: 10.1051/aas:1997136. URL: http://aas.aanda.org/10.1051/aas:1997136 (visited on 08/07/2023).

Bošnjak, Ž. et al. (Jan. 2014). "The Spectral Catalogue of INTEGRAL Gamma-Ray Bursts. Results of the Joint IBIS/SPI Spectral Analysis". In: *Astronomy and Astrophysics* 561, A25. ISSN: 0004-6361. DOI: 10.1051/0004-6361/201322256. (Visited on 06/16/2024).

Cano, Zach et al. (2017). "The Observer's Guide to the Gamma-Ray Burst-Supernova Connection". In: *Advances in Astronomy* 2017, pp. 1–41. ISSN: 1687-7969, 1687-7977. DOI: 10.1155/2017/8929054. arXiv: 1604.03549 [astro-ph]. URL: http://arxiv.org/abs/1604.03549 (visited on 03/05/2024).

Carine, Amoros. and Rouaix. Gilbert (2011). *Rapport du contrôle dimensionnel des détecteurs CdTe (278-RP_Controle_dimensionnel_detecteurs_CdTe-V1.pdf)*. Tech. rep. IRAP.

Cenko, S. B. et al. (May 1, 2011). "Afterglow Observations of Fermi Large Area Telescope Gamma-ray Bursts and the Emerging Class of Hyper-energetic Events". In: *The Astrophysical Journal* 732, p. 29. ISSN: 0004-637X. DOI: 10.1088/0004-637X/732/

1/29. URL: https://ui.adsabs.harvard.edu/abs/2011ApJ...732...29C (visited on 03/05/2024).

Charmeau, Marie-Claire et al. (May 28, 2018). "SVOM Payload Mission Operation Concept". In: *2018 SpaceOps Conference*. 2018 SpaceOps Conference. Marseille, France: American Institute of Aeronautics and Astronautics. ISBN: 978-1-62410-562-3. DOI: 10.2514/6.2018-2655. URL: https://arc.aiaa.org/doi/10.2514/6.2018-2655 (visited on 02/11/2024).

Chen, Wei et al. (Nov. 1, 2017). "Signature of a Newborn Black Hole from the Collapse of a Supra-massive Millisecond Magnetar". In: *The Astrophysical Journal* 849, p. 119. ISSN: 0004-637X. DOI: 10.3847/1538-4357/aa8f4a. URL: https://ui.adsabs.harvard.edu/abs/2017ApJ...849..119C (visited on 03/02/2024).

Cordier, B. et al. (Dec. 2015). "The SVOM gamma-ray burst mission". In: *arXiv e-prints*, arXiv:1512.03323, arXiv:1512.03323. DOI: 10.48550/arXiv.1512.03323. arXiv: 1512.03323 [astro-ph.IM].

Costa, E. et al. (June 1, 1997). "Discovery of an X-ray Afterglow Associated with the Gamma-Ray Burst of 28 February 1997". In: *Nature* 387, pp. 783–785. ISSN: 0028-0836. DOI: 10.1038/42885. URL: https://ui.adsabs.harvard.edu/abs/1997Natur.387..783C (visited on 03/05/2024).

Cucchiara, A. et al. (June 2011). "A PHOTOMETRIC REDSHIFT OF z 9.4 FOR GRB 090429B". In: *The Astrophysical Journal* 736.1, p. 7. ISSN: 0004-637X. DOI: 10.1088/0004-637X/736/1/7. URL: https://dx.doi.org/10.1088/0004-637X/736/1/7 (visited on 03/04/2024).

Dagoneau, N and S Schanne (2022). "Astronomy The SVOM/ECLAIRs image trigger with wavelet-based background correction optimised with a one-year simulation of observations". In: *Astronomy & Astrophysics* 665, p. 40. DOI: 10.1051/0004-6361/202141891. URL: https://doi.org/10.1051/0004-6361/202141891.

Dagoneau, N. et al. (Jan. 1, 2021). "Onboard Catalogue of Known X-ray Sources for SVOM/ECLAIRs". In: *Astronomy & Astrophysics* 645, A18. ISSN: 0004-6361, 1432-0746. DOI: 10.1051/0004-6361/202038995. URL: https://www.aanda.org/articles/aa/abs/2021/01/aa38995-20/aa38995-20.html (visited on 02/13/2024).

Dagoneau, Nicolas (Oct. 2020). "Détection de sursauts gamma ultra-longs et traitement d'images embarqué pour le télescope spatial SVOM/ECLAIRs". Theses. Université Paris-Saclay. URL: https://theses.hal.science/tel-03009638.

Dai, Z. G. and T. Lu (May 1, 1998). "Gamma-Ray Burst Afterglows and Evolution of Post-burst Fireballs with Energy Injection from Strongly Magnetic Millisecond Pulsars". In: *Astronomy and Astrophysics* 333, pp. L87–L90. ISSN: 0004-6361. DOI: 10.48550/arXiv.astro-ph/9810402. URL: https://ui.adsabs.harvard.edu/abs/1998A&A...333L..87D (visited on 03/01/2024).

Dermer, C. D. and K. E. Mitman (June 2004). "External Shock Model for the Prompt Phase of Gamma Ray Bursts: Implications for GRB Source Models". In: 312, p. 301. DOI: 10.48550/arXiv.astro-ph/0301340. (Visited on 03/08/2024).

Dermer, Charles D. (Oct. 1, 2004). "Curvature Effects in Gamma-Ray Burst Colliding Shells". In: *The Astrophysical Journal* 614, pp. 284–292. ISSN: 0004-637X. DOI: 10.1086/426532. URL: https://ui.adsabs.harvard.edu/abs/2004ApJ...614..284D (visited on 03/05/2024).

Drenkhahn, G. and H. C. Spruit (Sept. 2002). "Efficient Acceleration and Radiation in Poynting Flux Powered GRB Outflows". In: *Astronomy & Astrophysics* 391.3, pp. 1141–1153. ISSN: 0004-6361, 1432-0746. DOI: 10.1051/0004-6361:20020839. (Visited on 06/18/2024).

Dubos, Sebastien et al. (2013). "Low energy characterization of Caliste HD, a fine pitch CDTE-based imaging spectrometer". In: *IEEE Transactions on Nuclear Science* 60.5, pp. 3824–3832. ISSN: 00189499. DOI: 10.1109/TNS.2013.2281572.

Emmanuel, COURTADE (2022). *2022 08 29-FIB XRDPIX compressed-MoM.pptx*. Tech. rep. SVOM XRDPIX test.

Fan, Xuewu, Gangyi Zou, Yulei Qiu, et al. (Apr. 1, 2020). "Optical Design of the Visible Telescope for the SVOM Mission". In: *Applied Optics* 59.10, p. 3049. ISSN: 1559-128X, 2155-3165. DOI: 10.1364/AO.386177. URL: https://opg.optica.org/abstract.cfm?URI=ao-59-10-3049 (visited on 10/06/2023).

Fan, Xuewu, Gangyi Zou, Jianyan Wei, et al. (2020). "The Visible Telescope onboard the Chinese-French SVOM satellite". In: *Space Telescopes and Instrumentation 2020: Optical, Infrared, and Millimeter Wave*. Ed. by Makenzie Lystrup et al. Vol. 11443. International Society for Optics and Photonics. SPIE, 114430Q. DOI: 10.1117/12.2561854. URL: https://doi.org/10.1117/12.2561854.

Friedrich, Peter et al. (Oct. 11, 2004). "The Dark Universe Observatory (DUO): Telescope Concept". In: *UV and Gamma-Ray Space Telescope Systems*. UV and Gamma-Ray Space Telescope Systems. Vol. 5488. SPIE, pp. 837–848. DOI: 10.1117/12.552526. URL: https://www.spiedigitallibrary.org/conference-proceedings-of-spie/5488/0000/The-Dark-Universe-Observatory-DUO-telescope-concept/10.1117/12.552526.full (visited on 03/06/2024).

Frontera, Filippo (Dec. 1, 2019). "The Key Role of BeppoSAX in the GRB History". In: *Rendiconti Lincei. Scienze Fisiche e Naturali* 30.1, pp. 171–184. ISSN: 1720-0776. DOI: 10.1007/s12210-019-00766-z. URL: https://doi.org/10.1007/s12210-019-00766-z (visited on 01/18/2024).

Fuentes-Fernández, J. et al. (Mar. 2020). "Optical Design of COLIBRÍ: A Fast Follow-up Telescope for Transient Events". In: *Journal of Astronomical Instrumentation* 09.01, p. 2050001. ISSN: 2251-1717, 2251-1725. DOI: 10.1142/S2251171720500014. URL: https://www.worldscientific.com/doi/10.1142/S2251171720500014 (visited on 02/10/2024).

Funaki, Minoru et al. (2007). "Development of CdTe detectors in Acrorad". In: *International Workshop on Semiconductor PET*, pp. 1–8.

Gevin, Olivier et al. (Aug. 2009). "IDeF-X ECLAIRs: A CMOS ASIC for the Readout of CdTe and CdZnTe Detectors for High Resolution Spectroscopy". In: *IEEE Transactions on Nuclear Science* 56.4, pp. 2351–2359. ISSN: 1558-1578. DOI: 10.1109/TNS.

2009.2023989. URL: https://ieeexplore.ieee.org/document/5204747 (visited on 02/20/2024).

Godet, O. et al. (2014). "The x-/gamma-ray camera ECLAIRs for the gamma-ray burst mission SVOM". In: *Space Telescopes and Instrumentation 2014: Ultraviolet to Gamma Ray* 9144, p. 914424. ISSN: 1996756X. DOI: 10.1117/12.2055507. arXiv: 1406.7759.

Godet, Olivier et al. (Sept. 2022). "On-ground calibration highlights for the SVOM/ECLAIRs camera". en. In: *Space Telescopes and Instrumentation 2022: Ultraviolet to Gamma Ray*. Ed. by Jan-Willem A. Den Herder, Kazuhiro Nakazawa, and Shouleh Nikzad. Montréal, Canada: SPIE, p. 253. DOI: 10.1117/12.2628932. URL: https://www.spiedigitallibrary.org/conference-proceedings-of-spie/12181/2628932/On-ground-calibration-highlights-for-the-SVOMECLAIRs-camera/10.1117/12.2628932.full (visited on 08/09/2023).

Goldwurm, Andrea and Aleksandra Gros (2023). "Coded Mask Instruments for Gamma-Ray Astronomy". In: pp. 1–57. DOI: 10.1007/978-981-16-4544-0_44-1. arXiv: 2305.10130 [astro-ph]. URL: http://arxiv.org/abs/2305.10130 (visited on 02/23/2024).

Goldwurm, A. et al. (2003). "The INTEGRAL/IBIS scientific data analysis*". In: *A&A* 411.1, pp. L223–L229. DOI: 10.1051/0004-6361:20031395. URL: https://doi.org/10.1051/0004-6361:20031395.

Götz, D., M. Boutelier, et al. (Apr. 1, 2023). "The Scientific Performance of the Microchannel X-ray Telescope on Board the SVOM Mission". In: *Experimental Astronomy* 55.2, pp. 487–519. ISSN: 1572-9508. DOI: 10.1007/s10686-022-09881-6. URL: https://doi.org/10.1007/s10686-022-09881-6 (visited on 09/28/2023).

Götz, D., S. Covino, et al. (June 2013). "The Polarized Gamma-Ray Burst GRB 061122". In: *Monthly Notices of the Royal Astronomical Society* 431, pp. 3550–3556. ISSN: 0035-8711. DOI: 10.1093/mnras/stt439. (Visited on 06/16/2024).

Götz, Diego et al. (Apr. 2009). "Variable Polarization Measured in the Prompt Emission of GRB 041219A Using IBIS on Board INTEGRAL". In: *The Astrophysical Journal* 695, pp. L208–L212. ISSN: 0004-637X. DOI: 10.1088/0004-637X/695/2/L208. (Visited on 06/16/2024).

Han, Xuhui et al. (June 2021). "The Automatic Observation Management System of the GWAC Network. I. System Architecture and Workflow". In: *Publications of the Astronomical Society of the Pacific* 133.1024, p. 065001. ISSN: 1538-3873. DOI: 10.1088/1538-3873/abfb4e. URL: https://dx.doi.org/10.1088/1538-3873/abfb4e (visited on 10/13/2023).

He, Jiang et al. (Oct. 2020). "In-Orbit Background Simulation Study of SVOM/GRM". In: *Astrophysics and Space Science* 365.10, p. 167. ISSN: 0004-640X, 1572-946X. DOI: 10.1007/s10509-020-03880-9. URL: https://link.springer.com/10.1007/s10509-020-03880-9 (visited on 09/27/2023).

Huang, Y. F., Z. G. Dai, and T. Lu (May 2002). "Failed Gamma-Ray Bursts and Orphan Afterglows". In: *Monthly Notices of the Royal Astronomical Society* 332.3, pp. 735–740. ISSN: 0035-8711. DOI: 10.1046/j.1365-8711.2002.05334.x. (Visited on 03/08/2024).

Kouveliotou, Chryssa et al. (Aug. 1, 1993). "Identification of Two Classes of Gamma-Ray Bursts". In: *The Astrophysical Journal* 413, p. L101. ISSN: 0004-637X. DOI: 10.1086/186969. URL: https://ui.adsabs.harvard.edu/abs/1993ApJ...413L.101K (visited on 02/25/2024).

Kulkarni, S. R. et al. (Oct. 1, 1998). "Radio Emission from the Unusual Supernova 1998bw and Its Association with the Gamma-Ray Burst of 25 April 1998". In: *Nature* 395, pp. 663–669. ISSN: 0028-0836. DOI: 10.1038/27139. URL: https://ui.adsabs.harvard.edu/abs/1998Natur.395..663K (visited on 03/05/2024).

Kumar, P. and R. Barniol Duran (Nov. 21, 2010). "External Forward Shock Origin of High-Energy Emission for Three Gamma-Ray Bursts Detected by Fermi". In: *Monthly Notices of the Royal Astronomical Society* 409.1, pp. 226–236. ISSN: 0035-8711. DOI: 10.1111/j.1365-2966.2010.17274.x. URL: https://doi.org/10.1111/j.1365-2966.2010.17274.x (visited on 02/29/2024).

Lacombe, K. et al. (Dec. 2018). "Spectral Performance of ECLAIRs Flight Detectors on SVOM Mission". In: *Astroparticle Physics* 103, pp. 131–141. ISSN: 09276505. DOI: 10.1016/j.astropartphys.2018.08.002. URL: https://linkinghub.elsevier.com/retrieve/pii/S0927650518300987 (visited on 08/04/2023).

Lamb, D. Q., T. Q. Donaghy, and C. Graziani (Feb. 2005). "A Unified Jet Model of X-Ray Flashes, X-Ray-rich Gamma-Ray Bursts, and Gamma-Ray Bursts. I. Power-Law-shaped Universal and Top-Hat-shaped Variable Opening Angle Jet Models". In: *The Astrophysical Journal* 620, pp. 355–378. ISSN: 0004-637X. DOI: 10.1086/426099. (Visited on 03/04/2024).

Le Provost, Hervé et al. (2013). "A Scientific Trigger Unit for space-based Real-Time Gamma Ray Burst detection II - Data Processing Model and benchmarks". In: *2013 IEEE Nuclear Science Symposium and Medical Imaging Conference (2013 NSS/MIC)*, pp. 1–6. DOI: 10.1109/NSSMIC.2013.6829557.

Li, Liang et al. (Sept. 2012). "A COMPREHENSIVE STUDY OF GAMMA-RAY BURST OPTICAL EMISSION. I. FLARES AND EARLY SHALLOW-DECAY COMPONENT". In: *The Astrophysical Journal* 758.1, p. 27. ISSN: 0004-637X. DOI: 10.1088/0004-637X/758/1/27. URL: https://dx.doi.org/10.1088/0004-637X/758/1/27 (visited on 03/07/2024).

LIGO et al. (Oct. 20, 2017). "Multi-Messenger Observations of a Binary Neutron Star Merger". In: *The Astrophysical Journal Letters* 848.2, p. L12. ISSN: 2041-8205, 2041-8213. DOI: 10.3847/2041-8213/aa91c9. arXiv: 1710.05833 [astro-ph, physics:gr-qc]. URL: http://arxiv.org/abs/1710.05833 (visited on 03/05/2024).

Liu, Tong et al. (Jan. 1, 2018). "Black Hole Hyperaccretion Inflow-Outflow Model. I. Long and Ultra-long Gamma-Ray Bursts". In: *The Astrophysical Journal* 852, p. 20. ISSN: 0004-

637X. DOI: 10.3847/1538-4357/aa9e4f. URL: https://ui.adsabs.harvard.edu/abs/2018ApJ...852...20L (visited on 02/29/2024).

Lloyd-Ronning, Nicole M., Xinyu Dai, and Bing Zhang (Jan. 1, 2004). "On the Structure of Quasi-universal Jets for Gamma-Ray Bursts". In: *The Astrophysical Journal* 601, pp. 371–379. ISSN: 0004-637X. DOI: 10.1086/380483. URL: https://ui.adsabs.harvard.edu/abs/2004ApJ...601..371L (visited on 03/04/2024).

Lyons, N. et al. (Feb. 1, 2010). "Can X-ray Emission Powered by a Spinning-down Magnetar Explain Some Gamma-Ray Burst Light-Curve Features?" In: *Monthly Notices of the Royal Astronomical Society* 402, pp. 705–712. ISSN: 0035-8711. DOI: 10.1111/j.1365-2966.2009.15538.x. URL: https://ui.adsabs.harvard.edu/abs/2010MNRAS.402..705L (visited on 03/04/2024).

Malesani, D. et al. (July 2004). "SN 2003lw and GRB 031203: A Bright Supernova for a Faint Gamma-Ray Burst". In: *The Astrophysical Journal* 609, pp. L5–L8. ISSN: 0004-637X. DOI: 10.1086/422684. (Visited on 06/16/2024).

Mate, Sujay et al. (Dec. 2019a). "Simulations of the SVOM/ECLAIRs Dynamic Background: A Fast, Accurate and General Approach for Wide-Field Hard X-ray Instruments". In: *Experimental Astronomy* 48.2-3, pp. 171–198. ISSN: 0922-6435, 1572-9508. DOI: 10.1007/s10686-019-09643-x. URL: http://link.springer.com/10.1007/s10686-019-09643-x (visited on 09/15/2023).

— (Nov. 2019b). "Simulations of the SVOM/ECLAIRs dynamic background: a fast, accurate and general approach for wide-field hard X-ray instruments". In: *Experimental Astronomy* 48.2–3, pp. 171–198. ISSN: 1572-9508. DOI: 10.1007/s10686-019-09643-x. URL: http://dx.doi.org/10.1007/s10686-019-09643-x.

Meegan, C. (1993). "The Burst and Transient Source Experiment". In: DOI: 10.2514/6.1993-4255. (Visited on 01/18/2024).

Meegan, Charles et al. (Sept. 1, 2009). "THE *FERMI* GAMMA-RAY BURST MONITOR". In: *The Astrophysical Journal* 702.1, pp. 791–804. ISSN: 0004-637X, 1538-4357. DOI: 10.1088/0004-637X/702/1/791. URL: https://iopscience.iop.org/article/10.1088/0004-637X/702/1/791 (visited on 01/29/2024).

Meidinger, Norbert et al. (Nov. 30, 2006). "Next Generation of pnCCDs for X-ray Spectroscopy and Imaging". In: *Nuclear Instruments and Methods in Physics Research Section A: Accelerators, Spectrometers, Detectors and Associated Equipment*. New Developments in Radiation Detectors 568.1, pp. 141–148. ISSN: 0168-9002. DOI: 10.1016/j.nima.2006.05.268. URL: https://www.sciencedirect.com/science/article/pii/S0168900206010977 (visited on 02/05/2024).

Meszaros, P. and M. J. Rees (Jan. 13, 2014). *Gamma-Ray Bursts*. DOI: 10.48550/arXiv.1401.3012. arXiv: 1401.3012 [astro-ph]. URL: http://arxiv.org/abs/1401.3012 (visited on 02/29/2024). preprint.

Mészáros, P., E. Ramirez-Ruiz, et al. (Oct. 20, 2002). "X-Ray-rich Gamma-Ray Bursts, Photospheres, and Variability". In: *The Astrophysical Journal* 578.2, p. 812. ISSN: 0004-637X.

DOI: 10.1086/342611. URL: https://iopscience.iop.org/article/10.1086/342611/meta (visited on 03/07/2024).

Mészáros, P. and M. J. Rees (Feb. 1997). "Optical and Long-Wavelength Afterglow from Gamma-Ray Bursts". In: *The Astrophysical Journal* 476, pp. 232–237. ISSN: 0004-637X. DOI: 10.1086/303625. (Visited on 05/14/2024).

Metzger, M. R. et al. (June 1, 1997). "Spectral Constraints on the Redshift of the Optical Counterpart to the gamma-Ray Burst of 8 May 1997". In: *Nature* 387, pp. 878–880. ISSN: 0028-0836. DOI: 10.1038/43132. URL: https://ui.adsabs.harvard.edu/abs/1997Natur.387..878M (visited on 02/25/2024).

Mochkovitch, R. et al. (Jan. 1993). "Gamma-Ray Bursts as Collimated Jets from Neutron Star/Black Hole Mergers". In: *Nature* 361, pp. 236–238. ISSN: 0028-0836. DOI: 10.1038/361236a0. (Visited on 05/14/2024).

Moretti, A. (2009). "A new measurement of the Cosmic X-ray background". In: *AIP Conference Proceedings* 1126, pp. 223–226. ISSN: 0094243X. DOI: 10.1063/1.3149419.

Nagataki, Shigehiro (Jan. 2018). "Theories of Central Engine for Long Gamma-Ray Bursts". In: *Reports on Progress in Physics* 81.2, p. 026901. ISSN: 0034-4885. DOI: 10.1088/1361-6633/aa97a8. URL: https://dx.doi.org/10.1088/1361-6633/aa97a8 (visited on 02/29/2024).

Narayan, Ramesh, Bohdan Paczynski, and Tsvi Piran (Aug. 1, 1992). "Gamma-Ray Bursts as the Death Throes of Massive Binary Stars". In: *The Astrophysical Journal* 395, p. L83. ISSN: 0004-637X. DOI: 10.1086/186493. URL: https://ui.adsabs.harvard.edu/abs/1992ApJ...395L..83N (visited on 03/01/2024).

Narayan, Ramesh, Tsvi Piran, and Pawan Kumar (Aug. 1, 2001). "Accretion Models of Gamma-Ray Bursts". In: *The Astrophysical Journal* 557, pp. 949–957. ISSN: 0004-637X. DOI: 10.1086/322267. URL: https://ui.adsabs.harvard.edu/abs/2001ApJ...557..949N (visited on 03/01/2024).

Niu, Bing-Li et al. (Apr. 2022). "The Simultaneous Three-channel Multicolor CCD Photometric System of the 1.2 m Telescope at Jilin Astronomical Observatory*". In: *Research in Astronomy and Astrophysics* 22.5, p. 055009. ISSN: 1674-4527. DOI: 10.1088/1674-4527/ac5afc. URL: https://dx.doi.org/10.1088/1674-4527/ac5afc (visited on 02/08/2024).

Nouvel de la Flèche, Alix et al. (Dec. 1, 2023). "CAGIRE: A Wide-Field NIR Imager for the COLIBRI 1.3 Meter Robotic Telescope". In: *Experimental Astronomy* 56.2, pp. 645–685. ISSN: 1572-9508. DOI: 10.1007/s10686-023-09903-x. URL: https://doi.org/10.1007/s10686-023-09903-x (visited on 02/10/2024).

Paczynski, Bohdan and James E. Rhoads (Nov. 1993). "Radio Transients from Gamma-Ray Bursters". In: *The Astrophysical Journal* 418, p. L5. ISSN: 0004-637X. DOI: 10.1086/187102. (Visited on 05/13/2024).

Pélangeon, A. et al. (2008). "Intrinsic properties of a complete sample of HETE-2 gamma-ray bursts* - A measure of the GRB rate in the Local Universe". In: *A&A* 491.1, pp. 157–171. DOI: 10.1051/0004-6361:200809709. URL: https://doi.org/10.1051/0004-6361:200809709.

Peterson, Laurence E. (1975). "Instrumental Technique in X-Ray Astronomy". In: *Annual Review of Astronomy and Astrophysics* 13.1, pp. 423–509. DOI: 10.1146/annurev.aa.13.090175.002231. eprint: https://doi.org/10.1146/annurev.aa.13.090175.002231. URL: https://doi.org/10.1146/annurev.aa.13.090175.002231.

Popham, Robert, S. E. Woosley, and Chris Fryer (June 1, 1999). "Hyperaccreting Black Holes and Gamma-Ray Bursts". In: *The Astrophysical Journal* 518, pp. 356–374. ISSN: 0004-637X. DOI: 10.1086/307259. URL: https://ui.adsabs.harvard.edu/abs/1999ApJ...518..356P (visited on 02/29/2024).

Qin, Ying et al. (Dec. 2012). "A COMPREHENSIVE ANALYSIS OF FERMI GAMMA-RAY BURST DATA. III. ENERGY-DEPENDENT T90 DISTRIBUTIONS OF GBM GRBs AND INSTRUMENTAL SELECTION EFFECT ON DURATION CLASSIFICATION". In: *The Astrophysical Journal* 763.1, p. 15. ISSN: 0004-637X. DOI: 10.1088/0004-637X/763/1/15. URL: https://dx.doi.org/10.1088/0004-637X/763/1/15 (visited on 03/07/2024).

Rees, M. J. and P. Meszaros (Sept. 1, 1992). "Relativistic Fireballs - Energy Conversion and Time-Scales." In: *Monthly Notices of the Royal Astronomical Society* 258, p. 41. ISSN: 0035-8711. DOI: 10.1093/mnras/258.1.41P. URL: https://ui.adsabs.harvard.edu/abs/1992MNRAS.258P..41R (visited on 02/25/2024).

Remoué, N. et al. (2010). "Extensive testing of Schottky CdTe detectors for the ECLAIRs X-/gamma-ray camera on board the SVOM mission". In: *Nuclear Instruments and Methods in Physics Research, Section A: Accelerators, Spectrometers, Detectors and Associated Equipment* 618.1-3, pp. 199–208. ISSN: 01689002. DOI: 10.1016/j.nima.2010.02.137. arXiv: 1003.0455.

Rhoads, James E. (Nov. 1, 1999). "The Dynamics and Light Curves of Beamed Gamma-Ray Burst Afterglows". In: *The Astrophysical Journal* 525, pp. 737–749. ISSN: 0004-637X. DOI: 10.1086/307907. URL: https://ui.adsabs.harvard.edu/abs/1999ApJ...525..737R (visited on 02/25/2024).

Sakamoto, T et al. (July 2011). "The Second Swift Burst Alert Telescope Gamma-Ray Burst Catalog". In: *The Astrophysical Journal Supplement Series* 195, p. 2. ISSN: 0067-0049. DOI: 10.1088/0067-0049/195/1/2. (Visited on 06/19/2024).

Sakamoto, T. et al. (May 2005). "Global Characteristics of X-ray Flashes and X-ray Rich GRBs Observed by HETE-2". In: *Nuovo Cimento C Geophysics Space Physics C* 28, p. 339. ISSN: 0390-5551. DOI: 10.1393/ncc/i2005-10055-y. (Visited on 03/04/2024).

Sakamoto, Takanori et al. (2008). "Global properties of X-ray flashes and X-ray-rich gamma-ray bursts observed by Swift". In: *The Astrophysical Journal* 679.1, p. 570.

Salafia, O. S. et al. (July 1, 2015). "Structure of Gamma-Ray Burst Jets: Intrinsic versus Apparent Properties". In: *Monthly Notices of the Royal Astronomical Society* 450, pp. 3549–3558. ISSN: 0035-8711. DOI: 10.1093/mnras/stv766. URL: https://ui.adsabs.harvard.edu/abs/2015MNRAS.450.3549S (visited on 03/04/2024).

Sari, Re'em, Tsvi Piran, and J. P. Halpern (July 1, 1999). "Jets in Gamma-Ray Bursts". In: *The Astrophysical Journal* 519, pp. L17–L20. ISSN: 0004-637X. DOI: 10.1086/312109.

URL: https://ui.adsabs.harvard.edu/abs/1999ApJ...519L..17S (visited on 03/04/2024).

Sari, Re'em, Tsvi Piran, and Ramesh Narayan (Apr. 1, 1998). "Spectra and Light Curves of Gamma-Ray Burst Afterglows". In: *The Astrophysical Journal* 497, pp. L17–L20. ISSN: 0004-637X. DOI: 10.1086/311269. URL: https://ui.adsabs.harvard.edu/abs/1998ApJ...497L..17S (visited on 02/25/2024).

Savchenko, V. et al. (Oct. 2017). "INTEGRAL Detection of the First Prompt Gamma-Ray Signal Coincident with the Gravitational-wave Event GW170817". In: *The Astrophysical Journal* 848, p. L15. ISSN: 0004-637X. DOI: 10.3847/2041-8213/aa8f94. (Visited on 06/16/2024).

Schanne, S. et al. (Jan. 2019). "The SVOM ECLAIRs gamma-ray burst trigger". In: Mem. Soc. Astron. Italiana 90, p. 267.

Schanne, Stéphane, Bertrand Cordier, et al. (2014). "The ECLAIRs GRB-trigger telescopeonboard the future mission SVOM". In: *Proceedings of Science* December 2014, pp. 1–6. ISSN: 18248039. arXiv: 1508.05851.

Schanne, Stéphane, Hervé Le Provost, et al. (2013). "A Scientific Trigger Unit for space-based real-time gamma ray burst detection I - Scientific software model and simulations". In: *2013 IEEE Nuclear Science Symposium and Medical Imaging Conference (2013 NSS/MIC)*, pp. 1–5. DOI: 10.1109/NSSMIC.2013.6829408.

Shirasaki, Y. et al. (Jan. 1, 2000). "Wide-Field X-ray Monitor for HETE-II". In: *Advances in Space Research*. Broad Band X-Ray Spectra of Cosmic Sources 25.3, pp. 893–896. ISSN: 0273-1177. DOI: 10.1016/S0273-1177(99)00862-5. URL: https://www.sciencedirect.com/science/article/pii/S0273117799008625 (visited on 12/26/2023).

Siegel, Daniel M., Riccardo Ciolfi, and Luciano Rezzolla (Apr. 1, 2014). "Magnetically Driven Winds from Differentially Rotating Neutron Stars and X-Ray Afterglows of Short Gamma-Ray Bursts". In: *The Astrophysical Journal* 785, p. L6. ISSN: 0004-637X. DOI: 10.1088/2041-8205/785/1/L6. URL: https://ui.adsabs.harvard.edu/abs/2014ApJ...785L...6S (visited on 03/01/2024).

Sizun, Patrick (2011). *Synthesis of ECLAIRs Geant4 Simulations*. Tech. rep.

Skinner, Gerald K. (May 1, 2008). "Sensitivity of Coded Mask Telescopes". In: *Applied Optics* 47, pp. 2739–2749. ISSN: 0003-6935. DOI: 10.1364/AO.47.002739. URL: https://ui.adsabs.harvard.edu/abs/2008ApOpt..47.2739S (visited on 02/23/2024).

Stanek, K. Z. et al. (July 1, 2003). "Spectroscopic Discovery of the Supernova 2003dh Associated with GRB 030329". In: *The Astrophysical Journal* 591, pp. L17–L20. ISSN: 0004-637X. DOI: 10.1086/376976. URL: https://ui.adsabs.harvard.edu/abs/2003ApJ...591L..17S (visited on 02/25/2024).

Starling, R. L. C. et al. (Dec. 2012). "A Search for Thermal X-ray Signatures in Gamma-Ray Bursts - I. Swift Bursts with Optical Supernovae". In: *Monthly Notices of the Royal Astronomical Society* 427.4, pp. 2950–2964. ISSN: 0035-8711, 1365-2966. DOI: 10.1111/j.1365-2966.2012.22116.x. (Visited on 03/08/2024).

Thompson, C. (Oct. 1, 1994). "A Model of Gamma-Ray Bursts." In: *Monthly Notices of the Royal Astronomical Society* 270, pp. 480–498. ISSN: 0035-8711. DOI: 10.1093/mnras/270.3.480. URL: https://ui.adsabs.harvard.edu/abs/1994MNRAS.270..480T (visited on 03/01/2024).

Usov, V. V. (June 1, 1992). "Millisecond Pulsars with Extremely Strong Magnetic Fields as a Cosmological Source of Gamma-Ray Bursts". In: *Nature* 357, pp. 472–474. ISSN: 0028-0836. DOI: 10.1038/357472a0. URL: https://ui.adsabs.harvard.edu/abs/1992Natur.357..472U (visited on 03/01/2024).

Vasileiou, V. et al. (June 4, 2013). "Constraints on Lorentz Invariance Violation from Fermi-Large Area Telescope Observations of Gamma-Ray Bursts". In: *Physical Review D* 87.12, p. 122001. DOI: 10.1103/PhysRevD.87.122001. URL: https://link.aps.org/doi/10.1103/PhysRevD.87.122001 (visited on 02/29/2024).

Villar, V. A. et al. (Dec. 1, 2017). "The Combined Ultraviolet, Optical, and Near-infrared Light Curves of the Kilonova Associated with the Binary Neutron Star Merger GW170817: Unified Data Set, Analytic Models, and Physical Implications". In: *The Astrophysical Journal* 851, p. L21. ISSN: 0004-637X. DOI: 10.3847/2041-8213/aa9c84. URL: https://ui.adsabs.harvard.edu/abs/2017ApJ...851L..21V (visited on 03/05/2024).

Wei, J. et al. (2016). *The Deep and Transient Universe in the SVOM Era: New Challenges and Opportunities - Scientific prospects of the SVOM mission.* arXiv: 1610.06892 [astro-ph.IM].

Wen, Xing et al. (2021). "Calibration study of the Gamma-Ray Monitor onboard the SVOM satellite". In: *Nuclear Instruments and Methods in Physics Research Section A: Accelerators, Spectrometers, Detectors and Associated Equipment* 1003, p. 165301. ISSN: 0168-9002. DOI: https://doi.org/10.1016/j.nima.2021.165301. URL: https://www.sciencedirect.com/science/article/pii/S0168900221002850.

Winkler, C. et al. (Nov. 2003). "The INTEGRAL mission". In: *Astronomy & Astrophysics* 411.1, pp. L1–L6. ISSN: 0004-6361. DOI: 10.1051/0004-6361:20031288. URL: https://www.aanda.org/articles/aa/abs/2003/43/aaINTEGRAL9/aaINTEGRAL9.html.

Xie, Wenjin et al. (Mar. 1, 2024). "Study of SVOM/ECLAIRs Inhomogeneities in the Detection Plane below 8 keV and Their Mitigation for the Trigger Performances". In: *Astronomy & Astrophysics* 683, A60. ISSN: 0004-6361, 1432-0746. DOI: 10.1051/0004-6361/202347695. URL: https://www.aanda.org/articles/aa/abs/2024/03/aa47695-23/aa47695-23.html (visited on 03/06/2024).

Xin, Liping et al. (Apr. 10, 2023). "Prompt-to-Afterglow Transition of Optical Emission in a Long Gamma-Ray Burst Consistent with a Fireball". In: *Nature Astronomy* 7.6, pp. 724–730. ISSN: 2397-3366. DOI: 10.1038/s41550-023-01930-0. arXiv: 2304.04669 [astro-ph]. URL: http://arxiv.org/abs/2304.04669 (visited on 02/07/2024).

Xu, Y., L. P. Xin, X. H. Han, et al. (Sept. 1, 2021). "The GWAC Data Processing and Management System". In: 53, pp. 174–179. DOI: 10.22201/ia.14052059p.2021.53.36. URL: https://ui.adsabs.harvard.edu/abs/2021RMxAC..53..174X (visited on 10/13/2023).

Xu, Y., L. P. Xin, J. Wang, et al. (May 1, 2020). "A Real-time Automatic Validation System for Optical Transients Detected by GWAC". In: *Publications of the Astronomical Society of the Pacific* 132.1011, p. 054502. ISSN: 0004-6280, 1538-3873. DOI: 10.1088/1538-3873/ab7a73. URL: https://iopscience.iop.org/article/10.1088/1538-3873/ab7a73 (visited on 10/13/2023).

Yamazaki, Ryo, Kunihito Ioka, and Takashi Nakamura (May 1, 2002). "X-Ray Flashes from Off-Axis Gamma-Ray Bursts". In: *The Astrophysical Journal* 571, pp. L31–L35. ISSN: 0004-637X. DOI: 10.1086/341225. URL: https://ui.adsabs.harvard.edu/abs/2002ApJ...571L..31Y (visited on 03/04/2024).

Yonetoku, D. et al. (July 1, 2004). "Gamma-Ray Burst Formation Rate Inferred from the Spectral Peak Energy-Peak Luminosity Relation". In: *The Astrophysical Journal* 609, pp. 935–951. ISSN: 0004-637X. DOI: 10.1086/421285. URL: https://ui.adsabs.harvard.edu/abs/2004ApJ...609..935Y (visited on 03/05/2024).

Yuan, Weimin et al. (2022). "The Einstein Probe Mission". In: pp. 1–30. DOI: 10.1007/978-981-16-4544-0_151-1. arXiv: 2209.09763 [astro-ph]. URL: http://arxiv.org/abs/2209.09763 (visited on 10/04/2023).

Zhang, Bin-Bin et al. (Mar. 2011). "A COMPREHENSIVE ANALYSIS OF FERMI GAMMA-RAY BURST DATA. I. SPECTRAL COMPONENTS AND THE POSSIBLE PHYSICAL ORIGINS OF LAT/GBM GRBs". In: *The Astrophysical Journal* 730.2, p. 141. ISSN: 0004-637X. DOI: 10.1088/0004-637X/730/2/141. URL: https://dx.doi.org/10.1088/0004-637X/730/2/141 (visited on 02/29/2024).

Zhang, Bing (Dec. 31, 2018). *The Physics of Gamma-Ray Bursts*. 1st ed. Cambridge University Press. ISBN: 978-1-139-22653-0. DOI: 10.1017/9781139226530. URL: https://kns.cnki.net/kcms/detail/detail.aspx?FileName=TWJZ199403001&DbName=CJFD9495&DbCode=CJFD (visited on 01/28/2024).

Zhang, Bing, Xinyu Dai, et al. (Feb. 1, 2004a). "Quasi-Universal Gaussian Jets: A Unified Picture for Gamma-Ray Bursts and X-Ray Flashes". In: *The Astrophysical Journal* 601, pp. L119–L122. ISSN: 0004-637X. DOI: 10.1086/382132. URL: https://ui.adsabs.harvard.edu/abs/2004ApJ...601L.119Z (visited on 03/04/2024).

— (Feb. 2004b). "Quasi-universal Gaussian Jets: A Unified Picture for Gamma-Ray Bursts and X-Ray Flashes". In: *The Astrophysical Journal* 601. ADS Bibcode: 2004ApJ...601L.119Z, pp. L119–L122. ISSN: 0004-637X. DOI: 10.1086/382132. URL: https://ui.adsabs.harvard.edu/abs/2004ApJ...601L.119Z (visited on 03/04/2024).

Zhang, Bing, Y. Z. Fan, et al. (May 1, 2006). "Physical Processes Shaping Gamma-Ray Burst X-Ray Afterglow Light Curves: Theoretical Implications from the Swift X-Ray Telescope Observations". In: *The Astrophysical Journal* 642.1, p. 354. ISSN: 0004-637X. DOI: 10.1086/500723. URL: https://iopscience.iop.org/article/10.1086/500723/meta (visited on 03/04/2024).

Zhang, Bing and Peter Mészáros (Apr. 2001). "Gamma-Ray Burst Afterglow with Continuous Energy Injection: Signature of a Highly Magnetized Millisecond Pulsar". In: *The Astrophysical Journal* 552.1, p. L35. ISSN: 0004-637X. DOI: 10.1086/320255. (Visited on 06/19/2024).

Zhang, Bing, Bin-Bin Zhang, et al. (Oct. 1, 2009). "Discerning the Physical Origins of Cosmological Gamma-ray Bursts Based on Multiple Observational Criteria: The Cases of z = 6.7 GRB 080913, z = 8.2 GRB 090423, and Some Short/Hard GRBs". In: *The Astrophysical Journal* 703, pp. 1696–1724. ISSN: 0004-637X. DOI: 10.1088/0004-637X/703/2/1696. URL: https://ui.adsabs.harvard.edu/abs/2009ApJ...703.1696Z (visited on 03/05/2024).

Zhao, Donghua et al. (Aug. 2012). "Influence of the Earth on the background and the sensitivity of the GRM and ECLAIRs instruments aboard the Chinese-French mission SVOM". In: *Experimental Astronomy*. ISSN: 1572-9508. DOI: 10.1007/s10686-012-9313-2. URL: http://dx.doi.org/10.1007/s10686-012-9313-2.

Acknowledgments

It's the first time I've lived abroad for an extended period and these three years have given me a lot. Not only have I progressed academically, but I've also made a lot of progress in life. I've received a lot of help from my friends over these three years, and I'd like to thank my teachers, colleagues and friends from the bottom of my heart!

First of all, I'd like to thank my director, Bertrand CORDIER, who, in Chinese terms 'Shen Xian Dao Shi', is a 'magic teacher, a superb person who is hard to meet. Bertrand is a very nice person. He made me feel like family in France. He had a unique perspective on research, which helped me develop my vision and thinking. I've always felt lucky to be able to do research with him.

Secondly, I'd like to thank Nicolas DAGONEAU, my co-director, who is very young but very good at his job, very efficient and very kind. He's always able to help me find a solution to my problems, and I feel it's a pleasure to work with him.

Thanks to my colleagues, without their help, my life and work would not have gone so smoothly. Thank you to Stéphane SCHANNE, who is a very joyful and friendly person. He's the one who always gives me the most precise answers to my professional questions. Thanks to Damien TURPIN, Kamshat TAZHENOVA, Tatyana SADIBEKOVA, Clara PLASSE, Tristan BOUCHET, Leila GODINAUD and the rest of my friends, who are not only friendly colleagues but also my French teachers. We had so much fun together! Thanks to Philippe FERRANDO, Diego GOTZ, Francois DALY, Aleksandra GROS, Florence ARDELLIER-DESAGES, Christelle DUVAL, Laura RICCHI and the rest of my colleagues, who are always there to help me.

Thanks also to my Chinese friends, we had a great time playing ball together, cooking together, traveling and exploring France together. They are all very good friends. It's a privilege to be a teammate.

I would like to thank all the members of the jury for their work and advice on my thesis. They provided me with numerous comments and improved the scientific quality of my work.

Finally, I'd like to thank my family for their selfless love and support.

Remerciements

C'est la première fois que je vis à l'étranger pendant une longue période et ces trois années m'ont beaucoup apporté. J'ai non seulement progressé sur le plan académique, mais j'ai aussi beaucoup progressé dans la vie. J'ai reçu beaucoup d'aide de la part de mes amis au cours de ces trois années, et je voudrais remercier mes professeurs, mes collègues et mes amis du fond du cœur !

Tout d'abord, je voudrais remercier mon directeur, Bertrand CORDIER, qui, en termes chinois ‘Shen Xian Dao Shi', est un "professeur de magie", une personne superbe qu'il est difficile de rencontrer. Bertrand est une personne très sympathique. Il m'a fait sentir que j'étais une famille en France. Il avait un point de vue unique sur la recherche, ce qui m'a aidé à développer ma vision et ma pensée. Je me suis toujours senti chanceux de pouvoir faire de la recherche avec lui.

Ensuite, je voudrais remercier Nicolas DAGONEAU, mon co-directeur, qui est très jeune, mais qui fait très bien son travail, il est très efficace et très gentil. Il est toujours capable de m'aider à trouver une solution à mes problèmes, et je trouve que c'est un plaisir de travailler avec lui.

Merci à mes collègues, sans leur aide, ma vie et mon travail ne se seraient pas aussi bien déroulés. Merci à Stéphane SCHANNE, qui est une personne très joyeuse et sympathique. C'est à lui que j'obtiens toujours les réponses les plus précises à mes questions professionnelles. Merci à Damien TURPIN, Kamshat TAZHENOVA, Tatyana SADIBEKOVA, Clara PLASSE, Tristan BOUCHET, Leila GODINAUD et au reste de mes amis, qui sont non seulement des collègues sympathiques mais aussi mes professeurs de français. Nous nous sommes beaucoup amusés ensemble ! Merci à Philippe FERRANDO, Diego GOTZ, Francois DALY, Aleksandra GROS, Florence ARDELLIER-DESAGES, Christelle DUVAL, Laura RICCHI et au reste de mes collègues, qui sont toujours là pour m'aider.

Grâce aussi à mes amis chinois, nous avons passé de bons moments à jouer au ballon ensemble, à cuisiner ensemble, à voyager et à explorer la France ensemble. Ce sont tous de très bons amis. C'est un privilège d'être votre coéquipier.

Je voudrais remercier tous les membres du jury pour leur travail et leurs conseils sur ma thèse. ils m'ont fourni de nombreux commentaires et ont améliorer la qualité scientifique de mon travail scientifique.

Enfin, je voudrais remercier ma famille pour son amour et son support désintéressés.